Summer 8-15-2016

Crumpled Graphene Oxide: Aerosol Synthesis and Environmental Applications

Yi Jiang
Washington University in St. Louis

WASHINGTON UNIVERSITY IN ST. LOUIS

School of Engineering and Applied Science
Department of Energy, Environmental and Chemical Engineering

Dissertation Examination Committee:
Pratim Biswas, Co-Chair
John Fortner, Co-Chair
Prarag Banergee
Baolin Deng
Viatcheslav Freger
Wei-Ning Wang
Fuzhong Zhang

Crumpled Graphene Oxide: Aerosol Synthesis and Environmental Applications

By

Yi Jiang

A dissertation presented to the
Graduate School
of Washington University in
partial fulfillment of the
requirements for the degree
of Doctor of Philosophy

August 2016
St. Louis, Missouri

Contents

List of Figures

Chapter 4

Chapter 5

Chapter 6

Chapter 7

Chapter 8

List of Tables

Acknowledgements

I would like to sincerely thank my advisors, Drs. John Fortner and Pratim Biswas. Without their careful guidance, this dissertation would have never been what it is with regard to rigor and quality. I thank them for initiating and continuously supporting my doctoral project, and for the freedom I had to fully explore my research interests. They are outstanding scientists, respected leaders, and kind people. Their respect for independence, appreciation of creative ideas, and always positive outlook, will be a great source of inspiration for me in the decades to come. I also thank them for letting me have the chance to see and learn from the different approaches they take in managing a lab, training students, communicating ideas, and so on. These are experiences I will cherish for the rest of my life. Thanks to them, my doctoral study has been an enjoyable and fruitful journey. They will always be role models for me, wherever my future career takes me.

I would also like to acknowledge other members of my committee. I am particularly grateful to Dr. Wei-Ning Wang for his mentoring at the beginning of my PhD study, and for many valuable life and career suggestions. Drs. Fuzhong Zhang, Baolin Deng, Viatcheslav Freger, and Prarag Banergee were instrumental to the planning of this work, and their suggestions have considerably improved the quality of the research. I thank them for their time and efforts.

I enjoyed working with many colleagues and interns. I thank Di Liu, Dr. Ramesh Raliya, Yao Nie, Christine Le, Siyuan An, Daniel Plants, Isaac Fuhrman, Qingqing Zeng, Sungyoon Jung, Dr. Mingjun Cho, Dr. Seungsoo Lee, Dr. Fei Wu, Jiaxi Fang, Tandeep Chadha, Dr. Wenlu Li, Jiewei Wu, and Peng Liao for their contribution to this work. I would also like to express my sincere thanks to all the members of both labs - the AAQRL and the Fortner Lab. I have had a very joyful time of working in both labs, thanks to their help and assistance in many ways. Many thanks

go to the department staff, Kim Coleman, Patty Wurm, Trisha Sutton, and Rose Baxter, for their assistance. Additionally, I thank the funding support from the National Science Foundation (CBET 1454656), the United States Environmental Protection Agency (CPC1402WA009), and the McDonnell Academy Global Energy and Environment Partnership. I thank Mr. and Mrs. Buescher for kindly providing the scholarship for my first year study.

Tremendous thanks go to many friends, both near and far. They have made my PhD life much more colorful.

Finally and most importantly, I want to thank my parents. Without their unconditional love and endless support, I could have never been where I am.

Abstract of the Dissertation

Crumpled Graphene Oxide: Aerosol Synthesis and Environmental Applications
by

Yi Jiang

Doctor of Philosophy in Energy, Environmental & Chemical Engineering

Washington University in St. Louis, 2016

Professors John Fortner and Pratim Biswas (Co-Chairs)

Environmental technologies, such as for water treatment, have advanced significantly due to the rapid expansion and application of nanoscale material science and engineering. In particular, two-dimensional graphene oxide (GO), has demonstrated considerable potential for advancing and even revolutionizing some of these technologies, such as engineered photocatalysts and membranes. To realize such potential, an industrially scalable process is needed to produce monomeric and aggregation-resistant GO nanostructures/composites, in addition to new knowledge of material properties, behavior, and performance within an environmental context.

Research presented in this thesis addresses both scientific and engineering gaps through the development of a simple, yet robust aerosol-based synthesis approach and demonstrations of two applications, photocatalysts and membranes. The aerosol-based process was developed to engineer the 2D GO nanosheets into 3D crumpled balls (crumpled GO, CGO), which have excellent aggregation- and compression-resistant properties, while allowing for the incorporation (encapsulation) of other (multi)functional particles inside. The five focus areas of this dissertation are: 1) Crumpling and thermal reduction of GO nanosheets in aerosolized droplets, 2) (Multi)functional nanocomposite synthesis, 3) Colloidal behavior in water as a function of material

properties and selected environmental constituents/conditions, 4) Photocatalytic applications, 5) Composite assemblies/nanoscale fillers for advanced water treatment membranes.

Results reveal that the evaporation rate of water droplets plays a critical role in controlling the crumpling process, and thermal reduction leads to temperature-dependent removal of oxygen functional groups. (Multi)functional composites can be achieved through encapsulation of single or multiple types of nanoparticles, such as TiO_2, magnetite, and silver. Morphological transformation by crumpling, increased degree(s) of oxidation, and presence of natural organic matters act to enhance the stability of GO in water. CGO-TiO_2 composites are shown to possess superior aqueous-based photocatalytic properties, including efficient photo-reduction reaction pathways. Furthermore, assemblies of CGO nanoparticles show superior permeation, separation, and reactive (photo-reactive and antimicrobial) properties. In addition, in situ surface-based photocatalyzed synthesis of Ag nanoparticles at the surface of membrane assemblies, is demonstrated as an approach to (re)generate, thus maintain, enhanced antimicrobial activity.

This work identifies and solves several key issues regarding the industrially attractive processing and applications of (crumpled) graphene-based materials for water treatment technologies. Knowledge obtained, as part of this thesis, will impact aerosol processing of materials, environmental nanotechnology, environmental catalysis, and water treatment membrane technology, among other fields.

Chapter 1. Introduction

1.1 Motivation

Today, more than ever, adequate water quantity and quality underpin major, yet interwoven global development and sustainability foci spanning from human health to the techno-economics of energy production. Over 750 million people still lack access to improved sources of drinking water, and > 2.3 billion are without improved sanitation.[1] More than 3 million people, primarily in developing countries, die each year from water, sanitation, and hygiene-associated diseases, such as diarrheal diseases.[2] Globally, diarrheal diseases are the leading cause of illness, with 88% of diarrheal caused deaths due to a lack of access to sanitation facilities, together with unsafe drinking water and inadequate availability of water for hygiene.[1] Meanwhile, even as developed regions regularly engineer water treatment systems for common macropollutants (e.g. nitrogen) and disease-causing microbes, a wide range of micropollutants, associated with chronic health effects (e.g. halogenated organics, hormone mimicking compounds, pesticides, and heavy metals) remain difficult and costly to manage.[3]

Water quality, availability, and management are also critical for basic development and sustainability of economic activities in both developing and developed regions. This fact is particularly highlighted with regard to energy production. In 2005, thermoelectric freshwater usage alone accounted for 41% of all freshwater withdrawals in the US, surpassing irrigation-based withdrawals;[4] in 2011, direct consumption by the industrial sector, which is dominated by the thermoelectric (sub)sector, reached 46%.[5] Furthermore, and of particular concern in water-scarce regions, the issue of water availability may be exacerbated by rapid technological advancements and substantial investments in unconventional areas of energy production, such as highly water-intensive shale gas production.[6] Based on the Energy Information Administration (EIA) energy forecasts, water withdrawals will increase by 18-24% from 2010 usage to meet the expected total

energy demands in the US by 2035.[7] Effectively addressing these broad yet critical challenges must not only include an integrated policy framework focused on resource management and sustainability, but also technological advances to improve, if not revolutionize, treatment processes and strategies.[8]

In line with the rapid expansion and application of materials science and nanoscale engineering over the last two to three decades, water treatment technologies have experienced significant advances. These technologies include, among others, engineered photocatalysts for chemical degradation of pollutants and inactivation of pathogens, as well as advanced membranes for physical and chemical separation. Even more recently, treatment technologies incorporating engineered carbon nanomaterials, such as graphene, carbon nanotubes (CNT), and fullerenes, have demonstrated superior (and sometimes unique) physical and chemical properties compared to traditional analogues, and may eventually prove economically advantageous, as they are primarily composed of carbon - an abundant, available, and relatively low-cost elemental component. Further, engineered carbon nanomaterial costs continue to decline with the ongoing development of industrial scale production processes.[9-11]

In particular, graphene holds enormous promise for use in water treatment. The graphene 'gold rush' began with the unexpected discovery of a free-standing, 2D atomically-thin carbon 'film', which earned Geim and Novoselov the 2010 Nobel Prize in Physics.[12] Isolated graphene crystals, which demonstrate exceptional electronic properties, extreme surface-area-to-volume ratios, and broad (chemical) functionalization possibilities, are now being applied to a number of environmental technologies.[9] For example, graphene oxide (GO) 'paper' can be nearly impermeable to liquids, vapors, and gases, including helium. However, when appropriately modified, GO paper allows the unimpeded permeation of water (e.g., H_2O permeates through the

membranes at least 10^{10} times faster than He), making the material a promising candidate for high-quality, low-energy, low-cost separation and purification processes.[13] Although the potential for graphene-based advanced material technologies in environmental applications is easy to imagine, the science and engineering that enable production and environmental applications remain relatively nascent.

1.2 Key Scientific and Engineering Issues

To apply the numerous varieties of graphene materials in water treatment technologies, the first step is to identify the most applicable and advantageous type. Graphene is recognized as a family of materials which consists of graphene itself (a 2D framework of carbon atoms) and derivatives. The size, quality (defects), chemistry, and costs to make different 'types' can differ by orders of magnitude. While material scientists are currently (and successfully) pushing towards larger and larger defect-free graphene films for electronic/energy applications (such as those produced by roll-to-roll chemical vapor deposition), imperfect graphene oxide (GO), which is accessible, economical, and perhaps the mostly studied graphene material, may meet many of the water treatment technology needs.

With such an approach, the second issue is the scalable production and processing of GO. Currently, a major bottleneck in the scaled-up production of sheet-like materials, such as GO, is their tendency to restack due to strong van der Waals attraction.[14] Restacking reduces the potential for processing by solution techniques, and it also compromises favorable properties such as accessible surface area. Moreover, the most immediate application for graphene in environmental applications is likely its use as a composite material.[9] Common solution-based approaches to make composite nanomterials at an industrial scale can be difficult, because increasing the reaction volumes during syntheses often results in changes to crystallite size, shape, and monodispersity as

well as to the overall architecture and composition of the resulting material. These challenges require new, robust, affordable, and controllable engineering approaches to make tailored GO materials.

Third, new knowledge is needed to correlate GO material behaviors in water with material properties and environmental constituents (e.g., natural organic matters). This issue is complicated by the complexity of possible chemical and physical variations of GO, and the lack of convenient and consistently reproducible techniques for characterizing and controlling these properties. This knowledge is essential to realizing practical applications of graphene-enabled technologies for water treatment.

Finally, the supply side (a promising candidate material of comparative advantages, here as GO) needs to be continuously aligned with the demand side (a desired technological evolution or revolution in water treatment), through appropriate engineering approaches. Evaluating and discussing next-generation water treatment technologies, Shannon et al.[8] have outlined a few basic principles in an influential review article published in *Nature*, emphasizing lower cost, reduced energy usage, minimized use of chemicals, and minimal impact on the environment. When considering the complexity of the problems we are facing, ultimately, future solutions will likely involve a mixed matrix of technologies, both conventional and new.

While it is difficult to imagine what a 'holy grail' solution/technology would look like, if there will be one, it is likely to be solar driven to some degree. The harvesting and converting of photons enabled by engineered nanostructures and advanced materials is likely to have significant potential in future disinfection and decontamination technologiess.[8] However, critical issues must still be addressed for photocatalysts to be applicable at the needed scale. These challenges include extension of the light absorption range (in particular, into the visible range), reduction of hole-

electron recombination, targeted utilization of hole and electron for various reactions (applications), and recycling of photocatalysts.

Another technology that is being considered as an integrated part of next-generation water treatment facilities is membrane-based processes. Due to their high separation efficacies, low chemical inputs, relatively low energy consumption, modest space requirements, and overall simplicity of operation, global deployment of membrane technologies is rapidly increasing. They are also being demonstrated in a number of showcase projects for next-generation water treatment (e.g., Singaporean NEWater). The employment of advanced materials will likely make possible the concurrent pursuit of high permeability and satisfying rejection and anti-fouling properties. In addition, new functions can be enabled by the broad functionalization possibilities of GO, such as simultaneous decontamination and/or disinfection.

1.3 Objectives and Approaches

This work addresses the key issues highlighted above, and bridges scientific and engineering gaps in treatment technologies which incorporate graphene oxide. The overarching objective for this work is the development, characterization, and demonstration of three dimensional, nanoscale, crumpled graphene oxide (CGO) platform materials (Figure 1.1), as multifunctional, advanced photocatalyts and as novel membrane film assembly components.

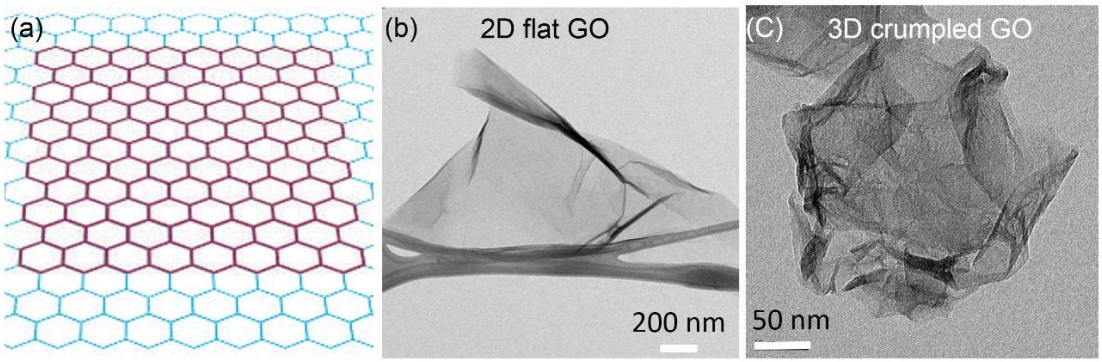

Figure 1.1 (a) Graphene: a layer of honeycomb-like carbon structure (source: Geim et al., 2007) [9]; (b) TEM image of 2D flat GO; (c) TEM image of 3D Crumpled GO.

Three broad research objectives, are as follows:

Objective G1−Material synthesis and material behavior in water

1) Understand physical and chemical transformations of GO sheets during aerosol processing
2) Synthesize a library of composite materials using well controlled aerosol methodologies
3) Correlate colloidal behavior with material properties and environmental conditions

The physical and chemical properties of GO/CGO were characterized by both in-line measurements (aerosol particle sizing) and off-line (microscopic and spectroscopic) measurements. These data yielded a fundamental understanding of temperature-dependent property evolution of GO. Further, these data allow us to relate the process parameters (such as the furnace temperature and types of precursor and aerosol generator) to realize consistent (reproducible) control of material properties. The process is also described by a universally applicable equation relating the confinement force and various parameters. Based on the newly generated knowledge, a library of CGO nanocomposites have been developed and characterized, including CGO-TiO_2 (GOTI), CGO-Magnetite (GOM), CGO-Ag (GOAg), and ternary CGO-TiO_2-Magnetite (GOTIM). Further,

these material properties have been correlated with aqueous colloidal behavior (such as the critical coagulation concentrations). Major material factors taken into consideration were ζ-potential, C/O ratios, carboxyl group concentrations, and C-C fractions, in addition to environmental factors, such as pH, ionic strength, and natural organic matters. The colloidal behavior was also described using DLVO theory.

Objective G2−Photocatalyst development and application

4) Develop and evaluate magnetically recoverable, high-performance photocatalysts

5) Fundamentally describe the reaction mechanisms of CGO-TiO_2 in aqueous systems

6) Synthesize metal nanoparticles via (ion) reduction reaction pathways

A ternary CGO-TiO_2-Magnetite (GOTIM) nanocomposite has been developed as a recyclable, high-performance photocatalyst. Its photocatalytic performance enhancement was evaluated and described via the degradation of model dye molecules (methyl orange). In addition, its low field magnetic susceptibility was demonstrated. Detailed reaction mechanisms of photo-induced electrons and holes have been examined by using a suite of hole and radical scavengers (EDTA, *tert*-butanol, catalase), in both oxic and anoxic conditions. In situ formation of Ag NPs on GOTI via photocatalytic reduction of Ag^+ was also demonstrated and characterized under both UV and solar light irradiations. A detailed characterization of as-synthesized Ag NPs (shape, size (evolution) with reaction time, crystal structure) was performed with high-resolution transmission electron microscopy techniques.

Objective G3−Membrane development and application

7) Develop a process to assemble CGOs as composite membranes

8) Characterize and evaluate the as-synthesized membranes

9) Develop a photoreduction-based in situ regenerative antimicrobial strategy

10) Fabrication of polymeric UF membranes incorporated with GO/CGO particles

A simple vacuum filtration method, along with a chemical cross-linking scheme, was designed and employed to deposit CGO nanostructures onto a polyethersulfone (PES) support to produce a composite membrane structure. Extensive membrane characterization using SEM, FTIR, AFM, and water contact angle measurement techniques was performed and reported for each membrane employed. Membrane permeation was evaluated in a dead-end constant pressure mode, and filtration capacity was evaluated by filtering molecules of two different sizes, methyl orange and bovine serum albumin. Reactivity was evaluated by degradation of the dye molecule (methyl orange) in a customized filtration set-up with UV irradiation (photo-reactivity), or by inactivation of two bacteria, *Escherichia coli* and *Bacillus subtilis* (antimicrobial). Based on the knowledge obtained in Objective G2, in situ formation of Ag NPs on the membrane surface was also demonstrated and evaluated, showing enhanced and regenerative antimicrobial activity. Further, as an alternative strategy, GO/CGO particles were incorporated into polymeric ultrafiltration membranes (e.g., polysulfone) during the phase inversion process, leading to augmented water flux while maintaining rejection performances.

1.4 Dissertation Organization

The dissertation begins with the identification of key scientific and engineering issues that currently need to be addressed, followed by a related technical overview of the current literature/state of the art. In Chapter 2, graphene, as a family of materials, is briefly described, followed by an introduction of the key elements of an aerosol process (used to crumple 2D GO, chapter 3). The chapter ends with an overview of environmental applications/technologies incorporating GO, focused on photocatalyst and membrane applications. This chapter is designed

to provide the technical background for the dissertation, while highlighting the opportunities and challenges for future advanced GO applications.

Chapter 3 addresses the physical aspect (crumpling) of GO during the aerosol synthesis process. A detailed understanding of the crumpling of GO nanosheets is presented by a systematic investigation conducted in aerosolized droplets by means of in-line measurements (e.g., scanning mobility particle sizer) and off-line (e.g., electron microscopy) measurements. The relationship between confinement force and various parameters, such as the evaporation rate and precursor concentration, is mathematically established. This chapter reveals the importance of the evaporation rate of aerosolized droplets in controlling the crumpling process.

Chapter 4 addresses the chemical aspect (thermal reduction) of GO during the aerosol process, and further correlates physical and chemical properties with aqueous aggregation behaviors. Flat GO and five CGOs (with different degrees of thermal reduction, and thus different oxygen functionality) are synthesized. The evolution of their surface chemistries and morphologies is characterized using various spectroscopic (UV-vis, FTIR, XPS) and microscopic (SEM and TEM) techniques. Based on extensive characterization and aggregation kinetic results, the critical coagulation concentration (CCC) values for three ionic systems (NaCl, $CaCl_2$, and $MgCl_2$) are correlated with the physical and chemical properties of GO/CGO (ζ-potentials, C/O ratios, carboxyl, and C-C fractions).

Chapter 5 addresses the application and environmental implications of CGO materials in more realistic aquatic conditions. The aggregation behavior of three GO/CGO materials, in the presence of three model natural organic matters (Suwannee River humic acid, Suwannee River fulvic acid, and Aldrich humic acid) are measured and compared. Electrophoretic mobility and adsorption measurements are performed to understand the differences in colloidal behaviors.

Chapter 6 advances the aerosol synthesis process further by encapsulating functional nanoparticles, and also demonstrates application of (multi)functional nanocomposites as advanced photocatalysts. The aerosol route is utilized to effectively crumple GO and subsequently encapsulate commercially available TiO_2 and magnetite nanoparticles. The photocatalytic performance of as-synthesized GOTIM is evaluated, in addition to detailed oxidative and reductive reaction mechanisms of holes and electrons, respectively. Furthermore, low-field magnetic susceptibility and low-energy in situ material separations are demonstrated. The chapter highlights the aerosol process as a fast and facile technique to synthesize monomeric, aggregation-resistant, crumpled graphene-based photocatalysts for advanced water treatment applications.

Chapter 7 and 8 focus on the development and application demonstration of CGO materials in advanced water treatment membranes. In Chapter 7, CGO porous nanocomposites are assembled as advanced, reactive water treatment membranes. The pure water flux and separation efficiencies for model organic foulants are evaluated and compared with those of commercial ultrafiltration membranes. In addition, multifunctionality is demonstrated through the in situ photocatalytic degradation of methyl orange (MO), as a model organic, under fast flow conditions ($t_{res} < 0.1$ s). The membranes' antimicrobial properties are evaluated for both biofilm (contact) and suspended growth scenarios (*Escherichia coli*).

In chapter 8, facile in situ photocatalytic synthesis of nAg particles by crumpled GO-TiO_2 (GOTI) nanocomposites is demonstrated as a novel approach to (re)generate, and thus maintain, enhanced antimicrobial activity over extended operation times. Earlier, in Chapter 6, the CGO-TiO_2 nanocomposites were shown to have enhanced photo-reductive properties (using MO as a probe molecule) due to decreased electron-hole recombination and unique core-shell structure(s). Chapter 8 further demonstrates the photocatalyzed (re)formation of nAg on GOTI nanocomposites

and assembled membranes under UV and simulated solar light (AM 1.5) conditions. Detailed characterization of the resulting particle (nAg) morphology, size (evolution), and crystal structures is included. Membrane (surface-based) antimicrobial properties are also demonstrated for two model bacteria, *Escherichia coli* and *Bacillus subtilis.*

Lastly, Chapter 9 summarizes the dissertation's key findings and details its major contributions. Concluding remarks discuss the implications of these findings within a broader context of nano-/advanced materials-enabled water treatment technologies, and offer perspectives on potential future directions of such technologies.

References

1. WHO/UNICEF *Progess on Drinking Water and Sanitation: 2012 Update*; WHO/UNICEF: Geneva/New York, 2012.
2. Montgomery, M. A.; Elimelech, M., Water and Sanitation in Developing Countries: Including Health in the Equation. *Environ. Sci. Technol.* **2007,** *41* (1), 17-24.
3. Schwarzenbach, R. P.; Escher, B. I.; Fenner, K.; Hofstetter, T. B.; Johnson, C. A.; von Gunten, U.; Wehrli, B., The Challenge of Micropollutants in Aquatic Systems. *Science* **2006,** *313* (5790), 1072-1077.
4. Kenny, J. F.; Barber, N. L.; Hutson, S. S.; Linsey, K. S.; Lovelace, J. K.; Maupin, M. A. *Estimated Use of Water in the United States in 2005*; U.S. Geological Survey: Reston, VA, 2009.
5. The World Bank, World Development Indicators: Annual Freshwater Withdrawals. In 2012.
6. Entrekin, S.; Evans-White, M.; Johnson, B.; Hagenbuch, E., Rapid Expansion of Natural Gas Development Poses a Threat to Surface Waters. *Front. Ecol. Environ.* **2011,** *9* (9), 503-511.

7. McDonald, R. I.; Olden, J. D.; Opperman, J. J.; Miller, W. M.; Fargione, J.; Revenga, C.; Higgins, J. V.; Powell, J., Energy, Water and Fish: Biodiversity Impacts of Energy-Sector Water Demand in the United States Depend on Efficiency and Policy Measures. *PLoS ONE* **2012,** *7* (11), e50219.
8. Shannon, M. A.; Bohn, P. W.; Elimelech, M.; Georgiadis, J. G.; Marinas, B. J.; Mayes, A. M., Science and Technology for Water Purification in the Coming Decades. *Nature* **2008,** *452* (7185), 301-310.
9. Geim, A. K.; Novoselov, K. S., The Rise of Graphene. *Nat. Mater.* **2007,** *6* (3), 183-191.
10. Baughman, R. H.; Zakhidov, A. A.; de Heer, W. A., Carbon Nanotubes--the Route Toward Applications. *Science* **2002,** *297* (5582), 787-792.
11. Prato, M., [60]Fullerene Chemistry for Materials Science Applications. *J. Mater. Chem.* **1997,** *7* (7), 1097-1109.
12. Novoselov, K. S.; Geim, A. K.; Morozov, S. V.; Jiang, D.; Zhang, Y.; Dubonos, S. V.; Grigorieva, I. V.; Firsov, A. A., Electric Field Effect in Atomically Thin Carbon Films. *Science* **2004,** *306* (5696), 666-669.
13. Nair, R. R.; Wu, H. A.; Jayaram, P. N.; Grigorieva, I. V.; Geim, A. K., Unimpeded Permeation of Water Through Helium-Leak-Tight Graphene-Based Membranes. *Science* **2012,** *335* (6067), 442-444.
14. Luo, J.; Jang, H. D.; Sun, T.; Xiao, L.; He, Z.; Katsoulidis, A. P.; Kanatzidis, M. G.; Gibson, J. M.; Huang, J., Compression and Aggregation-Resistant Particles of Crumpled Soft Sheets. *ACS Nano* **2011,** *5* (11), 8943-8949.

Chapter 2. Aerosol Processing and Environmental Applications of Graphene Oxide Materials

Partial content of this chapter has been written into a review article: Jiang, Y., Biswas, P., Fortner, J., A Review of Recent Developments in Graphene-Enabled Membranes for Water Treatment. submitted to *Environmental Science: Water Research and Technology*.

2.1 What We Talk About When We Talk About Graphene?

The graphene 'gold rush' began with the discovery of a free, 2D atomically-thin carbon film which earned Geim and Novoselov the 2010 Nobel Prize in Physics.[1] Graphene is one layer of carbon atoms packed into honeycomb pattern (Figure 2.1a), which is ultrathin (0.35 nm in thickness), while being ultrastrong and exceptionally conductive. Graphene can have different sizes and quality (i.e., degree of defects), depending on the fabrication methods, such as mechanical exfoliation of graphite,[1] chemical vapor deposition (CVD),[2] and reduction of graphene oxide (reduced graphene oxide, RGO).[3] Its dimensions can span from < 20 nm, described as quantum dots, to μm sizes of nanosheets and meter-scale of films,[4, 5] which underpin applications in various specific fields and correspondingly require different characterization and engineering approaches. Additionally, graphene materials can have very different surface chemistries resulting from a number of synthesis and/or subsequent chemical functionalization processes.

Currently, an important and widely studied derivative is graphene oxide (GO) (Figure 2.1b). GO, as functionalized (oxidized) form of graphene, is the product of exfoliation of graphite oxide and is the precursor for RGO (Figure 2.1c) synthesis by either chemical or thermal reductions.[3, 6] Detailed chemical structure (surface chemistry) of GO has not been completely resolved due to the random chemical functionalization of each layer and variations in composition.[7, 8] In principle, GO partially remains as a one-atom-thick planar sheet with a sp^2-bonded carbon structure while being derivatized with oxygen functional groups both on the basal plane (e.g. hydroxyl and epoxy groups) and at the sheet edges (e.g. carboxyl and carbonyl, etc.) (a generic structure shown in Figure 2.1b). Compared to graphene, GO has the distinctive feature of being water-dispersible due to electrostatic repulsions between deprotonated carboxyl groups. This important feature makes the processing of graphene materials much more convenient as water can be used in place of

organic solvents. For applications, such as membranes, oxygen functionality also facilitates the hydrophilicity, which is discussed later. Further, graphene (oxide) can undergo various physical transformations. For example, 2D GO was structurally engineered to have various crumpled morphologies to give specific properties (e.g., aggregation-resistant), such as paper ball-like spheres[9, 10] and corrugated surfaces (Figure 2.1d).[11]

Another interesting feature of GO is its intrinsic antimicrobial properties, which will likely lead to applications in anti-microbial coatings and antifouling membranes. The main proposed mechanisms of bacterial inactivation are induced cell membrane damage, as a result of physical disruption,[12] oxidative stress,[13] and extraction of phospholipids from cell membranes.[14]

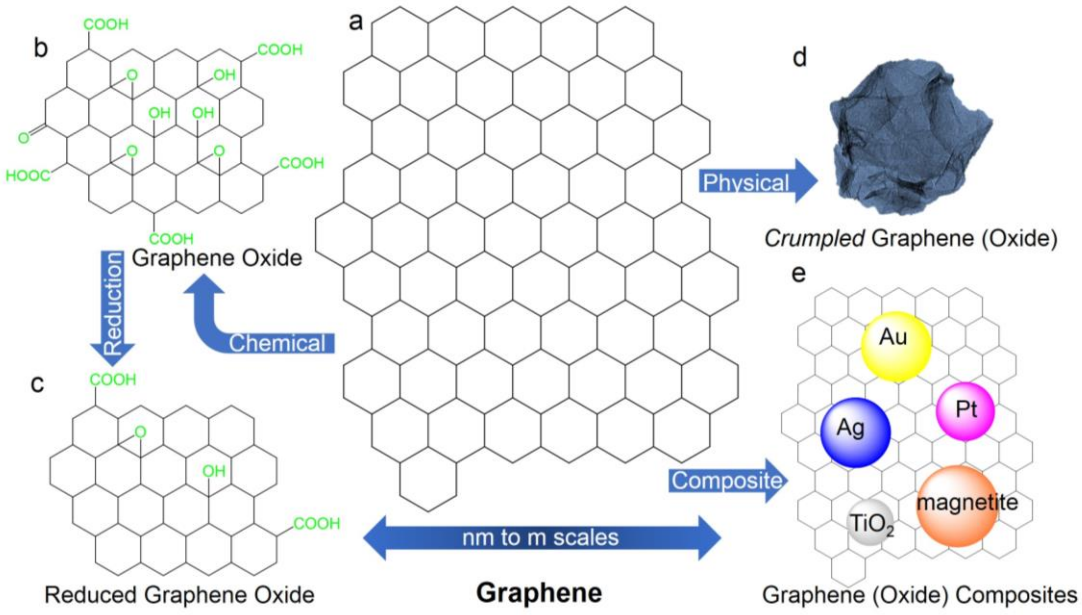

Figure 2.1 Depicted generic chemical and physical structures of graphene-based materials

Interestingly, graphene can be used as part(s) of a variety of composite materials,[15] due to their extremely high specific surface area and ease of functionalization, which offer abundant anchoring sites for various functional nanoparticles, including magnetic Fe_3O_4,[16] photo-reactive

TiO_2,[17] antimicrobial Ag[18] and Au,[19] and multifunctional nanocomposites such as graphene-TiO_2-magnetite,[20] graphene-Au-magnetite,[21] etc. (Figure 2.1e).

As discussed above, due to strong π-π attraction (London dispersive forces) between flat graphene nanosheets, flat graphene nanostructures tend to restack, resulting in subsequent, significant decreases in accessible surface area and aqueous stability normally observed in water, thus lowering material efficacy.

2.2 Aerosol Processing of Graphene Materials

Aerosols are suspensions of small liquid or solid particles in gases.[22] They are produced by gas-to-particle conversion, liquid/solid-to-solid conversion, resuspension of powdered material or the break-up of agglomerates. Unlike solution-based and colloidal approaches, aerosol routes maintain small reaction volumes and enable the production of high quality particles and assembles on an industrial, manufacturing scale. They have been used to prepare size-, shape- and architecturally controlled nanostructures (including particles and films) for a range of inorganic, organic, and composite materials. For example, with a gas-to-particle conversion scheme (Figure 2.2a), flame aerosol synthesis is a dominant method for the production of many commercial nanoparticles such as titanium dioxide (6 Mtons/year), carbon black (1.5 Mtons/year), and fumed silica (50 ktons/year),[23] in addition to a few emerging nanomaterials, including quantum dots, fullerenes, and carbon nanotubes.[24] In a typical liquid-to-solid scenario (Figure 2.2b), a precursor solution is nebulized and the resulting aerosol is introduced to a heat source where (1) solvent evaporation can facilitate assembly of nanoscale building blocks (spray drying), and/or (2) precursor decomposition or reaction (spray pyrolysis) can occur to produce materials. In a few cases, solid particles are directly aerosolized and passed through a reaction zone (Figure 2.2c). For example, silicon kerf was aerosolized before being delivered into a furnace to remove its carbon

contamination.[25] Products can be collected in gas washing bottles or similar solvent containing vessels, on filters, or deposited as films. This work is focused on the liquid-to-solid conversion scheme, which include aerosol (droplet) generation, solvent evaporation, precursor reaction, and particle collection steps (Figure 2.2b).

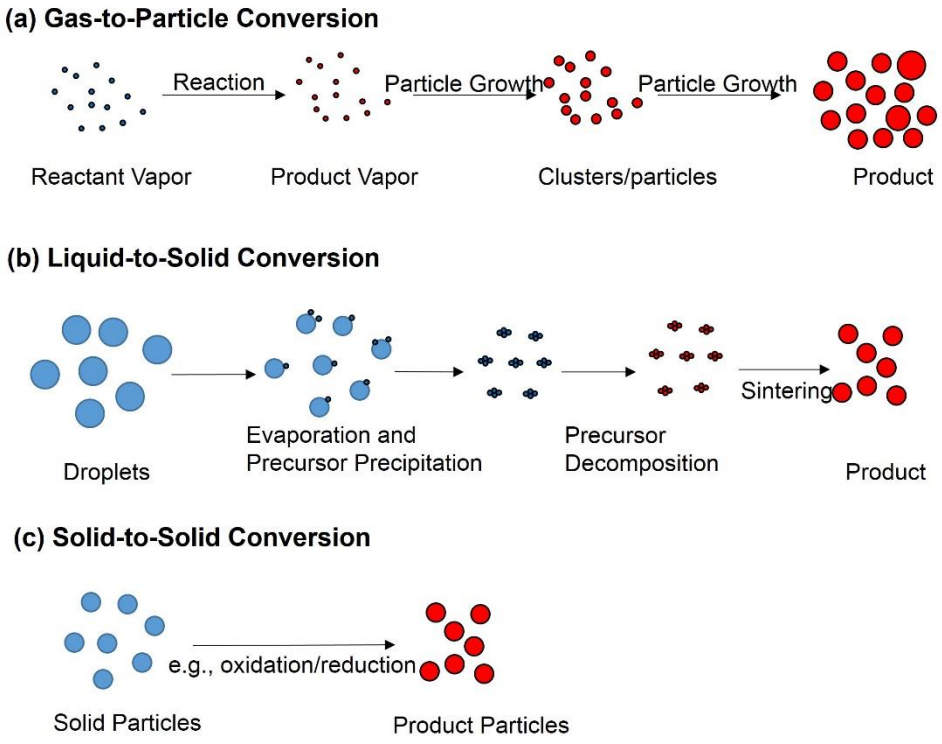

Figure 2.2 Simplified schemes of gas-to-particle, liquid-to-solid, and solid-to-solid conversion processes

2.2.1 Aerosol (Droplet) Generation Methods

Nebulization is the creation of mist from a liquid using various methods. There are several common nebulization techniques for aerosol generation that could be applied to the aerosol synthesis and assembly of nanomaterials, including pressure (pneumatic) nebulizers, electrostatic nebulizers (electrospray), and ultrasonic nebulizers, among others.

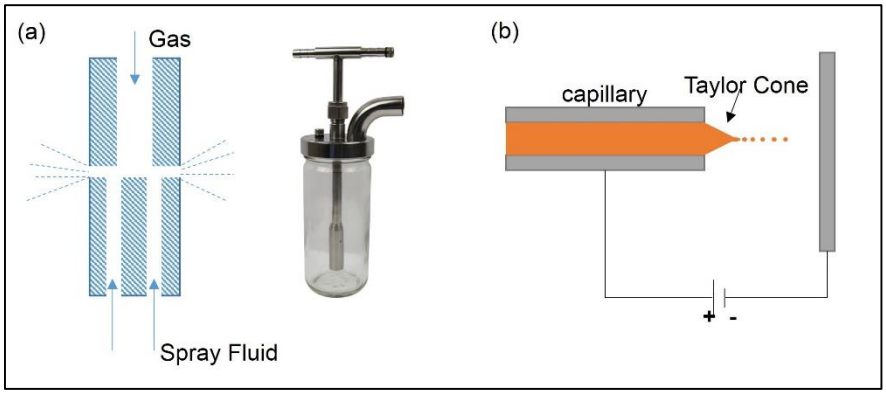

Figure 2.3 (a) Schematic diagram and photo of a Collison Nebulizer (source: BGI Inc.); (b) Schematic diagram of an electrospray system.

Pressure nebulizers produce aerosols by forcing a liquid through a small opening under high pressure using a carrier gas or centrifugal force, typically resulting in high droplet concentrations. This technique produces a broad distribution of relatively large droplets (sizes: a few to 1000 μm). An example of pressure nebulizers is the Collison nebulizer (Figure 2.3a, BGI incorporated),[26] which is being used in our study. It contains a fluid glass jar, and 1, 3, 6, or 24 jets, with applied pressure in the range of 20 to 100 psig. In the nebulizer, the liquid/gas jet is impacted against the inside wall of the jar to remove larger fraction of the droplets.

For electrostatic nebulizers (electrospray), a charge is imparted to a liquid stream in a needle (maintained at a few kilovolts), and the resulting electric field at the needle tip charges the surface of the emerging liquid, dispersing it by Coulomb forces into a fine spray of charged droplets (usually < 2 μm) (Figure 2.3b). When operated in the stable Taylor cone-jet mode, the droplets formed by this process are highly charged and fairly monodispersed.[27, 28]

Ultrasonic nebulizers use the periodic mechanical vibration of ultrasound (50 kHz to 2.4 MHz) to destabilize liquid films to a point of break-up and formation of droplets.[29] Common examples of ultrasonic nebulizers include ultrasonic cleaning baths, direct-immersion ultrasonic horns, and flow reactors.

The produced droplet size distribution and overall output will depend on the aerosol generation method. Monodisperse aerosols have narrow size distributions and lower geometric standard deviation values (σ_g). The geometric standard deviation value at which an aerosol can be considered generally monodisperse is quite subjective, but a good rule of thumb is $\sigma_g \leq 1.25$. The primary droplets generated by electrospray are smaller and more monodlsperse ($\sigma_g \leq 1.15$), compared to those generated by pneumatic nebulizers ($\sigma_g > 1.5$).[30]

2.2.2 Aerosol Synthesis and Assembly of Nanomaterials

After generation, the aerosols are passed through a heating zone, which is usually either a flame or furnace. In the heating environment where solvent evaporates, supersaturation of solutes can be quickly reached, and the solutes begin to precipitate at the surface of the droplet. If the evaporation occurs slowly and the solute has a relatively high solubility, a solid particle can be formed. On the other hand, if the heating and evaporation occur rapidly enough and the solute has relatively low solubility, a shell of solute can lead to production of hollow particles. The precursor can thermally decompose (spray pyrolysis), or only be dried without chemical reactions (spray drying). Release of gas trapped inside the hollow spheres can result in porous particles, and rapid evolution of gas can even break the shell structure. In addition, the molecules or nanoscale building blocks within the aerosolized droplets can also self-assemble into architecturally defined (e.g., porous or hollow structures), hierarchical, and composite nanostructures (evaporation-induced self-assembly, EISA).[31] Two types of heat applications are widely used:

2.2.2.1 Furnace Reactors

The generated aerosols are carried by carrier gas (e.g., N_2 or air) to a heated tube furnace, which is usually dozens of centimeters to one meter long. The residence time is on the order of seconds and maximum temperatures are generally lower than 1300 ℃. The furnace reactors are

widely used for both spray pyrolysis and spray drying. Each aerosolized droplet can be regarded as one micro-droplet reactor, undergoing solvent evaporation, precursor precipitation and decomposition, and particle formation. As each aerosol droplet typically contains multiple sites from material nucleation, polycrystalline nanoscale or microscale particles are produced. Sintering and densification can further occur in the extended heated zones.

2.2.2.2 Flame Reactors

The precursor aerosols are passed through a flame (flame spray pyrolysis). The residence time of precursor within a flame is on the order of milliseconds (the flame length usually on the order of centimeters), and the maximum temperature can reach as high as 3000 ℃. The small particles nucleate, coagulate quickly and subsequently agglomerate into product material. The necessary presence of O_2 in the fuel for combustion makes it difficult to make non-oxide materials as pure samples. Besides, the short residence time in the heat source can make controlling particle nucleation and agglomeration difficult, and the high flame temperatures limit the production of metastable materials, both in terms of crystalline phase and shape.[31]

2.2.3 Synthesis of Crumpled Graphene Oxides

To generate water droplets containing GO nanosheets, both pressure and ultrasonic nebulizers have been demonstrated.[9, 32] Crumpling of GO sheets under ambient temperature were observed using low concentration of GO precursor solution (e.g., 2 mg/L),[33] while in other cases, a heating element, usually a furnace, is applied to induce the rapid evaporation of water. For this work, the aerosol synthesis of crumpled graphene oxide (CGO) is accomplished using a furnace aerosol reactor (FuAR), which consists of a 6-jet Collison nebulizer, a tube furnace, a diffusion dryer, and a membrane filter (Figure 2.4). The precursor was initially atomized into micrometer-sized droplets by using a Collison nebulizer (BGI Incorporated). These water droplets containing

flat GO nanosheets (and nanoparticles, if needed) are subsequently delivered by N_2 into the tubular alumina reactor (1 m ×25 mm ID) maintained at preset temperature (room temperature to 1000 ℃). The flow rate is generally operated at 12.4 L/min (nebulizer pressure 14 psi (96.53 kPa)), resulting in ~1.6 s residence time. Finally, the nanocomposites are collected downstream of the reactor using a membrane filter (Millipore), weighed and dispersed into water to obtain 200 mg/L dispersion. For in-line measurement of particle sizes, a split stream is introduced into a scanning mobility particle sizer (SMPS).

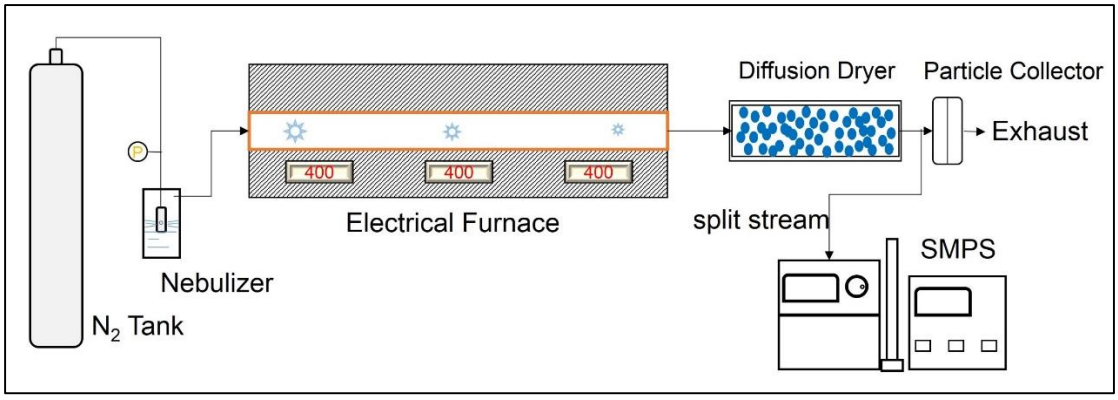

Figure 2.4 Scheme diagram of a FuAR employed to synthesize CGO

2.3 Environmental Applications of Graphene Oxide Material

With regard to environmental applications, graphene oxide has been demonstrated in a number of technologies, including sorbents, photocatalysts, water treatment membranes, and electrodes for contaminant degradation and sensing.[34] For example, high surface areas and unique structures (co-presence of hydrophobic and hydrophilic parts) underpin broad applications as novel sorbents. Adsorption of many metal/radionuclide ions and organic pollutants have been demonstrated., including $As^{3+}$and As^{5+},[16] Cu^{2+},[35] Co^{2+},[36] Hg^{2+},[37] U^{6+} and Eu^{3+},[38] dyes,[39] polycyclic aromatic hydrocarbons (PAH),[40] and organophosphorus pesticides.[41] Some of these values are among the highest reported adsorption capacities. In the following sections, an overview of its

applications as photocatalysts and water treatment membranes, which are directly related to this work, is provided:

2.3.1 Photocatalysts

Photocatalysts, as a pollution mitigation strategy, have attracted tremendous amount of research interest and investment, as the concept of directly harvesting and utilizing sunlight is appealing both economically and with regard to process scale-up. Various photocatalysts have been developed, including semiconductors and organic compound-based photocatalysts, such as TiO_2, ZnO, CdS, $ALa_4Ti_4O_{15}$ (A = Ca, Sr, and Ba) and rhenium complexes.[42] Photocatalytic reaction mechanisms have been well documented. Take the most commonly employed photocatalyst, TiO_2, as the example, whereby the TiO_2 semiconductor produces electron-hole pairs upon UV irradiation with energies greater than its band gap (3.2 eV).[43] The photo-induced hole-electron pairs are separated in the space-charge layer, and can lead to oxidation and reduction reactions, respectively, due to their strong redox potentials (valence band hole: 2.5 V vs. SCE and conduction band electron: -0.7 V vs. SCE).[44]

For many photocatalysts, a major hurdle to overcome is the rapid recombination of holes and electrons. Coating the photocatalyst with metal nanoparticles, such as platinum[42] or copper,[45, 46] is a viable approach to enhance the separation (time) of holes and electrons, if the metal has high electron conductivity and can work as an effective electron trap. An issue with this approach is that small noble metal nanoparticles sinter into large ones, leading to a decrease in the enhancement effect over time. The benefits of incorporating graphene for such enhancement have been shown to be multiple-fold. Graphene can act as additional adsorption sites, as sensitizers, and decrease the band gap, depending on the specific case/combination. Most importantly, a substantial

suppression of the recombination of separated holes and electrons can occur, leading to increased reactivity via electrons and holes and radicals.[47]

To synthesize graphene-based photocatalysts, in situ growth of photocatalyst nanoparticles is preferred over other routes, such as simple mixing. Graphene has a large surface area, which means abundant active sites for such reactions to occur. For example, in a typical hydrothermal approach, dissolved TiO_2 (P25) molecules precipitate on the graphene sheets when the solution condition changed.[17] Such in situ growth leads to close contact between graphene and nanoparticles, and in some cases forming a covalent bonding (e.g., Ti-O-C bond[17]), which is shown to increase the absorption range (red-shift) and decrease the band gap.

Photocatalysts applied for pollution remediation/transformation purposes primarily rely on photo-induced holes and electrons. The photo-induced holes can directly oxidize other pollutants (depending on redox potential), or oxidize water to produce a suite of reactive oxygen species (ROS), thus allowing for indirect oxidation to take place; on the other hand, electrons can directly reduce pollutants, or reduce oxygen to produce oxidative super oxide anions.[47, 48] According to the nature and purpose of related reactions, the applications of photocatalyst have been categorized into three primary groups: oxidative decontamination, reductive decontamination, and disinfection.

Oxidative reactions involve direct reactions of holes and indirect oxidations of ROS. The production of ROS results from a series of chain reactions (Eqn. 1-5), with major species produced being $OH^{\cdot}$, $O_2^{-\cdot}$, $HO_2^{\cdot}$, and H_2O_2. Among these, $OH^{\cdot}$ is considered the strongest species, and is capable of transforming a wide range of organic pollutants. Many oxidative reactions by graphene-based photocatalysts have been evaluated with model organic dyes (such as methyl orange, methylene blue, and Rhodamine B[17, 49, 50]) and pharmaceutical compounds.[48]

$h^+ + H_2O \rightarrow OH^{\cdot} + H^+$ (1)

$e + O_2 \rightarrow O_2^{-\cdot}$ (2)

$O_2^{-\cdot} + H^+ \rightarrow HO_2^{\cdot}$ (3)

$HO_2^{\cdot} + O_2^{-\cdot} + H^+ \rightarrow H_2O_2 + O_2$ (4)

$H_2O_2 + e \rightarrow OH^{\cdot} + OH^-$ (5)

While such oxidation by holes and indirect oxidation by ROS are considered to be the main reaction mechanisms for graphene-based photocatalysts, significantly less attention has been paid to the effect of increased electron production (via charge separation), which could potentially promote strong photocatalytic *reduction* pathways. Photocatalytic reduction reactions can be utilized for pollutant removal in both gas and aqueous phases. For example, photo-reduction of CO_2 (into hydrocarbon fuels, such as CO and CH_4) is considered as a promising alternative route for greenhouse gas management and utilization.[51] For water purification, photocatalysts have been mainly shown in the reduction of oxyanions (e.g., BrO_3^-,[52] ClO_4^-,[53]) and metal ions (e.g., Cr^{6+},[54]). However, these reductive applications are still limited for graphene-based photocatalysts.

Disinfection by graphene-based photocatalysts has been also demonstrated for model pathogens (both viruses and bacteria). For example, graphene-tungsten oxide composites were shown to effectively inactivate bacteriophage MS2 virus under visible light.[55] Reduced GO-coated TiO_2 thin films were shown to have inactivated *E. coli* under solar light irradiation, demonstrating a ×7.5 enhancement factor compared to TiO_2 alone.[56] The oxidative stress induced by ROS has been proposed as the reaction mechanism, and presence of graphene has enhanced the generation of ROS, thus inactivation performance.[34]

2.3.2 Membrane Development and Application

2.3.2.1 Monolayer Nanoporous Graphene for Desalination

Despite being only one atom thick, graphene is considered to be impermeable to all gases and liquids.[57] Yet in its nanoporous form, graphene has been hailed as an ideal candidate for reverse osmosis (RO) membranes as it is atomically thin and mechanically robust. The ultimately thin selective layer can maximize the permeability, as water permeability typically scales inversely with the selective layer thickness. It is intuitive to imagine 'knocking out' carbon atoms from the matrix to form pores for the separation purposes, which was initially examined by a series of theoretical studies.[58, 59] The concept of nanoporous graphene RO membrane was tested and proved by Cohen-Tanugi and Grossman in their molecular dynamics (MD) simulations.[59] The MD simulations included two water reservoirs separated by a nanoporous graphene layer, and water and ions were subjected to a driving force across the membrane (i.e. pressure) (Figure 2.5a). They estimated that the water permeability could reach as high as ~ 10^3 L/(m^2 ћ ƀar), which is 2-3 orders of magnitude greater than that of typical thin film composite RO membranes (~ 1-10 L/(m^2 ћ ƀar)).[59] They also revealed that full salt rejection can be achieved with very small nanopores (radius ≤ 0.27 nm), and precise and highly uniform nanopores are critical to achieve such high salt rejections. Experimentally, researchers began to fabricate graphene nanosheets and develop various methods of creating controlled pores (0.4-10 nm) in the past two years. In one recent study,[60] Surwade et al. created nanopores in monolayer graphene using an oxygen plasma etching process (Figure 2.5b). With 1.5 s exposure to oxygen plasma, nanopores with size range of 0.5-1 nm and a density of 10^{12} cm^{-2} were created. The resulted membranes exhibited a salt rejection rate of nearly 100% and water flux as high as 70 g/(m^2 s ƪtm) (~250 L/(m^2 ћ ƀar)) when measured using osmotic pressure as a driving force.[60]

Nanoporous graphene has shown great promise for desalination membranes (demonstrated in both theoretical and experimental studies), however, these demonstrations were accomplished at very small scales (micrometer sizes) and under nearly perfect reaction/processing conditions. Achieving highly uniform, sub-nanometer pores in large-area sheets of graphene remains the critical challenge for nanoporous graphene membranes to be mass produced.[61] Manufacturing of large-area graphene films has made recent progress, and monolayer film as large as > 30 inch can be manufactured by the roll-to-roll CVD processes.[5] Deficiencies in CVD graphene sheets, such as defects from growth and transfer processes, may be a source of potential problems for the desalination applications, which decrease the salt rejections by serving as ion channels, and affect membrane mechanical integrity. This underpins the current need for technological improvements in fabricating large-area and almost intact graphene and/or approaches to mitigate the adverse effects such as by remediation of the defects. While complete elimination of defects seems improbable; sealing, blocking, or reducing molecular permeation through defects may be more realistic. For example, hafnia and nylon were deposited onto defects-embedded monolayer graphene to respectively block nanoscale and large defects, which has showed effective reduction of potassium chloride leakage from the membrane.[62] Furthermore, novel methods to create evenly distributed and uniform nanopores need to be developed, in addition to what has been demonstrated (e.g. electron beam exposure, oxidative etching, and ion/cluster bombardment). The challenges with mass application of nanoporous graphene membranes do not only exist in the fabrication of nanoporous graphene itself, but also in the integrated manufacturing process of the filtration system, such as integration of the graphene layer and support, which has yet to be demonstrated. In this regard, developing detailed experimental understanding of deformation and fracture micro-mechanisms under typical RO conditions is crucial.[63]

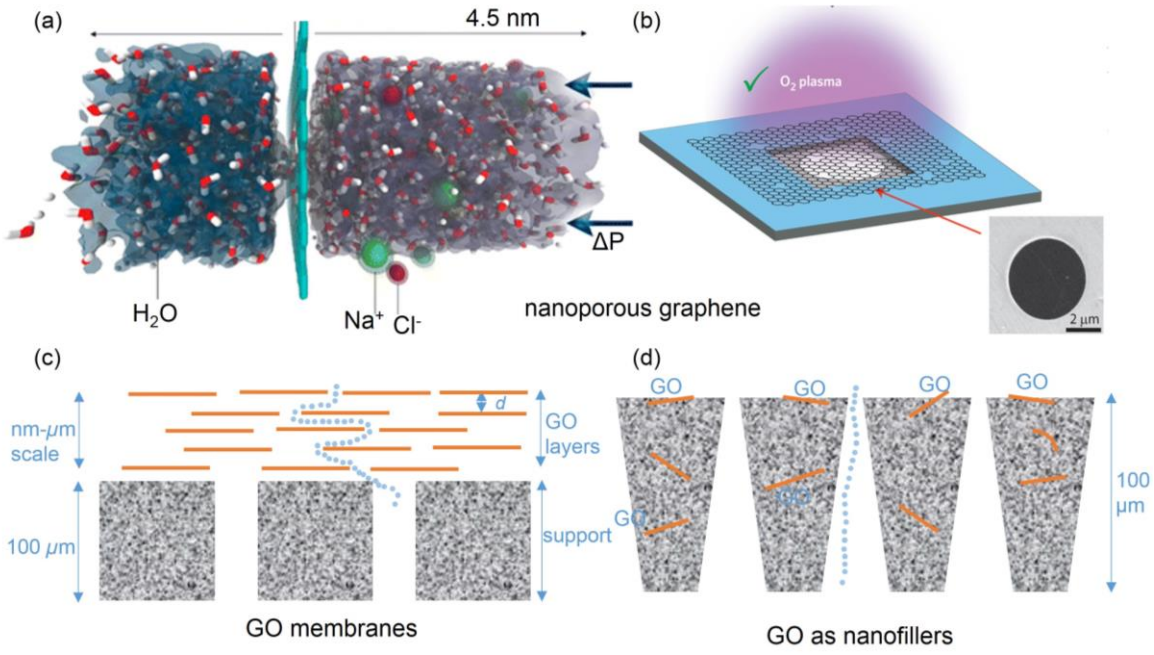

Figure 2.5 (a) Computational system used in previous study by Cohen-Tanugi and Grossman,[41] reprinted with permission from reference 41, copyright 2012 American Chemical Society; (b) Schematic and SEM image of single-layer graphene suspended on a 5-μm-diameter hole. O_2 plasma treatment was found to successfully create controlled nanopores in graphene.[42] Reprinted with permission from reference 42, copyright 2015 Nature Publishing Group. (c) Schematic diagram of GO membranes, the deposited GO layers can be GO nanosheets or nanocomposites; (d) Schematic diagram of GO as nanofillers in polymeric membranes.

2.3.2.2 GO Membranes

GO-based membrane demonstrations began with so-called GO paper(s) (here for convenience, we arbitrarily distinguish GO papers as free-standing GO laminates (without polymer support), while GO membranes as GO-polymeric composite membranes). GO paper is free-standing, paper-like laminates, which are a collection of micron-sized GO crystallites forming an interlocked layered structure.[64] Scanning electron microscopy (SEM) imaging reveals that well-packed layers through almost the entire cross-section of the papers. The layer-to-layer distance (d-

spacing) was estimated to be about 0.83 nm from X-ray diffraction experiments.[64] The spacing allows the low-friction flow of a monolayer of water, but rejects all other vapors and gases, including helium (i.e. H_2O vapor permeates through the membranes at least 10^{10} times faster than He).[65] They are vacuum-tight in the dry state but, if immersed in water, act as molecular sieves, blocking all solutes with hydrated radii larger than 4.5 angstroms.[66] Interestingly, smaller ions permeate through the membranes at rates thousands of times faster than what is expected for simple diffusion, which is attributed to capillary-like high pressures acting on ions inside the graphene capillaries.[66] Nevertheless, the permeation (flux) through these GO papers remains insufficient to allow them to compete with commercial pressure-driven membranes.[67]

GO membranes are GO paper-like surface selective and/or functional layers on top of porous supports (e.g., polymeric polysulfone (Psf), polyethersulfone (PES) membranes) (Figure 2.5c). Conceptually, such membranes were made by deposition of a thin layer of GO or GO nanocomposites (a few nm to μm) onto a relatively thicker support membrane (usually > 100 μm) via various techniques, such as vacuum filtration[68] and layer by layer deposition.[69] The GO layers deposited onto polymeric supports were usually thinner than the free-standing GO papers. The deposited layer was hypothesized to form particular nanochannels which could facilitate fast water transport, and meanwhile achieve selective functions.[18, 69]

Hu and Mi created a selective surface layer atop Psf support by layer-by-layer depositing cross-linked flat GO nanosheets.[69] The as-synthesized membranes showed a 4-10 times higher water flux (~ 8-27 L/(m^2 ћ ƀar)) than that of most commercial, comparable nanofiltration membranes.[69] The high water flux was partially attributed to the unique water transport properties of the GO nanochannels formed between two horizontally paralleled GO nanosheets. In our recent work,[24] we designed and demonstrated assemblies of crumpled graphene oxide (CGO) with

vertically tortuous nanochannels for ultrafiltration, which have water flux as high as ~400 L/(m^2 ħ ƀar) (3.7 g/m^2 deposition), outperforming comparable commercial ultrafiltration membranes. In both studies,[18, 69] surface charge is believed to play a role in rejection performance, in addition to size exclusion effect. Huang et al. demonstrated the development of channels of 3-5 nm in size by sacrificially etching out copper hydroxide nanostrands (~2.5 nm in diameter) sandwiched within the GO membranes.[67] By 'opening up' the channels, a much higher water permeation was achieved (~700 L/(m^2 ħ ƀar)) compared to pristine GO membranes, while still having fairly high rejection of small model foulants (e.g., complete rejection of 5 nm gold nanoparticles).[67] Other methods employed in a similar manner include intercalating carbon nanotubes,[68] and carbon dots.[70] Further, for bio-fouling control, (partial) coverage of thin-film composite polyamide membranes by GO nanosheets were achieved using amide coupling between carboxyl groups of GO and carboxyl groups of polyamide.[71] The membranes have shown potential antibacterial activity - for example, 65% *E. coli* inactivation was observed after 1 h surface contact, without causing detrimental effect to the membrane transport properties.[71]

When combined with other functional nanoparticles, GO membranes can be further engineered to be photo-reactive[18, 72] or (more) antimicrobial,[18, 71] achieving simultaneous filtration and pollutant destruction/pathogen inactivation. For example, the antimicrobial properties of a GO membrane were further enhanced through the incorporation of Ag NPs in the GO layer, achieving almost complete inactivation of bacteria.[18] Ray et al. modified the polyamide membranes with GO and Au nanostars, and showed additional bactericidal property by photothermal effects of Au upon laser irradiation.[19] In addition, photo-reactive (reduced) GO-TiO_2 composite membrane surfaces were created via layer-by-layer deposition[72] and vacuum filtration.[18, 73] In batch mode, the membrane coupons had approximately one order of magnitude lower photo-reaction rate constants

compared to those of monomeric (suspended) graphene-TiO_2 nanocomposites, due to decrease of available surface areas to both light and model organic pollutants.[24] They all showed higher permeate fluxes (and pollutant removals) under UV light irradiation conditions when evaluated in the flow-through mode.[18, 72, 73]

Other advantages of GO membranes include the fact that they do not need to meet the high quality (low defect) requirement of graphene materials like nanoporous graphene. GO membranes utilizes (functionalized) GO nanosheets or nanocomposites, and some of the simple and well understood synthesis approaches. They also can be tuned accordingly to, cover a broader spectrum of membrane applications from MF to RO. In addition, GO membranes are less material-intensive compared to other approaches such as using GO as nanofillers (component impregnation, discussed later), considering the (ultra)thin nature of the surface layer. The top layer could be as thin as a few atomic layers (~ 10 nm), corresponding to a mass density of only dozens of mg/m^2, while as component impregnated into the entire membrane matrix, the material consumption can be tens or hundreds of times higher (g/m^2). Taken together, GO membranes do have unique technological and economic comparative advantages over the other two types discussed.

Nevertheless, synthesizing GO membranes involves fairly complicated chemical processes, including support membrane pre-treatment, cross-linking of GO sheets, and sometimes pre-functionalization of GO sheets. More concerted efforts will be needed to understand and develop each individual process and their integration. Current technical schemes are focused on vacuum filtration,[18, 73] or chemical cross-linking using 1,3,5-benzenetricarbonyl trichloride (TMC)[69] or amine-based agents.[18, 71] Approaches like electrostatic layer-by-layer deposition, in situ synthesis will also be of great interests. For (re)active GO membranes (e.g. GO-Ag and GO-TiO_2 membranes), it can be difficult to integrate functional materials into current membrane fabrication

and application processes. There needs to be regeneration strategies for dissolution-based mechanism of bacterial inactivation (e.g. GO-Ag membranes). In addition, new system design of photo-reactive membranes, which will include light irradiation apparatus besides GO-TiO_2 membranes, could potentially have limited application avenues.

GO membranes can have very different water transport mechanisms. For example, it was found that water flux did not decrease monotonically as the number of flat GO layers increased;[69] however, for crumpled GO membranes shown in our recent work,[18] the water flux did decrease with the increase of CGO mass, similar to conventional polymeric membranes. For GO-based membrane surfaces, water transport mechanisms were proposed based on previous understandings of free-standing GO papers (as discussed earlier), which could deviate as a result of chemical functionalization of GO. Furthermore, separation mechanisms are still not well understood, which could include size exclusion, depth filtration and charge-based mechanisms. Knowledge on the fundamental aspects of water transport and molecular/ion retention will lead to new design and development of robust and effective GO membranes.

2.3.2.3 GO as Nanoscale Fillers

The incorporation of nanoparticles into polymeric membranes have been extensively studied with nanoparticles such as CNT and TiO_2. Nanoparticles can be easily blended into the solvents used in the phase inversion or interfacial polymerization processes of membrane fabrication. In the same manner, a very small amount of GO (usually 0.1-2 wt.% with respect to polymer) was incorporated into conventional polymer structures, which include Psf,[74, 75] PES,[76] polyvinylidene fluoride (PVDF)[77] UF and polyamide RO membranes[78, 79] (Figure 2.5d). Graphene oxide was directly blended into the polymer casting solution with the assistance of sonication and no changes of the operations were needed with regard to the phase inversion process. GO was

hypothesized to have migrated to the top surface during the phase inversion, making it more hydrophilic, which was supported by the observation of an average decrease of ~20° in water contacting angle measurements. In addition to increases in surface hydrophilicity, overall porosity also increased and as a result, 2-20 fold enhancements in water fluxes were observed due to the addition.[75, 76] Rejection improvement can vary from a few percent[76] to almost 3 times,[77] depending on the polymers, GO percentage, and test foulants. Generally, an optimal GO percentage was identified to balance the water permeability and rejection rates, which was believed to conform to the classical trade-off associated with ultrafiltration membranes. Size-fractionated GO (10-200 nm) was dispersed in the aqueous solution of m-phenylenediamine (MPD) before interfacial polymerization to make GO-embedded polyamide RO membranes. The water permeability and anti-biofouling property were found to have enhanced by approximately 80% and 98% (based on the biovolume), respectively, without loss of salt rejection.[78]

To date, most applications have been demonstrated using a phase inversion process to fabricate UF/NF membranes, and only a few focused on impregnation of GO into the polyamide layer with an interfacial polymerization process. The most distinctive advantage for GO as nanofillers is the ease with which it can be coupled with current state-of-art technologies of membrane fabrication, such as phase inversion or interfacial polymerization. Some scientific questions still need to be addressed though, for example, and perhaps most importantly, how GO properties (size, surface chemistry, etc.) affect the fabrication process and the performance of the resulted membranes; and better dispersion approaches of GO or GO nanocomposites in polymer solutions. In addition, top skin layer can be selectively engineered instead of the entire membrane structure so as to reduce material usage. In general, a detailed understanding of GO addition effects

on thermodynamic and kinetic aspects of the phase inversion and interfacial polymerization processes must be elucidated. .

References

1. Novoselov, K. S.; Geim, A. K.; Morozov, S. V.; Jiang, D.; Zhang, Y.; Dubonos, S. V.; Grigorieva, I. V.; Firsov, A. A., Electric Field Effect in Atomically Thin Carbon Films. *Science* **2004,** *306* (5696), 666-669.
2. Li, X.; Cai, W.; An, J.; Kim, S.; Nah, J.; Yang, D.; Piner, R.; Velamakanni, A.; Jung, I.; Tutuc, E.; Banerjee, S. K.; Colombo, L.; Ruoff, R. S., Large-Area Synthesis of High-Quality and Uniform Graphene Films on Copper Foils. *Science* **2009,** *324* (5932), 1312-1314.
3. Li, D.; Muller, M. B.; Gilje, S.; Kaner, R. B.; Wallace, G. G., Processable Aqueous Dispersions of Graphene Nanosheets. *Nat. Nanotechnol.* **2008,** *3* (2), 101-105.
4. Ritter, K. A.; Lyding, J. W., The influence of edge structure on the electronic properties of graphene quantum dots and nanoribbons. *Nat. Mater.* **2009,** *8* (3), 235-242.
5. Bae, S.; Kim, H.; Lee, Y.; Xu, X.; Park, J.-S.; Zheng, Y.; Balakrishnan, J.; Lei, T.; Ri Kim, H.; Song, Y. I.; Kim, Y.-J.; Kim, K. S.; Ozyilmaz, B.; Ahn, J.-H.; Hong, B. H.; Iijima, S., Roll-to-roll production of 30-inch graphene films for transparent electrodes. *Nat. Nanotechnol.* **2010,** *5* (8), 574-578.
6. Mkhoyan, K. A.; Contryman, A. W.; Silcox, J.; Stewart, D. A.; Eda, G.; Mattevi, C.; Miller, S.; Chhowalla, M., Atomic and Electronic Structure of Graphene-Oxide. *Nano Lett.* **2009,** *9* (3), 1058-1063.
7. Cai, W.; Piner, R. D.; Stadermann, F. J.; Park, S.; Shaibat, M. A.; Ishii, Y.; Yang, D.; Velamakanni, A.; An, S. J.; Stoller, M.; An, J.; Chen, D.; Ruoff, R. S., Synthesis and Solid-

State NMR Structural Characterization of 13C-Labeled Graphite Oxide. *Science* **2008,** *321* (5897), 1815-1817.

8. Bagri, A.; Mattevi, C.; Acik, M.; Chabal, Y. J.; Chhowalla, M.; Shenoy, V. B., Structural evolution during the reduction of chemically derived graphene oxide. *Nat. Chem.* **2010,** *2* (7), 581-587.
9. Luo, J.; Jang, H. D.; Sun, T.; Xiao, L.; He, Z.; Katsoulidis, A. P.; Kanatzidis, M. G.; Gibson, J. M.; Huang, J., Compression and Aggregation-Resistant Particles of Crumpled Soft Sheets. *ACS Nano* **2011,** *5* (11), 8943-8949.
10. Wang, W.-N.; Jiang, Y.; Biswas, P., Evaporation-Induced Crumpling of Graphene Oxide Nanosheets in Aerosolized Droplets: Confinement Force Relationship. *J. Phys. Chem. Lett.* **2012,** *3* (21), 3228-3233.
11. Wang, M. C.; Chun, S.; Han, R. S.; Ashraf, A.; Kang, P.; Nam, S., Heterogeneous, Three-Dimensional Texturing of Graphene. *Nano Lett.* **2015,** *15* (3), 1829–1835.
12. Akhavan, O.; Ghaderi, E., Toxicity of Graphene and Graphene Oxide Nanowalls Against Bacteria. *ACS Nano* **2010,** *4* (10), 5731-5736.
13. Perreault, F.; de Faria, A. F.; Nejati, S.; Elimelech, M., Antimicrobial Properties of Graphene Oxide Nanosheets: Why Size Matters. *ACS Nano* **2015,** *9* (7), 7226-7236.
14. Tu, Y.; Lv, M.; Xiu, P.; Huynh, T.; Zhang, M.; Castelli, M.; Liu, Z.; Huang, Q.; Fan, C.; Fang, H.; Zhou, R., Destructive extraction of phospholipids from Escherichia coli membranes by graphene nanosheets. *Nat. Nanotechnol.* **2013,** *8* (8), 594-601.
15. Geim, A. K.; Novoselov, K. S., The Rise of Graphene. *Nat. Mater.* **2007,** *6* (3), 183-191.

16. Chandra, V.; Park, J.; Chun, Y.; Lee, J. W.; Hwang, I.-C.; Kim, K. S., Water-Dispersible Magnetite-Reduced Graphene Oxide Composites for Arsenic Removal. *ACS Nano* **2010,** *4* (7), 3979-3986.
17. Zhang, H.; Lv, X. J.; Li, Y. M.; Wang, Y.; Li, J. H., P25-Graphene Composite as a High Performance Photocatalyst. *ACS Nano* **2010,** *4* (1), 380-386.
18. Jiang, Y.; Wang, W.-N.; Liu, D.; Nie, Y.; Li, W.; Wu, J.; Zhang, F.; Biswas, P.; Fortner, J. D., Engineered Crumpled Graphene Oxide Nanocomposite Membrane Assemblies for Advanced Water Treatment Processes. *Environ. Sci. Technol.* **2015,** *49* (11), 6846-6854.
19. Ray, J. R.; Tadepalli, S.; Nergiz, S. Z.; Liu, K.-K.; You, L.; Tang, Y.; Singamaneni, S.; Jun, Y.-S., Hydrophilic, Bactericidal Nanoheater-Enabled Reverse Osmosis Membranes to Improve Fouling Resistance. *ACS Appl. Mater. Interfaces* **2015,** *7* (21), 11117-11126.
20. Jiang, Y.; Wang, W.-N.; Biswas, P.; Fortner, J. D., Facile Aerosol Synthesis and Characterization of Ternary Crumpled Graphene–TiO_2–Magnetite Nanocomposites for Advanced Water Treatment. *ACS Appl. Mater. Interfaces* **2014,** *6* (14), 11766-11774.
21. Chen, Y.; Guo, F.; Qiu, Y.; Hu, H.; Kulaots, I.; Walsh, E.; Hurt, R. H., Encapsulation of Particle Ensembles in Graphene Nanosacks as a New Route to Multifunctional Materials. *ACS Nano* **2013,** *7* (5), 3744-3753.
22. Friedlander, S. K., *Smoke, Dust, and Haze: Fundamentals of Aerosol Dynamics*. 2nd ed.; Oxford University Press: New York, Oxford, 2000.
23. Fang, J.; Wang, Y.; Attoui, M.; Chadha, T. S.; Ray, J. R.; Wang, W.-N.; Jun, Y.-S.; Biswas, P., Measurement of Sub-2 nm Clusters of Pristine and Composite Metal Oxides during Nanomaterial Synthesis in Flame Aerosol Reactors. *Anal. Chem.* **2014,** *86* (15), 7523-7529.

24. Wang, Y.; Fang, J.; Attoui, M.; Chadha, T. S.; Wang, W.-N.; Biswas, P., Application of Half Mini DMA for sub 2 nm particle size distribution measurement in an electrospray and a flame aerosol reactor. *J. Aerosol Sci* **2014,** *71*, 52-64.

25. Vazquez-Pufleau, M.; Chadha, T. S.; Yablonsky, G.; Erk, H. F.; Biswas, P., Elimination of Carbon Contamination from Silicon Kerf Using a Furnace Aerosol Reactor Methodology. *Industrial & Engineering Chemistry Research* **2015,** *54* (22), 5914-5920.

26. May, K. R., The collison nebulizer: Description, performance and application. *J. Aerosol Sci* **1973,** *4* (3), 235-243.

27. Chen, D.-R.; Pui, D. Y.; Kaufman, S. L., Electrospraying of conducting liquids for monodisperse aerosol generation in the 4 nm to 1.8 μm diameter range. *J. Aerosol Sci* **1995,** *26* (6), 963-977.

28. Basak, S.; Chen, D.-R.; Biswas, P., Electrospray of ionic precursor solutions to synthesize iron oxide nanoparticles: Modified scaling law. *Chem. Eng. Sci.* **2007,** *62* (4), 1263-1268.

29. Bang, J. H.; Suslick, K. S., Applications of ultrasound to the synthesis of nanostructured materials. *Adv. Mater.* **2010,** *22* (10), 1039-1059.

30. Zarrin, F.; Kaufman, S. L.; Socha, J. R., Droplet size measurements of various nebulizers using differential electrical mobility particle sizer. *J. Aerosol Sci* **1991,** *22, Supplement 1*, S343-S346.

31. Motl, N. E.; Mann, A. K. P.; Skrabalak, S. E., Aerosol-assisted synthesis and assembly of nanoscale building blocks. *J. Mater. Chem. A* **2013,** *1* (17), 5193-5202.

32. Ma, X.; Zachariah, M. R.; Zangmeister, C. D., Reduction of Suspended Graphene Oxide Single Sheet Nanopaper: The Effect of Crumpling. *J. Phys. Chem. C* **2013,** *117* (6), 3185-3191.

33. Ma, X.; Zachariah, M. R.; Zangmeister, C. D., Crumpled Nanopaper from Graphene Oxide. *Nano Lett.* **2012,** *12* (1), 486-489.

34. Perreault, F.; Fonseca de Faria, A.; Elimelech, M., Environmental applications of graphene-based nanomaterials. *Chem. Soc. Rev.* **2015,** *44* (16), 5861-5896.

35. Li, J.; Zhang, S.; Chen, C.; Zhao, G.; Yang, X.; Li, J.; Wang, X., Removal of Cu(II) and Fulvic Acid by Graphene Oxide Nanosheets Decorated with Fe_3O_4 Nanoparticles. *ACS Appl. Mater. Interfaces* **2012,** *4* (9), 4991-5000.

36. Liu, M.; Chen, C.; Hu, J.; Wu, X.; Wang, X., Synthesis of Magnetite/Graphene Oxide Composite and Application for Cobalt(II) Removal. *J. Phys. Chem. C* **2011,** *115* (51), 25234-25240.

37. Chandra, V.; Kim, K. S., Highly Selective Adsorption of Hg^{2+} by a Polypyrrole-reduced Graphene Oxide Composite. *Chem. Commun.* **2011,** *47* (13), 3942-3944.

38. Sun, Y.; Shao, D.; Chen, C.; Yang, S.; Wang, X., Highly Efficient Enrichment of Radionuclides on Graphene Oxide-Supported Polyaniline. *Environ. Sci. Technol.* **2013,** *47* (17), 9904-9910.

39. Sun, H.; Cao, L.; Lu, L., Magnetite/Reduced Graphene Oxide Nanocomposites: One Step Solvothermal Synthesis and Use as a Novel Platform for Removal of Dye Pollutants. *Nano Res.* **2011,** *4* (6), 550-562.

40. Wang, J.; Chen, Z.; Chen, B., Adsorption of Polycyclic Aromatic Hydrocarbons by Graphene and Graphene Oxide Nanosheets. *Environ. Sci. Technol.* **2014,** *48* (9), 4817-4825.

41. Liu, X.; Zhang, H.; Ma, Y.; Wu, X.; Meng, L.; Guo, Y.; Yu, G.; Liu, Y., Graphene-Coated Silica as a Highly Efficient Sorbent for Residual Organophosphorus Pesticides in Water. *J. Mater. Chem. A* **2013,** *1* (5), 1875-1884.

42. Wang, W.-N.; An, W.-J.; Ramalingam, B.; Mukherjee, S.; Niedzwiedzki, D. M.; Gangopadhyay, S.; Biswas, P., Size and Structure Matter: Enhanced CO_2 Photoreduction Efficiency by Size-Resolved Ultrafine Pt Nanoparticles on TiO_2 Single Crystals. *J. Am. Chem. Soc.* **2012,** *134* (27), 11276-11281.
43. Williams, G.; Seger, B.; Kamat, P. V., TiO_2-Graphene Nanocomposites. UV-Assisted Photocatalytic Reduction of Graphene Oxide. *ACS Nano* **2008,** *2* (7), 1487-1491.
44. Li, W.; Li, D.; Xian, J.; Chen, W.; Hu, Y.; Shao, Y.; Fu, X., Specific Analyses of the Active Species on $Zn_{0.28}Cd_{0.72}S$ and TiO_2 Photocatalysts in the Degradation of Methyl Orange. *J. Phys. Chem. C* **2010,** *114* (49), 21482-21492.
45. Tseng, I.-H.; Wu, J. C.; Chou, H.-Y., Effects of sol–gel procedures on the photocatalysis of Cu/TiO 2 in CO 2 photoreduction. *J. Catal.* **2004,** *221* (2), 432-440.
46. Wang, W.-N.; Park, J.; Biswas, P., Rapid synthesis of nanostructured Cu-TiO_2-SiO_2 composites for CO_2 photoreduction by evaporation driven self-assembly. *Catalysis Science & Technology* **2011,** *1* (4), 593-600.
47. Zhang, Y.; Tang, Z.-R.; Fu, X.; Xu, Y.-J., TiO_2−Graphene Nanocomposites for Gas-Phase Photocatalytic Degradation of Volatile Aromatic Pollutant: Is TiO_2−Graphene Truly Different from Other TiO_2−Carbon Composite Materials? *ACS Nano* **2010,** *4* (12), 7303-7314.
48. Pastrana-Mart ńez, L. M.; Morales-Torres, S.; Likodimos, V.; Figueiredo, J. L.; Faria, J. L.; Falaras, P.; Silva, A. M. T., Advanced Nanostructured Photocatalysts Based on Reduced Graphene Oxide–TiO_2 Composites for Degradation of Diphenhydramine Pharmaceutical and Methyl Orange Dye. *Appl. Catal., B* **2012,** *123–124* (0), 241-256.

49. Xiong, Z.; Zhang, L. L.; Ma, J.; Zhao, X. S., Photocatalytic degradation of dyes over graphene-gold nanocomposites under visible light irradiation. *Chem. Commun.* **2010,** *46* (33), 6099-6101.

50. Arif Sher Shah, M. S.; Zhang, K.; Park, A. R.; Kim, K. S.; Park, N.-G.; Park, J. H.; Yoo, P. J., Single-step solvothermal synthesis of mesoporous Ag-TiO_2-reduced graphene oxide ternary composites with enhanced photocatalytic activity. *Nanoscale* **2013,** *5* (11), 5093-5101.

51. Wang, W.-N.; Jiang, Y.; Fortner, J. D.; Biswas, P., Nanostructured Graphene-Titanium Dioxide Composites Synthesized by a Single-Step Aerosol Process for Photoreduction of Carbon Dioxide. *Environ. Eng. Sci.* **2014,** *31* (7), 428-434.

52. Zhao, X.; Liu, H.; Shen, Y.; Qu, J., Photocatalytic reduction of bromate at C60 modified Bi_2MoO_6 under visible light irradiation. *Appl. Catal., B* **2011,** *106* (1–2), 63-68.

53. Ye, L.; Wang, S.; You, H.; Yao, J.; Kang, X., Photocatalytic reduction of perchlorate in aqueous solutions in UV/Cu–TiO_2/SiO_2 system. *Chem. Eng. J.* **2013,** *226*, 434-443.

54. Qiu, R.; Zhang, D.; Diao, Z.; Huang, X.; He, C.; Morel, J.-L.; Xiong, Y., Visible light induced photocatalytic reduction of Cr(VI) over polymer-sensitized TiO_2 and its synergism with phenol oxidation. *Water Res.* **2012,** *46* (7), 2299-2306.

55. Akhavan, O.; Choobtashani, M.; Ghaderi, E., Protein Degradation and RNA Efflux of Viruses Photocatalyzed by Graphene–Tungsten Oxide Composite Under Visible Light Irradiation. *J. Phys. Chem. C* **2012,** *116* (17), 9653-9659.

56. Akhavan, O.; Ghaderi, E., Photocatalytic Reduction of Graphene Oxide Nanosheets on TiO_2 Thin Film for Photoinactivation of Bacteria in Solar Light Irradiation. *J. Phys. Chem. C* **2009,** *113* (47), 20214-20220.

57. Bunch, J. S.; Verbridge, S. S.; Alden, J. S.; van der Zande, A. M.; Parpia, J. M.; Craighead, H. G.; McEuen, P. L., Impermeable atomic membranes from graphene sheets. *Nano Lett.* **2008,** *8* (8), 2458-2462.

58. Jiang, D.-e.; Cooper, V. R.; Dai, S., Porous Graphene as the Ultimate Membrane for Gas Separation. *Nano Lett.* **2009,** *9* (12), 4019-4024.

59. Cohen-Tanugi, D.; Grossman, J. C., Water Desalination across Nanoporous Graphene. *Nano Lett.* **2012,** *12* (7), 3602-3608.

60. Surwade, S. P.; Smirnov, S. N.; Vlassiouk, I. V.; Unocic, R. R.; Veith, G. M.; Dai, S.; Mahurin, S. M., Water desalination using nanoporous single-layer graphene. *Nat. Nanotechnol.* **2015,** *10*, 459–464.

61. Cohen-Tanugi, D.; Grossman, J. C., Nanoporous graphene as a reverse osmosis membrane: Recent insights from theory and simulation. *Desalination* **2015,** *366*, 59-70.

62. O'Hern, S. C.; Boutilier, M. S. H.; Idrobo, J.-C.; Song, Y.; Kong, J.; Laoui, T.; Atieh, M.; Karnik, R., Selective Ionic Transport through Tunable Subnanometer Pores in Single-Layer Graphene Membranes. *Nano Lett.* **2014,** *14* (3), 1234-1241.

63. Mahmoud, K. A.; Mansoor, B.; Mansour, A.; Khraisheh, M., Functional graphene nanosheets: The next generation membranes for water desalination. *Desalination* **2015,** *356* (0), 208-225.

64. Dikin, D. A.; Stankovich, S.; Zimney, E. J.; Piner, R. D.; Dommett, G. H. B.; Evmenenko, G.; Nguyen, S. T.; Ruoff, R. S., Preparation and Characterization of Graphene Oxide Paper. *Nature* **2007,** *448* (7152), 457-460.

65. Nair, R. R.; Wu, H. A.; Jayaram, P. N.; Grigorieva, I. V.; Geim, A. K., Unimpeded Permeation of Water Through Helium-Leak-Tight Graphene-Based Membranes. *Science* **2012,** *335* (6067), 442-444.

66. Joshi, R. K.; Carbone, P.; Wang, F. C.; Kravets, V. G.; Su, Y.; Grigorieva, I. V.; Wu, H. A.; Geim, A. K.; Nair, R. R., Precise and Ultrafast Molecular Sieving Through Graphene Oxide Membranes. *Science* **2014,** *343* (6172), 752-754.

67. Huang, H.; Song, Z.; Wei, N.; Shi, L.; Mao, Y.; Ying, Y.; Sun, L.; Xu, Z.; Peng, X., Ultrafast viscous water flow through nanostrand-channelled graphene oxide membranes. *Nat. Commun.* **2013,** *4*.

68. Han, Y.; Jiang, Y.; Gao, C., High-Flux Graphene Oxide Nanofiltration Membrane Intercalated by Carbon Nanotubes. *ACS Appl. Mater. Interfaces* **2015,** *7* (15), 8147-8155.

69. Hu, M.; Mi, B., Enabling Graphene Oxide Nanosheets as Water Separation Membranes. *Environ. Sci. Technol.* **2013,** *47* (8), 3715-3723.

70. Wang, W.; Eftekhari, E.; Zhu, G.; Zhang, X.; Yan, Z.; Li, Q., Graphene oxide membranes with tunable permeability due to embedded carbon dots. *Chem. Commun.* **2014,** *50* (86), 13089-13092.

71. Perreault, F.; Tousley, M. E.; Elimelech, M., Thin-Film Composite Polyamide Membranes Functionalized with Biocidal Graphene Oxide Nanosheets. *Environ. Sci. Technol. Lett.* **2013,** *1* (1), 71-76.

72. Gao, Y.; Hu, M.; Mi, B., Membrane surface modification with TiO_2–graphene oxide for enhanced photocatalytic performance. *J. Membr. Sci.* **2014,** *455* (0), 349-356.

73. Pastrana-Mart ńez, L. M.; Morales-Torres, S.; Figueiredo, J. L.; Faria, J. L.; Silva, A. M. T., Graphene oxide based ultrafiltration membranes for photocatalytic degradation of organic pollutants in salty water. *Water Res.* **2015,** *77*, 179-190.

74. Ganesh, B. M.; Isloor, A. M.; Ismail, A. F., Enhanced hydrophilicity and salt rejection study of graphene oxide-polysulfone mixed matrix membrane. *Desalination* **2013,** *313* (0), 199-207.

75. Crock, C. A.; Rogensues, A. R.; Shan, W.; Tarabara, V. V., Polymer nanocomposites with graphene-based hierarchical fillers as materials for multifunctional water treatment membranes. *Water Res.* **2013,** *47* (12), 3984-3996.

76. Zinadini, S.; Zinatizadeh, A. A.; Rahimi, M.; Vatanpour, V.; Zangeneh, H., Preparation of a novel antifouling mixed matrix PES membrane by embedding graphene oxide nanoplates. *J. Membr. Sci.* **2014,** *453* (0), 292-301.

77. Zhang, J.; Xu, Z.; Mai, W.; Min, C.; Zhou, B.; Shan, M.; Li, Y.; Yang, C.; Wang, Z.; Qian, X., Improved Hydrophilicity, Permeability, Antifouling and Mechanical Performance of PVDF Composite Ultrafiltration Membranes Tailored by Oxidized Low-Dimensional Carbon Nanomaterials. *J. Mater. Chem. A* **2013,** *1* (9), 3101-3111.

78. Chae, H.-R.; Lee, J.; Lee, C.-H.; Kim, I.-C.; Park, P.-K., Graphene oxide-embedded thin-film composite reverse osmosis membrane with high flux, anti-biofouling, and chlorine resistance. *J. Membr. Sci.* **2015,** *483* (0), 128-135.

79. Yin, J.; Zhu, G.; Deng, B., Graphene oxide (GO) enhanced polyamide (PA) thin-film nanocomposite (TFN) membrane for water purification. *Desalination* **2016,** *379*, 93-101.

Chapter 3. Evaporation-Induced Crumpling of Graphene Oxide Nanosheets in Aerosolized Droplets: Confinement Force Relationship

Abstract

A possible solution to solve the restacking issue of graphene oxide (GO) nanosheets during large-scale production is to turn the 2D nanosheets into 3D crumpled balls that have excellent compressive properties but still maintain high free volumes. An aerosol-based process has been proven to be a rational method for this purpose, in which, the crumpling phenomenon, however, has hitherto remained unclear. Here we present a detailed understanding of the crumpling of GO nanosheets by a systematic investigation conducted in aerosolized droplets by means of in-line (e.g., scanning mobility particle sizer) and off-line (e.g., electron microscopy) measurements. Correlations between the confinement force and various parameters, such as evaporation rate and precursor concentration were established to derive a universally applicable equation. Both calculation and experimental results revealed that the evaporation rate plays an important role in controlling the crumpling process.

3.1 Introduction

Two-dimensional (2D) graphene oxide (GO) nanosheets are attracting tremendous attention due to their remarkable properties stemming from unique morphology.[1, 2] Theoretically, GO nanosheets have a large specific surface area of over 2500 m^2/g,[3] making them highly desirable for use as a 2D support for various applications. These nanosheets exhibit high flexibility, enabling the possibility of encapsulation for drug delivery, photocatalysis, solar cells, and electrical energy storage systems.[3-6] The challenges of using these 2D nanosheets are related to their mass production. One particular issue is the tendency to aggregate (restacking) due to strong intersheet adhesion (van der Waals attraction).[7] Restacking of these nanosheets reduces their accessible surface area and hence adversely affects the properties and subsequent applications.

One possible solution is to turn the 2D nanosheets into three-dimensional (3D) crumpled 'ball' like structures. Unlike flat sheets, the crumpled GO balls have high free volume and excellent compressive properties, and can tightly pack without significantly reducing the accessible surface area.[8] At a crumpled equilibrium, approximately 58.6% of the accessible surface area, i.e. over 1500 m^2/g is maintained,[9] which is still much larger than those of conventional laminar or porous materials.

The exploration of crumpled or folded nanosheets is an active area of research, both theoretically and experimentally.[9-13] Although GO nanosheets are very strong in terms of Young's modulus (207.6 ± 23.4 GPa for monolayer GO),[14] they have a propensity to be warped out-of-plane, exhibiting ripples, folds, and scrolls.[9] Theoretical exploration showed that thin sheets of almost all materials crumple in the same way, such that the stress energy is concentrated in the network of narrow folding ridges.[9-13, 15] The diameter (D_p) of a randomly crumpled GO ball mainly

depends on the confinement force (F), which is the capillary force responsible for the crumpling of the GO nanosheets.[10]

An aerosol-based process has been shown to be a rational method to realize the crumpling of GO nanosheets.[8, 16] In this process, the GO aqueous suspension was atomized into fine droplets. Crumpled GO particles were formed by capillary compression due to rapid evaporation of the aerosol droplets. The method is simple yet effective, with an extremely short processing time of several seconds.[17, 18] In addition, it is applied in a continuous manner, avoiding batch-to-batch variations. The crumpling of the 2D nanosheets, however, is complex, in which many parameters are involved. Although the production of crumpled GO particles has been demonstrated using aerosol methods,[8, 16, 19, 20] systematic investigations on the correlations between the confinement force and various parameters, such as evaporation rate and precursor concentration, have not yet been established. In this work, we report an understanding of evaporation-induced crumpling of GO nanosheets in aerosolized fine droplets. A theoretical equation of the confinement force by considering these parameters was derived and validated by experimental results.

3.2 Experimental

Experimental procedures are detailed in the Supporting Information and also briefly described here. The GO nanosheets were prepared by using the modified Hummers method.[21] The GO aqueous suspension is stable for months with negligible sedimentation observed (see Supporting Information, Figure S3.1a and S3.1b). This high stability stems from the mutual columbic repulsion between negatively charged GO surfaces as confirmed by the measured high negative zeta potential (-37 mV) (see Supporting Information, Figure S3.1c), which is consistent with reported values.[22, 23] The mass concentration (C) of GO was determined by measuring its optical absorbance using a UV-Vis spectrometer (Cary 100, Varian Inc.) based on the Beer-

Lambert law.[24] The typical absorption spectra of GO and the calibration curve are shown in Supporting Information, Figure S3.2. The crumpled graphene oxide particles were synthesized by the FuAR method (Figure 3.1a). The droplet size was controlled from 2 to 4 μm by adjusting nebulizer pressure (P_{neb}) and was measured by using an aerodynamic particle sizer (APS) (see Supporting Information Figure S3.3 for details). The morphology and size of the GO samples were examined by TEM (Tecnai^{TM} Spirit, FEI Co.) and FESEM (NOVA NanoSEM 230, FEI Co.). Online particle size measurements were performed by using the SMPS (TSI, Inc.) system, which consists of a DMA (TSI 3081, TSI, Inc.) and a CPC (TSI 3025, TSI, Inc.). During online measurements, a 0.3 lpm slip-stream of aerosols was drawn into the SMPS system. The above size measurements for each sample were performed five times and average data and standard deviations were obtained.

3.3 Results and Discussion

The GO nanosheets were prepared by using a modified Hummers method (see Experimental Section and Supporting Information S3.1 for details).[21] The GO aqueous suspension was used as the precursor for synthesis of crumpled GO particles by means of a furnace aerosol reactor (FuAR) method (Figure 3.1a, see also Supporting Information S3.1).[25] A possible formation pathway of the crumpled GO particles inside the FuAR is shown in Figure 3.1b. The precursor was atomized into micrometer-sized (2-4 μm) droplets by a six-jet Collison nebulizer (BGI Incorporated), and the aerosol was delivered by nitrogen gas into an alumina reactor maintained at predetermined temperatures to heat it for several seconds (see Table 3.1 for residence times). The aerosolized droplets then underwent solvent evaporation, evaporation-driven crumpling of GO nanosheets, and further drying to form the final GO or reduced GO (r-GO) particles. The magnitude of the confinement force is a critical factor determining the morphology

as well as the size of the dry GO particles. If the evaporation rate is slow, the confinement force is weak; hence only GO nanosheets with ripples (the so-called rippled GO[26]) are formed (see Figure 3.1b). On the other hand, crumpled GO balls are obtained when the confinement force is high due to rapid evaporation. These GO samples were then collected downstream of the reactor using a glass microfiber filter for further characterization.

Table 3.1 Effect of solvent evaporation rate[a]

Furnace temperature (°C)	Residence time (s)	Diffusion coefficient (m^2/s)	Evaporation rate (g/s)	Evaporation time (s)	Particle diameter[b] (nm)	Confinement force[c] (μN)
200	1.87	6.38×10^{-5}	4.43×10^{-7}	2.65×10^{-5}	88.22±0.49	29.75
400	1.63	1.14×10^{-4}	7.88×10^{-7}	1.49×10^{-5}	84.32±0.16	34.87
600	1.26	1.59×10^{-4}	1.11×10^{-6}	1.06×10^{-5}	83.40±0.77	37.80
800	1.02	2.06×10^{-4}	1.43×10^{-6}	8.22×10^{-6}	80.99±0.89	45.58
1000	0.86	2.53×10^{-4}	1.76×10^{-6}	6.69×10^{-6}	75.14±1.74	56.23

[a]Precursor concentration = 0.3 mg/ml, nebulizer pressure = 96.53 kPa (D_d = 2.82 μm), [b]Geometric mean diameter, obtained by SMPS measurements for the "0 dryer" case; [c]Calculated for the "0 dryer" case.

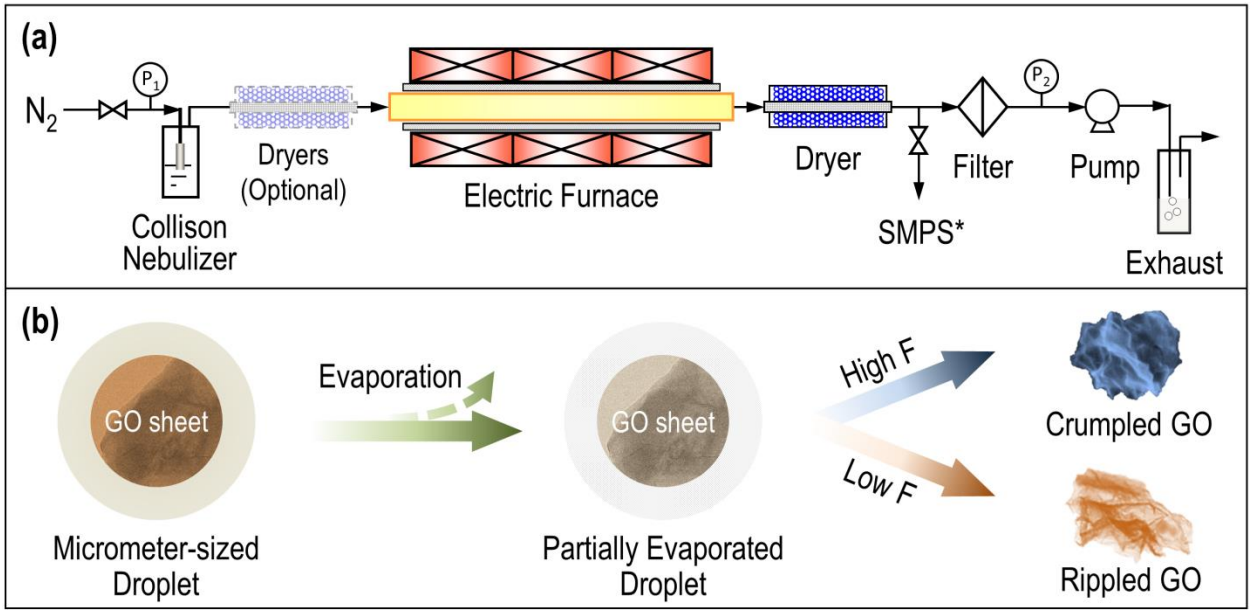

Figure 3.1 Experimental setup. (a) Schematic diagram of a furnace aerosol reactor (FuAR) and (b) the possible formation mechanism of crumpled graphene oxide. SMPS: Scanning mobility particle sizer, an in-line particle size measurement system.

The morphology of the GO samples was examined by transmission electron microscopy (TEM) and field emission scanning electron microscopy (FESEM). Figure 3.2 shreds light on the morphology evolution of the GO samples prepared at different furnace temperatures (T_f) (see Table 1 for corresponding evaporation rates). At low temperatures, e.g., 200°C, only rippled GO nanosheets rather than crumpled GO particles were obtained as verified by both FESEM and TEM images (Figure 3.2a and 3.2e). The GO nanosheets are warped with ripples and ridges, but no crumpled GO balls were observed due to the weak confinement force generated by slow water evaporation. The color of the GO sample collected at this temperature is pale yellow (see the digital photo in Figure 3.2a and 3.2e), indicating a low reduction percentage of GO to graphene. At temperatures of 400°C and higher, crumpled GO particles were formed. A typical crumpled GO particle was highlighted in Figure 3.2b (inset), which has a quasi-spherical morphology with

relatively smooth surfaces. More sharp ridges emerged on the crumpled GO particles with increasing furnace temperature (see inset in Figure 3.2c). At even higher temperatures, such as 1000°C, crumpled GO particles also tended to agglomerate due to sintering effect (Figure 3.2d and 3.2h).[27] The color of the GO samples changes from pale yellow to dark brown to black with increase in furnace temperature, as seen when the reduction of GO proceeds. This has been suggested as partial restoration of the π network within the carbon structure (thermal reduction) and has been witnessed through chemical reduction of the GO sheets.[28] The reduction of GO is not a significant factor to be considered in the crumpling process and hence is not the major focus of this work. The particle size distribution (PSD) of the crumpled GO particles was analyzed from the FESEM images and an example can be found in Supporting Information (Figure S3.4), from which a peak diameter of around 200 nm is observed for the crumpled GO particles synthesized from a diluted GO suspension. It should be noted that the particle sizes obtained from SEM/TEM images are often overestimated due to particle agglomeration caused during sample preparation.

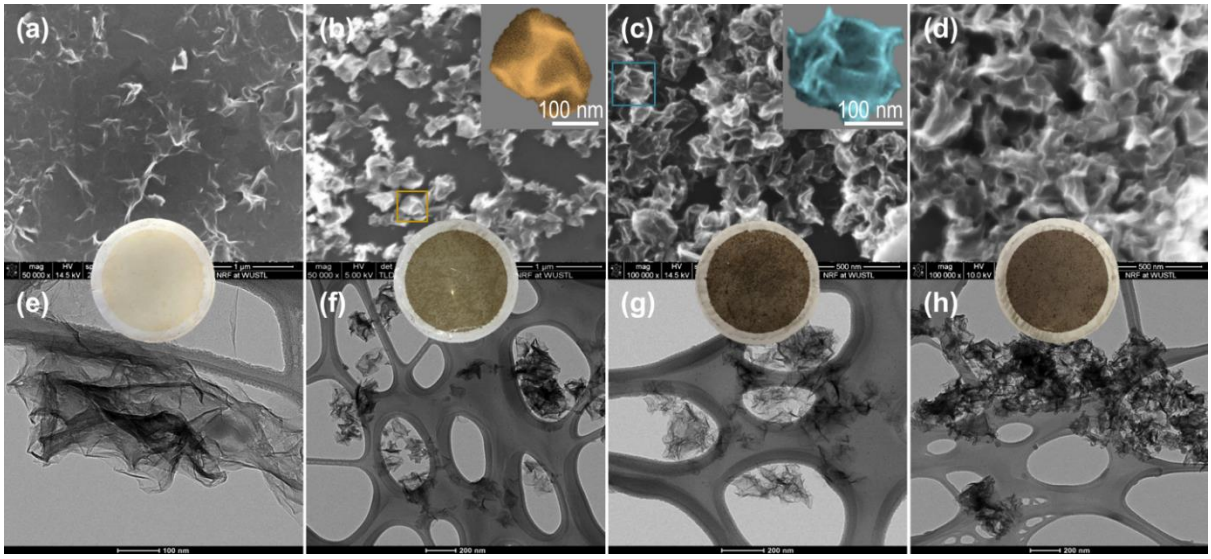

Figure 3.2 Morphology evolution of graphene oxide particles as a function of furnace temperature. (a) to (d) are FESEM images and (e) to (h) are corresponding TEM images. (a)/(e) 200°C, (b)/(f) 400°C, (c)/(g) 800°C, and (d)/(h) 1000°C. The spherical inset at each condition is the corresponding digital photo of graphene oxide collected on a filter. Individual crumpled GO particles are highlighted in Figure 3.2b (gold) and 3.2c (aqua).

In addition to the off-line particle size analysis, in-line particle size measurements of GO particles were also carried out by using a scanning mobility particle sizer (SMPS, TSI Inc.), consisting of a differential mobility analyzer (DMA) for particle size classification and condensation particle counter (CPC) for particle number concentration measurements. It is a highly reliable methodology, having a capability of measuring aerosol sizes ranging from several to several hundred nanometers; and the number concentration up to 10^7 particles/cm^3. Details of the operating principles of the instrument are well documented.[27] A typical PSD of the crumpled GO particles synthesized from a diluted GO aqueous suspension is shown in Figure 3.3a, from which the geometric mean diameter (D_{pg}) of 84.32 ± 0.16 nm was obtained. Similar measurements of crumpled GO particles by SMPS were also conducted by Ma et al.[16] The above PSD was achieved for the crumpled GO particles prepared without adding a diffusion dryer in front of the furnace

(the "0 dryer" case, see inset in Figure 3.3a). In this case, D_{pg} of the crumpled GO particles decreases with increasing evaporation rate (see Table 1 for corresponding T_f) (open squares with solid line, Figure 3.3b). The reason for this is attributed to the increased confinement force as the solvent evaporation rate increased. Although the determination of the confinement force exerted on the GO nanosheets is complex due to the large number of physical and geometric uncertainties,[16] the correlation between the confinement force and solvent evaporation rate is of vital importance and should be understood quantitatively.

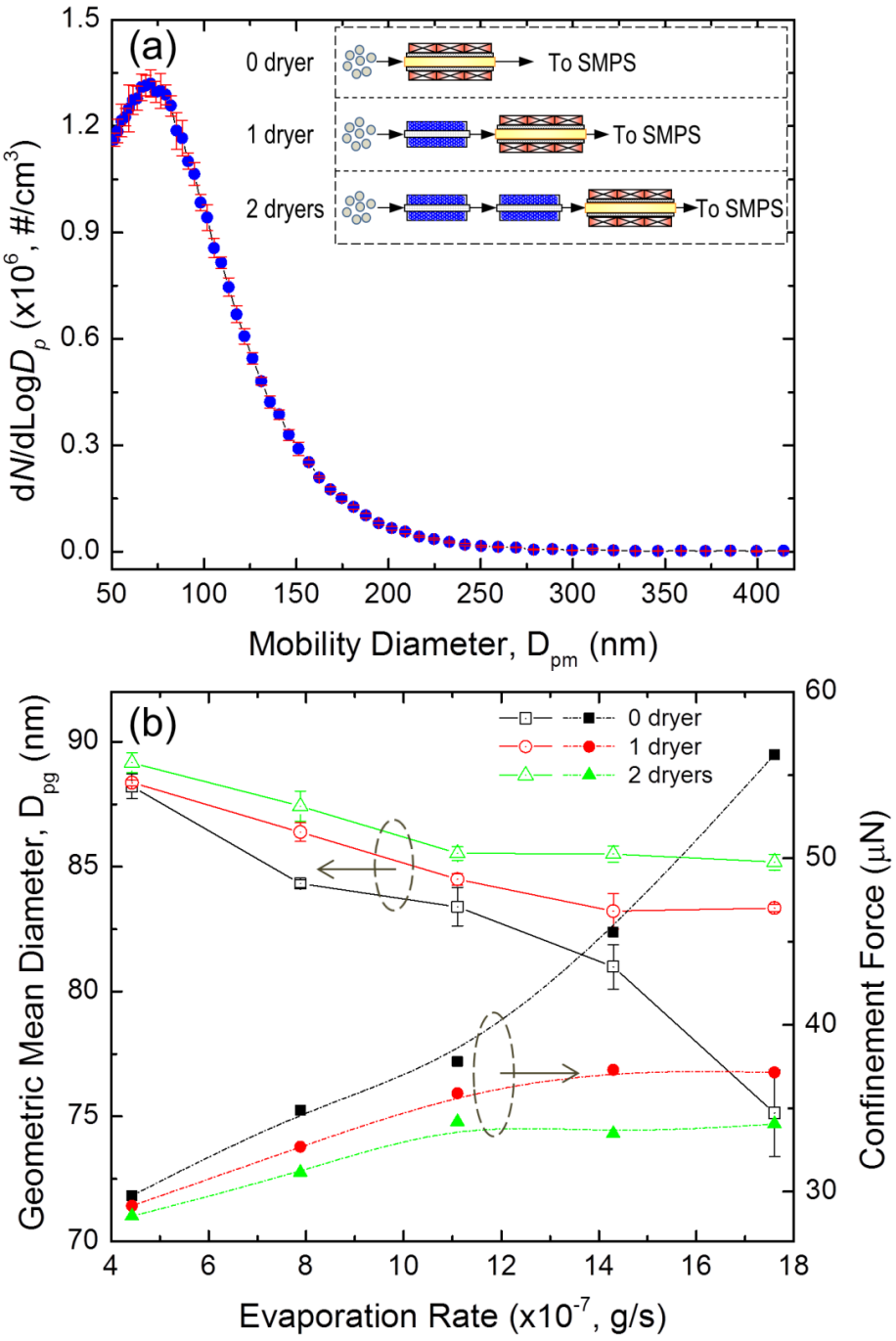

Figure 3.3 Particle size measurements and confinement force calculations. (a) A typical particle size distribution of crumpled GO particles synthesized at 400°C from 0.3 mg/ml suspension measured by SMPS, (b) Geometric mean diameters of crumpled GO particles and the corresponding confinement force as a function of evaporation rate. The above measurements and calculations were carried out at the following conditions: P_{neb} = 96.53 kPa (D_d = 2.82 μm) and C = 0.3 mg/ml.

The solvent evaporation rate (κ) of single droplet can be calculated using the follow equation[27]

$$\kappa = m_d / \tau_e \tag{1}$$

where m_d is the droplet mass, and τ_e is the evaporation time in the continuum region and can be estimated by the following equation[27]

$$\tau_e = \frac{R\rho_d D_d^2 T_d}{8 D_g M P_d} \tag{2}$$

where R is the gas constant, ρ_d is the droplet density, D_d is the droplet diameter, D_g is the gas-phase diffusion coefficient of the solvent (as a function of T_f), M is the molecular weight of the solvent, T_d is the droplet surface temperature (= boiling point of water when $T_f \geq 100$°C), and P_d is the vapor pressure of the solvent at the surface of the droplet.

On the other hand, the mass density of a crumpled spherical GO particle, ρ, follows a scaling equation[12]

$$\rho = \rho_m \left(\frac{F}{Yh}\right)^{\delta D} \left(\frac{D_p}{2h}\right)^{D-3} \tag{3}$$

where ρ_m is density of GO (1800 kg/m^3),[29] Y is the two-dimensional Young's modulus (145.32 N/m for a single GO sheet),[14] , δ is the force scaling exponent (0.25 for GO),[10] D is the characteristic fractal dimension (2.54 for GO),[16] h is the GO thickness (0.7 nm), and D_p is the particle diameter measured by SMPS. D_p of a crumpled GO particle can be also estimated following one-droplet-to-one-particle (ODOP) principle based on the mass conservation[18, 30]

$$D_p = D_d \left(C / \rho \right)^{1/3} \tag{4}$$

where C is the precursor (mass) concentration. Combining above equations yields the following equation of the confinement force

$$F = ABC^{1/\delta D} D_p^{-1/\delta} \left(\kappa T_d / P_d D_g \right)^{3/\delta D} \tag{5}$$

where A and B are constants ($A = Y 2^{\frac{D-3}{\delta D}} h^{1+\frac{D-3}{\delta D}} \rho_m^{-\frac{1}{\delta D}}$, $B = \left(3R / (4\pi M) \right)^{3/\delta D}$). In this work, the furnace temperature is always higher than 100°C, thus T_d and P_d become constant as well. From equation 5, the confinement force, F, is propositional to mass concentration of precursor ($F \propto C^{1.57}$) and the evaporation rate ($F \propto \kappa^{4.72}$), but inversely propositional to particle diameter ($F \propto D_p^{-4}$). At a fixed droplet size and precursor concentration, the evaporation rate is the only variable to be considered. Detailed derivation of equation 5 can be found in Supporting Information S3.2.

The corresponding confinement forces at different evaporation rates in the "0 dryer" case were calculated and plotted in Figure 3.3b (solid squares with dotted line), from which the direct proportionality of the confinement force with evaporation rate is observed. This clearly explains the reason for the smaller GO particles at higher evaporation rates, as the confinement force is larger and the GO nanosheets can be warped and compressed into smaller balls. The calculated confinement force associated with drying nanometer-scale water droplets has also been estimated both theoretically and experimentally.[16, 31] In this work, higher confinement forces (in the order of 20 to 60 μN) were obtained possibly due to higher evaporation rate and larger droplets as compared to previous studies. Further analyses of the confinement forces and the corresponding GO

morphologies at different evaporation rates suggest that a critical confinement force may exist at around 30 μN in this work. Only if the confinement force is higher than the critical value could the crumpled GO balls form. Detailed calculation results were also summarized in Table 3.1.

It is clear that the water removal from nanosheets drives the crumpling process, the so-called evaporation-induced crumpling.[8, 16] The furnace temperature is therefore the important parameter as it determines the evaporation rate. Previous research on the thermal stability analysis of self-adhered membranes, however, indicated that the heating has no significant effect on the crumpling process.[9, 13, 16] To verify this effect, diffusion dryers were added in front of the furnace (see inset in Figure 3.3a). The purpose of adding diffusion dryers was to absorb water from droplets before their entering into the furnace. By a simple calculation, two diffusion dryers are enough to absorb almost all water from droplets (see Supporting Information S3 for details). Therefore the crumpling should happen mostly inside the diffusion dryers rather than inside the furnace in the case of adding dryers. Figure 3.3b shows the particle sizes of crumpled GO particles as a function of evaporation rate (see corresponding T_f in Table S3.1) under different configurations of diffusion dryers. As explained above, the particle size decreases significantly with increasing furnace temperature in the case of no diffusion dryer installed. However, with diffusion dryers installed, the temperature effect becomes insignificant; where the particle size curves are rather flat (constant size). Furthermore, in the case of two dryers installed, the particle sizes are generally larger, and they did not decrease after temperatures increased from 600 to 1000°C (corresponding to 1.11×10^{-6} to 1.76×10^{-6} g/s). The larger particle sizes obtained are due to the weaker confinement force exerted on GO nanosheets resulting from slow evaporation rate (at room temperature inside the dryers). The results also confirmed that without evaporation of water in the furnace, the furnace temperature has no significant effect on the crumpling process, consistent with the previous

reports.[9, 13, 16] Additional results on the effect of diffusion dryers at different furnace temperatures are also summarized in Supporting Information, Table S3.1.

From a practical point of view, the precursor concentration is an important factor to be taken into account, which has been investigated as well (see Supporting Information, Table S3.2). From the results, the confinement force decreases with the precursor concentration. Based on equation 5, the confinement force should be proportional to the precursor concentration. On the other hand, as from equation 4, with increasing precursor concentration, the particle size also increases based on the mass conservation. The particle size, however, is inversely proportional to the confinement force (see equation 5). Therefore, the results are the compromise between the precursor concentration and particle size based on equations 4 and 5.

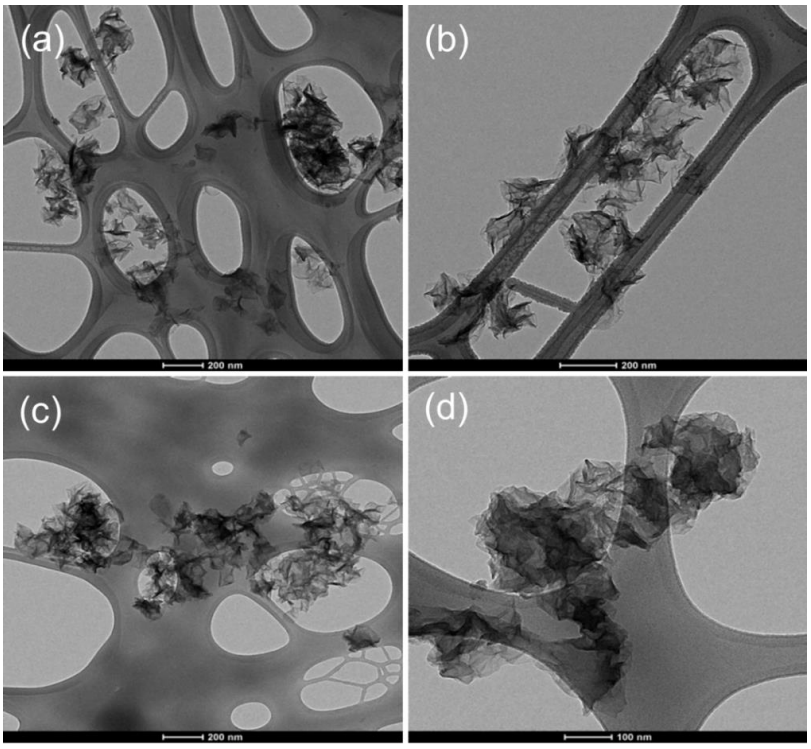

Figure 3.4 TEM images of the crumpled GO particles as a function of pH. (a) 2.80, (b) 4.16, (c) 7.19, and (d) 10.02. The crumpled GO was synthesized from a diluted GO suspension (C = 0.3 mg/ml) at 400°C.

pH is another crucial parameter to be considered that is closely related to the physiological activity of GO aqueous suspension.[32] The effect of pH on the stability of aqueous GO solution has also been studied (see Supporting Information S3.4 for details). The results reveal that the zeta potential increases with pH, indicating the increase in electrostatic repulsive force, which is responsible for stabilization (Figure S3.5).[22, 23] It is therefore expected that the number of multilayered GO sheets inside a crumpled GO particle may increase with decreasing zeta potential. However, there are no significant size and morphology variations of the crumpled GO particles prepared from GO aqueous solutions with different pH based on TEM (Figure 3.4) as well as SMPS analyses (Supporting Information, Figure S3.6). The reason may be due to the smaller magnitude of the electric repulsive force as compared to the corresponding confinement force, which needs further investigation in the near future.

3.4 Conclusion

In conclusion, the evaporation-induced crumpling of GO nanosheets in aerosolized fine droplets was investigated systematically leading to a fundamental understanding of the process. A universal equation of the confinement force was derived by considering various parameters, such as evaporation rate and precursor concentration. This was verified by our experimental results; and should be useful for future applications of crumpled GO particles.

Acknowledgements

This work was supported by funds from the Lopata Endowment at Washington University in St. Louis. Electron microscopy work was performed at the Nano Research Facility (NRF) at Washington University in St. Louis, a member of the National Nanotechnology Infrastructure Network (NNIN), supported by the National Science Foundation under Grant No. ECS-0335765.

References

1. Novoselov, K. S.; Geim, A. K.; Morozov, S. V.; Jiang, D.; Zhang, Y.; Dubonos, S. V.; Grigorieva, I. V.; Firsov, A. A., Electric field effect in atomically thin carbon films. *Science* **2004,** *306* (5696), 666-669.
2. Kamat, P. V., Graphene-Based Nanoarchitectures. Anchoring Semiconductor and Metal Nanoparticles on a Two-Dimensional Carbon Support. *J. Phys. Chem. Lett.* **2010,** *1* (2), 520-527.
3. Stankovich, S.; Dikin, D. A.; Dommett, G. H. B.; Kohlhaas, K. M.; Zimney, E. J.; Stach, E. A.; Piner, R. D.; Nguyen, S. T.; Ruoff, R. S., Graphene-based composite materials. *Nature* **2006,** *442* (7100), 282-286.
4. Rao, C. N. R.; Sood, A. K.; Subrahmanyam, K. S.; Govindaraj, A., Graphene: The New Two-Dimensional Nanomaterial. *Angew Chem. Int. Edit.* **2009,** *48* (42), 7752-7777.
5. Ng, Y. H.; Lightcap, I. V.; Goodwin, K.; Matsumura, M.; Kamat, P. V., To What Extent Do Graphene Scaffolds Improve the Photovoltaic and Photocatalytic Response of TiO_2 Nanostructured Films? *J. Phys. Chem. Lett.* **2010,** *1* (15), 2222-2227.
6. Kamat, P. V., Graphene-Based Nanoassemblies for Energy Conversion. *J. Phys. Chem. Lett.* **2011,** *2* (3), 242-251.
7. Dreyer, D. R.; Park, S.; Bielawski, C. W.; Ruoff, R. S., The chemistry of graphene oxide. *Chem. Soc. Rev.* **2010,** *39* (1), 228-240.
8. Luo, J. Y.; Jang, H. D.; Sun, T.; Xiao, L.; He, Z.; Katsoulidis, A. P.; Kanatzidis, M. G.; Gibson, J. M.; Huang, J. X., Compression and Aggregation-Resistant Particles of Crumpled Soft Sheets. *ACS Nano* **2011,** *5* (11), 8943-8949.

9. Cranford, S. W.; Buehler, M. J., Packing efficiency and accessible surface area of crumpled graphene. *Phys. Rev. B* **2011,** *84* (20), 205451.

10. Vliegenthart, G. A.; Gompper, G., Forced crumpling of self-avoiding elastic sheets. *Nat. Mater.* **2006,** *5* (3), 216-221.

11. Balankin, A. S.; Huerta, O. S.; De Oca, R. C. M.; Ochoa, D. S.; Trinidad, J. M.; Mendoza, M. A., Intrinsically anomalous roughness of randomly crumpled thin sheets. *Phys. Rev. E* **2006,** *74* (6), 061602.

12. Balankin, A. S.; Silva, I. C.; Martinez, O. A.; Huerta, O. S., Scaling properties of randomly folded plastic sheets. *Phys. Rev. E* **2007,** *75* (5), 051117.

13. Tallinen, T.; Astrom, J. A.; Kekalainen, P.; Timonen, J., Mechanical and Thermal Stability of Adhesive Membranes with Nonzero Bending Rigidity. *Phys. Rev. Lett.* **2010,** *105* (2).

14. Suk, J. W.; Piner, R. D.; An, J. H.; Ruoff, R. S., Mechanical Properties of Monolayer Graphene Oxide. *ACS Nano* **2010,** *4* (11), 6557-6564.

15. Lobkovsky, A.; Gentges, S.; Li, H.; Morse, D.; Witten, T. A., Scaling Properties of Stretching Ridges in a Crumpled Elastic Sheet. *Science* **1995,** *270* (5241), 1482-1485.

16. Ma, X. F.; Zachariah, M. R.; Zangmeister, C. D., Crumpled Nanopaper from Graphene Oxide. *Nano Lett.* **2012,** *12* (1), 486-489.

17. Wang, W. N.; Iskandar, F.; Okuyama, K.; Shinomiya, Y., Rapid synthesis of non-aggregated fine chloroapatite blue phosphor powders with high quantum efficiency. *Adv. Mater.* **2008,** *20* (18), 3422-3426.

18. Wang, W. N.; Kaihatsu, Y.; Iskandar, F.; Okuyama, K., Highly Luminous Hollow Chloroapatite Phosphors Formed by a Template-Free Aerosol Route for Solid-State Lighting. *Chem. Mater.* **2009,** *21* (19), 4685-4691.

19. Luo, J. Y.; Zhao, X.; Wu, J. S.; Jang, H. D.; Kung, H. H.; Huang, J. X., Crumpled Graphene-Encapsulated Si Nanoparticles for Lithium Ion Battery Anodes. *J. Phys. Chem. Lett.* **2012,** *3* (13), 1824-1829.

20. Jang, H. D.; Kim, S. K.; Chang, H.; Roh, K.-M.; Choi, J.-W.; Huang, J. X., A Glucose Biosensor Based on TiO_2–Graphene Composite. *Biosens. Bioelectron.* **2012,** *38* (1), 184-188.

21. Hummers, W. S.; Offeman, R. E., Preparation of Graphitic Oxide. *J. Am. Chem. Soc.* **1958,** *80* (6), 1339.

22. Li, X. L.; Zhang, G. Y.; Bai, X. D.; Sun, X. M.; Wang, X. R.; Wang, E.; Dai, H. J., Highly conducting graphene sheets and Langmuir-Blodgett films. *Nat. Nanotechnol.* **2008,** *3* (9), 538-542.

23. Hasan, S. A.; Rigueur, J. L.; Harl, R. R.; Krejci, A. J.; Gonzalo-Juan, I.; Rogers, B. R.; Dickerson, J. H., Transferable graphene oxide films with tunable microstructures. *ACS Nano* **2010,** *4* (12), 7367-72.

24. Atkins, P.; de Paula, J., *Atkins' Physical Chemistry*. 8th ed.; Oxford University Press: 2006.

25. Wang, W. N.; Park, J.; Biswas, P., Rapid synthesis of nanostructured Cu-TiO_2-SiO_2 composites for CO_2 photoreduction by evaporation driven self-assembly. *Catal. Sci. Technol.* **2011,** *1* (4), 593-600.

26. Fasolino, A.; Los, J. H.; Katsnelson, M. I., Intrinsic ripples in graphene. *Nat. Mater.* **2007,** *6* (11), 858-861.

27. Hinds, W. C., *Aerosol Technology: Properties, Behavior, and Measurement of Airborne Particles*. Second ed.; John Wiley & Sons, Inc.: New York, 1999.

28. Zhu, Y. W.; Murali, S.; Cai, W. W.; Li, X. S.; Suk, J. W.; Potts, J. R.; Ruoff, R. S., Graphene and Graphene Oxide: Synthesis, Properties, and Applications. *Adv. Mater.* **2010,** *22* (35), 3906-3924.

29. Dikin, D. A.; Stankovich, S.; Zimney, E. J.; Piner, R. D.; Dommett, G. H. B.; Evmenenko, G.; Nguyen, S. T.; Ruoff, R. S., Preparation and characterization of graphene oxide paper. *Nature* **2007,** *448* (7152), 457-460.

30. Wang, W. N.; Widiyastuti, W.; Lenggoro, I. W.; Kim, T. O.; Okuyama, K., Photoluminescence optimization of luminescent nanocomposites fabricated by spray pyrolysis of a colloid-solution precursor. *J. Electrochem. Soc.* **2007,** *154* (4), J121-J128.

31. Butt, H. J.; Kappl, M., Normal capillary forces. *Adv. Colloid Interface* **2009,** *146* (1-2), 48-60.

32. Shih, C. J.; Lin, S. C.; Sharma, R.; Strano, M. S.; Blankschtein, D., Understanding the pH-Dependent Behavior of Graphene Oxide Aqueous Solutions: A Comparative Experimental and Molecular Dynamics Simulation Study. *Langmuir* **2012,** *28* (1), 235-241.

Chapter 3 Supporting Information

Table of Contents

S3.1. Extended Experimental Methods

Synthesis of Graphene Oxide. The graphene oxide nanosheets were prepared by using the modified Hummers method.[1] Graphite powders (45 μm, Sigma-Aldrich) were used as the raw materials. In this method, 50 ml of concentrated sulfuric acid (H_2SO_4) was added into a beaker containing 2 g of graphite at room temperature. The beaker was cooled to 0°C by using an ice bath. Six gram of potassium permanganate ($KMnO_4$) was then slowly added to the above mixture while it was allowed to warm to room temperature. The suspension was stirred for 2 h at 35°C. After the suspension was cooled in an ice bath, it was diluted by 350 ml of deionized (DI) water. Then, hydroperoxide aqueous solution (H_2O_2, 30%) was added until the gas evolution ceased in order to reduce residual permanganate. The suspension was then filtered, washed by DI water, and dried at room temperature for 24 h to obtain brownish graphite oxide powder. The dry graphene oxide powder was redispersed in DI water and sonicated for 3 h to get exfoliated single nanosheets. The suspension was then centrifuged at 10,000 rpm for 30 min and the supernatant was used as the precursor for crumpled graphene oxide preparation. The GO aqueous suspension is stable for

months with negligible sedimentation observed (see Figure S3.1 for details). This great stability stems from the mutual columbic repulsion between negatively charged GO surfaces as confirmed by the measured negative zeta potential (-37 mV) (Figure S3.1c). Functional groups such as epoxides, hydroxyls, and carboxylic groups adorn the surface of GO to render it suspendable in polar solvents. The mass concentration of GO was determined by measuring its optical absorbance using UV-Vis spectra based on the Beer-Lambert law.[2] A linear relationship between the absorption intensity and the concentration of GO in a wide range has also been observed previously.[3] The typical absorption spectra of GO with different mass concentrations were plotted in Figure S3.2a and the calibration curves are shown in Figure S3.2b.

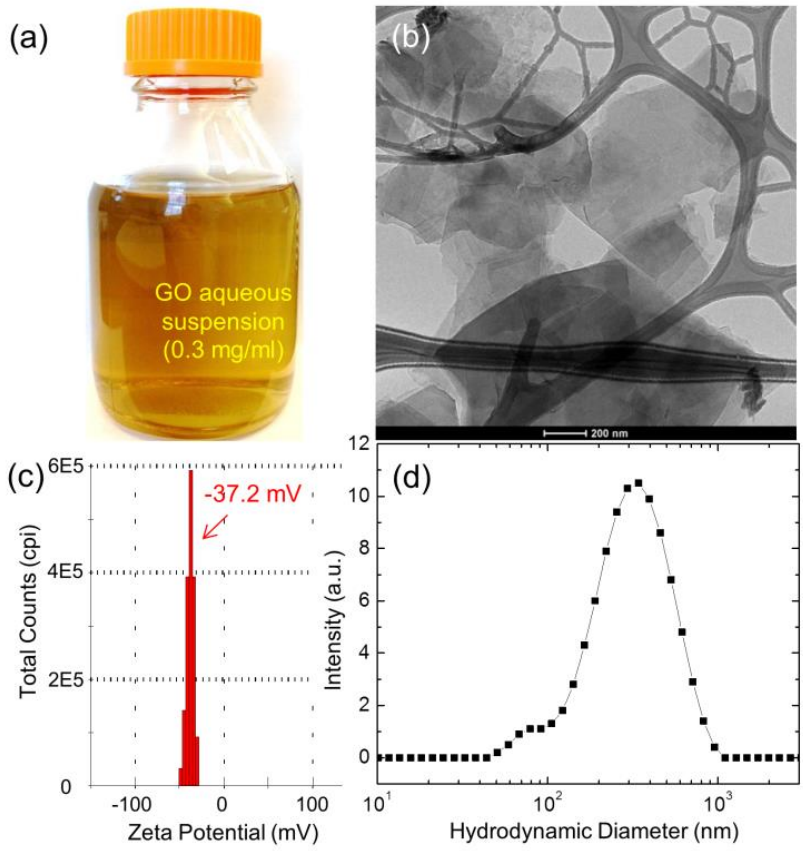

Figure S3.1. Representation characterization results of graphene oxide. (a) Photo of GO aqueous suspension, (b) Corresponding TEM image of GO nanosheets, (c) Zeta potential, and (d) intensity-based size distribution measured by DLS.

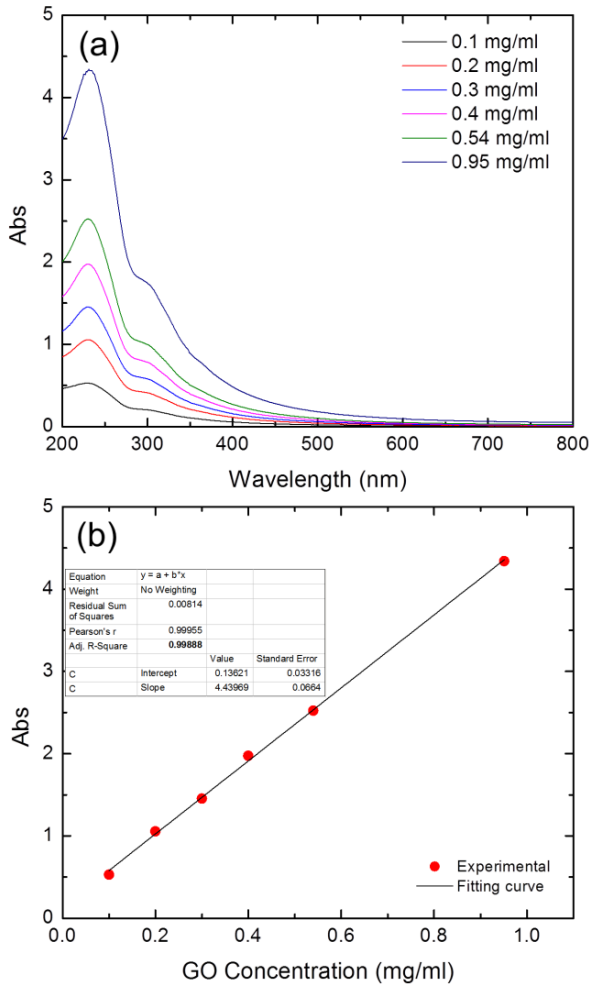

Figure S3.2. Mass concentration determination by UV-Vis measurements. (a) Typical UV-Vis absorption spectra of GO aqueous solutions with different concentrations, and (b) the corresponding calibration curve.

Synthesis of Crumpled Graphene Oxide Particles. The crumpled graphene oxide particles were synthesized by a furnace aerosol reactor (FuAR) method, which is schematically shown in Figure 3.1a. The FuAR consisted of a 6-jet Collison nebulizer (BGI Instruments, Waltham, MA) as the atomizer, an electric furnace, a tubular alumina reactor, a microfiber filter, an air pump, and cooling and gas feeding systems. The schematic diagram of crumpled GO particle formation inside the FuAR is shown in Figure 3.1b. The precursors were atomized into micrometer-sized droplets

by means of the atomizer, and the mist was delivered by air into the tubular alumina reactor (1 m in length and 25 mm in inner diameter) maintained at predetermined temperatures (from room temperature to 1000°C), followed by heating for several seconds. The droplet size (D_d) was controlled by adjusting nebulizer pressure (P_{neb}) and was measured by using an aerodynamic particle sizer (APS, TSI Inc.). Typical droplet size distributions and the geometric mean droplet diameters as a function of P_{neb} were plotted in Figure S3.3. The results reveal that the droplet sizes decreased monotonously from 3.7 μm at 40 kPa to 2.0 μm at 210 kPa. The droplet sizes of pure water and GO aqueous suspensions (C = 0.54 and 0.95 mg/ml) at a certain condition were almost the same due to the similarity of their physical properties. During the process, the micrometer-sized droplets underwent solvent evaporation, evaporation-driven crumpling of GO nanosheets, and further drying to form the final GO or reduced GO particles. These particles were collected downstream of the reactor using the glass microfiber filter (EPM 2000, Whatman Inc.) for characterization.

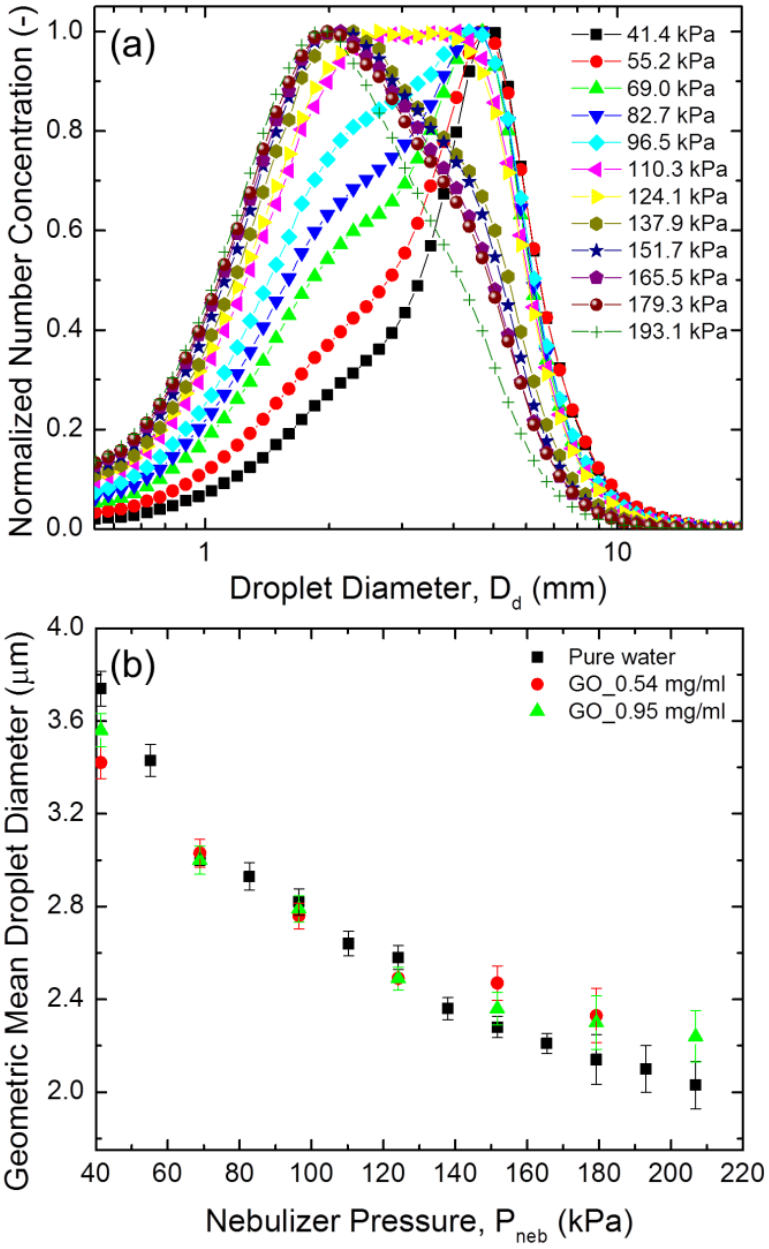

Figure S3.3. Droplet size measurements by using aerodynamic particle sizer. (a) droplet size distribution and (b) average droplet diameter as a function of pressure.

Materials Characterization. The morphology and size of the GO samples were examined by transmission electron microscopy (TEM, Tecnai^{TM} Spirit, FEI Co.) and field emission scanning electron microscopy (FESEM, NOVA NanoSEM 230, FEI Co.). The average diameters (geometric mean diameter, D_{pg}) were determined by randomly sampling more than 200 particles from the FESEM images. An example particle size distribution of the crumpled GO particles is shown in Figure S3.4, from which a peak diameter of around 200 nm is observed for the crumpled GO particles synthesized from a diluted GO suspension. It should be noted that the particle sizes obtained from SEM/TEM images are oftentimes overestimated due to agglomeration of particles caused by sample preparation. The hydrodynamic diameter of suspended GO was also measured using dynamic light scattering (DLS) using Zetasizer Nano ZS system (Malvern Instruments Ltd., Worcestershire, UK) with a measurable size range of 0.3 nm to 10 μm (see Figure S3.1d for an example). A red laser (λ = 633 nm) was used as the light source with a scattering angle of 173°. For each measurement, 3 runs with 14 cycles per run were carried out, and the average values were used. It is noteworthy that the DLS measurement is based on the assumption that all particles are effective spheres and undergo Brownian motion in the solution. Because of the special geometrical structure of GO, it appears that the DLS technique is not quantitatively reliable. Therefore, the DLS analysis presented here should be viewed only as a qualitative indicator to shed light on the pH-dependent aggregation of GO. Online particle size measurements were performed by using a scanning mobility particle sizer (SMPS, TSI Inc.) system, which consists of a differential mobility analyzer (DMA, TSI 3081, TSI Inc.) and a condensation particle counter (CPC, TSI 3025, TSI Inc.). During online measurements, a 0.3 lpm slip-stream of aerosols was drawn into the SMPS system, which measures particle size in the range of 9 ~ 425 nm and particle number concentration up to 10^7 #/cm^3. The above size measurements for each sample were performed five times and

average data and standard deviations were obtained. The ultraviolet-visible (UV-VIS) spectra analysis was also performed (Cary 100, Varian, Inc., Palo Alto, CA), to check optical properties of GO and determine the mass concentration of GO suspension as shown above (see Figure S3.2).

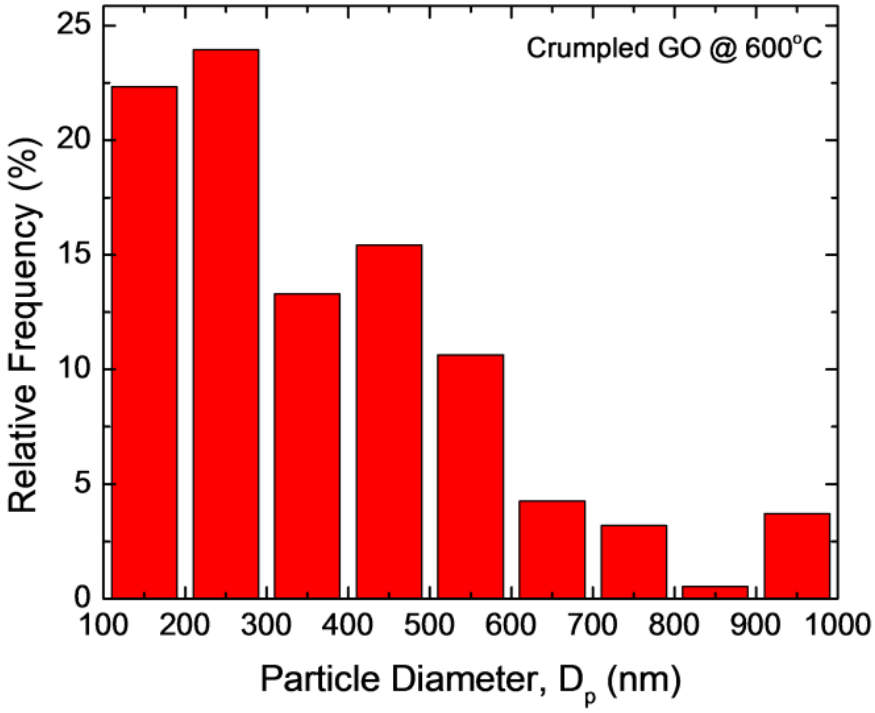

Figure S3.4. Particle size distribution of crumpled GO particles synthesized from 0.54 mg/ml GO suspension at 600°C obtained from FESEM images by sampling 200 particles. The peak diameter is around 200 nm.

S3.2. Derivation of the Confinement Force Equation

The solvent, i.e. water in this work, the evaporation rate of single micrometer-sized droplet at different furnace temperature could be simply calculated according to the follow equation.[4, 5]

$$\kappa = \frac{m_d}{\tau_e} \tag{1}$$

where κ is the evaporation rate (g/s), m_d the droplet mass (g), τ_e the evaporation time (s) in the continuum region, where the droplet size is much larger than the gas mean free path, λ ($Kn = \lambda / d_d \ll 1$). τ_e can be calculated based on the following equation.[5]

$$\tau_e = \frac{R\rho_d D_d^2}{8 D_g M \left(\frac{P_d}{T_d} - \frac{P_\infty}{T_\infty} \right)} \tag{2}$$

where D_d is droplet diameter (m), R is the gas constant, ρ_d is the droplet density (kg/m^3), D_g is the gas-phase diffusion coefficient of the solvent (as a function of furnace temperature, T_f), M is the molecular weight of the solvent (g/mol), T_∞ is the temperature far from the droplet (K), T_d is the temperature at the surface of the droplet (K) and becomes constant (= water boiling point) if the furnace temperature is larger than 100°C, P_∞ is the partial pressure of the solvent far from the droplet and can be can be neglected if dry gas is used (Pa), and P_d is the vapor pressure at the droplet surface (Pa). Combining equations (1) and (2), we get the following equation

$$D_d = \frac{3R\kappa T_d}{4\pi D_g M P_d} \tag{3}$$

The mass density of a folded spherical graphene oxide particle, ρ, follows a scaling equation:[6]

$$\rho = \rho_m \left(\frac{F}{Yh} \right)^{\delta D} \left(\frac{D_p}{2h} \right)^{D-3} \tag{4}$$

where ρ_m is density of GO (1800 kg/m^3),[7] Y is the two-dimensional Young's modulus (145.32 N/m for a single GO sheet with a thickness of 0.7 nm),[8] D_p is the mobility diameter (nm), h is the GO thickness (0.7 nm for single sheet GO), δ is the force scaling exponent for a self-avoiding sheet (0.25),[9] and D is the characteristic fractal dimension of GO (2.54).[10] The characteristic fractal dimension for any thin sheet material is independent of the bending rigidity as well as applied boundary conditions (e.g. confinement force and load rate).[9]

On the other hand, the particle diameter of a GO crumpled particle can also be calculated following one-droplet-to-one-particle (ODOP) principle based on mass conservation:[11, 12]

$$D_p = D_d \left(\frac{C}{\rho} \right)^{1/3} \tag{5}$$

where D_p and D_d are particle and droplet diameters (nm), respectively, C is the mass concentration (kg/m^3), and ρ is the mass density of a GO crumpled particle.

Combining equations (4) and (5), yields the following equation for confinement force:

$$F = Yh \left[\frac{C}{\rho_m} \left(\frac{D_d}{D_p} \right)^3 \left(\frac{D_p}{2h} \right)^{3-D} \right]^{1/\delta D} \tag{6}$$

The above equation can be further simplified into the follow form.

$$F = AC^{1/\delta D} D_p^{-1/\delta} D_d^{3/\delta D} \tag{7}$$

where A is constant ($A = Y 2^{\frac{D-3}{\delta D}} h^{1+\frac{D-3}{\delta D}} \rho_m^{-\frac{1}{\delta D}}$). D_d in equation 7 can be replaced by equation 3, which yields the new equation of the confinement force.

$$F = AC^{1/\delta D} D_p^{-1/\delta} \left(\frac{3\kappa R T_d}{4\pi D_g M P_d} \right)^{3/\delta D} \tag{8}$$

Equation 8 can be further simplified into the following equation.

$$F = ABC^{1/\delta D} D_p^{-1/\delta} \left(\kappa T_d / P_d D_g \right)^{3/\delta D} \tag{9}$$

where B is constant ($B = \left(3R/(4\pi M)\right)^{3/\delta D}$). In this work, the furnace temperature is always higher than 100°C, thus T_d and P_d become constant as well. From the above equation, one can find that the confinement force, F is propositional to mass concentration of precursor ($F \propto C^{1.57}$) and the evaporation rate and temperature ($F \propto \kappa^{4.72}$), but inversely propositional to particle diameter ($F \propto D_p^{-4}$). At a fixed precursor concentration and droplet size, evaporation rate (furnace temperature) becomes the only variable.

S3.3. Calculation of Residence Time

The residence time inside a diffusion dryer (L = 33 cm, $I.D.$ = 6 cm) can be estimated using the following equation:

$$\tau_r = \frac{nV_{dryer}}{Q_g} \quad (10)$$

where n and V_{dryer} are the number and volume of the diffusion dryer (m^3), respectively, and Q_g is the gas flow rate (m^3/s). The residence times at 14 psi and room temperature ($Q_g = 2.06\times10^{-4} m^3/s$) are calculated as 0.20 s a single diffusion dryer and 0.40 s for two diffusion dryers, which are much longer that the corresponding evaporation time (5.08×10^{-3} s). Based on the above calculation results, it seems that using one or two diffusion dryers should be the same since all water evaporated within 0.01 s. It should be noted that the estimation of the evaporation time is based on single droplet evaporation without considering the effects of population (number concentration) of droplets and gas flow rate. The actual evaporation times of droplets in this work may be longer than the calculated ones. This is also the reason for the different results obtained for using different diffusion dryers.

S3.4. pH Effect

To control the processes of exfoliation, dispersion, functionalization, and self-assembly of suspended GO nanosheets in aqueous media, a fundamental understanding of their solution behavior is also necessary.[13] In this sense, pH is another important parameter to be considered that is closely related to the physiological activity of GO aqueous suspension.[3, 14] The pH-dependent hydrophilicity of GO has been exploited to control its assembly behavior.[15] Recent analyses indicated that the peripheral carboxyl groups (-COOH) play a key role in determining the solution behavior of GO.[16, 17] The colloidal stability of aqueous GO solutions has been attributed to the electrostatic repulsions between ionized carboxyl groups,[16] which can be interpreted by measuring their zeta potential.[18, 19] As seen in Figure S3.5a, the dramatic change in the zeta potentials of GO aqueous suspensions at pH 1 and 12 reflects the fact that the edge carboxyl groups are highly

protonated at pH 1 resulting in weak electrostatic repulsive forces. However, in pH 12, zeta potential was achieved as high as -45 mV. The corresponding hydrodynamic diameters of GO nanosheets measured by DLS also showed similar trend as zeta potential. These findings suggest that the electrostatic repulsions between ionized carboxyl groups at the GO nanosheet edges provide the major barrier preventing the GO sheets from aggregating.[16, 20] Optical properties of the GO suspensions were also measured by UV-Vis spectroscopy as shown in Figure S3.5b, where two characteristic absorption peaks of GO were observed at 230 nm and 300 nm originating from π-π^* transition of the C=C band and n-π^* transition of the C=O band, respectively.[21] The pH-dependent absorption spectra of GO colloids suggest that the change in the concentration of H^+ and OH^- causes the electronic transition changes of π-π^* and n-π^* in GO refilling or depleting their valence band.[3, 22] Thus the protonation and deprotonation of carboxylate GO due to changes in pH may cause electrostatic doping/charging to the GO, thereby shifting the Fermi level similar to carboxylate SWCNTs.[22, 23] However, the absorption spectrum is also affected by the solvent in which the absorbent species are dissolved in. By changing the pH, we can alter the polarization forces between the solvent and the absorber. At low pH, the solvent is abundant with positively charged hydrogen ions, while at high pH, the solvent is abundant with negatively charged hydroxide ions.[24] Thus, lowering the pH of the GO solution will increase the polarization forces between the GO (of negative zeta potential) with the positively charged hydrogen ions. This lowers the energy levels of both the π and π^* state. However, because the effect is greater for the excited state, the gap between the π and π^* orbitals is reduced—thus causing a redshift in the spectra. However, there is no significant size and morphology variation of crumpled GO particles prepared from GO aqueous solutions with different pH based on electron microscopy analysis (Figure 3.4) and SMPS measurements (Figure S3.6). The reason may be due to the lower magnitude of electric

repulsive force as compared to the corresponding confinement force, which needs further investigation in the near future.

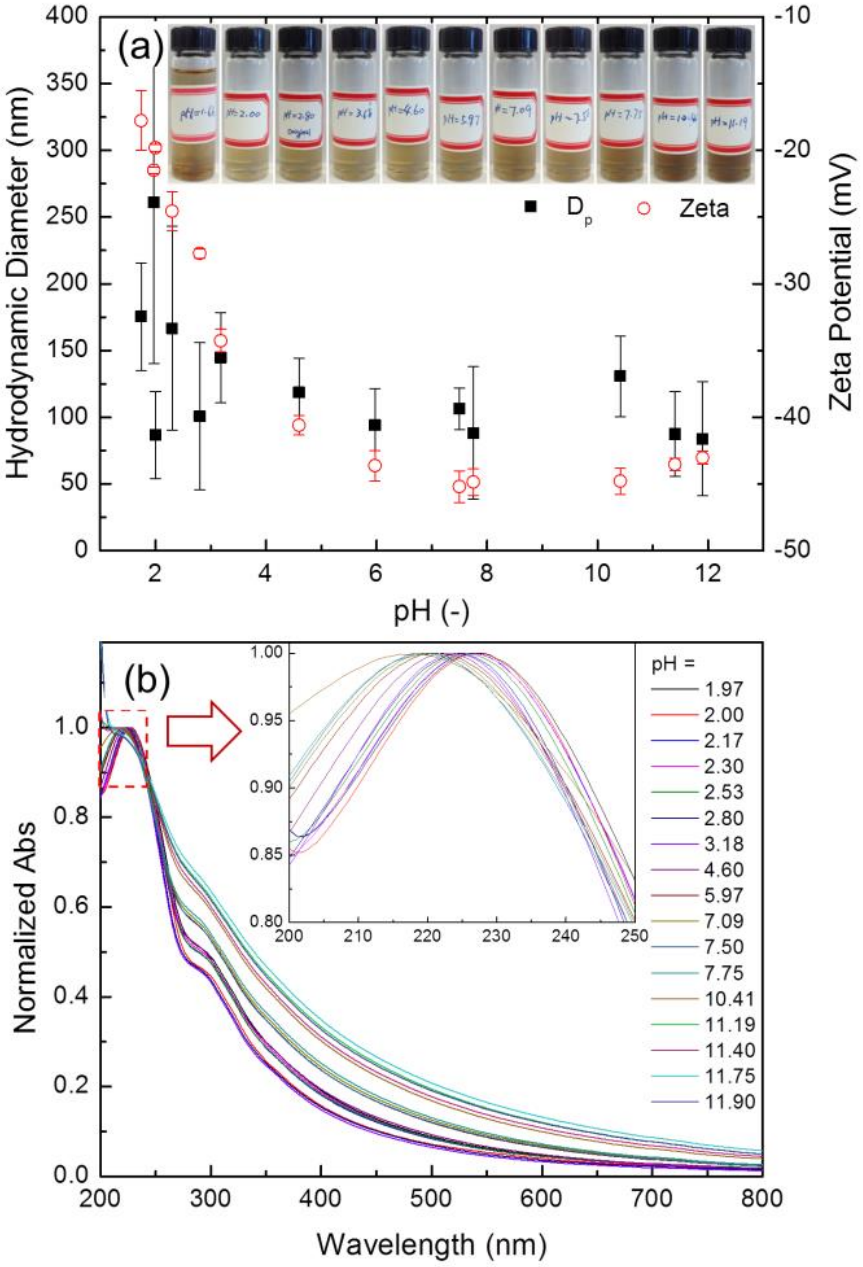

Figure S3.5. pH effect on the size and surface properties of graphene oxide. (a) Dynamic particle diameter and zeta potential, and (b) UV-Vis spectra of graphene oxide as a function of pH.

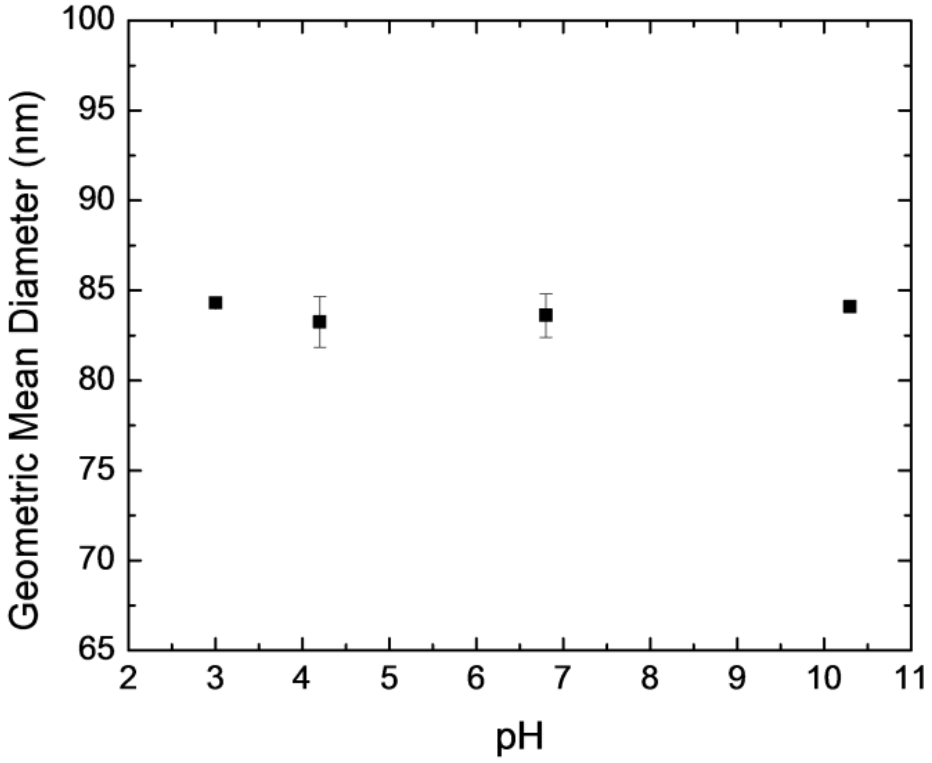

Figure S3.6. pH effect on the particle size of crumpled GO particles measured by SMPS.

Table S3.1. Effect of synthesis temperature with different diffusion dryers (C = 0.3 mg/ml, P_{neb} = 96.53 kPa).

Furnace temperature (°C)	Particle diameter _0dyer[b] (nm)	Confinement force _0dryer[c] (μN)	Particle diameter _1dyer[b] (nm)	Confinement force _1dryer[c] (μN)	Particle diameter _2dryers[b] (nm)	Confinement force _2dryers[c] (μN)
200	88.22±0.49	29.75±0.66	87.36±0.12	30.94±0.17	89.16±0.39	28.52±0.50
400	84.32±0.16	34.87±0.26	86.39±0.37	31.65±0.55	87.42±0.60	30.18±0.81
600	83.40±0.77	37.80±1.40	84.49±0.24	35.89±0.40	85.53±0.27	34.18±0.43
800	80.99±0.88	41.58±1.76	82.22±0.72	39.14±0.36	85.50±0.33	33.47±0.51
1000	75.14±1.70	56.23±5.10	83.35±0.15	37.14±0.26	85.18±0.31	34.05±0.50

Table S3.2. Effect of precursor concentration (T_f = 400°C, P_{neb} = 96.53 kPa)

Precursor concentration (mg/ml)	Droplet size (μm)	Evaporation rate (g/s)	Evaporation time (s)	Particle diameter (nm)	Confinement force (μN)
0.0375	2.82±0.06	7.88×10^{-7}	1.49×10^{-5}	78.09±0.21	47.40±0.51
0.1				81.95±0.17	39.08±0.32
0.3				84.32±0.16	34.87±0.26

S3.5. Supplementary References

1. Hummers, W. S.; Offeman, R. E., Preparation of Graphitic Oxide. *J. Am. Chem. Soc.* **1958,** *80* (6), 1339.
2. Atkins, P.; de Paula, J., *Atkins' Physical Chemistry*. 8th ed.; Oxford University Press: 2006.
3. Chen, J. L.; Yan, X. P., Ionic strength and pH reversible response of visible and near-infrared fluorescence of graphene oxide nanosheets for monitoring the extracellular pH. *Chem. Commun.* **2011,** *47* (11), 3135-3137.
4. Fuchs, N. A., *Evaporation and Droplet Growth in Gaseous Media*. Pergamon Press: London, 1959.
5. Hinds, W. C., *Aerosol Technology: Properties, Behavior, and Measurement of Airborne Particles*. Second ed.; John Wiley & Sons, Inc.: New York, 1999.
6. Balankin, A. S.; Silva, I. C.; Martinez, O. A.; Huerta, O. S., Scaling properties of randomly folded plastic sheets. *Phys. Rev. E* **2007,** *75* (5), 051117.
7. Dikin, D. A.; Stankovich, S.; Zimney, E. J.; Piner, R. D.; Dommett, G. H. B.; Evmenenko, G.; Nguyen, S. T.; Ruoff, R. S., Preparation and characterization of graphene oxide paper. *Nature* **2007,** *448* (7152), 457-460.
8. Suk, J. W.; Piner, R. D.; An, J. H.; Ruoff, R. S., Mechanical Properties of Monolayer Graphene Oxide. *ACS Nano* **2010,** *4* (11), 6557-6564.
9. Vliegenthart, G. A.; Gompper, G., Forced crumpling of self-avoiding elastic sheets. *Nat. Mater.* **2006,** *5* (3), 216-221.
10. Ma, X. F.; Zachariah, M. R.; Zangmeister, C. D., Crumpled Nanopaper from Graphene Oxide. *Nano Lett.* **2012,** *12* (1), 486-489.

11. Wang, W. N.; Widiyastuti, W.; Lenggoro, I. W.; Kim, T. O.; Okuyama, K., Photoluminescence optimization of luminescent nanocomposites fabricated by spray pyrolysis of a colloid-solution precursor. *J. Electrochem. Soc.* **2007,** *154* (4), J121-J128.
12. Wang, W. N.; Kaihatsu, Y.; Iskandar, F.; Okuyama, K., Highly Luminous Hollow Chloroapatite Phosphors Formed by a Template-Free Aerosol Route for Solid-State Lighting. *Chem. Mater.* **2009,** *21* (19), 4685-4691.
13. Dreyer, D. R.; Park, S.; Bielawski, C. W.; Ruoff, R. S., The chemistry of graphene oxide. *Chem. Soc. Rev.* **2010,** *39* (1), 228-240.
14. Shih, C. J.; Lin, S. C.; Sharma, R.; Strano, M. S.; Blankschtein, D., Understanding the pH-Dependent Behavior of Graphene Oxide Aqueous Solutions: A Comparative Experimental and Molecular Dynamics Simulation Study. *Langmuir* **2012,** *28* (1), 235-241.
15. Eda, G.; Fanchini, G.; Chhowalla, M., Large-area ultrathin films of reduced graphene oxide as a transparent and flexible electronic material. *Nat. Nanotechnol.* **2008,** *3* (5), 270-274.
16. Li, X. L.; Zhang, G. Y.; Bai, X. D.; Sun, X. M.; Wang, X. R.; Wang, E.; Dai, H. J., Highly conducting graphene sheets and Langmuir-Blodgett films. *Nat. Nanotechnol.* **2008,** *3* (9), 538-542.
17. Lerf, A.; He, H. Y.; Forster, M.; Klinowski, J., Structure of graphite oxide revisited. *J. Phys. Chem. B* **1998,** *102* (23), 4477-4482.
18. Ohshima, H., *Theory of Colloid and Interfacial Electric Phenomena*. Elsevier Academic Press: Amsterdam, 2006.
19. Hunter, R. J., *Zeta Potential in Colloid Science: Principles and Applications*. Academic Press: New York, 1981.

20. Hasan, S. A.; Rigueur, J. L.; Harl, R. R.; Krejci, A. J.; Gonzalo-Juan, I.; Rogers, B. R.; Dickerson, J. H., Transferable graphene oxide films with tunable microstructures. *ACS Nano* **2010,** *4* (12), 7367-72.

21. Clark, B. J.; Frost, T.; Russell, M. A., *UV Spectroscopy: Techniques, Instrumentation, Data Handling/UV Spectrometry Group*. Chapman & Hall: New York, 1993; Vol. 4.

22. Strano, M. S.; Huffman, C. B.; Moore, V. C.; O'Connell, M. J.; Haroz, E. H.; Hubbard, J.; Miller, M.; Rialon, K.; Kittrell, C.; Ramesh, S.; Hauge, R. H.; Smalley, R. E., Reversible, band-gap-selective protonation of single-walled carbon nanotubes in solution. *J. Phys. Chem. B* **2003,** *107* (29), 6979-6985.

23. Zhao, W.; Song, C. H.; Pehrsson, P. E., Water-soluble and optically pH-sensitive single-walled carbon nanotubes from surface modification. *J. Am. Chem. Soc.* **2002,** *124* (42), 12418-12419.

24. Palanna, O. G., *Engineering Chemistry*. Tata McGraw Hill Education Pvt, Ltd.: New Delhi, 2009.

Chapter 4. Graphene Oxides in Water: Correlating Morphology and Surface Chemistry with Aggregation Behavior

Abstract

Aqueous aggregation processes can significantly impact function, effective toxicity, environmental transport, and ultimate fate of advanced nanoscale materials, including graphene and graphene oxide (GO). In this work, we have synthesized flat graphene oxide (GO) and five physically crumpled GOs (CGO, with different degrees of thermal reduction, and thus oxygen functionality) using an aerosol method, and characterized the evolution of surface chemistry and morphology using a suite of spectroscopic (UV-vis, FTIR, XPS) and microscopic (AFM, SEM, and TEM) techniques. For each of these materials, critical coagulation concentrations (CCC) were determined for NaCl, $CaCl_2$, and $MgCl_2$ electrolytes. The CCCs were correlated with material ζ-potentials (R^2 = 0.94-0.99), which were observed to be mathematically consistent with classic DLVO theory. We further correlated CCC values with CGO chemical properties including C/O ratios, carboxyl group concentrations, and C-C fractions. For all cases, edge-based carboxyl functional groups are highly correlated to observed CCC values (R^2 = 0.89-0.95). Observations support the deprotonation of carboxyl groups with low acid dissociation constants (pKa) as the main contributors to ζ-potentials and thus material aqueous stability. We also observe CCC values to significantly increase (by 18-80%) when GO is physically crumpled as CGO. Taken together, the findings from both physical and chemical analyses clearly indicate that both GO shape and surface functionality are critical to consider with regard to understanding fundamental material behavior in water.

4.1 Introduction

Graphene oxide (GO) shares the one-atom-thick planar sheet with sp^2-bonded carbon structural framework as graphene, but with oxygen-containing functional groups which include basal hydroxyl and epoxy, and edge-associated carbonyl and carboxyl groups.[1, 2] Based on unique material properties, GO has been widely studied for a number of advanced applications including energy conversion and storage,[3] enhanced catalysis,[4, 5] antimicrobial,[6, 7] sorption,[8] and separations,[9, 10] among other technologies. Further, the production and application of GO-based materials are widely expected to grow significantly in the coming decade.[11] Upon commercial production and application, and thus environmental exposure, concerns have been raised regarding the potential biological effects, including to human health, as GO has been observed to be cytotoxic to mammalian cells and bacteria.[12-15] Interestingly, both material functionality and exposure, which is critical with respect to biological response, are a function of CGO aggregation state/behavior in water.[16, 17]

Despite being an essential component for quantitative material behavior models considering both application and potential negative implications, fundamental description of GO aggregation behaviors in water is currently incomplete. GO materials typically vary in nature, due to the random functionalization for each layer and variations in physical structure (such as molecular weight, shape, defects).[18, 19] Residual oxygen moieties can, depending on methods and degree of reduction, differ significantly from a few to dozens of percent in terms of atomic ratio.[19] Further, 2D GO can be physically modified, resulting in 3D structures, such as crumpled paper ball-like spheres[20, 21] and corrugated (wrinkled) surfaces.[22]

Initial reports on the aqueous aggregation and transport behavior of graphene materials have focused on pristine, flat GO.[23, 24] Compared to pristine GO, aqueous stability of GO

derivatives (e.g., GO with different degrees of reduction and morphological transformation) can differ significantly under similar aqueous chemistries. Due to the complexity of possible chemical and physical variations, a quantitative understanding on how such intrinsic structures and properties affect GO aqueous stabilities is needed. However, such understanding remains challenging due to the lack of convenient, yet consistent (reproducible) control and characterization of physical and chemical properties.

We have previously demonstrated GO morphological control by physically crumpling 2D flat GO into 3D crumpled structures (termed as CGO) via a furnace aerosol reactor (FuAR) method, using GO coupons as the starting material.[21] The method utilizes capillary compression induced by rapid evaporation of the aerosol droplets to effectively crumple flat GO. Furthermore, the surface chemistries (degree of thermal reduction) can be tuned by precisely varying the furnace temperature (200-800 ℃) while maintaining the crumpled structure. In this work, we synthesized GO using the modified Hummer's method,[25] and then five subsequent CGO materials, each with different degrees of reduction (crumpling GO at different furnace temperatures from 200 to 800 ℃, all with the same starting coupon structures). Based on extensive characterization and aggregation kinetic results, we have correlated critical coagulation concentration (CCC) values for three ionic systems (NaCl, $CaCl_2$, and $MgCl_2$) with physical and chemical properties of GO/CGO (ζ-potentials, C/O ratios, carboxyl, and C-C fractions). We also observe an increase of CCC values for CGO materials when compared to flat analogues (comparing GO and CGO with same surface chemistry). This is the first report that provides a quantitative description of GO aggregation as a function of both morphology and surface chemistry.

4.2 Materials and Methods

4.2.1 Synthesis of GO/CGOs

GO was synthesized using the modified Hummer's method[25] and was detailed in our previous work.[21] Functional groups such as epoxy, hydroxyl, and carboxyl adorn the surface of GO to render it dispersible in polar solvents including water.[26] Crumpled GO particles (CGO) were synthesized by a furnace aerosol reactor (FuAR) method using GO as the starting material.[21] 35 mL of ~50 mg/L GO solution was placed in a six-jet Collison nebulizer jar (BGI Incorporated), and the pressure nebulizer produced water droplets by forcing the solution through a small opening under applied pressure of 14 psi using nitrogen as the carrier gas. The liquid/gas jet was impacted against the inside wall of the jar to remove larger fraction of the droplets, and the size of the outflow water droplets was mainly micrometer-sized (2-4 μm) as previously measured by an aerosol particle sizer (APS).[21] The water droplets containing GO sheets were then delivered by nitrogen gas into an alumina reactor (1 m × 25 mm ID) maintained at predetermined temperatures (from room temperature to 1000 ℃) to heat it for several seconds. The flow rate is generally operated at 12.4 L/min (nebulizer pressure 14 psi (96.53 kPa)), resulting in ~1.6 s residence time. The formed CGO nanoparticles were finally collected at the end stream of the reactor, weighed and dispersed in water to get 200 mg/L dispersion.

4.2.2 Characterization of GO/CGOs

The morphology and size of the GO/CGO samples were examined by transmission electron microscopy (TEM, TecnaiTM Spirit, FEI Co.) and field emission scanning electron microscopy (FESEM, NOVA NanoSEM 230, FEI Co.). For GO SEM imaging, samples were sputter coated with gold for 90 s (Headway PWM32-PS-CB15PL). The size and thickness of GO were also measured using atomic force microscopy (AFM, Veeco Nanoman). The optical properties of

GO/CGO aqueous dispersions (20 mg/L) were measured by using a UV-vis spectrophotometer (Varian Bio 50). Surface chemistry information regarding molecular bond and functionality were obtained with fourier transform infrared spectrometer (FTIR, Nicolette Nexus 470) and X-ray photoelectron spectroscopy (XPS, PHI 5000 VersaProbe II equipped with monochromatic Al Kα (1486.6 eV) X-ray source). The XPS peaks were fitted to a mixed function having 80% Gaussian and 20% Lorentzian characters using the software PHI Multipak, after performing a Shirley background subtraction. In the fitting procedure, the FWHM values were fixed at 1.2 ±0.2 eV for all peaks, and the peak positions were constrained within 0.2 eV deviated from the assigned position. Calibration was carried out by alignment of the spectra with reference to the C 1s line at 284.8 eV associated with graphitic carbon. At least three measurements were performed at different samples (or locations). ζ-potential and hydrodynamic diameter (D_h) (in 40 mg/L aqueous solution) were measured with a ZetaSizer Nano ZS (Malvern Instruments, Worcestershire).

4.2.3 Aggregation Kinetics of GO/CGOs

The early-stage aggregation kinetics of GO/CGOs were assessed by the initial rate of change of the D_h with time *t*. In the early aggregation stage, the initial rate constant (k_a) is proportional to the initial rate of increase in D_h and inversely proportional to the initial (primary) nanoparticle concentration in the suspension (N_0) (Eqn. 1).[27]

$$k_a = \frac{1}{N_0}\left(\frac{d}{dt}D_h(t)\right)_{t\to 0} \quad (1)$$

The attachment efficiency (α) (also known as the inverse stability ratio) at different electrolyte concentrations was calculated by normalizing the aggregation rate constant obtained to the rate constant obtained under favorable (non-repulsive, fast) conditions ($k_{a,fast}$) (Eqn. 2).[27]

$$\alpha = \frac{k_a}{k_{fast}} = \frac{\frac{1}{N_0}\left(\frac{d}{dt}D_h(t)\right)_{t\to 0}}{\frac{1}{N_{0,fast}}\left(\frac{d}{dt}D_h(t)\right)_{t\to 0,fast}} \quad (2)$$

The initial rate of increase in D_h was measured by time-resolved dynamic light scattering (TR-DLS) (Malvern ZetaSizer Nano ZS). Equal volumes (500 μL) of GO/CGO dispersion and electrolyte solution (NaCl, $CaCl_2$, and $MgCl_2$ with different ionic strength) were mixed to reach the desired concentrations (GO/CGO: 40 mg/L; NaCl: 0 - 250 mM; $CaCl_2$ and $MgCl_2$: 0 - 50 mM). Previous studies on aggregation of carbon nanomaterials were usually conducted with a pH between 5 and 6 (e.g., graphene oxide, pH 5.5[23] and C_{60}, pH 5.2[27]) , and thus the pH of the GO/CGO dispersion was adjusted to 6.0 $\pm$ 0.3 (with 0.02 mM-0.5 mM NaOH and/or HCl) for comparison. The DLS glass cuvette was quickly vortexed and placed in the instrument for measurement. The rate was calculated for the initial stage defined as the period between t = 0 to the time when D_h reaches $1.30D_{h0}$.[27, 28] Since GO/CGO concentration remained identical, α was then determined to be the ratio of the initial rate of change of D_h in the reaction-limited regime over that in the diffusion-limited regime. Critical coagulation concentrations (CCC) were determined from the intersection of extrapolated lines through the diffusion and reaction limited regimes.

4.3 Results and Discussion

4.3.1 Materials Characterization

The aerosolized droplets then undergo solvent evaporation, and capillary compression induced by rapid evaporation can effectively crumple flat GO. The magnitude of the compression, which has been correlated to the evaporation rate of solvent, was identified as the critical factor determining the morphology as well as the size of the dry CGO particles.[21] While being crumpled, simultaneous thermal reduction leads to partial removal of surface functional groups, and restoration of aromatic carbon regions.[3, 5] Different degrees of reduction, while producing the same crumpled morphology, were achieved by varying the furnace temperatures (e.g., 200 to 800 ℃), as revealed in our previous work.[21]

As-synthesized GO/CGO samples were characterized by TEM (Figure 4.1a-c), FESEM (Figure S4.1), AFM (Figure 4.1d and Figure S4.1g), UV-vis (Figure S4.3), XPS (Figure 4.1g and Figure S4.4), and FTIR (Figure S4.5) for detailed size, morphology and surface chemistry information. Figure 4.1a-c compares the morphologies of GO and representative CGO materials prepared at furnace temperatures of 200 and 400 ℃ (CGO reduced at 200 ℃, denoted as CGO-200 hereafter; same denotation applied to other CGOs). Flat GO coupons are observed with sizes ranging from a few hundred nm to more than 1 μm (Figure 4.1a and S1a), and AFM examination of the height reveals that most GO sheets are single layer or double layers (h < 2 nm, Figure 4.1d), consistent with previous reports of GO synthesized by the modified Hummer's method.[23, 29] As-synthesized CGO particles, with crumpled morphology and sharp ridges (Figure 4.1b and c, and S1b-f), have a fractal dimension of ~2.5, similar to that of crumpled paper balls.[30] The fractal dimension (f) relates the particle mass (m) with the diameter of crumpled ball-like structures (d) through a power law expression ($m \sim d^f$). While crumpled particles may have same fractal dimension, they could have different diameters depending on the degree of applied confinement force.[21, 31] We have analyzed the size distribution of GO and CGOs from AFM (GO) and TEM (CGO) images using software ImageJ. For each measurement, approximately 150 particles were counted. For GO and CGO-200, they have a relatively wide size distribution from 100 to 500 nm, but for other CGOs, they have a similar and narrower size distribution, with about 80% between 100 and 300 nm (Figure 4.1e). This trend of size change is consistent with our previous study,[21] showing higher evaporation rate under higher furnace temperature leading to larger confinement force and thus smaller particle size. The hydrodynamic diameters of GO and CGOs are in the range of 200-350 nm as measured by dynamic light scattering (DLS) (Figure 4.1f). It should be noted that in DLS measurement, a non-spherical particle is treated as a sphere that has the same average

translational diffusion coefficient as the particle being measured. For flat GO sheets, the DLS measurement has been shown to underestimate the real particle size,[32] which is consistent with our observations. For GO and CGOs synthesized below 600 °C, ζ-potentials are below -40 mV; while for CGO-600 and CGO-800, due to significant thermal reduction, ζ-potentials increase to -20 mV; values higher than -30 mV are usually considered as threshold for colloidal stability in water (Figure 4.1d).[26]

The color of the suspended samples gradually changes from brown (GO and CGO-200) to black (CGOs synthesized at ≥ 400 °C) due to thermal reduction (Figure 4.1a-c insets and Figure S4.2), suggesting progressive restoration of the π network within the carbon structure.[33, 34] Two characteristic absorption peaks of GO are observed (Figure S4.3) at 230 nm and 300 nm for the π-π* C=C transition band and the n-π* C=O transition band, respectively.[35] Upon reduction, the major absorption peak (230 nm) is observed to be red shifted (to 270 nm, typical absorption peak of graphene), and the absorption in the whole spectral region (> 230 nm) increases with the degree of redution, indicating partial restoration of electronic conjugation.[26]

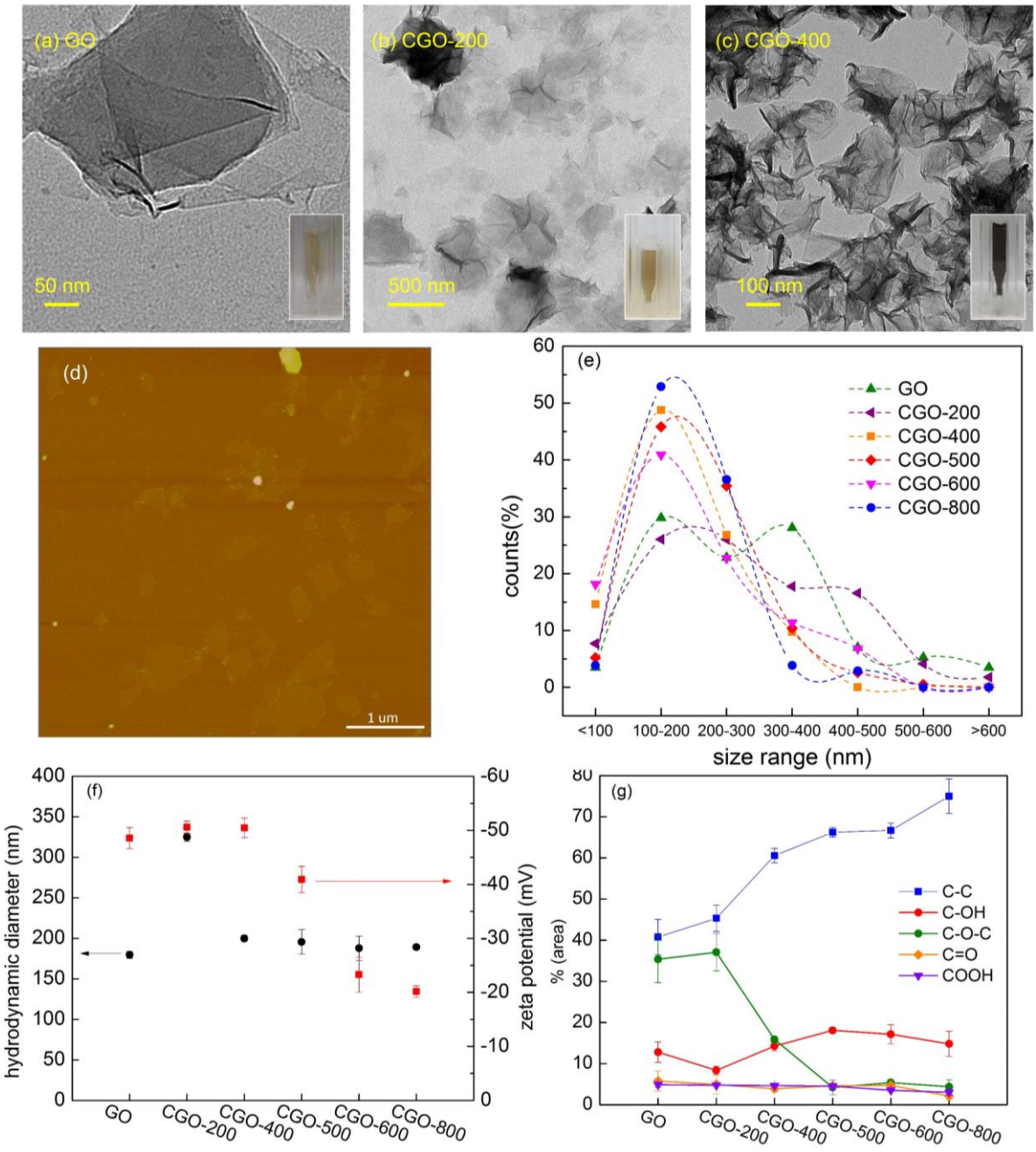

Figure 4.1 Materials characterization of GO and CGOs. (a-c) representative TEM images of GO, CGO-200 and CGO-400, with photos of 80 mg/L aqueous solution in the insets, (d) AFM image of GO; (e) size distribution measured from AFM and TEM images (dashed lines are guide lines for the eye only); (f) hydrodynamic diameters and ζ-potentials of GO and CGOs measured by dynamic light scattering and electrophoretic light scattering (40 mg/L aqueous solution), (g) fractions of each components to the C 1s peak obtained by deconvoluting the high-resolution C 1s XPS spectra. Detailed material characterization of all 6 GO and CGOs can be found in the Supporting Information.

XPS was employed to evaluate the evolution of oxygenated functionality during the thermal reduction process. Survey spectra show C/O ratio of GO to be 1.9 ± 0.1, which is typical of GO synthesized by the modified Hummer's method (~ 2.0).[36] While it does not change for CGO-200 (2.0), the C/O ratio increases to 3.2 ± 0.1 for CGO-400, and to 5.0 ± 0.7 for CGO-800. Further, high-resolution C 1s spectrum of GO exhibit well-defined, multi-peak formations, indicating extensive material oxidation (Figure S4.4a). When crumpled, CGO-200 has a very similar C 1s spectrum, due to preservation of surface chemistry as GO (Figure S4.4b) (also evidenced by the brown color of the solution (Figure S4.2), C/O ratios from XPS survey spectra (1.9 vs. 2.0), and similar FTIR spectra, which is shown in Figure S4.5). Upon further thermal reduction, the peak symbolizing lower oxidation state (C-C) becomes prominent, while peaks of higher oxidation states decreases (CGO-400, 500, 600 and 800, Figure S4.4c-f).

C 1s spectra were deconvoluted and analyzed for carbon oxidation states (Figure 4.1g and Figure S4.4a-f). All peak positions and FWHM were strictly constrained with ± 0.2 eV deviation. The FWHM values were fixed at 1.2 ± 0.2 eV for all major peaks, and the peak positions were constrained within 0.2 eV from the assigned position. The detailed peak position and FWHM information was provided in the supporting information (Figure S4.4g and h). The five most commonly accounted components, including the C-C (284.8 eV), C-OH (286.2 eV, 1-1.5 eV shift to higher binding energy (BE)), C-O-C (287.1 eV, higher BE compared to C-OH group), C=O (287.7 eV, 2.5-3 eV shift to higher BE) and COOH (288.8 eV, 4-4.5 eV shift to higher BE) functionalities,[36, 37] were identified.

The relative ratio of each component to the C 1s peak is illustrated in Figure 4.1e. The C-C area ratios increase gradually from ~41 ± 4 % of GO to 75 ± 4 % of CGO-800, with the range being similar to a previous study.[36] This trend coincides with the change in C/O ratio and

restoration of aromatic regions. Consistent with previous reports,[36] the total contribution of C-O (including C-OH and C-O-C) groups remains almost constant for CGO-200 (compared to GO), indicating the temperature and short residence time in the furnace was insufficient to significantly affect occurrence of these functional groups. However, above 200 ℃, C-O-C groups are observed to decrease dramatically, while the relative C-OH peak area ratio increases (Figure 4.1f). The C-OH groups first increase from 200 ℃, then decrease above 500 ℃, thereby remaining stable to 800 ℃, which is also similar to reports by others.[36] This increase is likely due to the transformation of C-O-C to C-OH groups. For GO synthesized by the Hummer's method, which typically has a C/O ratio of ~2, carboxyl groups were identified to have a contribution of around 6% (to relative carbon oxidation state).[38-40] In our analysis, the carboxyl fraction gradually (288.8 eV) decreases as a function of furnace temperature from 4.9 ± 0.6% of GO to 4.6 ± 0.3% of CGO-400 and 3.0 ± 0.6% of CGO-800 (Figure 4.1e).

In general, FTIR measurements agree with XPS analysis. For as-synthesized GO, a mixture of oxygen-based functional moieties including C-O (phenolic/epoxy/carboxyl), C=C (aromatic), C=O (carbonyl), and -OH (hydroxyl) stretches are observed (Figure S4.5).[5, 39, 41] Broad and strong OH bands at ~3200 cm^{-1} and 1620 cm^{-1} for GO and CGO-200 are indicative of bound water molecules,[39] revealing high hygroscopicity (hydrophilicity, and maintaining of surface functional groups). These bands decrease dramatically for samples synthesized at 400 ℃ and above, likely by restoration of the basal aromatic fractions. Further, the 1580 cm^{-1} adsorption, which corresponds to aromatic C=C band, is observed to be prominent for CGO-400, CGO-500, CGO-600, and CGO-800 materials. The evolution of bands at ~1730 cm^{-1} (carbonyl) and ~1425 cm^{-1} (C-O, carboxyl) also indicates carboxyl group reduction (Figure S4.5).[41] In the region between 1000 and 1300 cm^{-1}, two characteristic peaks typical of C-O functionality, are observed. The band

at 1050-1100 cm^{-1} is assigned to C-O-C groups (epoxy) groups, as it exists for GO and CGO-200, and subsequently reduces for the rest samples. Adsorption at 1250 cm^{-1} is likely from –C-OH groups as it appears as strong peaks for CGOs synthesized at ≥ 400 °C. Taken together, the data indicates that thermal reduction initially starts with the removal of basal plane functional groups (e.g., epoxy) and then proceeds to more chemically stable carbonyl and carboxyl functionalities at the material edge(s), which is also supported by previous observations of GO materials.[26]

4.3.2 Aggregation Kinetics

Early-stage aggregation kinetics of GO/CGOs were assessed by measuring the initial rate of change for hydrodynamic diameters as a function of time via time-resolved dynamic light scattering (TR-DLS). For these materials, particle-particle interaction behaviors are a function of both electrostatic repulsion (V_{EDL}, due to electrostatic double layer) and van der Waals attraction forces (V_{vdW}).[42, 43] Solution ionic strength (IS) influences the electrostatic repulsion forces by affecting the inverse Debye length (Debye length $\kappa \propto IS^{0.5}$), and at low IS (low κ) the interactions are described as long-range with high repulsion between interacting particles.[42] With additional electrolyte, electrostatic repulsion is further suppressed, and particle aggregation takes place, as shown in an example aggregation profile (Figure S4.6). With sufficient electrolyte present (over the critical coagulation concentration (CCC)), the total interaction becomes completely attractive, leading to the transition from reaction-limited aggregation (RLA) to diffusion-limited aggregation regimes (DLA) (Figure S4.6).

The attachment efficiency (α) (also known as the inverse stability ratio) at different electrolyte concentrations is calculated by normalizing the aggregation rate constant to the rate constant obtained under diffusion-limited (attractive, fast) conditions, and is used to index particle aqueous stability (details in Materials and Methods section). Particle-particle attachment

efficiencies were plotted as a function of electrolyte concentrations in Figure 4.2. Distinct reaction-limited and diffusion-limited regimes are observed for GO and CGOs within the concentration ranges of NaCl (0 - 250 mM, Figure 4.2a), $CaCl_2$ (0 - 50 mM, Figure 4.2b) and $MgCl_2$ (0 - 50 mM, Figure 4.2c), indicating that colloidal behavior follows classic Derjaguin-Landau-Verwey-Overbeek (DLVO) theory.[27]

CCC values were determined from the intersection of extrapolated lines through the diffusion- and reaction-limited regimes (Table 4.1). CCC values determined here for GO (68.7 mM NaCl, 1.57 mM $CaCl_2$, and 1.91 mM $MgCl_2$) are between the values recently reported by Chowdhury et al. (44 mM NaCl, 0.9 mM $CaCl_2$ and 1.3 mM $MgCl_2$)[23] and Wu et al. (188 mM NaCl, 2.6 mM $CaCl_2$ and 3.9 mM $MgCl_2$),[28] likely due to varied surface chemistries as discussed above. This highlights the importance of correlating the physical and chemical properties of GO to accurately predict colloidal behavior. In the presence of $MgCl_2$, CCC values are higher than those of $CaCl_2$, which is also consistent with previous reports,[23, 28] due to the relatively weaker tendency of Mg^{2+} compared to Ca^{2+} to form cation bridges (with carboxyl groups).[44, 45] According to the Schulze−Hardy rule, the ratio between $CaCl_2$ and NaCl CCC could be approximated as Z^{-6} for colloids with high negative ζ-potentials, where Z is the valence of Ca^{2+} ions (Z = 2).[46] In our study, the ratios of $CaCl_2$ and NaCl CCC values for GO and CGOs synthesized below 600 ℃ are between $Z^{-5.00}$ and $Z^{-5.45}$, which is in relatively good agreement with the rule. In contrast, such ratios were found to be $Z^{-3.86}$ and $Z^{-3.59}$ for CGO-600 and CGO-800, deviating from the Schulze-Hardy prediction (Table 4.1). We hypothesize such deviation is due to low ζ-potentials of CGO-600 and CGO-800, which violates the assumption of the Schulze−Hardy rule, namely, the surface potential needs to be sufficiently high and remain constant.[46] Similar observations were also obtained in the presence of $MgCl_2$ (Table 4.1).

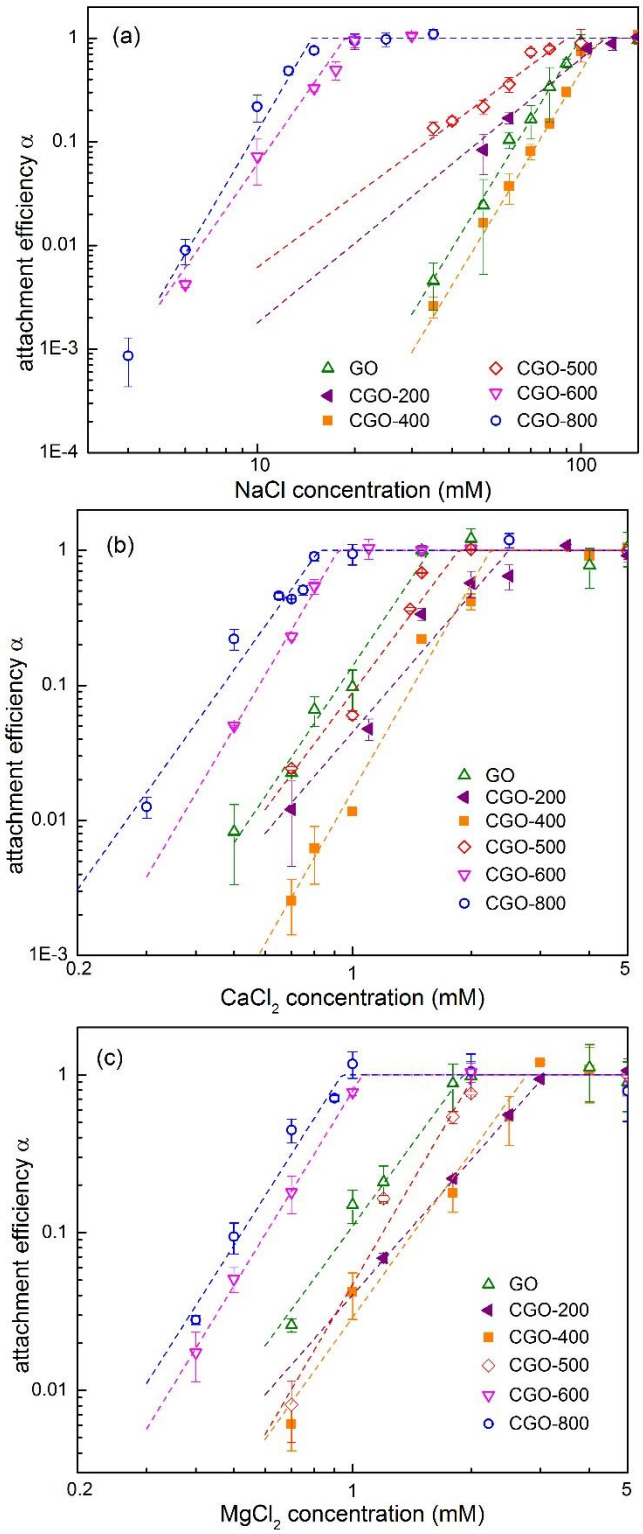

Figure 4.2 Attachment efficiencies (α) of GO/CGOs as a function of (a) NaCl, (b) $CaCl_2$, and (c) $MgCl_2$ concentrations. pH was pre-adjusted to be 6.0 ± 0.3. The CCCs were determined from the intersection of reaction-limited and diffusion-limited aggregation regime, and summarized in Table 4.1.

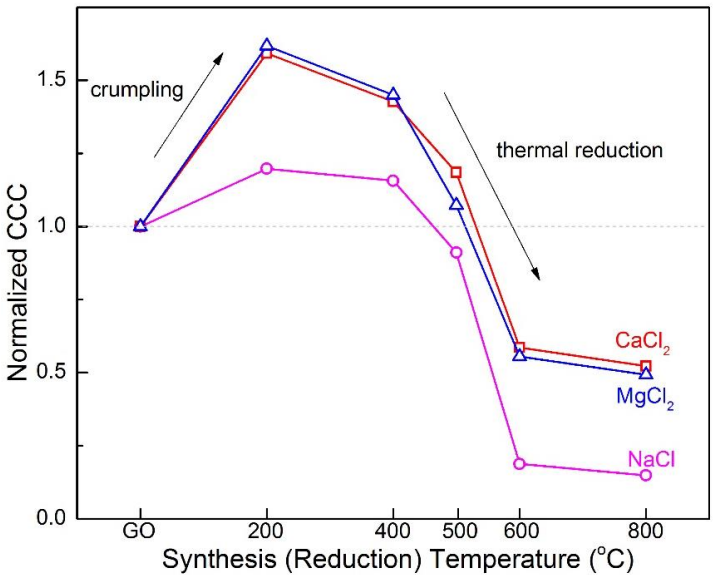

Figure 4.3 Comparison of NaCl, $CaCl_2$, and $MgCl_2$ critical coagulation concentrations (CCCs) of GO and as-synthesized CGOs (normalized by CCCs of GO).

Table 4.1 Critical Coagulation Concentration values of GO and CGO samples. Fitting of the Schulze−Hardy rule was presented in the last two columns, with Z being the valence of Ca^{2+}/Mg^{2+} ions (Z = 2).

Sample	NaCl (mM)	$CaCl_2$ (mM)	$MgCl_2$ (mM)	$CaCl_2$/NaCl	$MgCl_2$/NaCl
GO	68.7	1.57	1.91	$Z^{-5.45}$	$Z^{-5.17}$
CGO-200	81.7	2.50	3.09	$Z^{-5.03}$	$Z^{-4.72}$
CGO-400	73.9	2.24	2.77	$Z^{-5.04}$	$Z^{-4.74}$
CGO-500	59.3	1.86	2.05	$Z^{-5.00}$	$Z^{-4.86}$
CGO-600	13.4	0.92	1.06	$Z^{-3.86}$	$Z^{-3.66}$
CGO-800	9.9	0.82	0.94	$Z^{-3.59}$	$Z^{-3.40}$

Comparing the CCC values, it is also observed that, despite reduction, CGO-200, 400 and 500 have higher or similar CCC values compared to GO. For example, the NaCl CCC increased from 68.7 mM of GO to 81.7 mM of CGO-200, and 73.9 mM of CGO-400. This can be attributed to the crumpling of GO structures, which can reduce the π-π interaction between discrete sheets, resulting in aggregation-resistance.[20, 47, 48] In particular, CGO-200, which retained much of the original surface chemistry, compared to GO (see material characterization results), is more aggregation-resistant in the presence of NaCl, $CaCl_2$, and $MgCl_2$ (CCC values were 19%, 59% and 62% higher respectively (Figure 4.3)). The increases of CCC values in the presence of divalent cations (59% and 62% for Ca^{2+} and Mg^{2+} respectively) were greater compared to that of monovalent cations (19%), which is a result of bridging/crosslinking behavior(s) of Ca^{2+} and Mg^{2+} ions.[28, 49] With further reduction (at higher synthesis temperature), CCC values decrease for all systems with a sharp decrease occurring over the temperature window from 400 and 600 ℃. There is no significant difference between CCC values of CGO-600 and CGO-800 samples (Figure 4.3).

4.3.3 Correlating ζ-potentials and CCC

The CCC is defined as the minimum concentration of electrolyte required to induce the coagulation (aggregation) of a stable colloidal suspension and can be interpreted theoretically by the DLVO theory, which considers the electrostatic repulsion force and the van der Waals attraction force between two interacting particles.

Conventionally, the van der Waals interaction is determined by employing the volume integration approach (Hamaker's technique), and the electrostatic repulsion interaction is obtained by solving the Poisson-Boltzmann equation. However, for a complicated particle such as CGO, the exact mathematical solutions are difficult to precisely ascertain. Instead, here the Derjaguin approximation could be used, which scales the flat-plate interaction energy per unit area to the

corresponding interaction energy between two curved surfaces. The characterization length scales of CGO particles (diameter: hundred nm; surface roughness: dozens of nm[10]) are significantly larger than the interaction distance (e.g., Debye length: a few nm), thus making the Derjaguin approximation applicable. By employing the Derjaguin approximation, the DLVO interaction energies were solved by Hsu and Kuo[50] and applied in our analysis.

The electrical potential energy between two spherical particles V_{EDL} can be estimated:[50]

$$V_{EDL} = \frac{32(a+b)\pi X_0 n k_B T}{a{k_3}^2\kappa^3}[tanh^2(\frac{a\psi_0}{4})]exp(-k_3 L) \times \left[1 - \frac{1}{2k_3 X_0}(1 - exp(-2k_3 X_0))\right] \quad (3)$$

Where ψ_0 is dimensionless surface potential $\psi_0 = \frac{e\Phi_0}{k_B T}$; X_0 is the dimensionless radius of the particle, $X_0 = \kappa r_0$ (r_0 is the particle radius); L is the surface-to-surface distance between two particles. The reciprocal Debye length κ is calculated by $\kappa^2 = \frac{a(a+b)ne^2}{\varepsilon_0\,\varepsilon_r\,k_B T}$, where a and b are the valences of the cation and anion of the electrolyte, ε_0 and ε_r are the permeability of a vacuum and the relative permeability of the liquid phase (water) respectively, T is the absolute temperature (298 K), e is the elementary charge (1.6×10^{-19} C), k_B is the Boltzmann constant (1.38×10^{-23} m^2 Ꝁg s^{-2} ꝀK^{-1}), n is the number concentration of cations in bulk phase. k_3 is a parameter related to a and b, for NaCl, k_3=1; for $CaCl_2$ and $MgCl_2$, $k_3 \approx 1.078$.

Van der Waals attraction energy can be represented by the following equation in most cases (when particles are at close approach, e.g., separation smaller than 10% of the radius):[51]

$$V_{vdW} = -A_{GWG}X_0/12L \quad (4)$$

Where A_{GWG} is the Hamaker constant of the GO-water system (i.e., GO separated by water).

The total interaction energy V_{tot} is the sum of V_{EDL} and V_{vdW}.

At CCC, $V_{tot} = 0$ and $\frac{dV_{tot}}{dL} = 0$ (5)

By solving Eqns. 3-5, CCC (n as the cation number concentration) can be obtained:

$$n = \frac{\lambda tanh^4(\frac{a\psi_0}{4})}{a^5(a+b)k_3^6} \frac{(4\pi\varepsilon_0\,\varepsilon_r)^3(k_BT)^5 48^2}{e^6 {A_{GWG}}^2 \pi \exp(2)},$$

$$\lambda = \left[1 - \frac{1}{2k_3X_0}(1 - \exp(-2k_3X_0))\right]^2 \quad (6)$$

Thus CCC is proportional to ζ-potential (when assume the A_{GWG} values are the same for CGOs) by:

$$n/\lambda \propto tanh^4(\frac{a\psi_0}{4}) \quad (7)$$

λ was calculated to be between 0.944 to 0.991, depending on the type and concentration of the electrolyte (all particle radii were assumed to be 100 nm according to the DLS measurement. The particle radius mainly affects the calculation of λ, however, in a very minor way. For example, the λ values are between 0.988 and 0.996, when radii are assumed to be 200 nm). We plotted n/λ with $tanh^4(\frac{a\psi_0}{4})$ of CGOs in Figure 4.4. Regardless of the electrolytes, the CCC (n/λ) is found to be proportional to $tanh^4(\frac{a\psi_0}{4})$ (R^2 = 0.94-0.99), agreeing with the above analysis. Here, GO is an outlier in the presence of divalent electrolytes ($CaCl_2$ and $MgCl_2$), with CCC values being 43.2% and 42.8% (respectively) lower than the crumpled forms (by comparing the real and interpolated values) (Figure 4.4b and c). It is very interesting that the extrapolation of the fitting lines does not cross zero. This may be explained by additional interaction(s) that were not taken into account in the above analysis. Furthermore, the Hamaker constant A_{GWG} of the CGO-water system estimated from Eqn. 6, can range from 4.8 - 10 $\times 10^{-20}$ J. There is no direct report for this value except an effective Hamaker constant of GO via numerical evaluation $A_{GG} = 2.37 \times 10^{-21}$ J.[52] By employing the following relationship,[27] we can obtain:

$$A_{GWG} \approx (\sqrt{A_{GG}} - \sqrt{A_{WW}})^2 \quad (8)$$

where A_{GG} and A_{WW} are the Hamaker constants of GO nanoparticles and water interacting in vacuum, respectively, and $A_{WW} = 3.7 \times 10^{-20}$ J.[27] We calculated A_{GWG} to be 2.1×10^{-20} J. This is within the same order of magnitude as our calculated values ($\times 10^{-20}$ J).

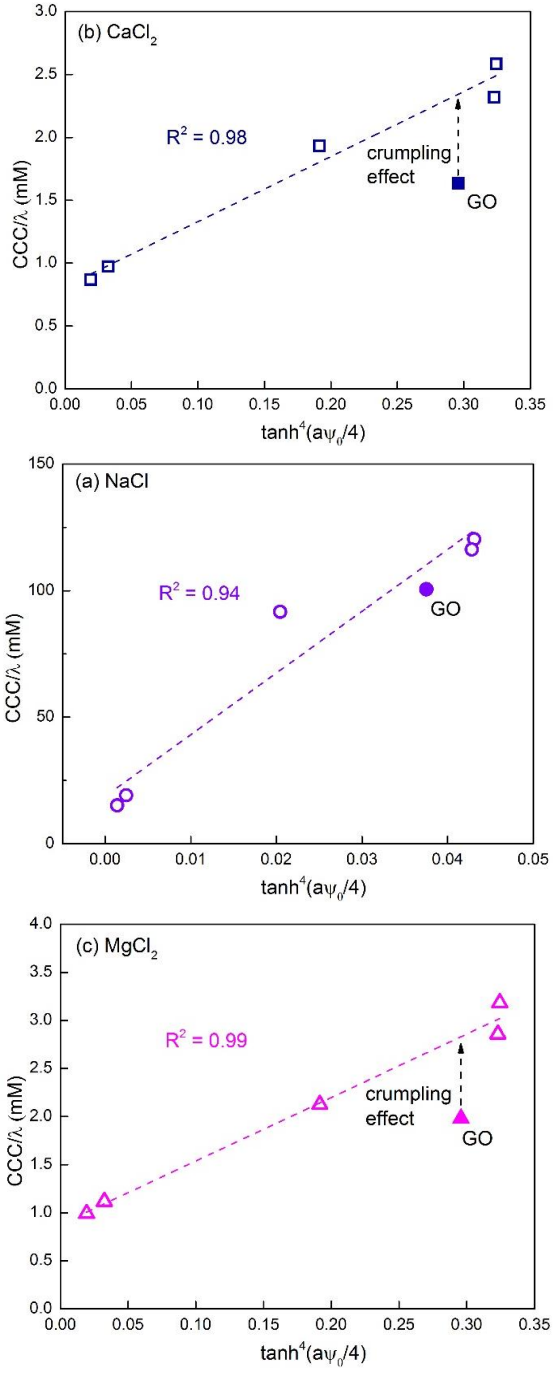

Figure 4.4 Correlation between the CCCs of CGOs and the ζ-potentials. The outlying of (flat) GO was attributed to the crumpling effect.

4.3.4 Correlating Surface Functionalities and CCC

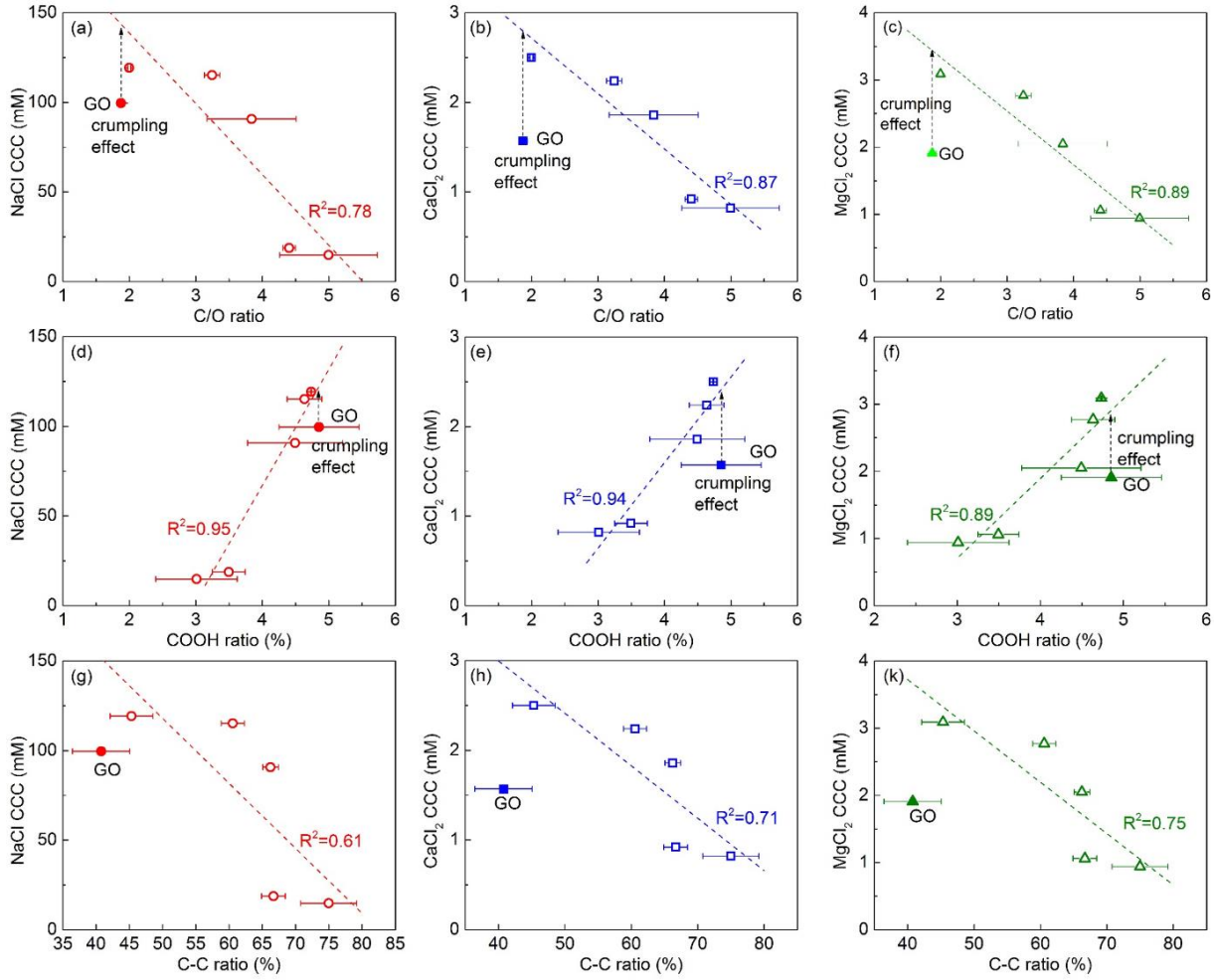

Figure 4.5 Correlation between the CCCs of CGOs and the C/O ratios (a-c), carboxyl fractions (d-f), and C-C fractions (g-k) identified by XPS. The outlying of (flat) GO was attributed to the crumpling effect. The error bars stand for the deviation of at least three measurements from different samples.

Previously, researchers have attributed the negative ζ-potential of GO to the deprotonation of carboxyl and phenolic groups, and emphasized the importance of carboxyl groups in determining GO aqueous stability.[26] In this work, we have correlated CCC values of CGOs with the C/O ratios, C-C fractions, and carboxyl fractions identified by XPS (Figure 4.5). As an

indication of oxidation degree, C/O ratios were negatively correlated to CCC values (R^2 = 0.82 - 0.89), as shown in Figure 4.5a-c. This indicates that the more oxidized CGO materials (with more functional groups such as carboxyl and phenolic) are relatively more stable in water. Moreover, we estimate the enhancement of aggregation-resistance by comparing the obtained GO CCC values, and, for all cases, 2D GO is observed to be an outlier, having 40% to 80% lower CCC values than corresponding crumpled forms. Further, carboxyl ratios (occurrence) are shown to have an even higher correlation with the CCC values (R^2 = 0.89-0.95, Figure 4.5d-f). There is a clear difference between carboxyl ratios of CGO-500 and CGO-600 (significant loss from CGO-500 to CGO-600), coinciding with the sharp decrease of CCC values within the temperature window between 500 and 600 ℃. Through this correlation, it was estimated that by crumpling GO, the CCC values can increase by ca. 18% and 52%, in the presence of monovalent and divalent ions respectively. The graphitic (C-C) fractions are negatively correlated to CCC values (R^2 = 0.65-0.75, Figure 4.5g-k), further supporting these conclusions.

The above correlations likely support the deprontonation of surface functional groups as the origin of surface charge. Surface functional groups, such as carboxyl and phenolic groups, are to be deprontonated, depending on its pKa value and solution pH. The pKa for carboxyl functional group on aromatic rings are usually lower than 4.2, and for phenolic groups, pKa values are generally around 10.[40, 53] In current work with a pH of ~6.0, carboxyl groups are primarily deprontonated while phenolic groups are not. As a result, carboxyl groups are regarded as the main contributors to surface charge for the studied pH range (pH = 6.0 ± 0.3 for GO/CGO solutions), and other common solution conditions. This was also evidenced in a previous study where the removal of oxygen functional groups with high pKa from GO by photoreduction, such as epoxy groups, only leads to a small decrease in surface charge density (< 10-20%).[38]

4.4 Environmental Implications

The understanding of environmental fate and transport of GO is complicated by its possible physical and chemical variations. Not only does GO in water tend to develop wrinkles and ripples as a result of minimizing the total free energy,[54] intentional engineering of GO morphologies turns out to be a promising way to augment its properties. Further, chemical transformation of GO has been proven common in natural environments, such as photochemical reactions in sunlight[55] and reduction by bacteria.[56] By combining theoretical and experimental studies, this work highlights the critical nature of both the physical (i.e., crumpling, ζ-potential) and chemical (in particular, carboxyl functional groups) properties of GO with regard to fundamental aqueous behaviors. Taken together, crumpling of GO significantly increases its aqueous stability, while reduction (as RGO) has been shown to exhibit much faster aggregation kinetics at relatively lower ionic strengths. While these findings broadly, yet quantitatively, inform studies on the fate and transport of graphene-based materials in water, further fundamental studies on the long term stabilities of GO material variations (physical and chemical) under realistic aquatic environments, including the presence of natural organic matter, are still needed for more accurate life cycle and risk analyses.

Acknowledgements

This work was partially supported by co-operative agreement CPC1402WA009 from the U.S. Environmental Protection Agency (EPA), by National Science Foundation's CAREER Award (CBET 1454656), and by McDonnell Academy Global Energy and Environment Partnership (MAGEEP), Washington University in St. Louis. Electron microscopy work was performed at the Nano Research Facility (NRF) at Washington University in St. Louis, a member of the National Nanotechnology Infrastructure Network (NNIN), supported by the National

Science Foundation under Grant No. ECS-0335765. XPS work was performed at Institute of Materials Science & Engineering, Washington University in St. Louis, with partial support from National Science Foundation under Grant NO. CBET-1337374. The conclusions represent the view of the authors and do not necessarily represent the opinions, policies or recommendations of the NSF or EPA.

References

1. Mkhoyan, K. A.; Contryman, A. W.; Silcox, J.; Stewart, D. A.; Eda, G.; Mattevi, C.; Miller, S.; Chhowalla, M., Atomic and Electronic Structure of Graphene-Oxide. *Nano Lett.* **2009,** *9* (3), 1058-1063.
2. Luo, D.; Zhang, G.; Liu, J.; Sun, X., Evaluation Criteria for Reduced Graphene Oxide. *J. Phys. Chem. C* **2011,** *115* (23), 11327-11335.
3. Luo, J.; Zhao, X.; Wu, J.; Jang, H. D.; Kung, H. H.; Huang, J., Crumpled Graphene-Encapsulated Si Nanoparticles for Lithium Ion Battery Anodes. *J. Phys. Chem. Lett.* **2012,** *3* (13), 1824-1829.
4. Zhang, H.; Lv, X. J.; Li, Y. M.; Wang, Y.; Li, J. H., P25-Graphene Composite as a High Performance Photocatalyst. *ACS Nano* **2010,** *4* (1), 380-386.
5. Jiang, Y.; Wang, W.-N.; Biswas, P.; Fortner, J. D., Facile Aerosol Synthesis and Characterization of Ternary Crumpled Graphene–TiO_2–Magnetite Nanocomposites for Advanced Water Treatment. *ACS Appl. Mater. Interfaces* **2014,** *6* (14), 11766-11774.
6. Qi, X.; Wang, T.; Long, Y.; Ni, J., Synergetic antibacterial activity of reduced graphene oxide and boron doped diamond anode in three dimensional electrochemical oxidation system. *Sci. Rep.* **2015,** *5*, 10388.

7. Jiang, Y.; Liu, D.; Cho, M.; Lee, S. S.; Zhang, F.; Biswas, P.; Fortner, J. D., In Situ Photocatalytic Synthesis of Ag Nanoparticles (nAg) by Crumpled Graphene Oxide Composite Membranes for Filtration and Disinfection Applications. *Environ. Sci. Technol.* **2016,** *50* (5), 2514–2521.
8. Cranford, S. W.; Buehler, M. J., Packing Efficiency and Accessible Surface Area of Crumpled Graphene. *Phys. Rev. B* **2011,** *84* (20), 205451.
9. Joshi, R. K.; Carbone, P.; Wang, F. C.; Kravets, V. G.; Su, Y.; Grigorieva, I. V.; Wu, H. A.; Geim, A. K.; Nair, R. R., Precise and Ultrafast Molecular Sieving Through Graphene Oxide Membranes. *Science* **2014,** *343* (6172), 752-754.
10. Jiang, Y.; Wang, W.-N.; Liu, D.; Nie, Y.; Li, W.; Wu, J.; Zhang, F.; Biswas, P.; Fortner, J. D., Engineered Crumpled Graphene Oxide Nanocomposite Membrane Assemblies for Advanced Water Treatment Processes. *Environ. Sci. Technol.* **2015,** *49* (11), 6846-6854.
11. Ren, W.; Cheng, H.-M., The global growth of graphene. *Nat. Nanotechnol.* **2014,** *9* (10), 726-730.
12. Akhavan, O.; Ghaderi, E., Toxicity of Graphene and Graphene Oxide Nanowalls Against Bacteria. *ACS Nano* **2010,** *4* (10), 5731-5736.
13. Liu, S.; Zeng, T. H.; Hofmann, M.; Burcombe, E.; Wei, J.; Jiang, R.; Kong, J.; Chen, Y., Antibacterial Activity of Graphite, Graphite Oxide, Graphene Oxide, and Reduced Graphene Oxide: Membrane and Oxidative Stress. *ACS Nano* **2011,** *5* (9), 6971-6980.
14. Tu, Y.; Lv, M.; Xiu, P.; Huynh, T.; Zhang, M.; Castelli, M.; Liu, Z.; Huang, Q.; Fan, C.; Fang, H.; Zhou, R., Destructive extraction of phospholipids from Escherichia coli membranes by graphene nanosheets. *Nat. Nanotechnol.* **2013,** *8* (8), 594-601.

15. Zhao, J.; Wang, Z.; White, J. C.; Xing, B., Graphene in the Aquatic Environment: Adsorption, Dispersion, Toxicity and Transformation. *Environ. Sci. Technol.* **2014,** *48* (17), 9995–10009.
16. Jiang, J.; Oberdörster, G.; Biswas, P., Characterization of size, surface charge, and agglomeration state of nanoparticle dispersions for toxicological studies. *J. Nanopart. Res.* **2009,** *11* (1), 77-89.
17. Wu, B.; Huang, R.; Sahu, M.; Feng, X.; Biswas, P.; Tang, Y. J., Bacterial responses to Cu-doped TiO_2 nanoparticles. *Sci. Total Environ.* **2010,** *408* (7), 1755-1758.
18. Cai, W.; Piner, R. D.; Stadermann, F. J.; Park, S.; Shaibat, M. A.; Ishii, Y.; Yang, D.; Velamakanni, A.; An, S. J.; Stoller, M.; An, J.; Chen, D.; Ruoff, R. S., Synthesis and Solid-State NMR Structural Characterization of 13C-Labeled Graphite Oxide. *Science* **2008,** *321* (5897), 1815-1817.
19. Bagri, A.; Mattevi, C.; Acik, M.; Chabal, Y. J.; Chhowalla, M.; Shenoy, V. B., Structural evolution during the reduction of chemically derived graphene oxide. *Nat. Chem.* **2010,** *2* (7), 581-587.
20. Luo, J.; Jang, H. D.; Sun, T.; Xiao, L.; He, Z.; Katsoulidis, A. P.; Kanatzidis, M. G.; Gibson, J. M.; Huang, J., Compression and Aggregation-Resistant Particles of Crumpled Soft Sheets. *ACS Nano* **2011,** *5* (11), 8943-8949.
21. Wang, W.-N.; Jiang, Y.; Biswas, P., Evaporation-Induced Crumpling of Graphene Oxide Nanosheets in Aerosolized Droplets: Confinement Force Relationship. *J. Phys. Chem. Lett.* **2012,** *3* (21), 3228-3233.
22. Wang, M. C.; Chun, S.; Han, R. S.; Ashraf, A.; Kang, P.; Nam, S., Heterogeneous, Three-Dimensional Texturing of Graphene. *Nano Lett.* **2015,** *15* (3), 1829–1835.

23. Chowdhury, I.; Duch, M. C.; Mansukhani, N. D.; Hersam, M. C.; Bouchard, D., Colloidal Properties and Stability of Graphene Oxide Nanomaterials in the Aquatic Environment. *Environ. Sci. Technol.* **2013,** *47* (12), 6288-6296.

24. Lanphere, J. D.; Luth, C. J.; Walker, S. L., Effects of Solution Chemistry on the Transport of Graphene Oxide in Saturated Porous Media. *Environ. Sci. Technol.* **2013,** *47* (9), 4255-4261.

25. Hummers, W. S.; Offeman, R. E., Preparation of Graphitic Oxide. *J. Am. Chem. Soc.* **1958,** *80* (6), 1339-1339.

26. Li, D.; Muller, M. B.; Gilje, S.; Kaner, R. B.; Wallace, G. G., Processable Aqueous Dispersions of Graphene Nanosheets. *Nat. Nanotechnol.* **2008,** *3* (2), 101-105.

27. Chen, K. L.; Elimelech, M., Aggregation and Deposition Kinetics of Fullerene (C60) Nanoparticles. *Langmuir* **2006,** *22* (26), 10994-11001.

28. Wu, L.; Liu, L.; Gao, B.; Muñoz-Carpena, R.; Zhang, M.; Chen, H.; Zhou, Z.; Wang, H., Aggregation Kinetics of Graphene Oxides in Aqueous Solutions: Experiments, Mechanisms, and Modeling. *Langmuir* **2013,** *29* (49), 15174-15181.

29. Dreyer, D. R.; Park, S.; Bielawski, C. W.; Ruoff, R. S., The chemistry of graphene oxide. *Chem. Soc. Rev.* **2010,** *39* (1), 228-240.

30. Ma, X.; Zachariah, M. R.; Zangmeister, C. D., Crumpled Nanopaper from Graphene Oxide. *Nano Lett.* **2012,** *12* (1), 486-489.

31. Balankin, A. S.; Silva, I. C.; Martínez, O. A.; Huerta, O. S., Scaling properties of randomly folded plastic sheets. *Phys. Rev. E* **2007,** *75* (5), 051117.

32. Lotya, M.; Rakovich, A.; Donegan, J. F.; Coleman, J. N., Measuring the lateral size of liquid-exfoliated nanosheets with dynamic light scattering. *Nanotechnology* **2013,** *24* (26), 265703.

33. Williams, G.; Seger, B.; Kamat, P. V., TiO_2-Graphene Nanocomposites. UV-Assisted Photocatalytic Reduction of Graphene Oxide. *ACS Nano* **2008,** *2* (7), 1487-1491.

34. Zhu, Y.; Murali, S.; Cai, W.; Li, X.; Suk, J. W.; Potts, J. R.; Ruoff, R. S., Graphene and Graphene Oxide: Synthesis, Properties, and Applications. *Adv. Mater.* **2010,** *22* (35), 3906-3924.

35. Clark, B.; Frost, T.; Russell, M., *UV Spectroscopy: Techniques, instrumentation and data handling*. Springer Science & Business Media: 1993; Vol. 4.

36. Ganguly, A.; Sharma, S.; Papakonstantinou, P.; Hamilton, J., Probing the Thermal Deoxygenation of Graphene Oxide Using High-Resolution In Situ X-ray-Based Spectroscopies. *J. Phys. Chem. C* **2011,** *115* (34), 17009-17019.

37. Yumitori, S., Correlation of C1s chemical state intensities with the O1s intensity in the XPS analysis of anodically oxidized glass-like carbon samples. *J. Mater. Sci.* **2000,** *35* (1), 139-146.

38. Silverberg, G. J.; Pearce, P.; Vecitis, C. D., Controlling Self-Assembly of Reduced Graphene Oxide at the Air–Water Interface: Quantitative Evidence for Long-Range Attractive and Many-Body Interactions. *ACS Appl. Mater. Interfaces* **2015,** *7* (6), 3807-3815.

39. Szabó, T.; Berkesi, O.; Forgó, P.; Josepovits, K.; Sanakis, Y.; Petridis, D.; Dékány, I., Evolution of Surface Functional Groups in a Series of Progressively Oxidized Graphite Oxides. *Chem. Mater.* **2006,** *18* (11), 2740-2749.

40. Xie, Y.; Helvenston, E. M.; Shuller-Nickles, L. C.; Powell, B. A., Surface Complexation Modeling of Eu(III) and U(VI) Interactions with Graphene Oxide. *Environ. Sci. Technol.* **2016,** *50* (4), 1821-1827.

41. Park, S.; Dikin, D. A.; Nguyen, S. T.; Ruoff, R. S., Graphene Oxide Sheets Chemically Cross-Linked by Polyallylamine. *J. Phys. Chem. C* **2009,** *113* (36), 15801-15804.
42. Kulkarni, P.; Sureshkumar, R.; Biswas, P., Multiscale simulation of irreversible deposition in presence of double layer interactions. *J. Colloid Interface Sci.* **2003,** *260* (1), 36-48.
43. Kulkarni, P.; Sureshkumar, R.; Biswas, P., Hierarchical approach to model multilayer colloidal deposition in porous media. *Environ. Sci. Technol.* **2005,** *39* (17), 6361-6370.
44. Nguyen, T. H.; Chen, K. L., Role of Divalent Cations in Plasmid DNA Adsorption to Natural Organic Matter-Coated Silica Surface. *Environ. Sci. Technol.* **2007,** *41* (15), 5370-5375.
45. Pham, M.; Mintz, E. A.; Nguyen, T. H., Deposition kinetics of bacteriophage MS2 to natural organic matter: Role of divalent cations. *J. Colloid Interface Sci.* **2009,** *338* (1), 1-9.
46. Hsu, J.-P.; Kuo, Y.-C., An Extension of the Schulze-Hardy Rule to Asymmetric Electrolytes. *J. Colloid Interface Sci.* **1995,** *171* (1), 254-255.
47. Luo, J.; Kim, J.; Huang, J., Material Processing of Chemically Modified Graphene: Some Challenges and Solutions. *Acc. Chem. Res.* **2013,** *46* (10), 2225-2234.
48. Dou, X.; Koltonow, A. R.; He, X.; Jang, H. D.; Wang, Q.; Chung, Y.-W.; Huang, J., Self-dispersed crumpled graphene balls in oil for friction and wear reduction. *Proc. Natl. Acad. Sci. U. S. A.* **2016**.
49. Yeh, C.-N.; Raidongia, K.; Shao, J.; Yang, Q.-H.; Huang, J., On the origin of the stability of graphene oxide membranes in water. *Nat. Chem.* **2015,** *7* (2), 166-170.
50. Hsu, J.-P.; Kuo, Y.-C., The Critical Coagulation Concentration of Counterions: Spherical Particles in Asymmetric Electrolyte Solutions. *J. Colloid Interface Sci.* **1997,** *185* (2), 530-537.

51. Elimelech, M.; Jia, X.; Gregory, J.; Williams, R., *Particle deposition & aggregation: measurement, modelling and simulation*. Butterworth-Heinemann: 1998.

52. McAllister, M. J.; Li, J.-L.; Adamson, D. H.; Schniepp, H. C.; Abdala, A. A.; Liu, J.; Herrera-Alonso, M.; Milius, D. L.; Car, R.; Prud'homme, R. K.; Aksay, I. A., Single Sheet Functionalized Graphene by Oxidation and Thermal Expansion of Graphite. *Chem. Mater.* **2007,** *19* (18), 4396-4404.

53. Schwarzenbach, R. P.; Gschwend, P. M.; Imboden, D. M., *Environmental organic chemistry*. John Wiley & Sons: 2005.

54. Fasolino, A.; Los, J. H.; Katsnelson, M. I., Intrinsic Ripples in Graphene. *Nat. Mater.* **2007,** *6* (11), 858-861.

55. Hou, W.-C.; Chowdhury, I.; Goodwin, D. G.; Henderson, W. M.; Fairbrother, D. H.; Bouchard, D.; Zepp, R. G., Photochemical Transformation of Graphene Oxide in Sunlight. *Environ. Sci. Technol.* **2015,** *49* (6), 3435-3443.

56. Salas, E. C.; Sun, Z.; Lüttge, A.; Tour, J. M., Reduction of Graphene Oxide via Bacterial Respiration. *ACS Nano* **2010,** *4* (8), 4852-4856.

Chapter 4 Supporting Information

Relationship between CCC and ζ-potential described by DLVO theory, summary of the experiments performed, representative SEM, TEM, and AFM images, digital photos, UV-vis absorption spectra, XPS and FTIR spectra of GO/CGOs, and example time-resolved aggregation profile of CGO-400 are included.

S4.1. Relationship between CCC and ζ-potential described by derived by Hsu and Kuo[1]

The distribution of dimensionless electrical potential around a charged planar surface immersed in an a:b electrolyte (e.g., NaCl, a=b=1; $CaCl_2$, a=2, b=1) solution can be approximated as:[2, 3]

$$\tanh(a\frac{\psi}{4}) = \tanh\left(a\frac{\psi_0}{4}\right)\exp(-k_3X)$$

Where dimensionless parameters include electrostatic potential $\psi = \frac{e\Phi}{k_BT}$ and distance X= κr. ψ_0 is the dimensionless surface potential. Debye length κ meets $\kappa^2 = \frac{a(a+b)ne^2}{\varepsilon_0\,\varepsilon_r\,k_BT}$. Φ is the electrostatic potential, r is the position variable, ε_0 and ε_r are the permeability of a vacuum and the liquid phase (water) respectively, T is the absolute temperature, e is the elementary charge (1.6×10^{-19} C), k_B is the Boltzmann constant, n is the number concentration of cations in bulk phase.

The parameter k_3 is related to the valences of cations and anions, and defined by

$$k_3 = \begin{cases} \frac{[(k-2)k_1+2k_2]}{k}, & k \le 4 \\ \frac{[2k_1+(k-2)k_2]}{k}, & k > 4 \end{cases}$$

$$k_1 = \frac{2}{k^{1/2}[\left(\frac{k}{2}\right)^{\frac{2}{k-2}} - 1]}, \quad k_2 = \frac{2}{k^{1/2}}, \; k = 2 + \frac{2b}{a}$$

For NaCl, k_3=1; for $CaCl_2$ and $MgCl_2$, $k_3 \approx 1.078$.

For a large X,

$$\psi = \frac{4}{\mathrm{a}} \tan\left(a\frac{\psi_0}{4}\right) \exp(-k_3 X)$$

The differential electrostatic repulsion force per unit area between surfaces dF_R, is

$$dF_R = -\rho d\Phi$$

The space charge density ρ is defined as $\rho = aen - ben_b$. n and n_b are the number concentration of cations and anions, respectively.

The electrostatic repulsion force F_R thus can be obtained by integrating the above equation from infinite to L/2, X=L/2 being the position of the middle plane between surfaces.

$$F_R = ank_BT\left\{\left(\frac{1}{b}\right)[\exp(b\psi_m) - 1] + (\frac{1}{a})[\exp(-a\psi_m) - 1]\right\}$$

Where ψ_m is the dimensionless potential at X = L/2.

When the separation distance L is large enough, ψ_m is low. Expanding F_R in its Taylor series around $\psi_m = 0$, the following was obtained:

$$F_R = \frac{a(a+b)nk_BT{\psi_m}^2}{2} = 32\left(1 + \frac{b}{a}\right)nk_BT[\tanh^2(\frac{a\psi_0}{4})]\exp(-k_3 L)$$

The electrostatic potential energy, V_R can be calculated by further integrating the force over the distance:

$$V_R = \kappa^{-1} \int_L^{\infty} F_R \, dL = \frac{32(a+b)nk_BT}{ak_3\kappa} [\tanh^2(\frac{a\psi_0}{4})]\exp(-k_3L)$$

If the Derjaguin approximation is applicable, the electrical potential energy between two spherical particles by be approximated by

$$V_{EDL} = \frac{\pi X_0}{\kappa^2} \int_0^{2X_0} (1 - \frac{L_1}{2X_0}) V_R dL_1$$

Where $L_1 = \kappa(L_2\text{-}L_0)$, L_2 is the surface to surface distance between two particles, and L_0 is the closest distance.

Then,

$$V_{EDL} = \frac{32(a+b)\pi X_0 nk_BT}{ak_3{}^2\kappa^3} [\tanh^2(\frac{a\psi_0}{4})]\exp(-k_3L) \times \left[1 - \frac{1}{2k_3X_0}(1 - \exp(-2k_3X_0))\right]$$

The van der Waals attraction energy can be represented in most cases by:[4]

$$V_{vdW} = -A_{GWG}X_0/12L$$

Where A_{GWG} is the Hamaker constant of the GO-water system (i.e., GO separated by water).

The total interaction energy V_{tot} is the sum of V_{EDL} and V_{vdW}.

At CCC, $V_{tot} = 0$ and $\frac{dV_{tot}}{dL} = 0$

Let L_c be the value of L at which coagulation occurs. L_c was calculated to be $1/k_3$.

Finally, we obtained that the CCC (n as the cation number concentration) equals:

$$n = \frac{\lambda tanh^4(\frac{a\psi_0}{4})}{a^5(a+b)k_3^6} \frac{(4\pi\varepsilon_0\,\varepsilon_r)^3(k_BT)^5 48^2}{e^6 A_{GWG}{}^2 \pi \exp(2)}$$

And

$$\lambda = \left[1 - \frac{1}{2k_3X_0}(1 - \exp(-2k_3X_0))\right]^2$$

Table S4.1. Summary of the experiments performed

Content	Conditions	Objective
1. Materials Synthesis	GO and CGOs synthesized at furnace temp.: 200, 400, 500, 600, 800 ℃	Establish materials library
2. Materials Characterization	UV-vis, FTIR, XPS, SEM, TEM, zeta potential, and hydrodynamic diameter	Identify evolution of surface chemistry and morphology during thermal reduction /crumpling
3. Aggregation Kinetics	Varied IS: NaCl: 0 - 250 mM; $CaCl_2$ and $MgCl_2$: 0 - 50 mM	Determine early-stage aggregation kinetics and critical coagulation concentrations

Figure S4.1. (a-d) representative SEM images of GO and CGOs; (e-f) TEM images of CGO-600 and CGO-800; (g) AFM measurement of GO sheets.

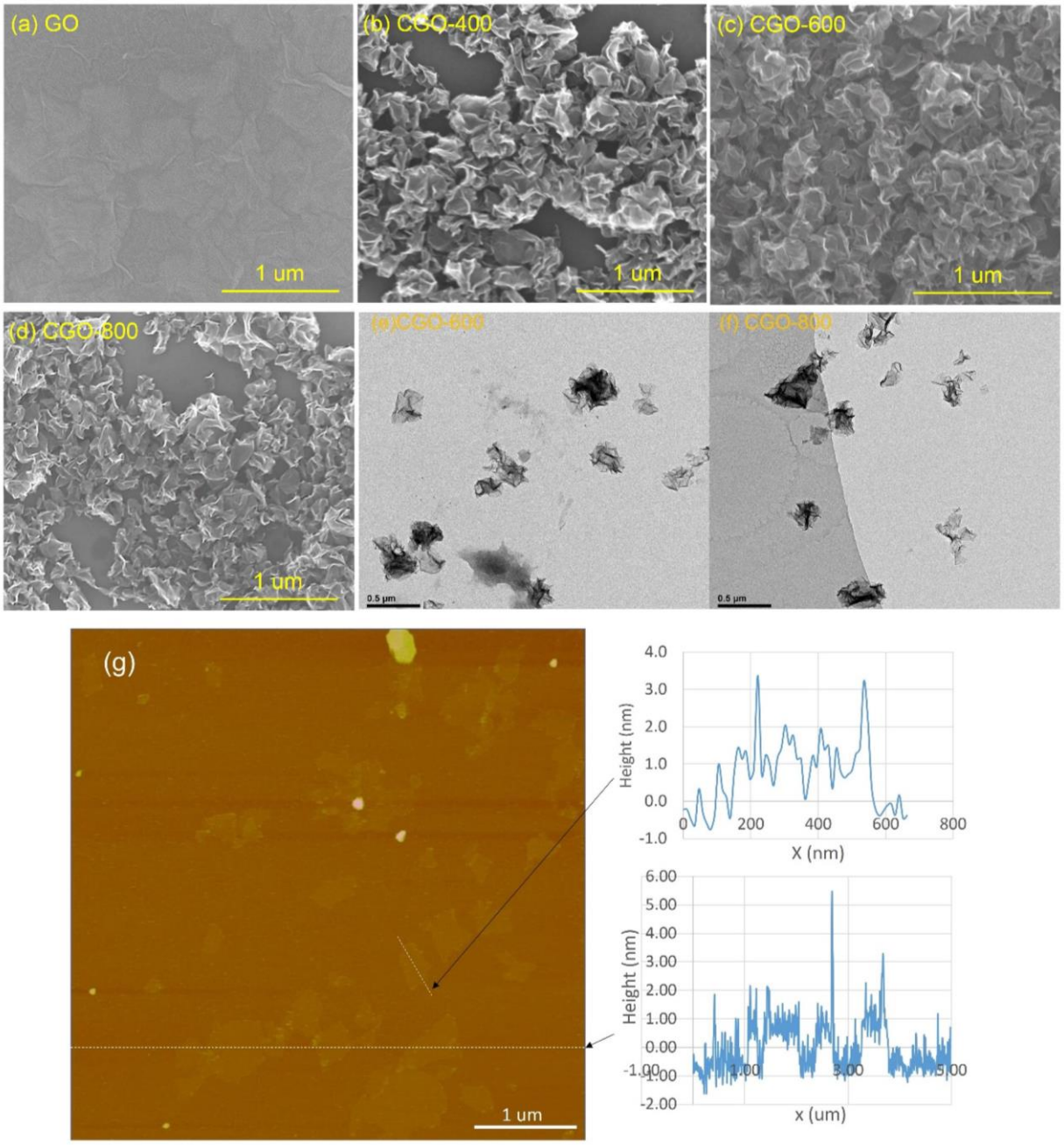

Figure S4.2. Photos of as-synthesized GO and CGO water dispersions. C = 80 mg/L. The color of the suspended samples gradually changed from brown (GO and CGO-200) to black (CGOs synthesized at ≥ 400 °C) upon thermal reduction, suggesting progressive restoration of the π network within the carbon structure.

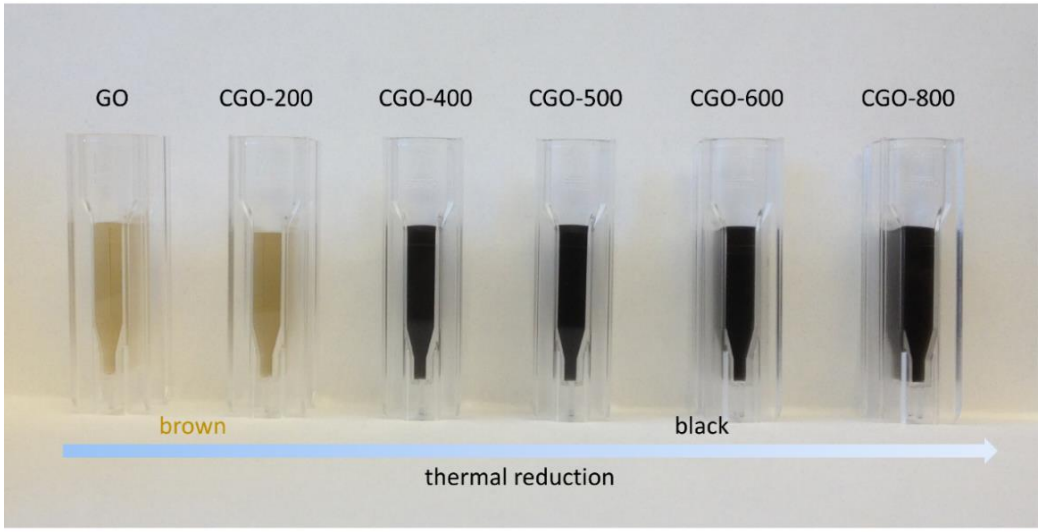

Figure S4.3. UV-vis absorption spectra of as-synthesized GO and CGO aqueous samples. C = 20 mg/L. Upon reduction, the major absorption peak (230 nm) shifted to further red (270 nm, typical absorption peak of graphene), and the absorption in the whole spectral region (> 230 nm) increased with the degree of redution.

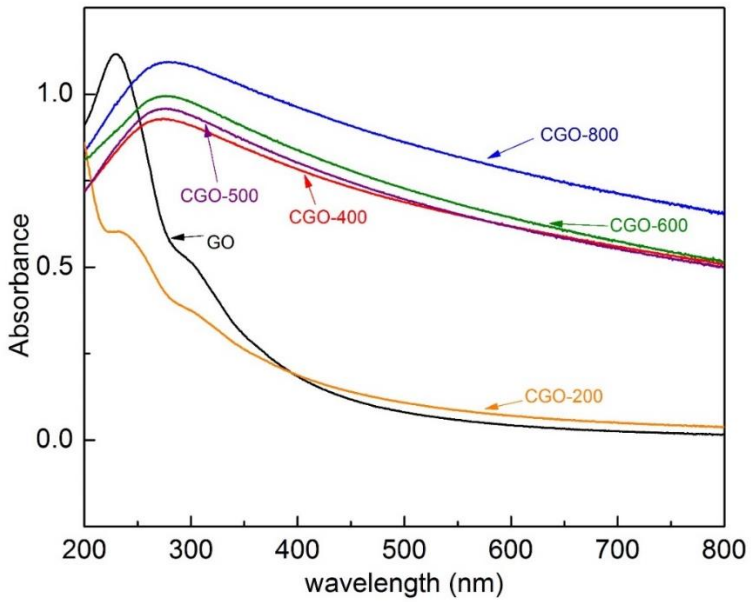

Figure S4.4. High resolution C1s XPS spectra of GO/CGOs. The C-C, C-OH, C-O-C, C=O, COOH functionalities were deconvoluted at peaks of 284.8, 286.2, 287.1, 287.7, and 288.8 eV respectively. The peak positions were constrained within 0.2 eV from the assigned position (Figure g), and the FWHM values were fixed at 1.2 ± 0.2 eV for all major peaks (Figure h).

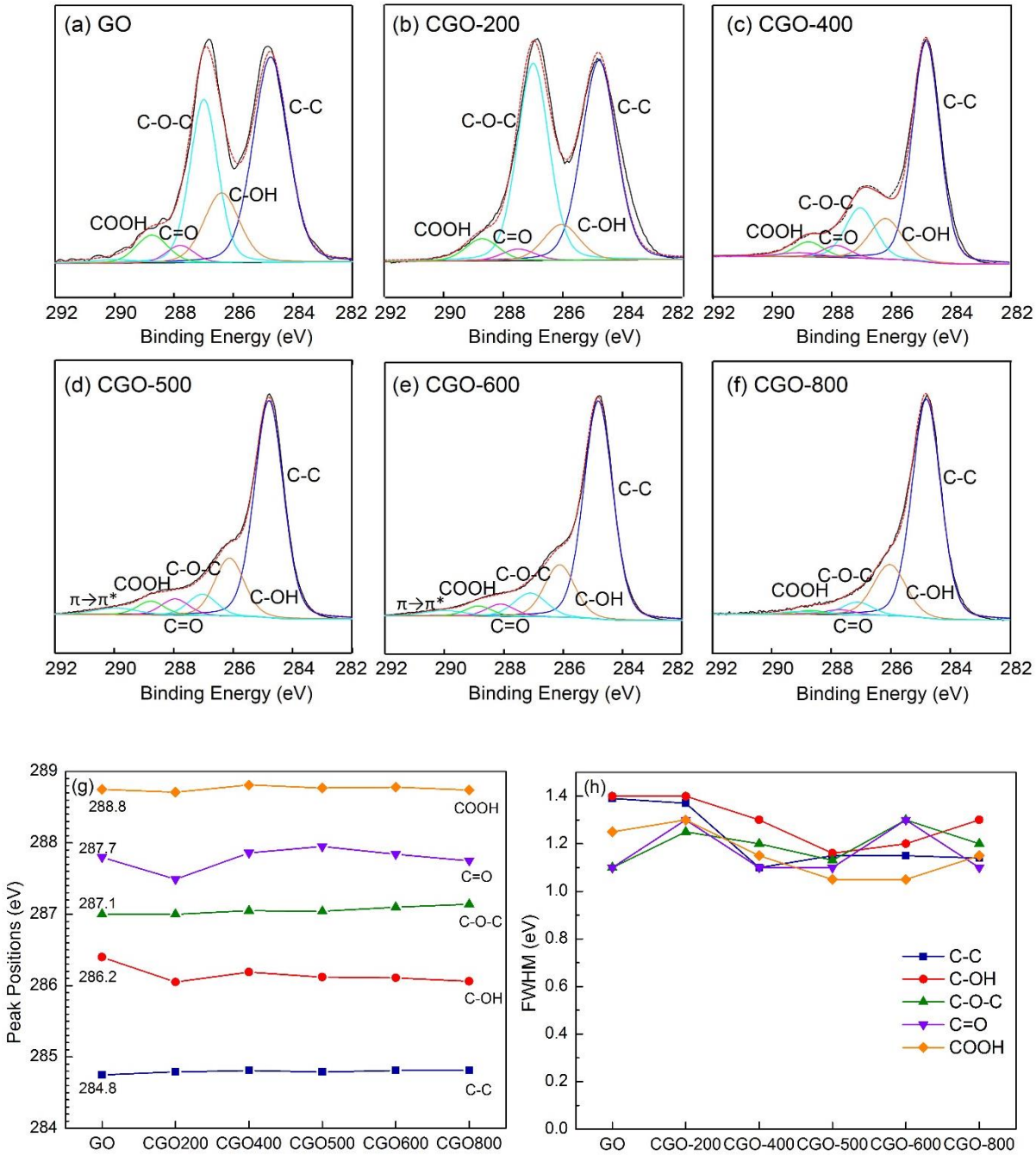

Figure S4.5. FTIR spectra (800-3800 cm^{-1} range) of GO and CGOs. GO and CGO-200 were observed to have almost the same spectra, indicating preservation of surface functionality under low temperature. The removal of carboxyl groups (decreasing of relative peak absorbance) happened with further reduction at higher temperature (e.g., CGO-600 and CGO-800).

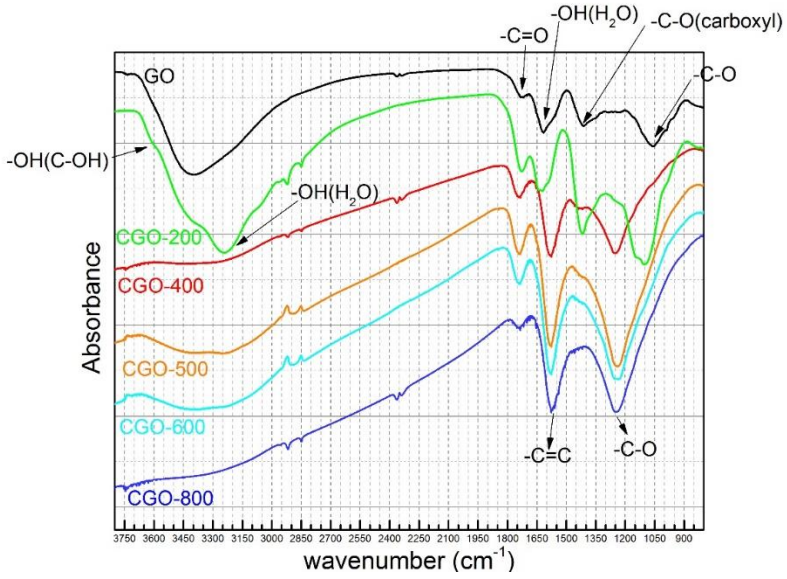

Figure S4.6. Example time-resolved aggregation profile of CGO-400 with presence of NaCl electrolytes. C = 40 mg/L, NaCl: 10-250 mM. pH was pre-adjusted to be 6.0 ± 0.3.

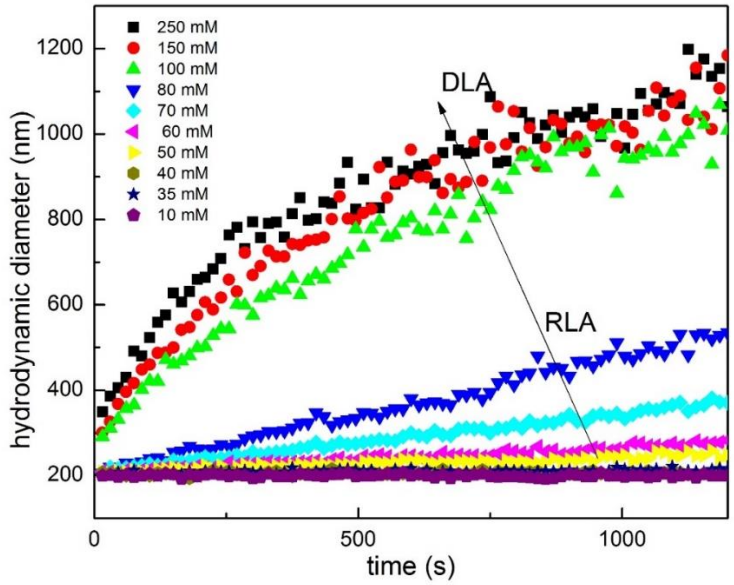

Supplementary References:

1. Hsu, J.-P.; Kuo, Y.-C., The Critical Coagulation Concentration of Counterions: Spherical Particles in Asymmetric Electrolyte Solutions. *J. Colloid Interface Sci.* **1997,** *185* (2), 530-537.
2. Hsu, J.-P.; Kuo, Y.-C., Approximate analytical expressions for the properties of an electrical double layer with asymmetric electrolytes. *J. Chem. Soc., Faraday Trans.* **1993,** *89* (8), 1229-1233.
3. Hsu, J.-P.; Kuo, Y.-C., An Extension of the Schulze-Hardy Rule to Asymmetric Electrolytes. *J. Colloid Interface Sci.* **1995,** *171* (1), 254-255.
4. Elimelech, M.; Jia, X.; Gregory, J.; Williams, R., *Particle deposition & aggregation: measurement, modelling and simulation*. Butterworth-Heinemann: 1998.

Chapter 5. Graphene Oxide Aqueous Aggregation: Interplay between Material and Natural Organic Matter Properties

This chapter has been written into a research article, Jiang, Y., Raliya, R., Fortner, J., Biswas, P., Graphene Oxide Aqueous Aggregation: Interplay between Material and Natural Organic Matter Properties, to be submitted to *Environmental Science & Technology*.

Abstract

Natural organic matter (NOM) is essential to consider when evaluating the stability of graphene oxide (GO) materials in realistic aquatic environments. However, such understanding has been confounded by the physical and chemical complexities of both NOMs and GO materials. In this work, the aggregation kinetics of three GO material types of varied geometries and surface chemistries (one flat and two crumpled, denoted as CGO) were investigated and compared in the presence of two salts (NaCl and $CaCl_2$) and three model NOMs (SRHA, SRFA, and Aldrich Humic Acid (AHA)). While the presence of NOM is found to have considerably increased the critical coagulation concentrations (CCC) of all GO evaluated, the stability enhancement for CGO is at least one order of magnitude higher than flat GO, regardless of surface chemistry. This augmented stability is primarily due to enhanced steric repulsion via adsorbed NOM, although electrostatic repulsion also plays a role in the case of highly reduced GO (e.g., CGO-800). Further, based on adsorption results, higher adsorption density and extended configurations of NOM on crumpled surfaces may be the reason for much higher CCC of CGOs. NOM with higher (net) aromaticity was correlated with increased (relative) stability enhancements (AHA > SRHA > SRFA > no HA in the presence of NaCl), suggesting π-π interactions likely play a key rolein interaction mechanisms, which is similar to previous reports describing carbon nanotube – NOM interactions. In summary, this report highlights the complex interplay between GO material properties (morphology, surface chemistry, etc.) and NOM characteristics (e.g., aromaticity) with regard to aqueous stability - which is crucial to fundamentally understand towards a predictive framework for describing GO fate in real-world environments.

5.1 Introduction

Graphene oxide (GO) materials are projected to be widely incorporated, at the industrial scale, into various technological applications, including energy production and storage,[1] catalysis,[2] electronics,[3] antimicrobial,[4] and separations.[5, 6] Due to anticipated mass production and extensive use, potential environmental release of GO and associated potential adverse effects on human health and ecological systems have raised concerns.[7-9] Aqueous aggregation (stability) of nanomaterials significantly impacts effective toxicity, environmental transport, and ultimate material fate, it is fundamental to study the aggregation of GO in more realistic environmental conditions when evaluating and managing its risks. However, this understanding has been hindered by the physical and chemical variations of GO materials, in addition to the complexity of environmental conditions, such as different natural organic matters (NOMs).

Previous aggregation behavior models are based on pristine flat GO nanosheets synthesized by the modified Hummer's method[10], without further chemical or physical transformation.[11-13] Due to high degree of oxygen functionality (with corresponding high ζ-potentials, usually -30 to -50 mV[14, 15]), pristine GO is proposed to be stable in typical freshwater aquatic environments (e.g., pH 7 and 10 mM monovalent cations).[11] However, GO material properties can vary by orders of magnitude. For example, the C/O ratio, which indicates the degree of oxidation/reduction, can increase from ~2.0 of GO to as high as 10 when reduction occurs.[16] Such reduction, and thus loss of functional groups, leads to significantly decreased GO stability in water. Further, while GO is generally considered as a 2D flat sheet, a variety of geometries have been proposed including conformation into a crumpled structure in water.[17] In our previous work,[16] we provided a quantitative description of GO aggregation as a function of both morphology and surface chemistry, by correlating critical coagulation concentration (CCC) values for three ionic systems

(NaCl, $CaCl_2$, and $MgCl_2$) with physical and chemical properties of GO (ζ-potentials, C/O ratios, carboxyl, and C-C fractions). Overall, reduction leads to decreased stability, and observed CCC values increase by 23-80% when GO is crumpled (CGO), compared to flat analogues.[16]

In addition to material properties, relevant environmental factors have been evaluated, including pH, salts, model/natural mineral particles (e.g., aluminum oxide,[18] montmorillonite, kaolinite, and goethite[13]), and NOM.[11] NOM, mostly humic substances, is ubiquitous in typical natural aqueous systems, with concentrations ranging from 0.1 to 2 mg/L (dissolved organic carbon) in ground waters and as high as 20 mg/L in surface waters.[19] Although NOM is typically complicated mixtures of heterogeneous organic-based molecules with varing degrees of aromatic, carboxylic, and phenolic functionalities, previous aggregation studies are limited to one type of model NOM as Suwannee River Humic Acid (SRHA).[17,20] SRHA was observed to significantly improve the stability of GO due to increased steric repulsion between GO particles.[11] However, to gain a comprehensive understanding of how NOMs affect GO stability requires a deeper look into the (physical and chemical) structural complexity of NOMs, which has already been shown to have a great impact on the aggregation of other nanomaterials, such as carbon nanotubes.[21] Such knowledge of GO – NOM interplay remains nascent.

As discussed, both material and environmental variables are critical to understand the net aggregation behaviors of GO in real world environments. In this work, we focus on exploring such underlying mechanisms between the material and environmental variables with regard to aggregation in water. Specifically, we evaluate and compare aggregation kinetics of a series of GO material types (flat GO and two crumpled GOs with different degrees of reduction) under different environmental conditions (two salts, NaCl and $CaCl_2$; three NOMs, SRHA, Suwannee River Fulvic Acid (SRFA), and Aldrich Humic Acid (AHA)). Results demonstrate that while NOM is

found to considerably enhance the aqueous stability of all GO materials, crumpled GO structures, regardless of surface chemistry, have much higher CCC values compared to flat GO structures. Electrophoretic mobility and adsorption experiments reveal that steric repulsion, resulted from higher adsorption density and extended configurations of NOM macromolecules, is likely the major reason for the increased stabilities of CGO, compared to flat GO.

5.2 Experimental

5.2.1 Synthesis of Flat and Crumpled GOs

GO was synthesized using the modified Hummer's method,[10] as described in detail in our earlier work.[14] As-synthesized flat GO nanosheets were used as the starting material to obtain crumpled GO particles (CGO) by a furnace aerosol reactor (FuAR) method.[14, 16] In brief, GO aqueous solution (~ 50 mg/L) was sprayed into micrometer-sized (2-4 μm) water droplets using a six-jet Collison nebulizer (BGI Incorporated) under a pressure of 14 psi, and the droplets were delivered by nitrogen gas into an alumina furnace reactor maintained at predetermined temperatures to heat it for several seconds. Each aerosolized droplet acts as a micro-reactor, in which flat GO sheets are crumpled under the capillary compression induced by rapid water evaporation. Two furnace temperatures, 400 and 800 ℃, were selected to achieve crumpling but different degrees of thermal reduction. The thermal reduction leads to partial removal of surface functional groups, and restoration of aromatic carbon regions. The CGO particles synthesized under the furnace temperatures of 400 and 800 ℃ were denoted as CGO-400 and CGO-800 respectively. The CGO nanoparticles were finally collected using a membrane filter (Millipore) at the end stream of the reactor, weighed and dispersed in water to get 200 mg/L dispersion.

5.2.2 Materials Charaterization

Detailed material characterization methods were described in our earlier work.[16] The morphology and size of the GO/CGO samples were examined by transmission electron microscopy (TEM, TecnaiTM Spirit, FEI Co.), field emission scanning electron microscopy (FESEM, NOVA NanoSEM 230, FEI Co.), and atomic force microscopy (AFM, Veeco Nanoman). ζ-potential and hydrodynamic diameter (D_h) (in 40 mg/L aqueous solution) were measured with a ZetaSizer Nano ZS instrument (Malvern Instruments, Worcestershire). Surface chemistry information was obtained with fourier transform infrared spectrometer (FTIR, Nicolette Nexus 470) and X-ray photoelectron spectroscopy (XPS, PHI 5000 VersaProbe II equipped with monochromatic Al Kα (1486.6 eV) X-ray source).

5.2.3 Preparation of NOMs

Two aquatic humic substances, Suwannee River humic acid (SRHA II) and fulvic acid (SRFA II) (International Humic Substances Society (IHSS), Atlanta, Georgia), and one terrestrial humic substance, Aldrich HA (Sigma Aldrich),[22, 23] were used as model NOM compounds. SRHA, SRFA, and AHA stock solutions were prepared by dissolving 100 mg of humic substances in 100 mL MilliQ water (1 g/L). The solutions were stirred overnight in the dark. The pH was adjusted to 10.5 with 0.1 M NaOH to ensure complete dissolution. The solutions were then filtered using a 0.45 μm nitrocellulose membrane filter (Millipore). The total organic carbon (TOC) content of the filtered solutions was determined through high temperature oxidation using a TOC analyzer (Shimadzu TOC-L). The stock solutions were diluted to be 30 mg TOC/L and pH was adjusted, if needed, to 7.0 ± 0.1. Specific UV absorbance at 254 nm ($SUVA_{254}$) values were calculated as the UV absorbance at 254 nm divided by TOC concentration (mg/L) and 0.01 m quartz cell path length (unit: L/(mg·m)).

5.2.4 Aggregation Kinetics of GO/CGOs

The pH of GO/CGO solutions was adjusted to be 6.0 ± 0.3 using HCl and/or NaOH before each experiment. The initial rate of increase in hydrodynamic diameter was measured by time-resolved dynamic light scattering (TR-DLS) (Malvern ZetaSizer Nano ZS). GO/CGO dispersion, electrolyte solution (NaCl and $CaCl_2$ with different ionic strength), and NOM solution were mixed to reach the desired concentration (GO/CGO: 20 mg/L; NaCl: 0-3,000 mM; $CaCl_2$: 0-10 mM; NOM: 0-2.7 mg/L). The DLS glass cuvette was quickly vortexed and placed in the instrument for measurement. The rate was calculated for the initial stage defined as the period between t = 0 to the time when D_h reaches $1.30D_{h0}$.[12, 24] Since GO/CGO concentration remained identical, the attachment efficiency α was then determined to be the ratio of the initial rate of change of D_h in the reaction-limited regime over that in the diffusion-limited regime.[16] Critical coagulation concentrations (CCC) were determined from the intersection of extrapolated lines through the diffusion and reaction limited regimes.

5.2.5 Adsorption of NOMs onto GO/CGOs

GO/CGO and NOM solutions were mixed in a centrifuge tube to reach concentrations of 20 mg/L and 18 mg C/L respectively. The tubes were placed on a shaker for 48 h to equilibrate at room temperature (21 ± 2 ℃) based on preliminary studies of adsorption rate. After 48 h, the mixture solution was filtered using a single use syringe filter (with nominal 50 nm pore size, nanocellulose, Millipore). The solutions before and after the filtration were measured using UV-vis spectrometer and TOC analyzer (after proper dilution). Careful control experiments were conducted by testing the filtration of pure GO/CGO, and NOM solutions using the same procedure. Three replicates were performed for each adsorption case.

5.3 Results

5.3.1 Materials Characterization

Size, morphology, and surface chemistry of GO, CGO-400, and CGO-800 are described in detail via AFM, TEM, SEM, FTIR, and XPS measurements (Figure 5.1).[16] AFM measurement of GO nanosheets show a primary coupon size distribution between 100 and 600 nm, with most as single or double layered (Figure 5.1a and d). CGO-400 and CGO-800, synthesized via an aerosol route using flat GO as the starting material, have a distinctive crumpled morphology (Figure 5.1b and c). CGO has a quasi-spherical morphology with relatively smooth surfaces and sharp ridges. During the aerosol synthesis process, water evaporation induces strong caplliary force, which effectively crumples flat GO sheets into 'paper-ball' like structures. CGO-400 and CGO-800 have very similar size distributions, and approximately >80% of these particles are between 100 and 400 nm (Figure 5.1e and f). The hydrodynamic diameters of GO and CGOs are around 200 nm as measured by dynamic light scattering (DLS) (Figure 5.1g). Size measurements from DLS, AFM, and TEM are consistent, due to the fact that that DLS can underestimate flat GO sheet (particle) size.[25] For GO and CGO-400, a highly negative ζ-potentials (below -40 mV) is observed which is in contrast to CGO-800 (ζ-potentials increase to -20 mV), due to significant thermal reduction, (Figure 5.1g).

Increase of ζ-potential indicates thermal reduction of GO sheets during the aerosol processing at higher temperatures as previously described. [16]GO is generally described as one-atom-thick highly oxidized graphene sheet, with oxygen-containing functional groups which include basal hydroxyl and epoxy, and edge-associated carbonyl and carboxyl groups.[26] Under furnace temperatures of 400 and 800 ℃, oxygen functional groups are expected to be partially removed. [16, 27] Here, the evolution of surface functional groups was analyzed via XPS carbon 1 S

peaks which were deconvoluted into five chemical states, which represent most commonly accounted surface functional components, including the C-C (284.8 eV), C-OH (286.2 eV, 1-1.5 eV shift to higher binding energy (BE)), C-O-C (287.1 eV, higher BE compared to C-OH group), C=O (287.7 eV, 2.5-3 eV shift to higher BE) and COOH (288.8 eV, 4-4.5 eV shift to higher BE) functionalities.[28, 29] As shown in Figure 5.1h, being highly oxidized, GO is rich in oxygen functional groups, including C-OH (~13% of area ratio), C-O-C (~ 35%), C=O (~6%), and COOH (~5%). With thermal reduction, oxygen-based functionality decreases and is accompanied by the restoration of C-C aromatic regions. For example, the C-C area ratios increased gradually from ~41 ± 4 % of GO to ~61 ± 2 % of CGO-400 and 75 ± 4 % of CGO-800, similar to a previous study.[28] Similarly, when analyzed by FTIR, GO has a mixture of oxygen-based functional moieties including C-O (phenolic/epoxy/carboxyl), C=C (aromatic), C=O (carbonyl), and -OH (hydroxyl) stretches (Figure S5.1).[2, 30, 31]

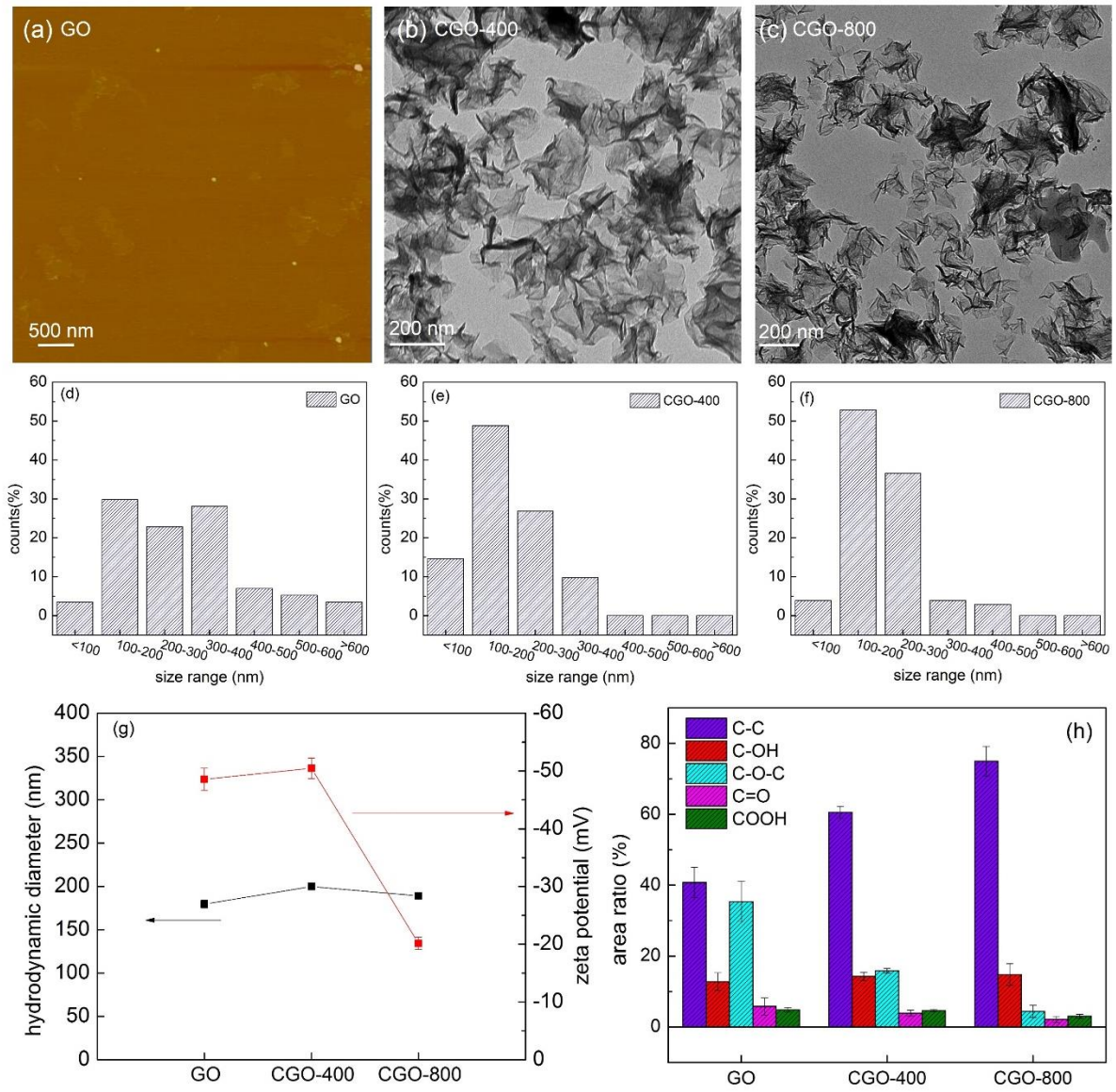

Figure 5.1 (a) AFM image of GO; (b-c) TEM images of CGO-400 and CGO-800; (d-f) particle size distribution obtained by analyzing ~ 150 particles from AFM and SEM images; (g) hydrodynamic diameters and ζ-potentials of GO, CGO-400, and CGO-800 measured by dynamic and electrophoretic light scattering; (h) fractions of each components to the C 1s peak obtained by deconvoluting the high-resolution C 1s XPS spectra of GO, CGO-400, and CGO-800.

5.3.2 Aggregation Kinetics in Presence of NOMs

2.7 mg C/L of SRHA, SRFA, and AHA were added to evaluate the effects of NOM properties on GO aqueous stability. As an index for particle aqueous stability, attachment efficiency (α) at different electrolyte concentrations was calculated by normalizing the initial aggregation rate constant to the rate constant obtained under diffusion-limited (attractive, fast) conditions.[24] The attachment efficiencies are plotted as a function of electrolyte concentrations in Figure 5.2. For all cases, distinct reaction-limited and diffusion-limited regimes were observed for GO and CGOs, indicating that colloidal behavior follows classic Derjaguin-Landau-Verwey-Overbeek (DLVO) theory.[32, 33]

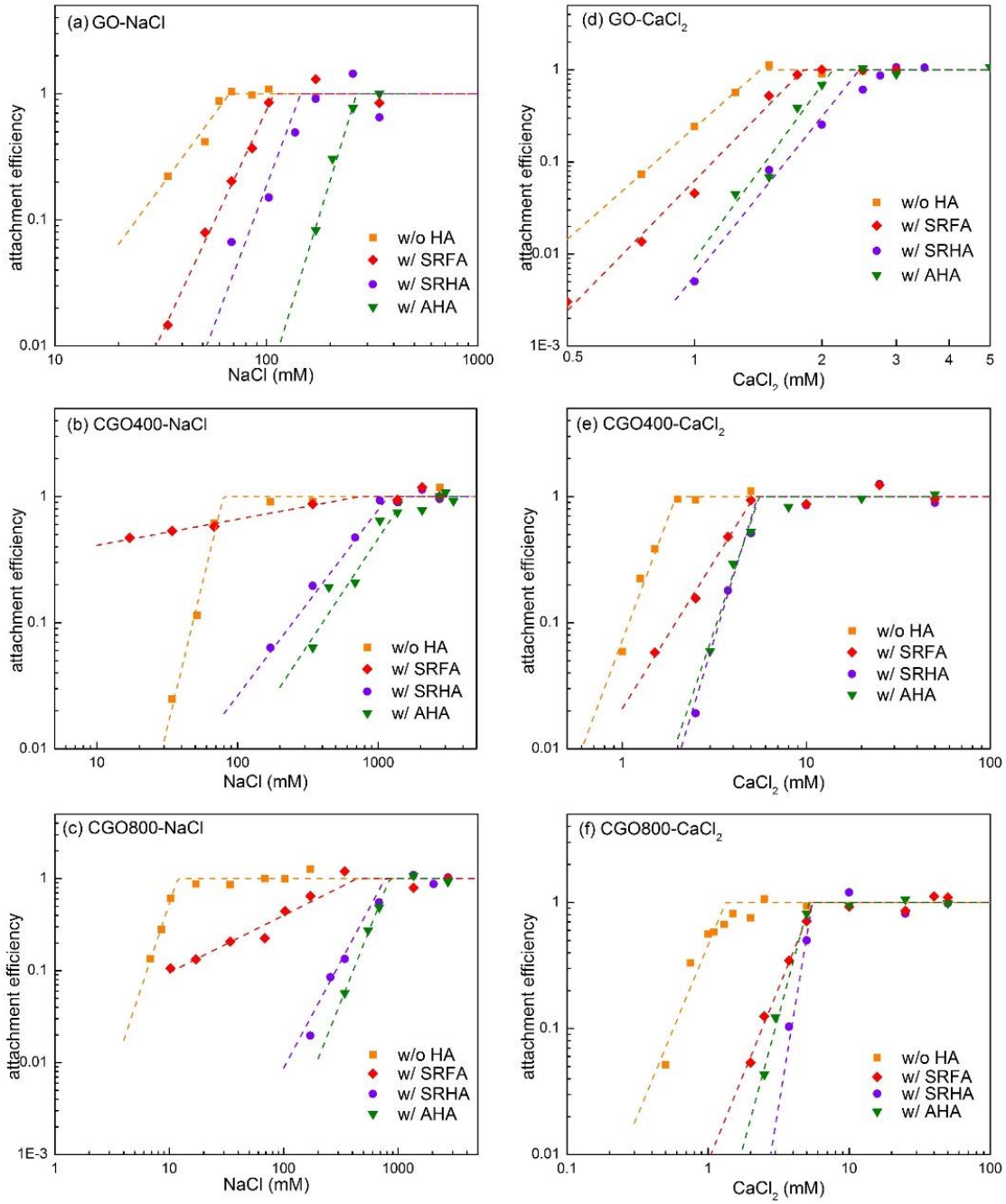

Figure 5.2 Attachment efficiencies (α) of GO/CGOs as a function of (a-c) NaCl and (d-f) $CaCl_2$ concentrations in presence of three NOMs (SRFA, SRHA, and AHA, 2.7 mg C/L). The pH of GO/CGO solutions was pre-adjusted to be 6.0 ±0.3 with 0.02 mM-0.5 mM NaOH or HCl. All NOMs were with pH of 7.0 ± 0.3. The CCC values were determined from the intersection of reaction-limited and diffusion-limited aggregation regime.

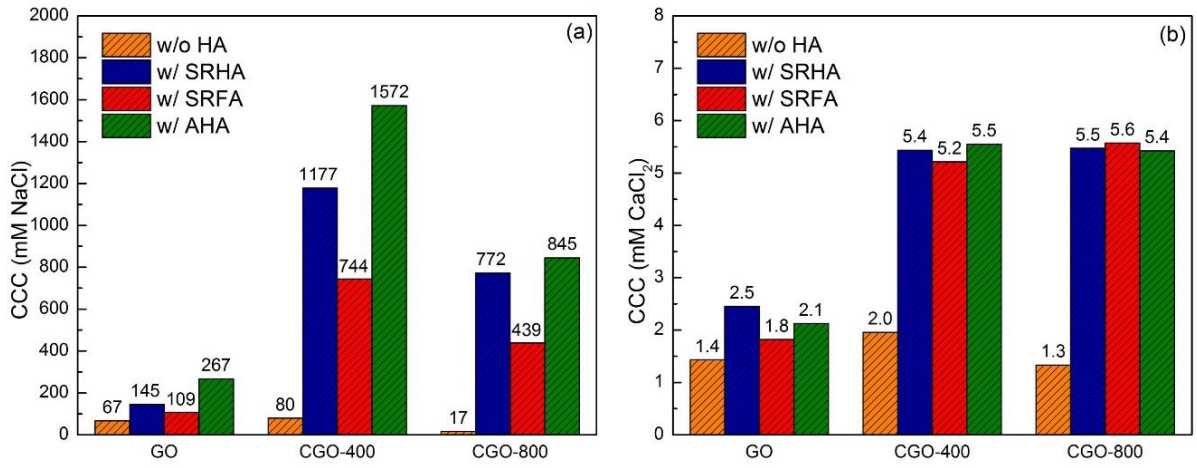

Figure 5.3 Comparison of CCC values of GO, CGO-400, and CGO-800, with or without three types of NOMs (2.7 mg C/L), SRHA, SRFA, and AHA, in NaCl (a) and $CaCl_2$ (b) electrolytes.

The critical coagulation concentration (CCC) value for each case was determined from the intersection of extrapolated lines through the diffusion- and reaction-limited regimes (Figure 5.2). The CCC values are compared as an index of relative aqueous stabilities. Without NOM, CCC values follow the same order for NaCl and $CaCl_2$ electrolytes: CGO-400 > GO > CGO-800. As described in our previous work,[16] despite being reduced, CGO-400 has higher CCC values due to morphological crumpling and thus reduced interacting surface area, compared to flat GO; CGO-800 has the lowest CCC values due to further thermal reduction and removal of surface functional groups (i.e., carboxyl groups). With the addition of NOM, the CCC values increases for all cases, indicating enhanced aqueous stabilities (Figure 5.3). Such an increase of CCC values is consistent with previous observations, which have shown that NOM strongly interacts with other carbon allotropes (e.g., nanotubes and C_{60}) via adsorption, acting to stabilize aqueous-based CNTs and C_{60}.[21, 33-36]

Interestingly, increases in CCC values of CGOs are considerably larger than those of GO. For example, the CCC values in NaCl electrolytes increased by only 0.6-3.0 times for GO in the

presence of NOM, which in comparison was 8.4-18.8 times for CGO-400, and 25.5-49.9 times for CGO-800 (Figure 5.3a). Such disparity was also observed in $CaCl_2$ electrolytes, although to a lesser degree. For GO, the CCC values increased by 0.3-0.7 times, while for CGO-400, they increased by 1.7-1.8 times and for CGO-800 by 3.1-3.2 times (Figure 5.3b). In the presence of monovalent electrolytes, CCC values of CGO-400 remain the highest with NOM, followed by CGO-800, and finally GO. For example, in presence of 2.7 mg C/L AHA, NaCl CCC for CGO-400 is 1572 mM, which is significantly higher than that of CGO-800 (845 mM) and GO (267 mM). For divalent electrolytes in the presence of NOM, CGO-400 and CGO-800 have similar CCC values (~ 5.5 mM $CaCl_2$), but are > 2 times higher than those of GO (~ 2 mM $CaCl_2$). The monovalent CCC values are significantly higher than divalent CCC values, which is expected due to the bridging/crosslinking behavior(s) of Ca^{2+} ions.[12, 37]

The relative effect of NOM concentration on the enhancement of stability is shown in Figure 5.4. AHA of two concentrations, 1.7 and 2.7 mg C/L, was added into GO/CGO solution and CCCs were determined. For these, CCC values increase with the addition of AHA. For example, the NaCl CCC value increases from 1354 mM in presence of 1.7 mg/L AHA to 1572 mM in presence of 2.7 mg/L. Similar trend occur for divalent cations, but less pronounced (Figure 5.4b). This observation show that high concentration of NOM in aqueous environment is likely to further enhance the stability of GO materials.

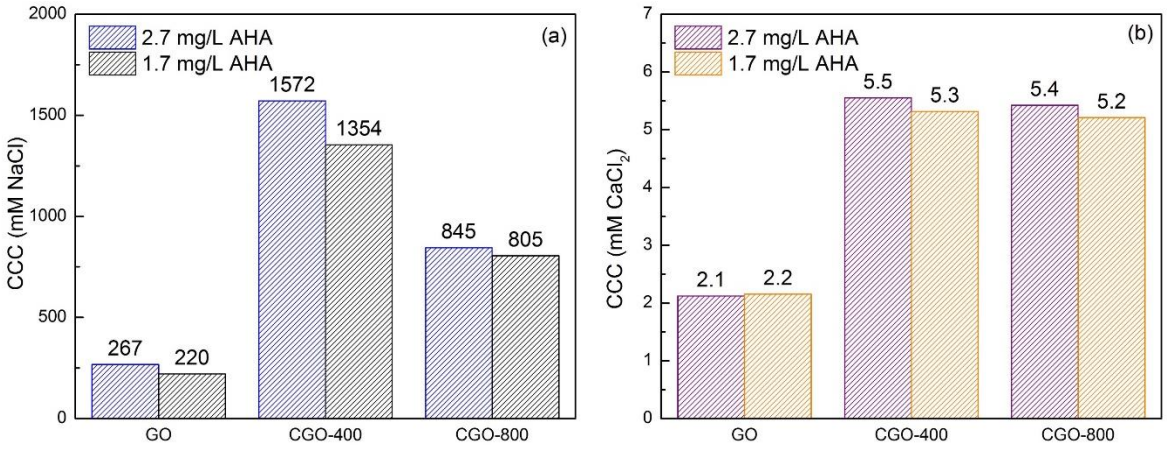

Figure 5.4 Comparison of CCC values in presence of 1.7 and 2.7 mg C/L AHA.

Overall, NOM has a significant impact on material stability, particularly in the presence of monovalent cations (Figure 5.3). For Na^+, CCC values follow the order: AHA > SRHA > SRFA > no HA, regardless of the material type (Figure 5.3a). Relative CCC values in presence of SRFA and SRHA were nearly half and 5491% compared to AHA, respectively. In other words, AHA has the strongest stabilizing effect. However, for divalent cations (Ca^{2+}), this trend is not as clear (Figure 5.3b).

5.3.3 Surface Charge in Presence of NOMs

In the presence of NOM, changes in electrostatic repulsion and steric repulsion can contribute to enhanced stability, as revealed in previous studies.[33, 35, 36] To evalauate the role of resulting elctrostatic repulsion processes, electrophoretic mobility of all samples with or without NOM, considering both electrolytes, 10 mM NaCl and 1.5 mM $CaCl_2$, were compared (Figure 5.5). Considering only electrolytes, the electrophoretic mobility values were observed to become more positive, indicaitng screening of surface charge by electrolytes (Figure 5.5). For example, with 10 mM NaCl, the electrophoretic mobility increased from -4.0 to -3.0 $m^2\ V^{-1}\ s^{-1}$ for GO and from -4.6 to -3.7 $m^2\ V^{-1}\ s^{-1}$ for CGO-400. Divalent Ca^{2+} has a more significant suppressing effect

on the surface charge compared to monovalent Na^+ - for 1.5 mM $CaCl_2$, the electrophoretic mobility values of all samples increased to be above -1.6 m^2 V^{-1} s^{-1}.

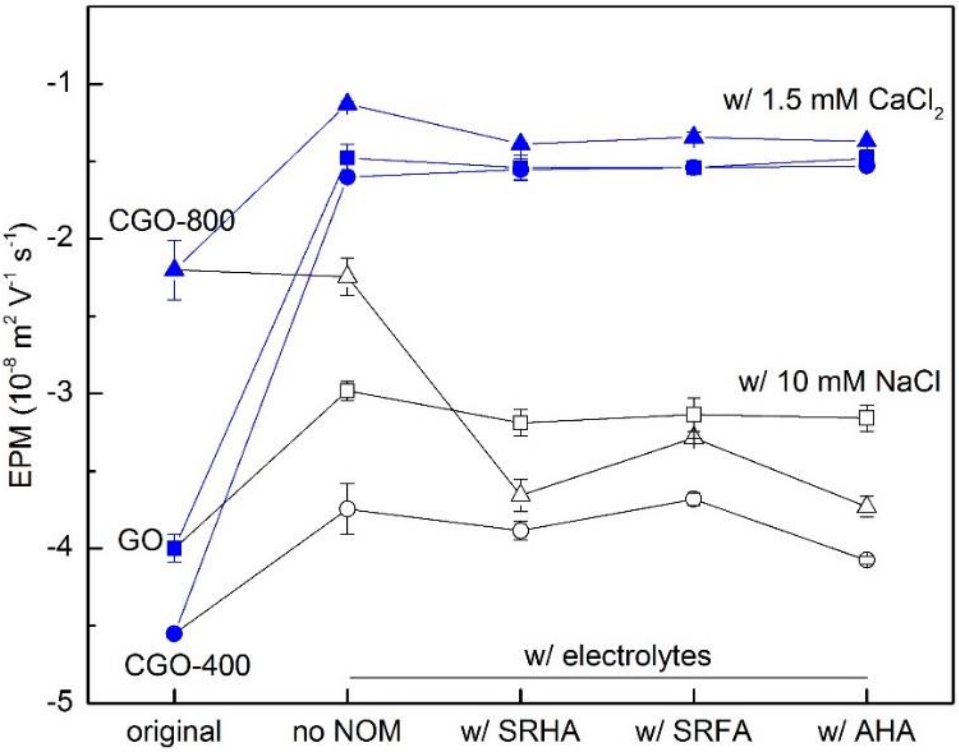

Figure 5.5 Electrophoretic mobilities (EPM) of GO, CGO-400, and CGO-800 nanoparticles in the presence of 10 mM NaCl and 1.5 mM $CaCl_2$. 2.7 mg C/L SRHA, SRFA, and AHA were present. The error bar represents the standard deviation from at least 3 samples.

With the addition of NOM, for GO and CGO-400, the electrophoretic mobility values remained almost unchanged, but the electrophoretic mobility of CGO-800 decreased from -2.2 to -3.3-3.7 m^2 V^{-1} s^{-1} in 10 mM NaCl and from -1.1 to -1.3-1.4 m^2 V^{-1} s^{-1} in 1.5 mM $CaCl_2$ (Figure 5.5). These observations are consistent with reports of other nanoparticles, including CNT and C_{60}, in that the electrophoretic mobility values remained unchanged[33, 35] or decreased with the presence of NOM.[36]

5.3.4 Adsorption of NOM

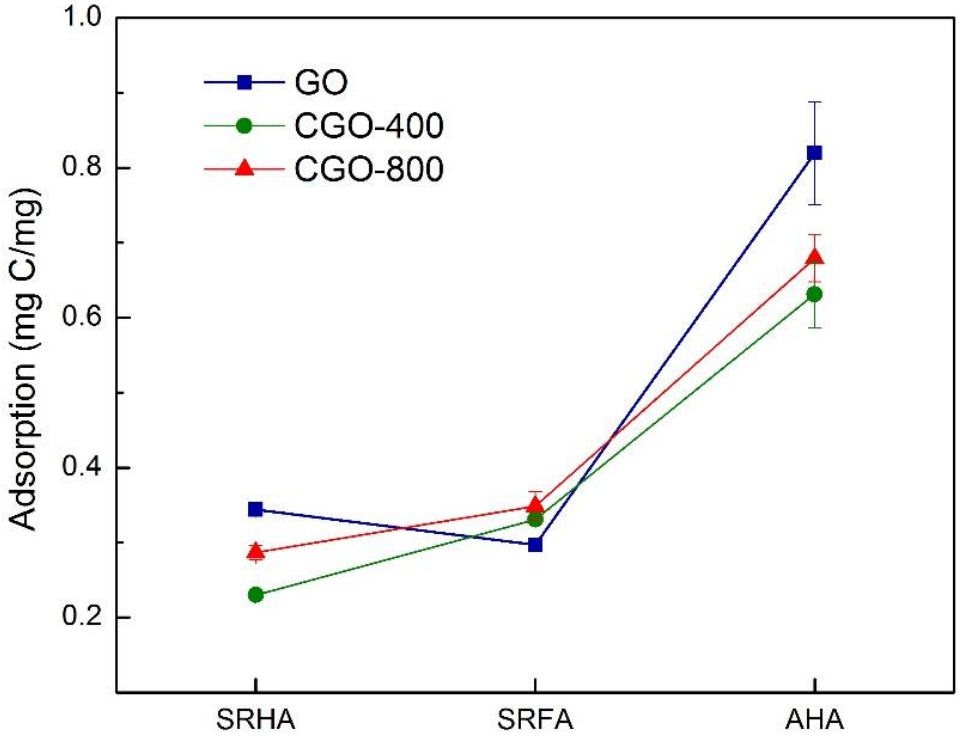

Figure 5.6 Adsorption of SRHA, SRFA, and AHA onto GO/CGOs.

The amount of NOM adsorbed onto GO/CGO is quantified through batch adsorption experiments ($C_{GO/CGO}$= 20 mg/L, NOM = 18 mg C/L). Adsorption quantities range from ~200 to 600 mg C/g adsorbent (Figure 5.6). For a comparison, previous reports show that adsorption of NOM onto CNTs are usually a few dozen(s) to ~ 200 mg C/g CNT.[21, 38] It was found that the adsorption of NOMs for all materials followed: AHA > SRHA ≈ SRFA (Figure 5.6).

5.4 Discussion

Overall, experimental results clearly show that NOM significantly increases the aqueous stability of graphene oxide materials. Such enhanced stability is generally explained by the change / effect of two interactions, electrostatic and steric repulsions. Increase in surface charge increases

electrostatic repulsion, thus enhancing the stability. Steric repulsion of two macromolecular layers can also lead to highly efficient material stabilization if the adsorbed layer thickness is larger than the Debye length when particles are less likely to approach at distances where vdW forces dominate.[39] These two repulsion effects are impacted by the characteristics of graphene materials and NOMs as discussed here:

5.4.1 Effects of Material Properties

The above results show that CGO, regardless of surface chemistry, has relatively higher CCC values and thus stability than flat GO in presence of NOM in water. Among the three material variables evaluated, the EPMs of CGO-800 became more negative with the presence of NOM, indicating an increase of electrostatic repulsion. However, such change was not observed with the more negatively charged GO and CGO-400, whereby the surface charge remained almost the same (Figure 5.5), which is similar to a previous report.[11] According to an analysis presented in our earlier work,[16] when considering only electrostatic and vdW interactions, the CCC has an approximate linear relationship with the function $tanh^4(\frac{\psi_0}{4})$, where ψ_0 is the dimensionless surface potential of particles (Supporting Information). For example, the CCC would increase by about 3.4 times if the surface potential of particles decreases from -30 mV to -45 mV. While when this surface potential change happened with CGO-800, CCC has increased by a few dozens of times, indicating steric repulsion plays a greater role in enhancing the aqueous stability. Taken together, for all cases studied here, steric repulsion is likely the major reason for enhanced aqueous stability in the presence of NOM.

For each specific NOM type, there appears to be no significant difference between adsorption quantities for material variables tested. This observation also indicates that among multiple adsorption mechanisms (e.g., electrostatic interaction, hydrophobic interaction, π-π

interaction, and hydrogen-bonding[38]), π-π interaction is a major mechanism. NOM adsorption likely results from a trade-off between increased aromatic regions and decreased accessible area. Upon thermal reduction, aromatic networks on CGO surface are restored, creating additional π-π interaction sites/areas between CGO and NOM molecules and thus leading to enhanced adsorption (and stronger steric repulsion). However, such effect may be negated by the decrease of accessible surface area due to crumpling. As a geometrical sheet, flat GO can adsorb on both material sides (while with a lower adsorption density), but for CGO, it is likely that most adsorption occurs on the outside surface of the crumpled ball. In other words, higher adsorption density (similar amount/decreased area) and extended configurations of NOMs on CGO surfaces are caused by different structural morphologies of CGO. It is possible that the GO and NOM molecules are parallel stacked, while for CGO, more extended configuration (outward) forms of NOMs exist, which increases the adsorbed layer thickness and thus the steric repulsion.

5.4.2 Effects of NOM Properties

SRHA and SRFA were reported to be taken from oxic environments whereby their organic constituents have undergone significant mineralization; while AHA has undergone, to a lesser degree, a milder degree of diagenesis in which biotic/abiotic processes have broken down amino acids and carbohydrates, leaving resistant organic matter such as lignins and waxy substances.[40] As a result, SRHA and SRFA are comprised of relatively small, polar and partially oxidized moieties, while AHA has more nonpolar, aromatic portion.[40, 41] Further comparing SRHA and SRFA, SRFA typically has lower molecular weight (e.g., 3-10 kDa for SRFA and 10-30 kDa for SRHA[42]), and tends to be more hydrophilic than SRHA, due to different ratios of oxygen moieties (SRHA with relatively more phenolic groups and relatively fewer carboxylic groups).[42] $SUVA_{254}$, as the bulk indicator of aromatic content of organic matter, represents the absorption by aromatic

bonds at wavelength of 254 nm.[43] The $SUVA_{254}$ for SRFA, SRHA, and AHA were calculated to be 3.7 ± 0.8, 5.9 ± 0.6, and 9.7 ± 1.5 L/(mg m). This result qualitatively agrees with the aromatic ratios estimated by ^{13}C NMR analysis (Table S5.1, SRFA, 22%, SRHA, 31%, and AHA, 40%).

This trend of aromaticity coincides with the adsorption and stability experimental results, where the highest adsorption and CCC occur in presence of AHA (Figure 5.3 and 6). These results further implicate π-π interactions as likely a (major) adsorption mechanism, as AHA is the most aromatic among the three types of NOM evaluated. This observation agrees with previous studies on adsorption of different NOM to MWNT,[21] which also correlated aromatic carbon content of NOM adsorption with π-π interactions / prevalence.[21] Additional reports have also shown that humic substances adsorb preferentially onto hydrophobic surfaces.[40, 43] However, we did not observe obvious difference between the adsorption quantities of SRHA and SRFA, which is likely due to the fact that the two observed values are close enough..

5.5 Environmental Implications

Results presented in this work clearly indicate that both material properties, NOM characteristics, and their respective interplay are critical to consider when investigating the aggregation behaviors of graphene-based materials in water. In the presence of NOM, GO materials will have higher aqueous stability, and crumpled morphologies will have much enhanced CCC values compared to flat GO structures. Observed enhanced aqueous stability was primarily due to steric repulsion imparted by adsorbed NOM macromolecules, and much higher CCC values associated with crumpled morphologies may be a result of high adsorption density and different configurations of NOM molecules on CGO surfaces. While this work provides new knowledge regarding graphene oxide behavior in water, additional research is needed to assess more complicated surface chemistries and morphologies of GO/CGO, in addition to material evaluation

in more complicated media (i.e. actual surface and ground waters) for a more accurate understanding of the long-term transport and fate of various graphene-based nanomaterials. Such information is critical for accurate life cycle assessments and ultimate material sustainability.

Acknowledgements

This work was partially supported by co-operative agreement CPC1402WA009 from the U.S. Environmental Protection Agency (EPA), by National Science Foundation's CAREER Award (CBET 1454656), by the McDonnell Academy Global Energy and Environment Partnership (MAGEEP), Washington University in St. Louis, and the Mindlin Foundation. XPS work was performed at Institute of Materials Science & Engineering, Washington University in St. Louis, with partial support from National Science Foundation under Grant NO. CBET-1337374. The authors thank Mr. Peng Liao for his kind help in preparing the NOM solutions. The conclusions represent the view of the authors and do not necessarily represent the opinions, policies or recommendations of the NSF or EPA.

References

1. Luo, J.; Zhao, X.; Wu, J.; Jang, H. D.; Kung, H. H.; Huang, J., Crumpled Graphene-Encapsulated Si Nanoparticles for Lithium Ion Battery Anodes. *J. Phys. Chem. Lett.* 2012, *3* (13), 1824-1829.
2. Jiang, Y.; Wang, W.-N.; Biswas, P.; Fortner, J. D., Facile Aerosol Synthesis and Characterization of Ternary Crumpled Graphene–TiO_2–Magnetite Nanocomposites for Advanced Water Treatment. *ACS Appl. Mater. Interfaces* 2014, *6* (14), 11766-11774.
3. Ritter, K. A.; Lyding, J. W., The influence of edge structure on the electronic properties of graphene quantum dots and nanoribbons. *Nat. Mater.* 2009, *8* (3), 235-242.

4. Perreault, F.; de Faria, A. F.; Nejati, S.; Elimelech, M., Antimicrobial Properties of Graphene Oxide Nanosheets: Why Size Matters. *ACS Nano* 2015, *9* (7), 7226-7236.
5. Jiang, Y.; Wang, W.-N.; Liu, D.; Nie, Y.; Li, W.; Wu, J.; Zhang, F.; Biswas, P.; Fortner, J. D., Engineered Crumpled Graphene Oxide Nanocomposite Membrane Assemblies for Advanced Water Treatment Processes. *Environ. Sci. Technol.* 2015, *49* (11), 6846-6854.
6. Zhao, G.; Li, J.; Ren, X.; Chen, C.; Wang, X., Few-Layered Graphene Oxide Nanosheets As Superior Sorbents for Heavy Metal Ion Pollution Management. *Environ. Sci. Technol.* 2011, *45* (24), 10454-10462.
7. Akhavan, O.; Ghaderi, E., Toxicity of Graphene and Graphene Oxide Nanowalls Against Bacteria. *ACS Nano* 2010, *4* (10), 5731-5736.
8. Liu, S.; Zeng, T. H.; Hofmann, M.; Burcombe, E.; Wei, J.; Jiang, R.; Kong, J.; Chen, Y., Antibacterial Activity of Graphite, Graphite Oxide, Graphene Oxide, and Reduced Graphene Oxide: Membrane and Oxidative Stress. *ACS Nano* 2011, *5* (9), 6971-6980.
9. Tu, Y.; Lv, M.; Xiu, P.; Huynh, T.; Zhang, M.; Castelli, M.; Liu, Z.; Huang, Q.; Fan, C.; Fang, H.; Zhou, R., Destructive extraction of phospholipids from Escherichia coli membranes by graphene nanosheets. *Nat. Nanotechnol.* 2013, *8* (8), 594-601.
10. Hummers, W. S.; Offeman, R. E., Preparation of Graphitic Oxide. *J. Am. Chem. Soc.* 1958, *80* (6), 1339-1339.
11. Chowdhury, I.; Duch, M. C.; Mansukhani, N. D.; Hersam, M. C.; Bouchard, D., Colloidal Properties and Stability of Graphene Oxide Nanomaterials in the Aquatic Environment. *Environ. Sci. Technol.* 2013, *47* (12), 6288-6296.

12. Wu, L.; Liu, L.; Gao, B.; Muñoz-Carpena, R.; Zhang, M.; Chen, H.; Zhou, Z.; Wang, H., Aggregation Kinetics of Graphene Oxides in Aqueous Solutions: Experiments, Mechanisms, and Modeling. *Langmuir* 2013, *29* (49), 15174-15181.
13. Zhao, J.; Liu, F.; Wang, Z.; Cao, X.; Xing, B., Heteroaggregation of Graphene Oxide with Minerals in Aqueous Phase. *Environ. Sci. Technol.* 2015, *49* (5), 2849–2857.
14. Wang, W.-N.; Jiang, Y.; Biswas, P., Evaporation-Induced Crumpling of Graphene Oxide Nanosheets in Aerosolized Droplets: Confinement Force Relationship. *J. Phys. Chem. Lett.* 2012, *3* (21), 3228-3233.
15. Li, D.; Muller, M. B.; Gilje, S.; Kaner, R. B.; Wallace, G. G., Processable Aqueous Dispersions of Graphene Nanosheets. *Nat. Nanotechnol.* 2008, *3* (2), 101-105.
16. Jiang, Y.; Raliya, R.; Fortner, J. D.; Biswas, P., Graphene Oxides in Water: Correlating Morphology and Surface Chemistry with Aggregation Behavior. *Environ. Sci. Technol.* 2016, *50* (13), 6964–6973.
17. Wen, X.; Garland, C. W.; Hwa, T.; Kardar, M.; Kokufuta, E.; Li, Y.; Orkisz, M.; Tanaka, T., Crumpled and collapsed conformation in graphite oxide membranes. *Nature* 1992, *355* (6359), 426-428.
18. Ren, X.; Li, J.; Tan, X.; Shi, W.; Chen, C.; Shao, D.; Wen, T.; Wang, L.; Zhao, G.; Sheng, G.; Wang, X., Impact of Al2O3 on the Aggregation and Deposition of Graphene Oxide. *Environ. Sci. Technol.* 2014, *48* (10), 5493-5500.
19. Howe, K. J.; Hand, D. W.; Crittenden, J. C.; Trussell, R. R.; Tchobanoglous, G., *Principles of water treatment*. John Wiley & Sons: 2012.

20. Chowdhury, I.; Mansukhani, N. D.; Guiney, L. M.; Hersam, M. C.; Bouchard, D., Aggregation and Stability of Reduced Graphene Oxide: Complex Roles of Divalent Cations, pH, and Natural Organic Matter. *Environ. Sci. Technol.* 2015, *49* (18), 10886-10893.
21. Hyung, H.; Kim, J.-H., Natural Organic Matter (NOM) Adsorption to Multi-Walled Carbon Nanotubes: Effect of NOM Characteristics and Water Quality Parameters. *Environ. Sci. Technol.* 2008, *42* (12), 4416-4421.
22. Hur, J.; Schlautman, M. A., Molecular weight fractionation of humic substances by adsorption onto minerals. *J. Colloid Interface Sci.* 2003, *264* (2), 313-321.
23. Reiller, P.; Amekraz, B.; Moulin, C., Sorption of Aldrich Humic Acid onto Hematite: Insights into Fractionation Phenomena by Electrospray Ionization with Quadrupole Time-of-Flight Mass Spectrometry. *Environ. Sci. Technol.* 2006, *40* (7), 2235-2241.
24. Chen, K. L.; Elimelech, M., Aggregation and Deposition Kinetics of Fullerene (C60) Nanoparticles. *Langmuir* 2006, *22* (26), 10994-11001.
25. Lotya, M.; Rakovich, A.; Donegan, J. F.; Coleman, J. N., Measuring the lateral size of liquid-exfoliated nanosheets with dynamic light scattering. *Nanotechnology* 2013, *24* (26), 265703.
26. Mkhoyan, K. A.; Contryman, A. W.; Silcox, J.; Stewart, D. A.; Eda, G.; Mattevi, C.; Miller, S.; Chhowalla, M., Atomic and Electronic Structure of Graphene-Oxide. *Nano Lett.* 2009, *9* (3), 1058-1063.
27. Larciprete, R.; Fabris, S.; Sun, T.; Lacovig, P.; Baraldi, A.; Lizzit, S., Dual Path Mechanism in the Thermal Reduction of Graphene Oxide. *J. Am. Chem. Soc.* 2011, *133* (43), 17315-17321.

28. Ganguly, A.; Sharma, S.; Papakonstantinou, P.; Hamilton, J., Probing the Thermal Deoxygenation of Graphene Oxide Using High-Resolution In Situ X-ray-Based Spectroscopies. *J. Phys. Chem. C* 2011, *115* (34), 17009-17019.
29. Yumitori, S., Correlation of C1s chemical state intensities with the O1s intensity in the XPS analysis of anodically oxidized glass-like carbon samples. *J. Mater. Sci.* 2000, *35* (1), 139-146.
30. Szabó, T.; Berkesi, O.; Forgó, P.; Josepovits, K.; Sanakis, Y.; Petridis, D.; Dékány, I., Evolution of Surface Functional Groups in a Series of Progressively Oxidized Graphite Oxides. *Chem. Mater.* 2006, *18* (11), 2740-2749.
31. Park, S.; Dikin, D. A.; Nguyen, S. T.; Ruoff, R. S., Graphene Oxide Sheets Chemically Cross-Linked by Polyallylamine. *J. Phys. Chem. C* 2009, *113* (36), 15801-15804.
32. Elimelech, M.; Jia, X.; Gregory, J.; Williams, R., *Particle deposition & aggregation: measurement, modelling and simulation*. Butterworth-Heinemann: 1998.
33. Chen, K. L.; Elimelech, M., Influence of humic acid on the aggregation kinetics of fullerene (C60) nanoparticles in monovalent and divalent electrolyte solutions. *J. Colloid Interface Sci.* 2007, *309* (1), 126-134.
34. Hyung, H.; Fortner, J. D.; Hughes, J. B.; Kim, J.-H., Natural Organic Matter Stabilizes Carbon Nanotubes in the Aqueous Phase. *Environ. Sci. Technol.* 2007, *41* (1), 179-184.
35. Saleh, N. B.; Pfefferle, L. D.; Elimelech, M., Aggregation Kinetics of Multiwalled Carbon Nanotubes in Aquatic Systems: Measurements and Environmental Implications. *Environ. Sci. Technol.* 2008, *42* (21), 7963-7969.

36. Smith, B.; Yang, J.; Bitter, J. L.; Ball, W. P.; Fairbrother, D. H., Influence of Surface Oxygen on the Interactions of Carbon Nanotubes with Natural Organic Matter. *Environ. Sci. Technol.* 2012, *46* (23), 12839-12847.
37. Yeh, C.-N.; Raidongia, K.; Shao, J.; Yang, Q.-H.; Huang, J., On the origin of the stability of graphene oxide membranes in water. *Nat. Chem.* 2015, *7* (2), 166-170.
38. Yang, K.; Xing, B., Adsorption of fulvic acid by carbon nanotubes from water. *Environ. Pollut.* 2009, *157* (4), 1095-1100.
39. Tiller, C. L.; O'Melia, C. R., Natural organic matter and colloidal stability: Models and measurements. *Colloids Surf. Physicochem. Eng. Aspects* 1993, *73* (0), 89-102.
40. Grasso, D.; Chin, Y.-P.; Weber, W. J., Structural and behavioral characteristics of a commercial humic acid and natural dissolved aquatic organic matter. *Chemosphere* 1990, *21* (10), 1181-1197.
41. Hong, S.; Elimelech, M., Chemical and physical aspects of natural organic matter (NOM) fouling of nanofiltration membranes. *J. Membr. Sci.* 1997, *132* (2), 159-181.
42. Jucker, C.; Clark, M. M., Adsorption of aquatic humic substances on hydrophobic ultrafiltration membranes. *J. Membr. Sci.* 1994, *97*, 37-52.
43. Cai, N.; Peak, D.; Larese-Casanova, P., Factors influencing natural organic matter sorption onto commercial graphene oxides. *Chem. Eng. J.* 2015, *273*, 568-579.

Chapter 5 Supporting Information

Table S5.1. ^{13}C NMR estimates of carbon distribution in HA samples. SRHA and SRFA data are excerpted from International Humic Substances Society (IHSS) (website: http://www.humicsubstances.org/thornnmr.html). AHA data are excerpted from Kim, J., G. Buckau, et al. (1990). Characterization and complexation of humic acid, Technische Univ. Muenchen.

Sample Name	Carbonyl	Carboxyl	Aromatic	Acetal	Heteroaliphatic	Aliphatic
SRHA II	6	15	31	7	13	29
SRFA II	5	17	22	6	16	35
AHA	14		40		5	41

Figure S5.1. FTIR spectra of GO, CGO-400, and CGO-800.

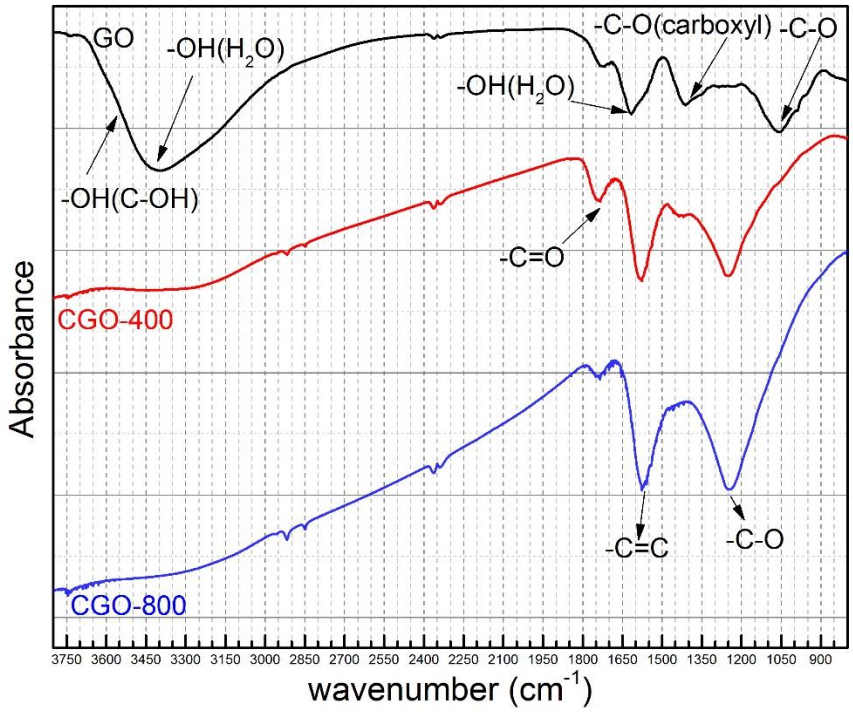

S5.1. Relationship between CCC and ζ-potential

When considering only electrostatic repulsion and vdW attraction, the relationship between CCC (n as the cation number concentration) and surface potential of particles can be approximated by the following equation:[1]

$$n = \frac{\lambda tanh^4(\frac{a\psi_0}{4})}{a^5(a+b)k_3^6} \frac{(4\pi\varepsilon_0\ \varepsilon_r)^3(k_BT)^5 48^2}{e^6 {A_{GWG}}^2 \pi \exp(2)},$$

$$\lambda = \left[1 - \frac{1}{2k_3X_0}(1 - \exp(-2k_3X_0))\right]^2$$

Thus CCC is proportional to ζ-potential (when assume the A_{GWG} values are the same for CGOs) by:

$$n/\lambda \propto tanh^4(\frac{a\psi_0}{4})$$

Where ψ_0 is dimensionless surface potential $\psi_0 = \frac{e\Phi_0}{k_BT}$; X_0 is the dimensionless radius of the particle, $X_0 = \kappa r_0$ (r_0 is the particle radius); L is the surface-to-surface distance between two particles. The reciprocal Debye length κ is calculated by $\kappa^2 = \frac{a(a+b)ne^2}{\varepsilon_0\ \varepsilon_r\ k_BT}$, where a and b are the valences of the cation and anion of the electrolyte, ε_0 and ε_r are the permeability of a vacuum and the relative permeability of the liquid phase (water) respectively, T is the absolute temperature (298 K), e is the elementary charge (1.6×10^{-19} C), k_B is the Boltzmann constant (1.38×10^{-23} m^2 Kg s^{-2} K^{-1}), n is the number concentration of cations in bulk phase. A_{GWG} is the Hamaker constant of the GO-water system (i.e., GO separated by water). k_3 is a parameter related to a and b, for NaCl, k_3=1; for $CaCl_2$ and $MgCl_2$, $k_3 \approx 1.078$.

For the above hyperbolic function $y = tanh^4(\frac{e\Phi_0}{4k_BT})$, the plot will appear as follows:

As the graph shows (Figure S5.2), when the surface potential decreases from -29 to -45 mV, the function y increases from 0.006 to 0.029 (about 5 times).

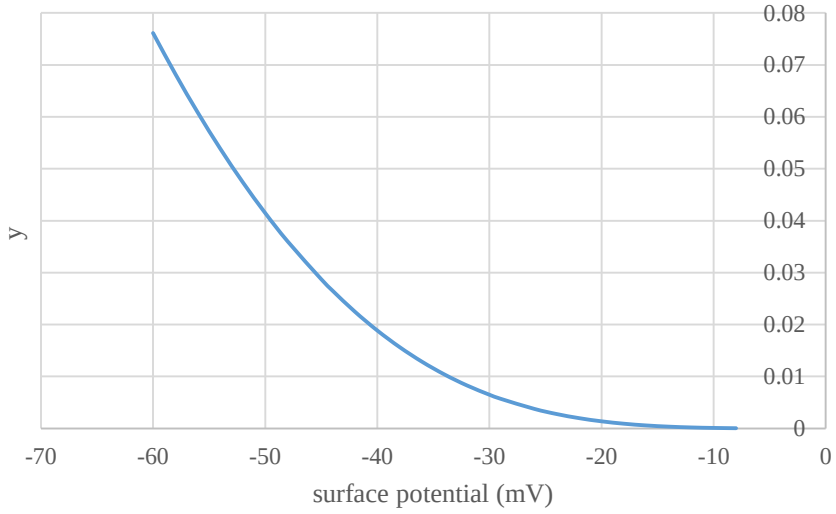

Figure S5.2. y as a function of surface potential Φ_0, $y = tanh^4(\frac{e\Phi_0}{4k_BT})$

Supplementary References:

1. Jiang, Y.; Raliya, R.; Fortner, J. D.; Biswas, P., Graphene Oxides in Water: Correlating Morphology and Surface Chemistry with Aggregation Behavior. Environ. Sci. Technol. 2016, 50 (13), 6964–6973

Chapter 6. Facile Aerosol Synthesis and Characterization of Ternary Crumpled Graphene-TiO_2-Magnetite Nanocomposites for Advanced Water Treatment

Abstract

In this work, the synthesis and characterization of multifunctional crumpled graphene-based ternary nanocomposite photocatalysts for advanced water treatment applications is described. Currently, a major hurdle for the scale-up and optimization of aqueous, graphene-based photocatalysts is restacking of graphene nanosheets due to strong π-π interactions. To overcome this hurdle, a fast and facile aerosol technique to synthesize monomeric, aggregation-resistant, crumpled graphene-based photocatalysts was developed. The aerosol route utilizes water evaporation-induced confinement forces to effectively crumple graphene oxide and subsequently encapsulate commercially available TiO_2 and magnetite nanoparticles. The as-synthesized crumpled graphene-TiO_2-magnetite (GOTIM) ternary core-shell nanostructures, are shown to possess superior aqueous-based photocatalytic properties (over a 20 fold enhancement in some cases) compared to TiO_2 alone. Total GOTIM photocatalytic reactivity is confirmed to also include efficient photo-reduction reaction pathways, in addition to expected oxidation routes typical of TiO_2 based photocatalysts, significantly expanding photocatalytic application potential compared to TiO_2 alone. Reaction kinetics and proposed mechanisms (both oxidative and reductive) are described for a model organic compound, here as methyl orange. Further, with the addition of hole scavengers such as EDTA, and/or lowering the O_2 concentration, we demonstrate further enhancement of photocatalyzed reduction reactions, suggesting potential for directed, controlled reduction applications. In addition to robust aqueous stability, low-field magnetic susceptibility is demonstrated, allowing for low-energy, in situ material separations, which are critical for material recycling and reuse.

6.1 Introduction

Water treatment using photocatalysts, particularly TiO_2, has garnered considerable attention and been successfully demonstrated in a number of applications.[1, 2] Recent material advances with combined TiO_2-carbon nanomaterial based photocatalysts, such as graphene and carbon nanotubes, have demonstrated superior and sometimes unique physical and chemical properties compared to traditional analogs. For example, fullerene (C_{60})-incorporated TiO_2 nanorods demonstrated enhancement of photocatalytic activity by nearly 2.7 times compared to Degussa P25;[3] while carbon nanotube (CNT)-TiO_2 materials, also demonstrated enhanced activity with rates dependent on dopant ratios (maximum oxidation rates were found at ~ 85 wt.% CNT);[4] a hybrid P25-graphene composite material, synthesized via a one-step, hydrothermal method, was demonstrated to be a superior photocatalyst compared to bare P25 (measured by the degradation rate of methylene blue), due to increased light absorption range, more pollutant adsorption (surface localization) and decreased recombination of photo-induced holes and electrons.[5] Further, graphene-based TiO_2 photocatalysts may eventually prove to be economical, as they are not only more efficient per unit mass when compared to traditional analogs, but also composed of abundant, available and relatively low cost elemental components in addition to rapidly decreasing graphene production costs. To date, one of the significant issues in the aqueous-based processing and applications of graphene composites lies in the material's tendency to restack due to strong π-π attractions between graphene nanosheets.[6] Restacking results in significant decreasing of accessible surface area and aqueous stability/accessibility, and thus loss of material efficacy over a short time.[7, 8] To avoid restacking/instabilities there have been a number of strategies employed such as spacer additions (e.g. CNT[9] and water[10]); however, the overall catalytic durability and

reliable recovery (separation), which both are needed for successful recycling/application strategies, for such materials has yet to be fully demonstrated.

Interestingly, there have been recent advancements in the development of three-dimensional (3D), nanoscale, graphene composite structures, which can be specifically engineered to avoid two-dimensional limitations stated above. Specifically, by 'crumpling' graphene and graphene oxide it has been observed that resulting 3D structures have outstanding compression- and aggregation-resistant properties in water.[6, 8] Further, aggregation-resistant, crumpled graphene-nanocrystal composites can be synthesized via direct aerosolization starting with either graphene oxide suspensions mixed with precursor ions[11] or pre-synthesized nanoparticles, resulting in binary and ternary composite materials.[12, 13] Such crumpled graphene based nanocomposites, which have been demonstrated to include the incorporation of Si,[14] Pt,[15] Mn_3O_4 and SnO_2,[11] TiO_2,[16, 17] Au/Fe_3O_4,[13] (either through encapsulation or sack-cargo surface complexes) have been primarily evaluated for electrochemical and magnetic applications. However, as a high performance aqueous-based photocatalyst, crumpled graphene-TiO_2 structures have not yet been thoroughly evaluated. Additionally, tailoring crumpled graphene-TiO_2 magnetic susceptibility through the incorporation of magnetite nanoparticles, and thus allowing for simple catalyst recovery strategies, is of high interest for material reuse/recycle, particularly in a context of economically sustainable processing.

Crumpled graphene-based nanocomposites can be readily produced by an aerosol-based approach.[11, 12] Briefly, graphene oxide precursors are aerosolized into micrometer-sized droplets by using a nebulizer and then delivered by N_2 into a furnace aerosol reactor (FuAR). During the flight time within the reactor, single graphene oxide sheet effectively crumples under evaporation-induced confinement forces allowing for the effective encapsulation of associated nanoparticles,

thus forming a core-shell type nanocomposite. The encapsulated nanocrystals can be pre-synthesized nanoparticles (e.g. citrate-stabilized Ag nanoparticles),[12] or grown from precursor ions.[11] Combined, the graphene oxide sheets and precursor content, either pre-synthesized nanoparticles or precursor ions, determine the size and composition, thus functionality, of the resulting material. For example, magnetic susceptibility can be achieved and tuned by incorporating a magnetic precursor component such as nanoscale magnetite (Fe_3O_4) particles, as described in this work.

Previous research describing (flat) graphene-TiO_2 photocatalytic reactions have primarily focused on oxidation pathways.[5, 18-21] Under UV irradiation (< 380 nm wavelength) photo-induced holes (h^+) and radical species, such as superoxide radicals ($O_2^{-\cdot}$) and hydroxyl radicals ($OH\cdot$) can oxidize model target species or pollutants.[18, 21] Targeted photocatalytic reduction of pollutants, such as U(VI),[22] Cr(VI),[23, 24] Cu(II),[25] 2,4,6-trinitrotoluene (TNT),[26] CO_2,[27] has not, however, been a focus area to date for graphene-TiO_2 structures despite the possibility of engineering reduction pathways as induced electrons lifetime and occurrence can be significantly enhanced under UV irradiation.[18] Based on this, a detailed exploration of both oxidation and reduction reaction pathways for photo-induced holes and excited electrons, uniquely enabled through engineered, crumpled graphene-TiO_2 materials for aqueous catalytic redox processes, is needed.

This work focuses on two significant aspects of crumpled graphene-TiO_2 aqueous photocatalysts: (1) Synthesis and evaluation of a new ternary crumpled graphene (or reduced graphene oxide)-TiO_2-magnetite (GOTIM) photocatalyst, which are highly stable, aggregation-resistant and magnetically recoverable in water; and (2) identification and exploration of extended aqueous reaction pathways for (UV) photo-induced holes and electrons for synthesized materials, including the enhancement of photocatalytic reduction based reactions. Together, this works

highlights the platform potential for crumpled graphene-TiO_2 photocatalysts to be broadly multifunctional, including the extension of reaction regimes, in addition to being recoverable via low magnetic fields, allowing for simple yet efficient separation/reuse strategies.

6.2 Experimental

6.2.1 Precursor Preparation

Graphene oxide (GO) was synthesized using the modified Hummer's method[28] and was reported in our previous work.[8] To obtain GOTIM ternary nanocomposite, dry GO powder (200 mg) and commercial magnetite nanoparticles (primary size < 50 nm, Sigma Aldrich, 100 mg) were premixed and dispersed in 200 mL water and ultrasonicated for 1 h using a microtip sonicator (Qsonica). This process allows the exfoliated GO nanosheets to associate with disaggregated magnetite nanoparticles. The suspension was then centrifuged at 10,000 rpm for another 1 h. The supernatant, with exfoliated GO nanosheets and attached magnetite nanoparticles, was then added with TiO_2 nanoparticles at different weight percentages (Evonik Degussa Aerodisp; 7, 14, 28 mg) and aerosolized (Figure 6.1). Crumpled graphene-TiO_2 (GOTI) nanocomposite was also synthesized for the photocatalytic reaction experiments. To obtain GOTI nanocomposite, GO solution was directly mixed with TiO_2 (28 mg TiO_2 into 200 mL GO solution); and the mixture was then aerosolized.

6.2.2 Crumpled Graphene Nanocomposite Synthesis

To obtain the crumpled graphene nanocomposite, a furnace aerosol reactor (FuAR) was utilized (Figure 6.1). The precursor solution was atomized into micrometer-sized droplets by using a Collison nebulizer (BGI Incorporated), and then delivered by N_2 into tubular alumina reactor (1 m × 25 mm ID) maintained at 400 ℃, to enable the successful crumpling of GO, yet partially preserve the functional groups, such as carboxyl and hydroxyl groups that are critical for

nanocomposite stability in water due to electrostatic repulsion.[8] The flow rate was operated at 12.4 L/min by adjusting the nebulizer pressure (14 psi, 96.53 kPa), resulting in ~1.6 s residence time. During the flight in the furnace, graphene oxide became crumpled under the evaporation-induced confinement force, and could effectively encapsulate nanoparticles dispersed in the precursor solution.[12] Finally, the nanocomposites were collected downstream of the reactor, weighed and dispersed into water to obtain 200 mg/L dispersion.

6.2.3 Nanoparticle Characterization

The optical properties of GOTIM aqueous dispersions (200 mg/L) were measured by using a UV-Vis spectrophotometer (Varian Bio 50). The ζ-potential and hydrodynamic diameter of aqueous GOTIMs were measured using Zetasizer Nano ZS system (Malvern Instruments). The morphology and size of the GOTIM nanoparticles were also examined by field emission scanning electron microscopy (FESEM, NOVA NanoSEM 230), transmission electron microscopy (TEM, Tecnai TM Spirit), and high resolution-TEM (HR-TEM, JEOL 2100). The crystal phase was determined by X-ray Diffraction (XRD) (Geigerflex D-MAX/A, Rigaku Denki) with CuK_{α} radiation ($\lambda = 1.548$ Å). The GOTIM nanoparticles were digested in concentrated HNO_3 at 110 ℃ for 10 h and diluted for inductively coupled plasma mass spectrometry (ICP-MS, Agilent 7500cc) analysis to quantify the TiO_2/magnetite ratios. GOTIM nanocomposite molecular bond and functionality analyses were performed with a Raman spectrometer (Renishaw InVia Reflex confocal Raman spectrometer with a 514 nm laser); and fourier transform infrared spectrometer (FTIR, Nicolette Nexus 470).

6.2.4 Photo-degradation of a Model Dye

The photocatalytic activity of synthesized GOTIMs was evaluated by the photo-degradation of a model pollutant, methyl orange (MO). Typically 50 mL MO solution (C_0 = 9.6 or 20 mg/L) and GOTIM photocatalyst (8 or 16 mg/L, suspended) was added into a quartz beaker. A Xenon lamp (with intensities of 14.4 or 18.8 mW/cm^2 in the effective UV range (250-387 nm)) was used as the irradiation light source; and an overhead stirrer was used to promote mass transfer in the solution. The distance between the center of the beaker and the light source was set to be 16 cm. Before each reaction, the solution was stirred in dark for 30 min to achieve adsorption equilibrium. During the reaction, 2 mL sample was collected at each time interval (10 min) and filtered using a syringe filter (Millex PES, 0.22 μm) before UV-Vis measurement to determine the remaining MO concentration at the absorption peak 463 nm. Photo-degradation of MO using bare TiO_2 nanoparticles was also conducted under the same conditions for comparison.

6.2.5 Identifying Reaction Pathways

To help identify and explore major reaction pathways, *tert*-butanol (*t*-BuOH, 10 mM, Sigma Aldrich),[29, 30] catalase (500 units/mL, Sigma Aldrich),[31] and ethylenediaminetetraacetic acid (EDTA, 4 mM, Sigma Aldrich)[32] were employed as $OH^{\cdot}$, H_2O_2, and h^+ scavengers, respectively. For anaerobic reactions, a capped quartz serum bottle was used instead and the solution was purged with N_2 for 30 min before the photocatalytic reactions.

6.2.6 Reuse/Cycling Experiments

To evaluate recycling potential and material reuse, after each reaction cycle (beginning with a batch reaction as described above), specified amount of MO stock solution (C = 500 mg/L) was added to keep $[MO]_0$ = 10 mg/L at the beginning of next reaction. After 5 cycles, the remaining GOTIM was collected using a magnet (ca. 1T neodymium, Applied Magnets) and the collection

efficiency was calculated from the difference between the GOTIM UV-Vis absorbance (320 nm) before and after the cyclic experiments.

6.3 Results and Discussion

6.3.1 Material Synthesis and Characterization

For materials described, the desired ternary crumpled GOTIM nanocomposite requires precursors containing three components - graphene oxide sheets, TiO_2 and magnetite together, either in the (original) form of pre-synthesized nanoparticles or precursor ions. The former (pre-synthesized nanoparticle) approach was chosen not only because of commercial availability of nanoscale TiO_2 and magnetite, but also because precursor ions can lead to incomplete growth and heterogeneous distribution of TiO_2 and magnetite in the resulting composites.

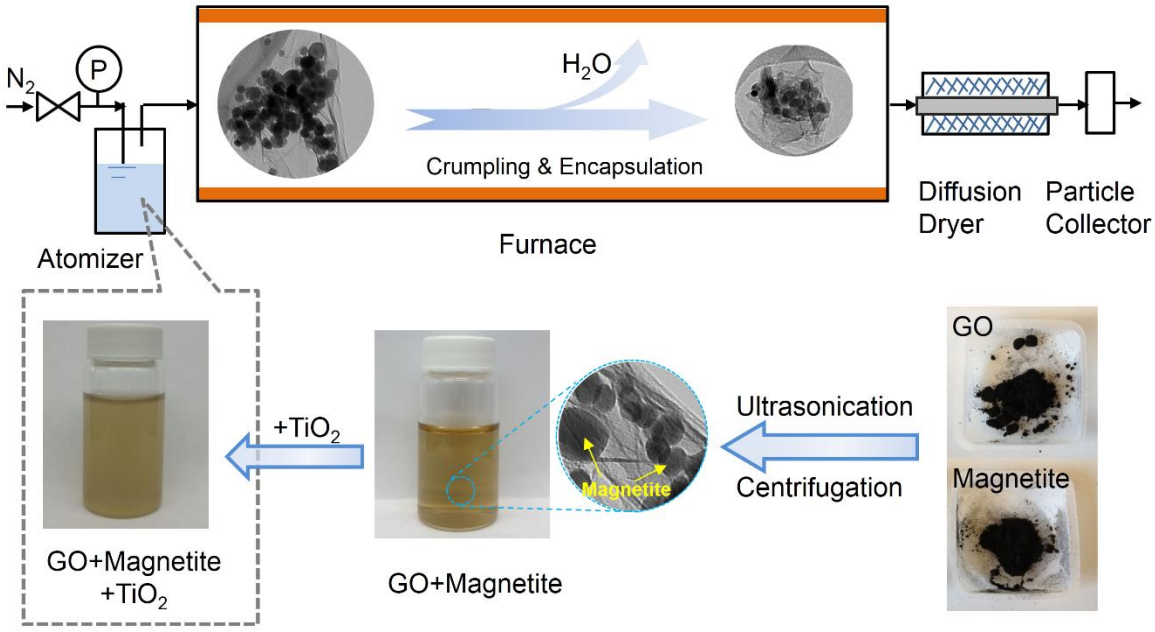

Figure 6.1 Experimental setup. Schematic diagram of a FuAR and the synthesis process.

Previous research highlights the key role of aqueous stability regimes (particularly electrostatic interactions between graphene based components) in determining the success of synthesis of GO-based ternary nanostructures.[13] Graphene oxide is stable in water with a ζ-potential usually being < -30 mV;[33] and TiO_2 can be prepared as an aqueous dispersion (Degussa). However, untreated/uncoated, commercial magnetite nanoparticles (Sigma Aldrich, < 50 nm) are not readily water-dispersible, based on high particle surface energies, preventing direct, homogenous atomization. Here, the aerosol-based technique was thus modified to first anchor magnetite nanoparticles onto GO nanosheets. By sonicating aqueous mixture of GO and magnetite nanoparticles, successful surface attachment of magnetite nanoparticles with GO took place, as shown in the TEM graph in Figure 6.1. It was observed that the commercially available magnetite nanoparticles were poly-dispersed, with diameter ranging from 10-50 nm, and either coupled onto the GO nanosheet surface or crumpled edges. Previous research reports that nanoparticles can interact with the GO nanosheets via various physical and chemical interactions, such as physisorption, electrostatic binding, and charge transfer interactions.[34-37] In this work, the ζ-potentials measured from electrophoretic light scattering show an increasing ζ-potential for GO-magnetite dispersion (-28 mV), as compared with pure GO solution (-48 mv), indicating electrostatic binding may facilitate the attachment of magnetite nanoparticles (thus lessening the total particle surface charge). Additionally, the point of zero charge (PZC) of magnetite ~7 as reported in other's work,[13] also provided support for the electrostatic binding mechanism; as the GO solution used in this work has a pH ~3. As produced, the GO-magnetite dispersion was next mixed with a TiO_2 aqueous suspension (varying concentration of TiO_2), then atomized and finally delivered by N_2 (flow rate 12.4 L/min) into the reactor (400 ℃), producing crumpled GOTIM composites (Figure 6.1).

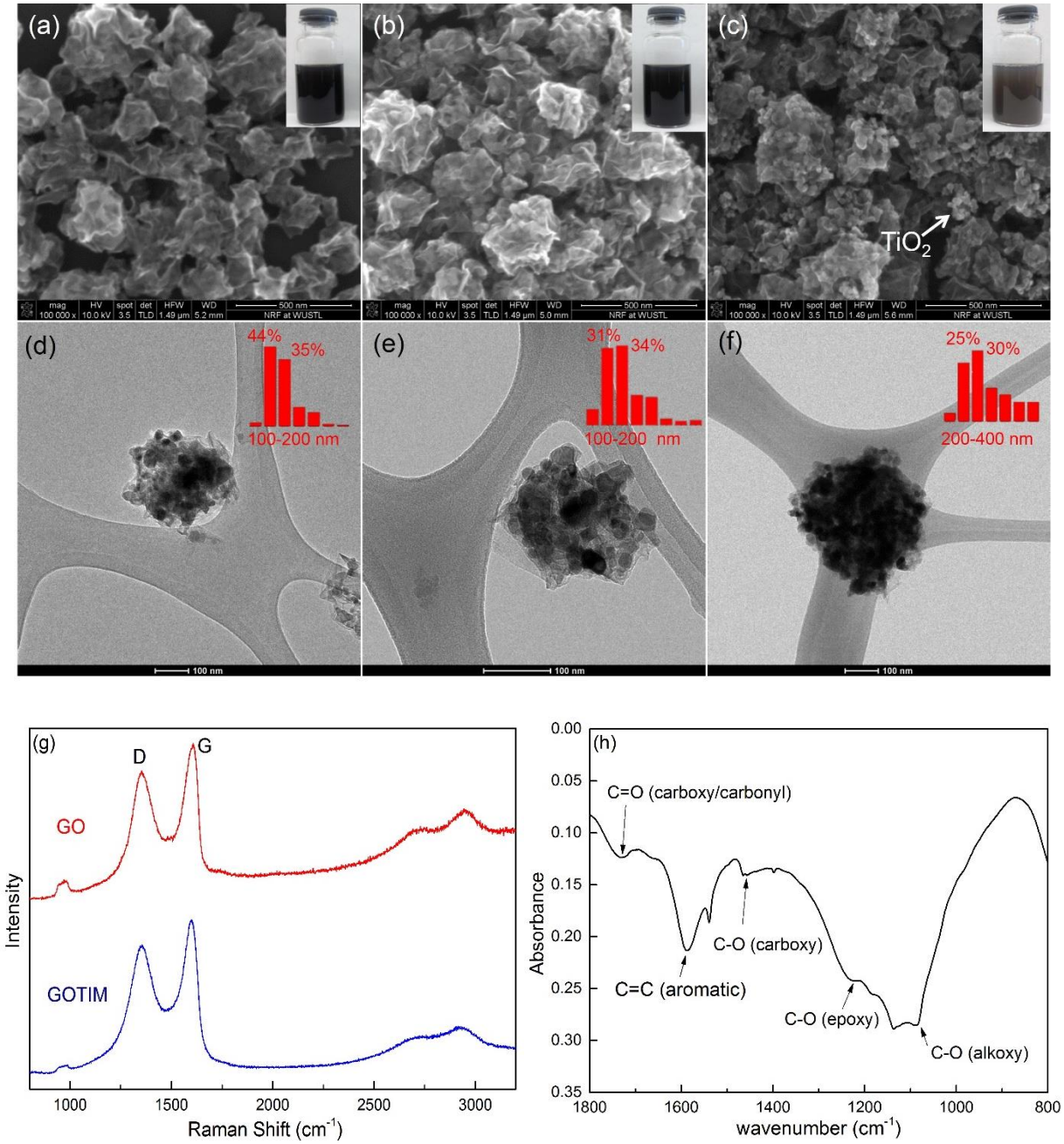

Figure 6.2 GOTIM with different TiO_2 contents. (a-c) SEM images of GOTIM-A, GOTIM-B and GOTIM-C as well as digital photos of corresponding dispersions in the insets (200 mg/L). (d-f) TEM images of GOTIM-A, GOTIM-B and GOTIM-C, with corresponding number-based PSD from DLS in the insets. The two percentages correspond to the highest two peaks.(g) Raman spectra of flat GO and GOTIM-B. (h) FTIR spectrum of GOTIM-B.

Crumpled GOTIM nanocomposites were collected using a membrane filter (Millipore ISOPORE, 0.2 um) downstream of the reactor and characterized. Figure 6.2 a-f shows digital photos, FESEM, TEM as well as number-based, particle size distribution (PSD) of synthesized GOTIM with three TiO_2/magnetite ratios (as calculated from inductively coupled plasma mass spectrometry (ICP-MS) measurements of acid digested samples, 1.8, 1.9 and 2.7; and denoted as GOTIM-A, B and C, respectively, hereafter). GOTIM dispersions are black, indicating GO being partially thermally reduced with graphene regions at 400 ℃ (Figure 6.2a and b insets), which has been observed previously.[38] Quasi-spherical, core-shell (also termed sack-cargo) nanostructures were observed for all GOTIMs as shown in Figure 6.2a, b, and c.[12] With the increase of interior particle volume (number/size), surface roughness was observed to decrease with visual identification of incorporation of TiO_2 and magnetite nanoparticles, which increased with higher (interior) loading ratios (from Figure 6.2a to c). For GOTIM-C, which has the highest TiO_2 mass loading, incomplete encapsulation of all TiO_2 nanoparticles was observed. For this case, TiO_2 nanoparticles also aggregated on the outer surface of GO, as indicated by the white arrow in Figure 6.2c. High TiO_2 mass loading was also reflected in the gray color of GOTIM-C dispersion (Figure 6.2c inset), compared to much darker suspensions for 2a-b. Figure 6.2d, e, and f show corresponding TEM images of GOTIM, with number-based PSD derived from dynamic light scattering (DLS) measurements in the insets. These TEM micrographs further confirmed the material structure as a crumpled GO shell, with TiO_2 and magnetite coexisting as the core. Further HR-TEM analysis reveals that TiO_2 nanoparticles have an orientation of anatase (101) plane; while magnetite nanoparticles reveal an orientation of (111) plane (Figure S6.1). In addition, XRD analysis of GOTIM and CGO was performed (Figure S6.2) and when compared with CGO alone, TiO_2 and magnetite diffraction patterns were observed in GOTIM samples. It was also observed

from the PSD data that the peak size of the nanocomposite increased from 100-200 nm to 200-400 nm with the encapsulation of more TiO_2 nanoparticles. This demonstrates that by employing an improved synthesis strategy (first GO-magnetite solution, then adding TiO_2 aqueous dispersion), instead of sonicating a pot of three components together (GO, magnetite, TiO_2),[13] GOTIM nanocomposites of tunable size and functionality can be readily achieved. Raman analysis of GOTIM-B shows the two characteristic bands of GO, D band (~1350 cm^{-1}, measuring hexagonal carbon pattern distortions, such as defects) and G band (~1600 cm^{-1}, pure sp^2 hybridized graphitic carbon). The ratio of D and G band intensities (I_D/I_G) for these samples remains virtually unchanged after aerosol (and thermal) processing (from 0.84 (flat GO) to 0.85 (GOTIM)), indicating an optimal balance of synthesis (crumpling) conditions while maintaining hydrophilicity (via surface oxidation). CGO FTIR spectrum in Figure 6.2h indicates a mixture of oxygen-based functional moieties present including C-O (alkoxy), C-O (epoxy), C-O (carboxy), C=C (aromatic), and C=O (carboxy/carbonyl) stretches.[39]

UV-Vis absorption spectra of GOTIM demonstrates a red shift with increasing TiO_2 content (e.g. ca. 20 nm shift for GOTIM-C compared to bare TiO_2) and for all GOTIM materials described an extended absorption range was observed when compared to bare TiO_2 which is due to the band gap narrowing of TiO_2 when participating in Ti-O-C interactions.[40, 41] This red shift enables the more efficient utilization of the solar spectrum and has been observed previously for flat graphene-TiO_2 nanocomposite (see S.I. Figure S6.3).[5, 18] As described, all materials had a net negative surface charge ($\zeta_{GOTIM\text{-}A}$= -46.6 mV, $\zeta_{GOTIM\text{-}B}$= -48.7 mV, $\zeta_{GOTIM\text{-}C}$= -41.0 mV) providing aqueous stability. No significant sedimentation was observed for months for GOTIM-A and GOTIM-B. For GOTIM-C, which had excess TiO_2 on the composite surface, partial sedimentation was observed after one month.

6.3.2 GOTIM Photocatalytic Characterization

The mechanism of graphene enhanced TiO_2 photocatalytic performance is hypothesized to be, in essence, the same for other carbon-TiO_2 structures, such as carbon nanotubes, fullerenes and activated carbon. Specifically, photocatalytic enhancement for these previously studied materials was proposed to result from an increased light absorption range, more pollutant adsorption and decreased recombination of photo-induced holes and electrons.[5, 18] However, how crumpled graphene (in contrast to 2D flat analogs) can specifically alter TiO_2's photocatalytic activity has not been assessed. Here we evaluated the simple photo-degradation of methyl orange, a model organic dye,[32, 42, 43] under a Xeon lamp irradiation (14.4 mW/cm^2 in the effective UV range (250-387 nm)). A typical photo-degradation kinetic analysis, using GOTIM-B as an example material, is shown in Figure 6.3. Although the TiO_2 mass ratio was significantly reduced (TiO_2 wt./total wt.:12.1%) compared to pure TiO_2 (100%); GOTIM-B still outperformed TiO_2 under the same conditions. For example, after a 90 min reaction in the case of 20 mg/L MO and 16 mg/L catalysts, ~ 41 % and ~28 % MO remained in the solution for TiO_2 and GOTIM-B respectively. Consistent with previous reports, agreeable fitting of pseudo first order kinetic parameters suggested a pseudo first order reaction (R^2 = 0.978-0.999) (See S.I. Table S6.1).[21]

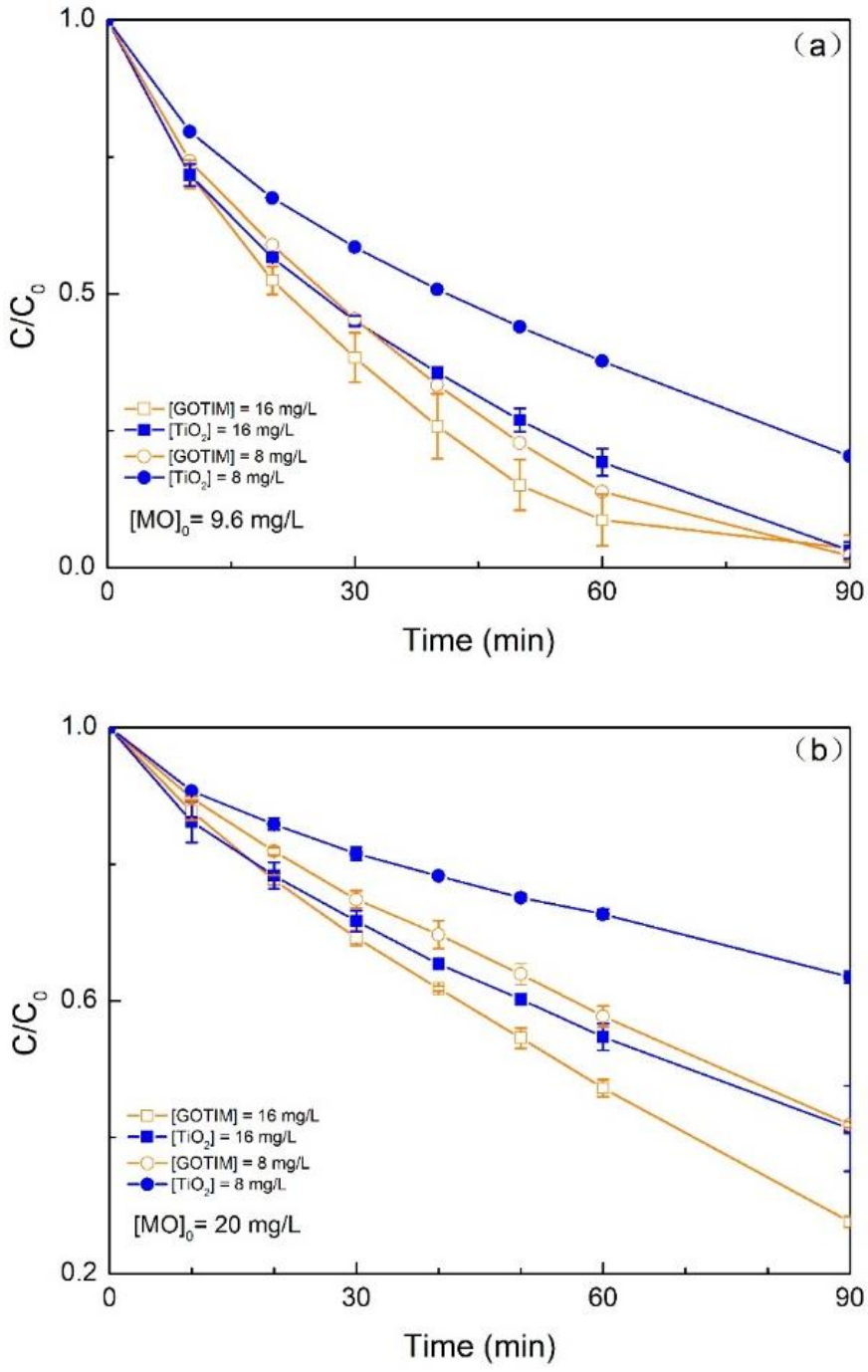

Figure 6.3 Methyl orange concentration (C/C_0) with time in the presence of GOTIM-B and TiO_2 under Xeon lamp irradiation (light intensity = 14.4 mW/cm^2 in the 250-387 nm region) (□: [GOTIM] = 16 mg/L; ■: [TiO_2] = 16 mg/L; ○: [GOTIM] = 8 mg/L; ●: [TiO_2] = 8 mg/L).

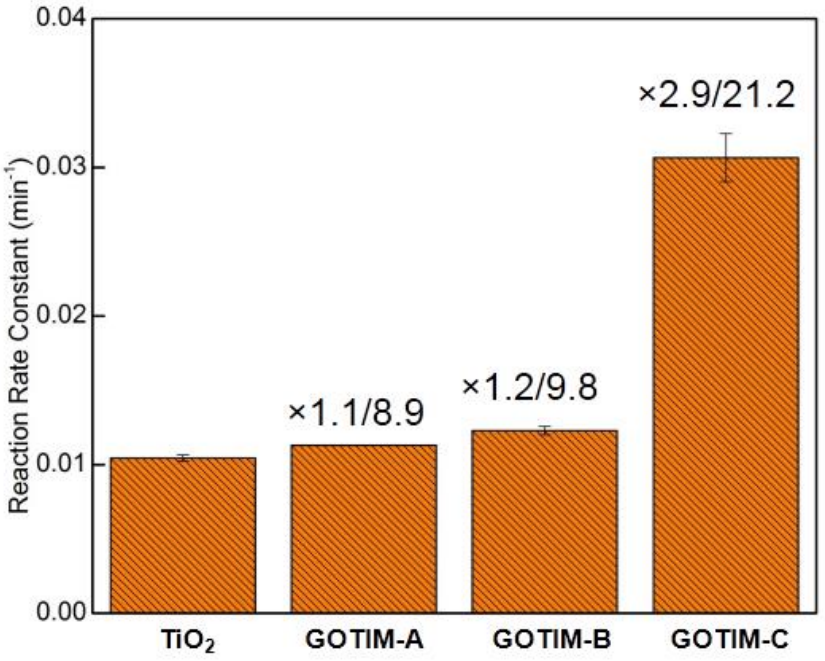

Figure 6.4 Comparison of reaction rate constants of GOTIMs. $[MO]_0$ = 20 mg/L, [Catalyst] = 16 mg/L; light intensity = 14.4 mW/cm^2 (250-387 nm). The enhancement factors in the right were ones normalized by TiO_2 ratios. TiO_2/magnetite ratios are 1.8, 1.9 and 2.7, for GOTIM-A, B, and C, respectively.

The reaction rate constants for TiO_2 and GOTIM are further compared in Figure 6.4. The direct observed enhancement factor for GOTIM-A, -B, and -C are 1.1, 1.2, and 2.9, respectively, when compared to bare TiO_2; while normalized to TiO_2 mass, the enhancement reached a >20 fold enhancement (GOTIM-C), demonstrating (further) enhanced material photocatalytic efficacy. This trend is in well accordance with the TiO_2/magnetite ratios (as calculated from ICP-MS results, 1.8, 1.9 and 2.7 respectively), which implicate the key role of TiO_2 in determining (and engineering) GOTIM photocatalytic performance. Meanwhile, crumpled graphene-TiO_2 (binary GOTI) was found to have a 4.5 times direct enhancement in performance compared with bare TiO_2 (see S.I. Figure S6.4). Such performance enhancement is comparable to recent reports of flat graphene-TiO_2 nanocomposites, which ranges from 2.5 to 8.5 times.[19, 20, 44] In addition,

experimental results also show that increased light intensity (18.8 mW/cm^2 in the effective UV range (250-387 nm)) further enhances the photocatalytic activity in a differential manner – indicating that GOTIM is more sensitive to light intensity than bare TiO_2 (e.g. 2.5 and 1.8 times enhancement for GOTIM-B and TiO_2 respectively with increased light intensity) (see S.I. Figure S6.4).

6.3.3 Reuse and Recovery of GOTIM

The reuse or recyclability, measured by the photo-degradation of methyl orange for consecutive five cycles (t_R= 60 min), was evaluated. After each cycle, specified amount of MO stock solution (500 mg/L) was added to maintain $[MO]_0$ = 10 mg/L at the beginning of each cyclic experiment. For the first cycle, after a 60 min reaction time, 98 % methyl orange was observed to be degraded; and for the fifth cycle, although only 85% remaining (of initial mass) GOTIM-B photocatalyst participated in the reaction (due to 4% sampling loss per cycle), MO removal has still reached to 91 % (see S.I. Figure S6.5), indicating catalytic stability under these conditions. After five cycles, GOTIM-B was separated and collected from the remaining solution by using a handheld, neodymium magnet (Applied Magnets). For the remaining GOTIM-B photocatalyst, ~50-60 % could be recovered with a low magnetic field, which decreased from a > 90% recovery rate before reaction cycling. This may be attributed to the dissolution of iron ions during the reaction[13] (which may undergo redox based reactions in proximity with TiO_2) and is currently being further investigated. Collected (GOTIM-B) nanoparticles did maintain aqueous (monomeric) stability after being redispersed into water (ζ= -30.5 mV).

6.3.4 Enhanced TiO_2-Based Photocatalytic Reduction Pathways

The photocatalyzed, oxidative reaction mechanisms of TiO_2 have been extensively described in literature reports. To summarize, TiO_2 as a semiconductor produces electron-hole pairs upon UV irradiation with energies greater than its band gap (3.2 eV) (Eqn.1).[34] The photo-induced hole-electron pairs are separated in the space-charge layer, and can lead to oxidation and reduction reactions, respectively, due to their strong redox potentials (valence band hole: 2.5 V vs. SCE and conduction band electron: -0.7 V vs. SCE).[42] The photo-induced holes can then directly oxidize pollutant; or oxidize water to produce hydroxyl radicals ($OH^{\cdot}$), whereby indirect oxidation (by $OH^{\cdot}$) takes place (Eqn. 2). Interestingly, when in contact with graphene (in either binary or ternary structures), which exists as an electron acceptor, an overall decrease in recombination kinetics of separated holes and electrons has been observed, leading to increased reactions (availability) of holes and radicals.[18] Direct oxidation by holes and indirect oxidation by formed radicals is widely considered to be the main (oxidation) reaction mechanism for pollutant degradation.[18, 21]

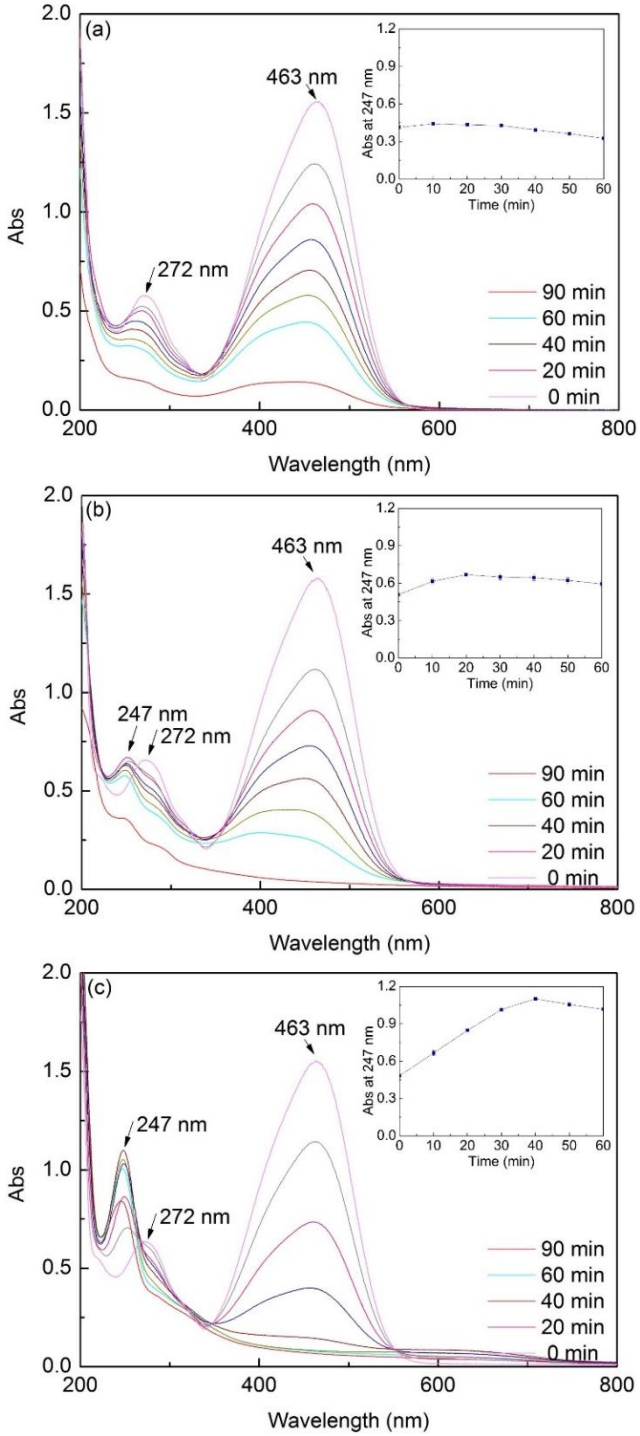

Figure 6.5 Evolution of UV-Vis absorption spectrum of MO with time in the presence of (a) TiO_2 with O_2; (b) GOTIM-B with O_2; and (c) GOTIM-B without O_2. The insets show the evolution of absorbance at 247 nm (MO reduced product concentration), with the highest absorbance for GOTIM-B (c) reaching ca. 3 times that of TiO_2 (a), indicating the potential of GOTIM to also efficiently photocatalyze available reduction pathways. $[MO]_0 = 20$ mg/L; [Catalyst] = 16 mg/L; light intensity = 18.8 mW/cm^2 (250-387 nm).

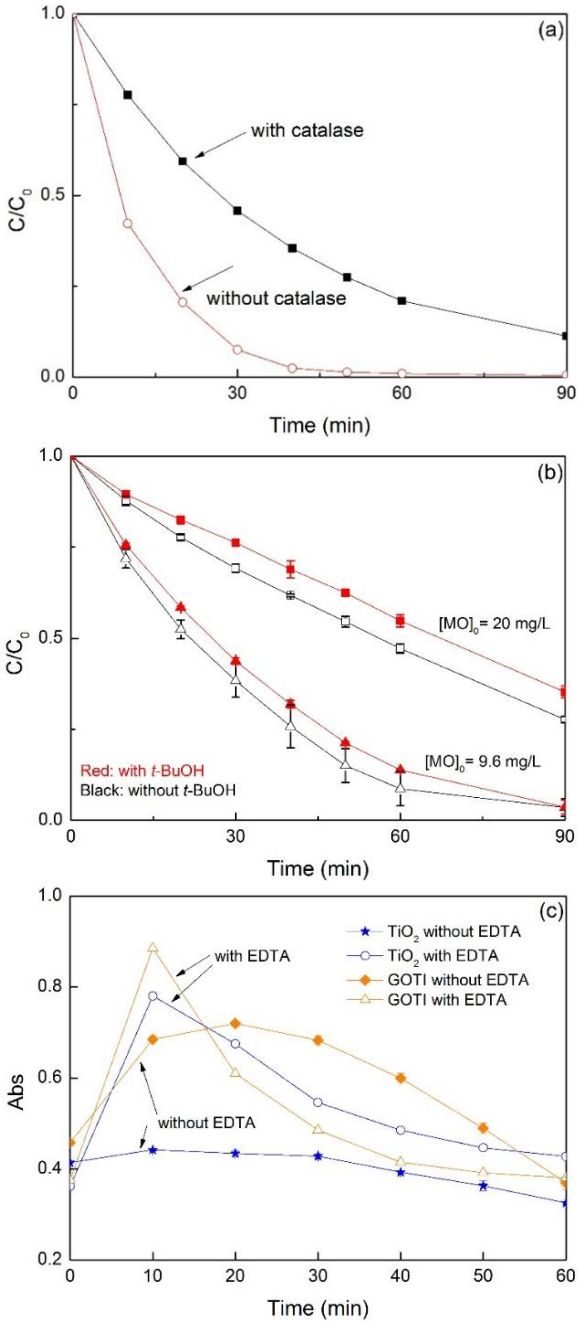

Figure 6.6 Photo-degradation of MO in the presence of scavengers. (a) Evolution of MO concentration (C/C_0, $[MO]_0$ = 20 mg/L) with time in the presence of GOTI (16 mg/L) with/without catalase as a H_2O_2 scavenger (500 units/mL). light intensity = 18.8 mW/cm^2. (b) Evolution of MO concentration (C/C_0) with time in the presence of GOTIM-B (16 mg/L) with/without *t*-BuOH as a hydroxyl radical scavenger (10 mM). light intensity = 14.4 mW/cm^2. (c) Evolution of absorbance at 247 nm with time in the presence of GOTI (16 mg/L) with/without EDTA as a hole scavenger (4 mM). $[MO]_0$ = 20 mg/L, light intensity = 18.8 mW/cm^2.

Compared to oxidation reactions, less attention has been given to the increase in electron production for such systems, which could potentially promote strong reduction reactions for TiO_2-based systems/materials. In this work, methyl orange also serves as probe for resulting reduction reactions based on a more positive reduction potential (-0.28 V vs. SCE) when compared with the conduction band electrons (-0.7 V vs. SCE).[45] Here, it was observed that graphene-TiO_2 has a significantly stronger photocatalytic reduction capacity when compared to pure TiO_2. A new absorption peak (247 nm), characteristic of the reduced product of methyl orange - a hydrazine derivative,[43] appears for irradiated reactions with GOTIM-B; whereas such peak was not obvious for bare irradiated TiO_2 (Figure 6.5a and b) (Eqn. 3). This peak (or concentration of reduced product) was further increased by depleting O_2, as shown in Figure 6.5c. Figure 6.5 insets show the evolution of the reduced product concentration (absorbance at 247 nm) in the first 60 min. The highest absorbance for GOTIM-B (Figure 6.5c inset) reaches ca. 3 times that of TiO_2 (Figure 6.5a inset), indicating the potential of GOTIM to also efficiently photocatalyze available reduction pathways (which was also evidenced by enhancement of photoreduction of CO_2 using crumpled graphene-TiO_2 photocatalyst in our another work[17]). The enhancement of photocatalytic reduction reactions by depleting O_2 suggest a competing role of O_2 with MO for the photo-induced reducing electrons. One electron reduction of O_2 into superoxide anion radical ($O_2^{-\cdot}$) has a redox potential of -0.57 V vs. SCE,[46] which is also more positive than that of conduction band electrons (Eqn. 4). Similar production of $O_2^{-\cdot}$ was also reported in previous research.[18]

Furthermore, $O_2^{-\cdot}$ directly promotes the production of other reactive oxygen species (ROS), such as $HO_2^{\cdot}$, H_2O_2, and $OH^{\cdot}$ (Eqns. 5-7).[42, 47] To further confirm such reaction pathways for this system, a H_2O_2 scavenger, catalase, was employed,[31] which significantly slowed the reaction kinetics compared with no scavenger (Figure 6.6a), implicating peroxide involvement (of MO

degradation) directly or in generation of other ROS species (which can then react). Further experiments with hydroxyl radical scavenger *t*-BuOH ($k_{[t\text{-BuOH} + OH^{\cdot}]} = 5 \times 10^8\ M^{-1}\ s^{-1}$; 10 mM) partially suppressed the degradation of MO as well (Figure 6.6b), suggesting that ROS species (from peroxide degradation or water) are involved in the MO degradation pathway(s) (Eqns 2 and 7).

$$TiO_2 + h\nu \rightarrow TiO_2 + h^+ + e^- \quad (1)$$

$$h^+ + H_2O \rightarrow OH^{\cdot} + H^+ \quad (2)$$

$$(CH_3)_2NC_6H_4N{=}NC_6H_4SO_3^- + 2H^+ + 2e \rightarrow (CH_3)_2NC_6H_4NHNHC_6H_4SO_3^{-\cdot} \quad (3)$$

$$e + O_2 \rightarrow O_2^{-\cdot} \quad (4)$$

$$O_2^{-\cdot} + H^+ \rightarrow HO_2^{\cdot} \quad (5)$$

$$HO_2^{\cdot} + O_2^{-\cdot} + H^+ \rightarrow H_2O_2 + O_2 \quad (6)$$

$$H_2O_2 + e \rightarrow OH^{\cdot} + OH^- \quad (7)$$

The effect of hole scavengers on promoting reduction reactions was evaluated with EDTA which has strong hole scavenging capacity, reacting with holes ca. 19000 times faster than the recombination of holes and electrons.[32] As observed in Figure 6.6c, with the addition of EDTA, the absorbance at 247 nm (indicating reduced product) increased considerably at an earlier time than without EDTA, indicating increased electron availability for MO reductions. These results suggest that by controlling or scavenging holes, higher reduction performance for these materials can be achieved.

Based on these results, we propose two reaction pathways for photo-induced holes and electrons for the described graphene-TiO_2 nanocomposites (S.I. Figure S6.6). Both photocatalytic oxidation and reduction pathways are possible with graphene-TiO_2 based photocatalysts, as described here for the case of methyl orange degradation. Enhanced photocatalytic oxidation

involves both direct oxidation by holes and indirect oxidation by multiple ROS, including $OH^{\cdot}$, $O_2^{-\cdot}$, and H_2O_2. For these materials, reactants such as methyl orange can also compete with O_2 for the reducing electrons, which subsequently leads to (direct) reductive reactions. Such pathways, increasing the production (or availability) of electrons, highlights crumpled graphene-TiO_2 as also a promising effective photocatalytic reductant with potentially wide applicability. Further, such reduction reactions can be engineered (or shifted) through depleting O_2 (or other electron scavengers) and adding hole scavengers, to effect recombination kinetics even further, thus achieving enhancement.

6.4 Conclusions

In summary, this work demonstrates the synthesis of novel ternary crumpled graphene-based nanocomposite platform materials by utilizing pre-synthesized nanoparticles via an aerosol route. Results clearly demonstrate significant material enhancement of TiO_2 photocatalytic performance that is in line (or better) with previously observed 2D graphene/graphene oxide composites. Moreover, as highly water stable, aggregation-resistant 3D structures, GOTIM not only maintains high surface to volume ratios (monomeric) in water, but can also be magnetically recoverable under low magnetic fields, allowing for a number of separation strategies for reuse/recycling. Further, GOTIM also demonstrates significant potential for broad photocatalytic reduction reactions, which could greatly expand the application potentials/processes considered for aqueous based TiO_2-carbon catalysts.

Acknowledgements

The authors thank McDonnell Academy Global Energy and Environment Partnership (MAGEEP), Washington University in St. Louis for funding support. Electron microscopy work was performed at the Nano Research Facility (NRF) at Washington University in St. Louis, a member of the National Nanotechnology Infrastructure Network (NNIN), supported by the National Science Foundation under Grant No. ECS-0335765.

References

1. Wei, C.; Lin, W. Y.; Zainal, Z.; Williams, N. E.; Zhu, K.; Kruzic, A. P.; Smith, R. L.; Rajeshwar, K., Bactericidal Activity of TiO_2 Photocatalyst in Aqueous Media: Toward a Solar-Assisted Water Disinfection System. *Environ. Sci. Technol.* **1994,** *28*, 934-938.
2. Shannon, M. A.; Bohn, P. W.; Elimelech, M.; Georgiadis, J. G.; Marinas, B. J.; Mayes, A. M., Science and Technology for Water Purification in the Coming Decades. *Nature* **2008,** *452*, 301-310.
3. Long, Y.; Lu, Y.; Huang, Y.; Peng, Y.; Lu, Y.; Kang, S.-Z.; Mu, J., Effect of C60 on the Photocatalytic Activity of TiO_2 Nanorods. *J. Phys. Chem. C* **2009,** *113*, 13899-13905.
4. Woan, K.; Pyrgiotakis, G.; Sigmund, W., Photocatalytic Carbon-Nanotube-TiO_2 Composites. *Adv. Mater.* **2009,** *21*, 2233-2239.
5. Zhang, H.; Lv, X. J.; Li, Y. M.; Wang, Y.; Li, J. H., P25-Graphene Composite as a High Performance Photocatalyst. *ACS Nano* **2010,** *4*, 380-386.
6. Luo, J.; Jang, H. D.; Sun, T.; Xiao, L.; He, Z.; Katsoulidis, A. P.; Kanatzidis, M. G.; Gibson, J. M.; Huang, J., Compression and Aggregation-Resistant Particles of Crumpled Soft Sheets. *ACS Nano* **2011,** *5*, 8943-8949.

7. Ma, X.; Zachariah, M. R.; Zangmeister, C. D., Crumpled Nanopaper from Graphene Oxide. *Nano Lett.* **2012,** *12*, 486-489.
8. Wang, W.-N.; Jiang, Y.; Biswas, P., Evaporation-Induced Crumpling of Graphene Oxide Nanosheets in Aerosolized Droplets: Confinement Force Relationship. *J. Phys. Chem. Lett.* **2012,** *3*, 3228-3233.
9. Wang, Y.; Wu, Y.; Huang, Y.; Zhang, F.; Yang, X.; Ma, Y.; Chen, Y., Preventing Graphene Sheets from Restacking for High-Capacitance Performance. *J. Phys. Chem. C* **2011,** *115*, 23192-23197.
10. Yang, X.; Zhu, J.; Qiu, L.; Li, D., Bioinspired Effective Prevention of Restacking in Multilayered Graphene Films: Towards the Next Generation of High-Performance Supercapacitors. *Adv. Mater.* **2011,** *23*, 2833-2838.
11. Mao, S.; Wen, Z.; Kim, H.; Lu, G.; Hurley, P.; Chen, J., A General Approach to One-Pot Fabrication of Crumpled Graphene-Based Nanohybrids for Energy Applications. *ACS Nano* **2012,** *6*, 7505-7513.
12. Chen, Y.; Guo, F.; Jachak, A.; Kim, S.-P.; Datta, D.; Liu, J.; Kulaots, I.; Vaslet, C.; Jang, H. D.; Huang, J.; Kane, A.; Shenoy, V. B.; Hurt, R. H., Aerosol Synthesis of Cargo-Filled Graphene Nanosacks. *Nano Lett.* **2012,** *12*, 1996-2002.
13. Chen, Y.; Guo, F.; Qiu, Y.; Hu, H.; Kulaots, I.; Walsh, E.; Hurt, R. H., Encapsulation of Particle Ensembles in Graphene Nanosacks as a New Route to Multifunctional Materials. *ACS Nano* **2013,** *7*, 3744-3753.
14. Luo, J.; Zhao, X.; Wu, J.; Jang, H. D.; Kung, H. H.; Huang, J., Crumpled Graphene-Encapsulated Si Nanoparticles for Lithium Ion Battery Anodes. *J. Phys. Chem. Lett.* **2012,** *3*, 1824-1829.

15. Jang, H. D.; Kim, S. K.; Chang, H.; Choi, J.-W.; Luo, J.; Huang, J., One-Step Synthesis of Pt-Nanoparticles-Laden Graphene Crumples by Aerosol Spray Pyrolysis and Evaluation of Their Electrocatalytic Activity. *Aerosol Sci. Technol.* **2012,** *47*, 93-98.
16. Jang, H. D.; Kim, S. K.; Chang, H.; Roh, K.-M.; Choi, J.-W.; Huang, J., A Glucose Biosensor Based on TiO_2–Graphene Composite. *Biosens. Bioelectron.* **2012,** *38*, 184-188.
17. Wang, W.-N.; Jiang, Y.; Fortner, J. D.; Biswas, P., Nanostructured Graphene-Titanium Dioxide Composites Synthesized by a Single Aerosol Process for Photoreduction of Carbon Dioxide. *Environ. Eng. Sci.* **2014,** DOI: 10.1089/ees.2013.0473.
18. Zhang, Y.; Tang, Z.-R.; Fu, X.; Xu, Y.-J., TiO_2−Graphene Nanocomposites for Gas-Phase Photocatalytic Degradation of Volatile Aromatic Pollutant: Is TiO_2−Graphene Truly Different from Other TiO_2−Carbon Composite Materials? *ACS Nano* **2010,** *4*, 7303-7314.
19. Guo, J.; Zhu, S.; Chen, Z.; Li, Y.; Yu, Z.; Liu, Q.; Li, J.; Feng, C.; Zhang, D., Sonochemical Synthesis of TiO_2 Nanoparticles on Graphene for Use as Photocatalyst. *Ultrason. Sonochem.* **2011,** *18*, 1082-1090.
20. Nguyen-Phan, T.-D.; Pham, V. H.; Shin, E. W.; Pham, H.-D.; Kim, S.; Chung, J. S.; Kim, E. J.; Hur, S. H., The Role of Graphene Oxide Content on the Adsorption-enhanced Photocatalysis of Titanium Dioxide/Graphene Oxide Composites. *Chem. Eng. J.* **2011,** *170*, 226-232.
21. Pastrana-Mart ńez, L. M.; Morales-Torres, S.; Likodimos, V.; Figueiredo, J. L.; Faria, J. L.; Falaras, P.; Silva, A. M. T., Advanced Nanostructured Photocatalysts Based on Reduced Graphene Oxide–TiO_2 Composites for Degradation of Diphenhydramine Pharmaceutical and Methyl Orange Dye. *Appl. Catal., B* **2012,** *123–124*, 241-256.

22. Selli, E.; Eliet, V.; Spini, M. R.; Bidoglio, G., Effects of Humic Acids on the Photoinduced Reduction of U(VI) in the Presence of Semiconducting TiO_2 Particles. *Environ. Sci. Technol.* **2000,** *34*, 3742-3748.
23. Selli, E.; De Giorgi, A.; Bidoglio, G., Humic Acid-Sensitized Photoreduction of Cr(VI) on ZnO Particles. *Environ. Sci. Technol.* **1996,** *30*, 598-604.
24. Kyung, H.; Lee, J.; Choi, W., Simultaneous and Synergistic Conversion of Dyes and Heavy Metal Ions in Aqueous TiO_2 Suspensions under Visible-Light Illumination. *Environ. Sci. Technol.* **2005,** *39*, 2376-2382.
25. Vinu, R.; Madras, G., Kinetics of Simultaneous Photocatalytic Degradation of Phenolic Compounds and Reduction of Metal Ions with Nano-TiO_2. *Environ. Sci. Technol.* **2007,** *42*, 913-919.
26. Schmelling, D. C.; Gray, K. A.; Kamat, P. V., Role of Reduction in the Photocatalytic Degradation of TNT. *Environ. Sci. Technol.* **1996,** *30*, 2547-2555.
27. Wang, W.-N.; An, W.-J.; Ramalingam, B.; Mukherjee, S.; Niedzwiedzki, D. M.; Gangopadhyay, S.; Biswas, P., Size and Structure Matter: Enhanced CO_2 Photoreduction Efficiency by Size-Resolved Ultrafine Pt Nanoparticles on TiO_2 Single Crystals. *J. Am. Chem. Soc.* **2012,** *134*, 11276-11281.
28. Hummers, W. S.; Offeman, R. E., Preparation of Graphitic Oxide. *J. Am. Chem. Soc.* **1958,** *80*, 1339-1339.
29. Ma, J.; Graham, N. J. D., Degradation of Atrazine by Manganese-Catalysed Ozonation-Influence of Radical Scavengers. *Water Res.* **2000,** *34*, 3822-3828.

30. Fortner, J. D.; Kim, D.-I.; Boyd, A. M.; Falkner, J. C.; Moran, S.; Colvin, V. L.; Hughes, J. B.; Kim, J.-H., Reaction of Water-Stable C60 Aggregates with Ozone. *Environ. Sci. Technol.* **2007,** *41*, 7497-7502.

31. Sarathy, S. R.; Mohseni, M., The Impact of UV/H_2O_2 Advanced Oxidation on Molecular Size Distribution of Chromophoric Natural Organic Matter. *Environ. Sci. Technol.* **2007,** *41*, 8315-8320.

32. Mills, A.; Williams, G., Methyl Orange as a Probe of the Semiconductor-Electrolyte Interfaces in CdS Suspensions. *J. Chem. Soc., Faraday Trans. 1* **1987,** *83*, 2647-2661.

33. Li, D.; Muller, M. B.; Gilje, S.; Kaner, R. B.; Wallace, G. G., Processable Aqueous Dispersions of Graphene Nanosheets. *Nat. Nanotechnol.* **2008,** *3*, 101-105.

34. Williams, G.; Seger, B.; Kamat, P. V., TiO_2-Graphene Nanocomposites. UV-Assisted Photocatalytic Reduction of Graphene Oxide. *ACS Nano* **2008,** *2*, 1487-1491.

35. Muszynski, R.; Seger, B.; Kamat, P. V., Decorating Graphene Sheets with Gold Nanoparticles. *J. Phys. Chem. C* **2008,** *112*, 5263-5266.

36. Yang, X.; Zhang, X.; Ma, Y.; Huang, Y.; Wang, Y.; Chen, Y., Superparamagnetic Graphene Oxide-Fe_3O_4 Nanoparticles Hybrid for Controlled Targeted Drug Carriers. *J. Mater. Chem.* **2009,** *19*, 2710-2714.

37. Chandra, V.; Park, J.; Chun, Y.; Lee, J. W.; Hwang, I.-C.; Kim, K. S., Water-Dispersible Magnetite-Reduced Graphene Oxide Composites for Arsenic Removal. *ACS Nano* **2010,** *4*, 3979-3986.

38. Larciprete, R.; Fabris, S.; Sun, T.; Lacovig, P.; Baraldi, A.; Lizzit, S., Dual Path Mechanism in the Thermal Reduction of Graphene Oxide. *J. Am. Chem. Soc.* **2011,** *133*, 17315-17321.

39. Park, S.; Dikin, D. A.; Nguyen, S. T.; Ruoff, R. S., Graphene Oxide Sheets Chemically Cross-Linked by Polyallylamine. *J. Phys. Chem. C* **2009,** *113*, 15801-15804.

40. Sakthivel, S.; Kisch, H., Daylight Photocatalysis by Carbon-Modified Titanium Dioxide. *Angew. Chem. Int. Ed.* **2003,** *42*, 4908-4911.

41. Chen, D.; Zhang, H.; Liu, Y.; Li, J., Graphene and its derivatives for the development of solar cells, photoelectrochemical, and photocatalytic applications. *Energy Environ. Sci.* **2013,** *6*, 1362-1387.

42. Li, W.; Li, D.; Xian, J.; Chen, W.; Hu, Y.; Shao, Y.; Fu, X., Specific Analyses of the Active Species on $Zn_{0.28}Cd_{0.72}S$ and TiO_2 Photocatalysts in the Degradation of Methyl Orange. *J. Phys. Chem. C* **2010,** *114*, 21482-21492.

43. Brown, G. T.; Darwent, J. R., Photoreduction of Methyl Orange Sensitized by Colloidal Titanium Dioxide. *J. Chem. Soc., Faraday Trans. 1* **1984,** *80*, 1631-1643.

44. Jiang, G.; Lin, Z.; Chen, C.; Zhu, L.; Chang, Q.; Wang, N.; Wei, W.; Tang, H., TiO_2 Nanoparticles Assembled on Graphene Oxide Nanosheets with High Photocatalytic Activity for Removal of Pollutants. *Carbon* **2011,** *49*, 2693-2701.

45. Yu, L.; Xi, J.; Li, M.-D.; Chan, H. T.; Su, T.; Phillips, D. L.; Chan, W. K., The Degradation Mechanism of Methyl Orange Under Photo-catalysis of TiO_2. *Phys. Chem. Chem. Phys.* **2012,** *14*, 3589-3595.

46. Wood, P. M., The Two Redox Potentials for Oxygen Reduction to Superoxide. *Trends Biochem. Sci.* **1987,** *12*, 250-251.

47. Deo, M.; Shinde, D.; Yengantiwar, A.; Jog, J.; Hannoyer, B.; Sauvage, X.; More, M.; Ogale, S., Cu_2O/ZnO Hetero-Nanobrush: Hierarchical Assembly, Field Emission and Photocatalytic Properties. *J. Mater. Chem.* **2012,** *22*, 17055-17062.

Chapter 6 Supporting Information

Figure S6.1. HR-TEM image of as-synthesized GOTIM nanocomposites

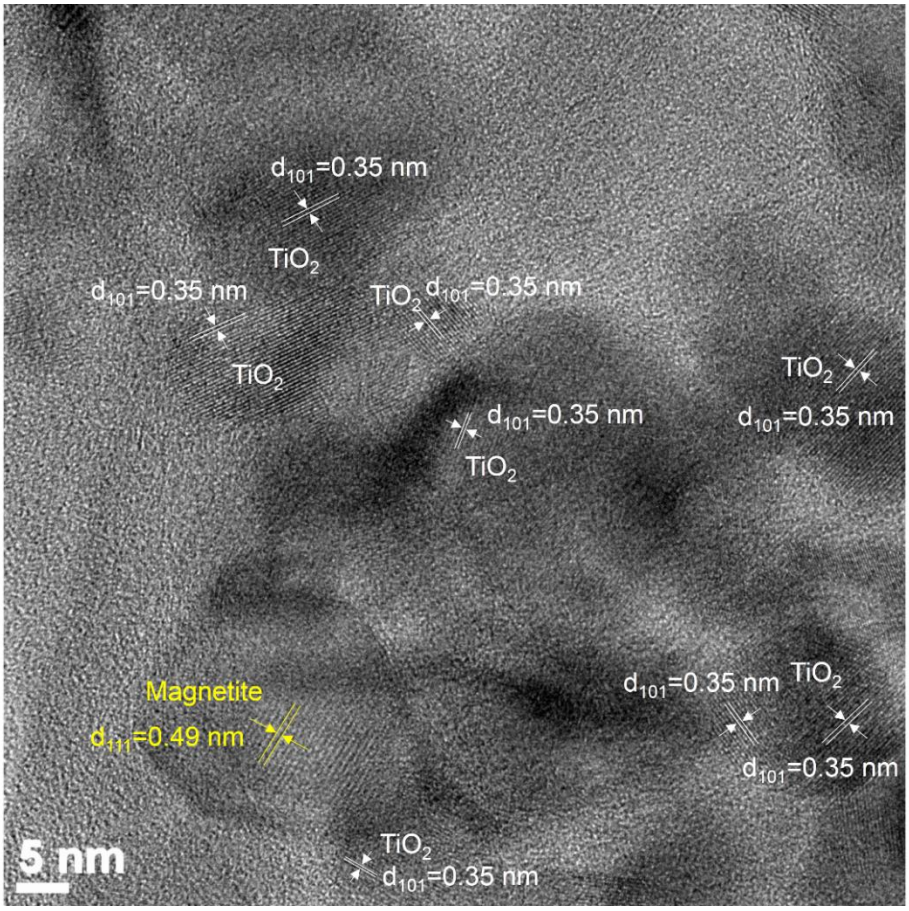

Figure S6.2. XRD patterns of GOTIM and CGO

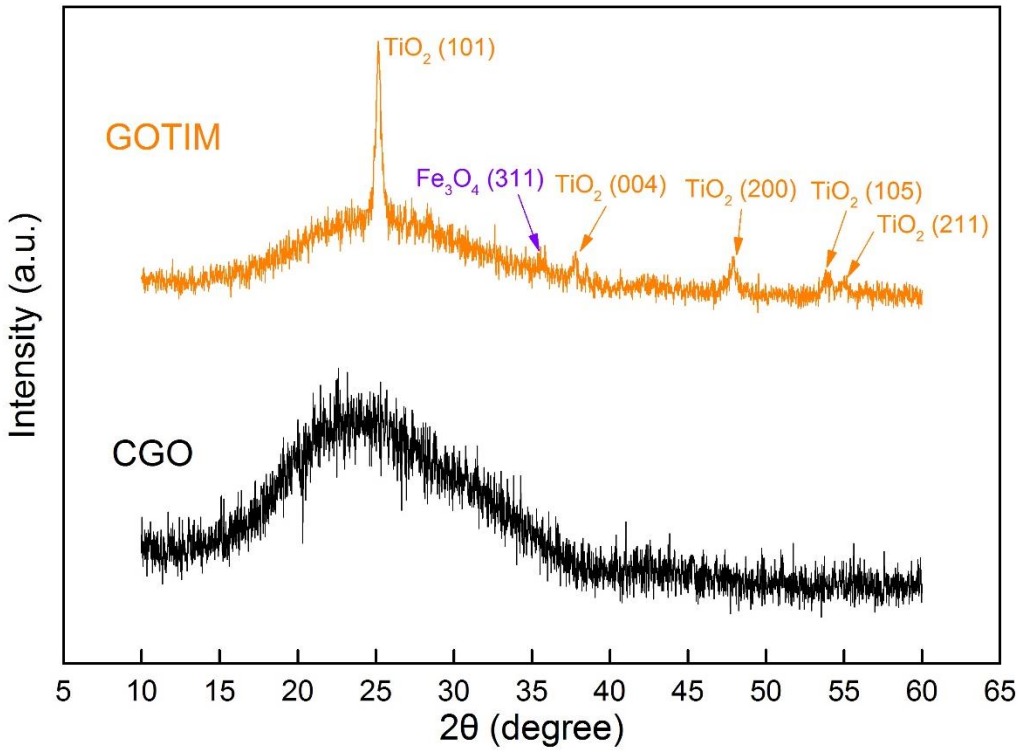

Figure S6.3. UV-Vis absorption spectrum of TiO_2, GOTIM-A, GOTIM-B, GOTIM-C, GOTI and also crumpled graphene-magnetite (GOM) (20 mg/L).

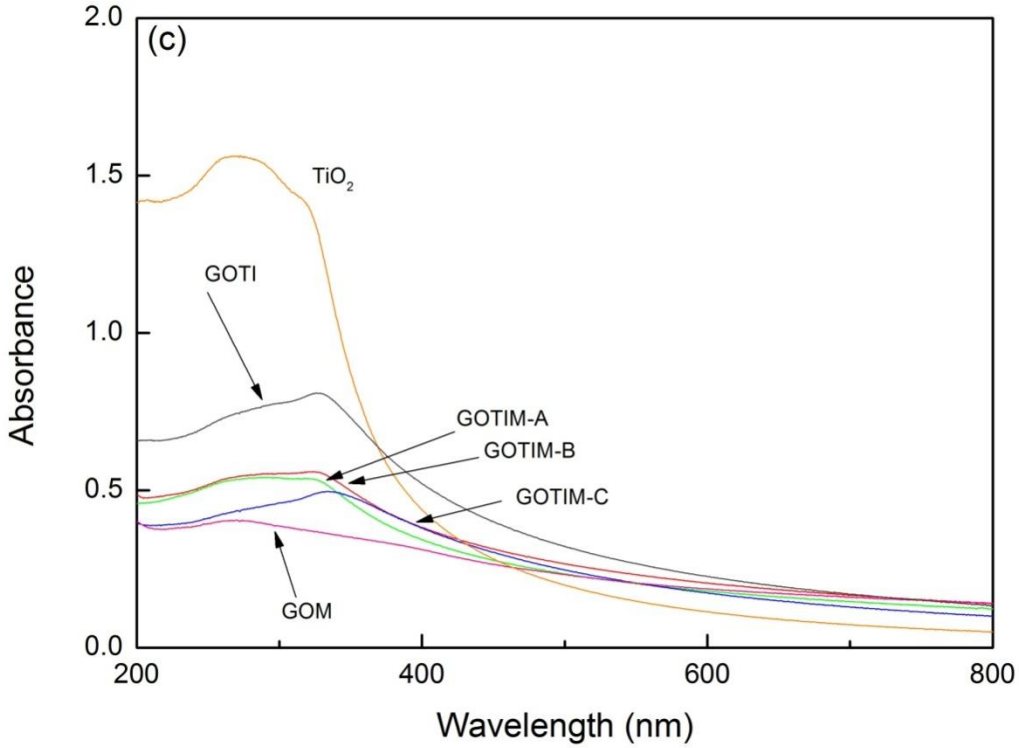

Figure S6.4. Comparison of reaction rate constants of TiO_2, GOTIM-B, and GOTI under increased light intensity (18.8 mW/cm^2 (250-387 nm). $[MO]_0$ = 20 mg/L, [Catalyst] = 16 mg/L.

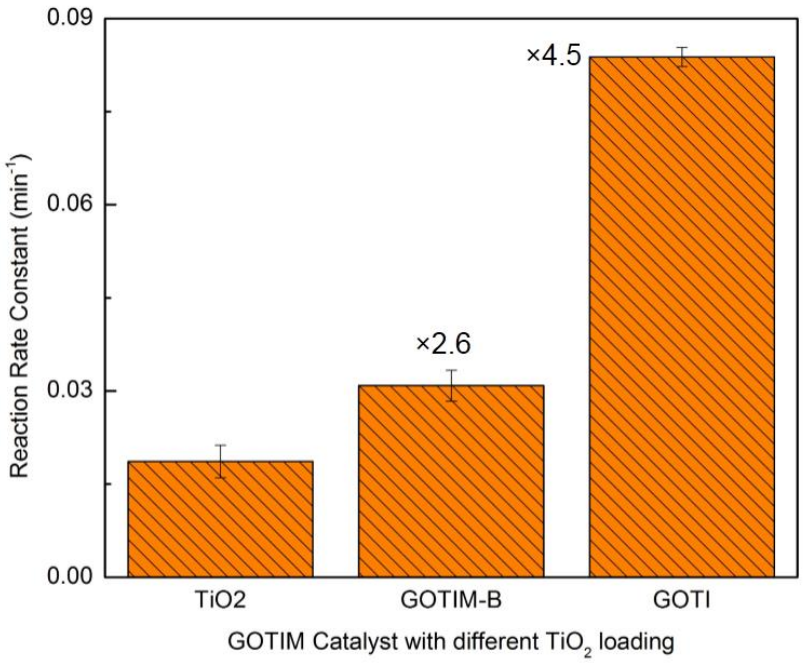

Figure S6.5. Cyclic photo-degradation of MO using GOTIM-B. $[MO]_0$ = 10 mg/L, [GOTIM-B] = 20 mg/L, light intensity = 18.8 mW/cm^2, and t_R = 60 min.

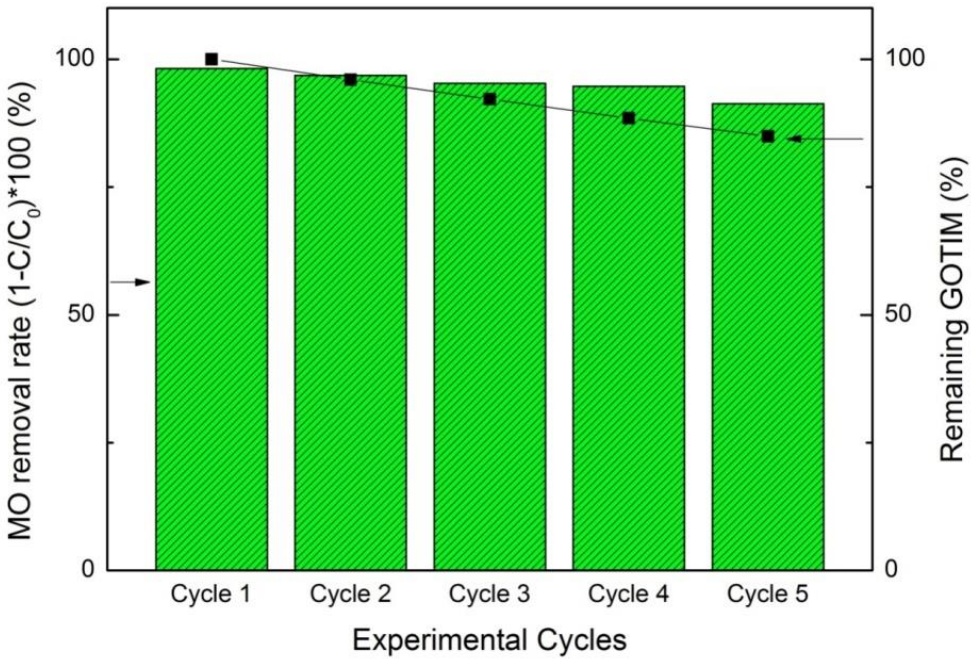

Figure S6.6. Proposed main reaction pathways for photo-induced holes and electrons.

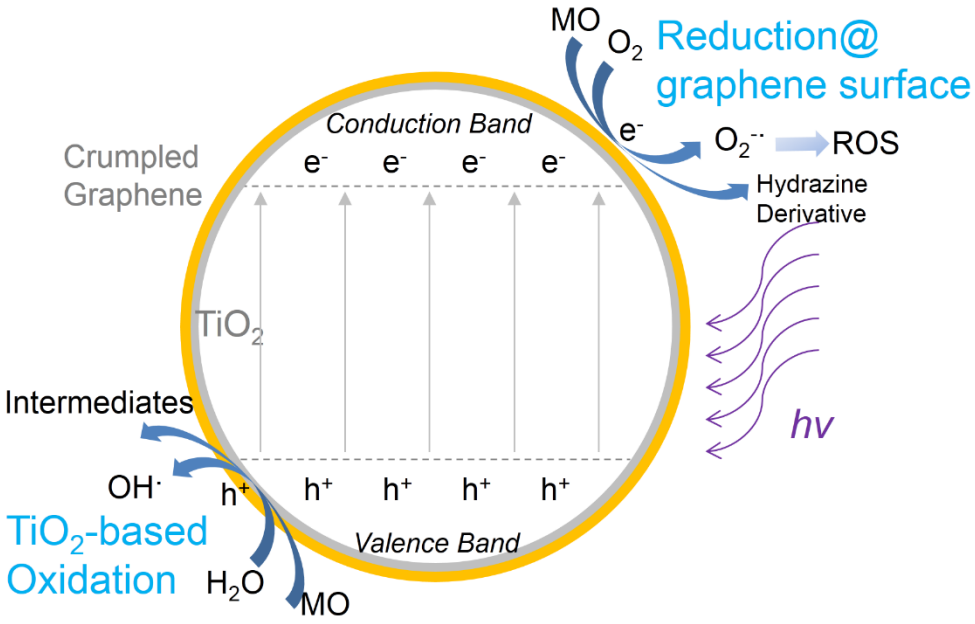

Table S6.1. Pseudo First Order Kinetics for MO Photo-degradation in the first 60 min (shadowed for GOTIM, blank for TiO_2)

$[MO]_0$ (mg/L)	[Catalyst] (mg/L)	Pseudo First Order Kinetics	Rate Constant (min^{-1})	R^2
20	16	$\ln(C_0/C)=0.0123t$	0.0123	0.999
20	16	$\ln(C_0/C)=0.0104t$	0.0104	0.983
20	8	$\ln(C_0/C)=0.0092t$	0.0094	0.996
20	8	$\ln(C_0/C)=0.0059t$	0.0059	0.936
9.6	16	$\ln(C_0/C)=0.0374t$	0.0374	0.978
9.6	16	$\ln(C_0/C)=0.0268t$	0.0268	0.995
9.6	8	$\ln(C_0/C)=0.0360t$	0.0301	0.980
9.6	8	$\ln(C_0/C)=0.0168t$	0.0168	0.986

Chapter 7. Engineered Crumpled Graphene Oxide Nanocomposite Membrane Assemblies for Advanced Water Treatment Processes

Abstract

In this work, we describe multifunctional, crumpled graphene oxide (CGO) porous nanocomposites that are assembled as advanced, reactive water treatment membranes. Crumpled 3D graphene oxide based materials fundamentally differ from 2D flat graphene oxide analogues in that they are highly aggregation and compression-resistant (*i.e.* π - π stacking resistant) and allow for the incorporation (wrapping) of other, multifunctional particles inside the 3D, composite structure. Here, assemblies of nanoscale, monomeric CGO with encapsulated (as a quasi core-shell structure) TiO_2 (GOTI) and Ag (GOAg) nanoparticles, not only allow high water flux via vertically tortuous nanochannels (achieving water flux of 246 ± 11 L/(m^2·h·bar) with 5.4 μm thick assembly, 7.4 g/m^2), outperforming comparable commercial ultrafiltration membranes, but also demonstrates excellent separation efficiencies for model organic and biological foulants. Further, multifunctionality is demonstrated through the in situ photocatalytic degradation of methyl orange (MO), as a model organic, under fast flow conditions (t_{res} < 0.1 s); while superior antimicrobial properties, evaluated with GOAg, were observed for both biofilm (contact) and suspended growth scenarios (> 3 log effective removal, *Escherichia coli*). This is the first demonstration of 3D, crumpled graphene oxide based nanocomposite structures applied specifically as (re)active membrane assemblies and highlights the material's platform potential for a truly tailored approach for next generation water treatment and separation technologies.

7.1 Introduction

In line with the rapid expansion and application of material science and nanoscale engineering over the last three decades, water treatment technologies have experienced significant material-based advancements. Such technologies include, among others, engineered photocatalysts for the degradation of pollutants and inactivation of pathogens, as well as advanced membranes for physical and chemical separations.[1, 2] More recently, treatment technologies incorporating engineered carbon nanomaterials, such as graphene (oxide), carbon nanotubes (CNTs) and fullerenes, have demonstrated superior and even unique physical and chemical properties compared to traditional analogues.[2] In particular, graphene (oxide) holds considerable potential for broad use in a variety of water treatment applications, including sorption,[3, 4] separation,[5] antimicrobial,[6] and catalysis.[7, 8] Recent progress in crumpling graphene (oxide) into 3D structures has made this end-point even more attractive,[9-11] as 3D crumpled graphene gives rise to *aggregation- and compression-resistant* material properties, while maintaining the high specific surface area and electronic properties of the 2D flat material analogues.[12, 13]

Traditional water treatment membranes manufactured from polymeric materials are designed either as a size-selective sieve or a dense physical barrier, permitting the transport of solutes based on size or differences in diffusion/deposition rates.[14] Membrane design has typically been optimized to balance water permeability with separation specificity, including pathogens, molecules and ionic retentates. In contrast to conventional, passive membrane technologies, (re)active membranes are designed and engineered to promote simultaneous filtration and pathogen inactivation/pollutant destruction.[14, 15] Such strategies usually incorporate functional materials into/onto traditional membranes, including Ag[15-17] and carbon nanomaterials[18, 19] for

pathogen inactivation, and zero valent iron,[20] iron ions (Fe^{2+})[14] and TiO_2[21] for pollutant transformation/destruction.

Engineered graphene and graphene oxide have demonstrated significant potential for ultrathin, ultrafast, and yet precise sieving membranes for gas and (aqueous) ions.[5,22-24] Further, graphene / graphene oxide potential as a reaction platform (large specific surface area and outstanding electronic properties), particularly for catalysis, has also been broadly described in numerous reports.[7, 11, 25] Recent observations of intrinsic antimicrobial material properties further highlight graphene based materials potential for (antimicrobial/fouling-resistant) water treatment membranes.[19, 26-29] Previously described (flat) GO membranes have shown ca. 4-10 times higher flux than that of commercial nanofiltration membranes,[30] while also demonstrating inactivation of 65% *Escherichia coli (E. coli)* after 1 h surface contact.[19]

Compared to flat GO, *crumpled* GO (CGO) nanostructures, which are structurally 3D as demonstrated in our previous work,[10, 11, 31] allow for facile, controlled encapsulation of functional nanoparticles (within the CGO structure) while remaining intrinsically porous. As a function of synthesis conditions, CGO structures have inherent physical defects (vacancies/holes), with high ridges and low valleys, readily forming nanoscale channels for potential fast water transport and permeation. Meanwhile, CGO nanocomposites containing functional nanoparticles (*e.g.*, $nTiO_2$ and nAg) allow for the rational design of system reactivities (*e.g.* surface chemistry, photo-reactivity, antimicrobial activity, etc.) for targeted application(s).

In this work, functional CGO nanocomposites as thin film, membrane assemblies are demonstrated to be superhydrophilic, selective at the nanoscale, (photo)reactive and highly antimicrobial. CGO based membranes, with abundant hydrophilic functional groups (such as -OH and -COOH groups) show high water permeability (246 ± 11 L/(m^2·h·bar)) (with deposited mass

of 7.4 g/m^2), outperforming most commercial ultrafiltration membranes with similar rejection performance. Filtration experiments and characterization results indicate assembled CGO membranes have an average effective pore size less than 10 nm, making it suitable to remove macromolecular organic, colloidal and biological constituents, through size exclusion, depth filtration and possible surface charge based mechanisms. Further, membrane surface layers composed of GOAg showed complete (> 99.9%) inactivation of *E. coli*, not only on the membrane surface, but also in the aqueous bulk phase, at a significantly higher level than pristine CGO/GO surfaces and controls. For GOTI based membrane assemblies, photo-reactivity (in terms of methyl orange (MO) degradation), was demonstrated even under fast flow (t_{res} < 0.1 s) and low intensity UV LED light irradiation conditions, achieving enhancement in both average flux and removal rate of a model organic (MO). This is the first demonstration of CGO composite structures applied as advanced membrane assemblies, and highlights the material's platform potential for a truly tailored approach for next generation water treatment and separation technologies.

7.2 Materials and Methods

7.2.1 CGO Nanocomposites Synthesis

GO was synthesized using the modified Hummer's method[32] as reported in our previous work.[10] An aerosol method, which utilizes rapid water evaporation-induced confinement force to crumple GO and encapsulate nanoparticles (NPs), was used to obtain CGO nanocomposites. Briefly, TiO_2 (Evonik Degussa Aerodisp 740X) or Ag (Sigma Aldrich) NPs and GO precursor mixture (with certain weight ratios) was sprayed into μm-sized water droplets and carried by N_2 into a tube furnace maintained at 400 ℃. During the flight in the furnace, GO became crumpled under the evaporation-induced confinement force (and partially thermally reduced), and

effectively encapsulated TiO_2 or Ag NPs, forming robust core-shell nanostructures.[11] As formed, nanocomposites were collected downstream of the reactor using a membrane filter (Millipore), weighed and dispersed into water to obtain 200 mg/L dispersion (experimental details in Supporting Information).

7.2.2 CGO Nanocomposite Characterization

The ζ-potential and hydrodynamic diameter of aqueous CGO nanocomposites were measured using a Zetasizer Nano ZS (Malvern Instruments). The morphology and size were examined by field emission scanning electron microscopy (FESEM, NOVA NanoSEM 230) and transmission electron microscopy (TEM, Tecnai TM Spirit). To quantify metal compositions, CGO nanocomposites were digested in concentrated HNO_3 and HCl (v:v = 3:1) at 100 ℃ for 10 h. The resulted solution was then filtered (TISCH, PES 20 nm) and diluted properly for inductively coupled plasma mass spectrometry (ICP-MS, Agilent 7500cc) analysis. CGO functionality and C-C bonding were investigated by Fourier transform infrared spectroscopy (FTIR, Nicolette Nexus 470) and Raman scattering (Renishaw InVia Reflex confocal Raman spectrometer with a 514 nm laser).

7.2.3 Membrane Fabrication

To enhance CGO assembly stability as a membrane, polyallylamine (PAA, Sigma Aldrich, Mw ~ 12000, 20 wt. % in H_2O, ρ =1.02 g/mL) was employed to cross-link CGO nanocomposites.[33] CGO nanocomposites (in 200 mg/L aqueous dispersion) and PAA mixture (6 mg CGO/150 μL PAA, 12 mg CGO/300 μL PAA, and 20 mg CGO/500 μL PAA) were sonicated for 3 h before being vacuum filtered onto a polyethersulfone (PES) support membrane (Sterlitech, nominal pore size 20 nm as provided by the manufacture, the observed pore size examined by SEM is described later) at a low flow rate (~0.3 mL/min). Membranes deposited with GOTI (6 mg) and GOAg (3

mg) nanocomposites were investigated for their photo-reactivity and antimicrobial properties, respectively, as described in the following sections, with blank PES membranes used as a control. The PES membrane was also soaked in 1% PAA aqueous solution for 3 h before the deposition. The final membrane assembly was then air-dried and used in subsequent characterization and performance evaluation experiments.

7.2.4 Membrane Characterization

Membrane surface morphology was investigated by FESEM (NOVA NanoSEM 230). Before imaging, membranes were spin-coated with gold for 60 s (Headway PWM32-PS-CB15PL). Membrane surface roughness was studied using an atomic force microscopy (AFM, Veeco NanoMan) in a tapping mode (spring constant of 40 N/m, resonance frequency of 325 kHz, tip radius of 8 nm, and a cantilever dimension of $125(L) \times 30(W) \times 4(H)$ μm). In addition, the PES support membrane and cross-linked CGO surface layer were also studied using FTIR and Raman spectroscopy (Renishaw inVia). Membrane surface hydrophilicity was studied by measuring water contact angle using a sessile drop method (VCA-2500 XE, AST products).

7.2.5 Membrane Permeability and Rejection Test

Permeability experiments were conducted for the as-synthesized membrane coupons under a direct flow and constant pressure dead-end filtration mode, while directly measuring the permeated water flux. Solutions in the storage tank (Millipore Amicon 8050) were pressurized by N_2 at 1 bar and connected to the filter holder (47 mm, Pall Life Science) which assembled membranes were placed into. Permeate was measured over time (thus flux) by an integrated electronic balance (Mettler Toledo ML1502E) with data automatically logged at 30 s intervals. Membrane rejection properties were evaluated by filtering two model contaminants, methyl orange (MO, 7.5 mg/L, M_w= 327.3 Da, Sigma Aldrich) and bovine serum albumin (BSA, 10 mg/L, M_w

=~ 66.5 kDa, Sigma Aldrich) as done by others.[34] The concentrations of MO and BSA were analyzed using a UV-vis spectrophotometer (Varian Bio 50) at wavelengths of 463 and 220 nm, respectively. The rejection rate R equals,

$$R = (1 - \frac{C_P}{C_F}) \times 100\%$$

whereby C_P and C_F are the concentrations in the permeate and feed water, respectively.

7.2.6 Membrane Antimicrobial Activity Test

To evaluate release of Ag^+, GOAg membranes were placed in 25 mL water and mildly shaked at a rate of 60 min^{-1}. Each 24 h, the water was replaced by fresh MilliQ water. The replaced water was acidified by HNO_3 and analyzed by ICP-MS to determine Ag^+ concentration.

The membrane antimicrobial activity was evaluated regarding bacterial inactivation using a standard plate counting method.[19, 35] Briefly, 400 µL *E. coli* K12 (ATCC 700926) suspension (10^7 CFU/mL) was contacted with the active side of membrane surface (4.3 cm^2) for 2 h at room temperature. After 2 h, the upper suspension was sampled (bulk phase) and then removed, and the membrane coupons were then washed with a 0.9% sterile saline solution. To measure *E. coli* viability on the surface (direct contact), the membrane coupons were then bath sonicated mildly for 7 min to remove the bacteria from the membrane surface according to a protocol reported previously.[15, 19] For all, resulting suspensions were spread onto LB agar plates (10 g/L bacto-tryptone, 5 g/L yeast extract, 10 g/L NaCl, 15 g/L agar) and incubated overnight at 37 ℃ before counting.

The ability of *E. coli* to grow in the presence of GOAg in a batch, suspended system, was studied in a minimal media (minimal Davis media with 10% of the recommended potassium phosphate) with glucose as the carbon and electron source (1 g/L).[36] Cell growth (10^7 #/mL, in the

presence of 0, 0.4, 4, 10 mg/L GOAg) was monitored for 24 h by measuring absorbance at 600 nm continuously (OD600) on an Infinite F200PRO (TECAN) plate reader.

7.2.7 Membrane Photo-reactivity Test

Photo-reactivity of GOTI membrane assemblies was evaluated by degradation of MO in both flow-through and batch modes. For flow-through evaluation, a customized filter holder modified with 10 UV LED lights (NSPU510CS, Nichia Corp., with peak wavelength 375 nm and operated at 3.6 V) was used. 180 mL 7.5 mg/L MO was filtered under 0.28 bar (4 psi) both with and without UV irradiation. The MO concentration in the outflow tank was monitored constantly, and the total flux / time was recorded. For batch mode, as-described membrane assemblies were placed into a quartz reactor and irradiated with UV light irradiation, which is centered at 351 nm at an intensity of 900 $\mu w/cm^2$ over described time (details in Supporting Information Figure S7.2).

7.3 Results and Discussion

7.3.1 CGO Nanocomposites Synthesis and Characterization

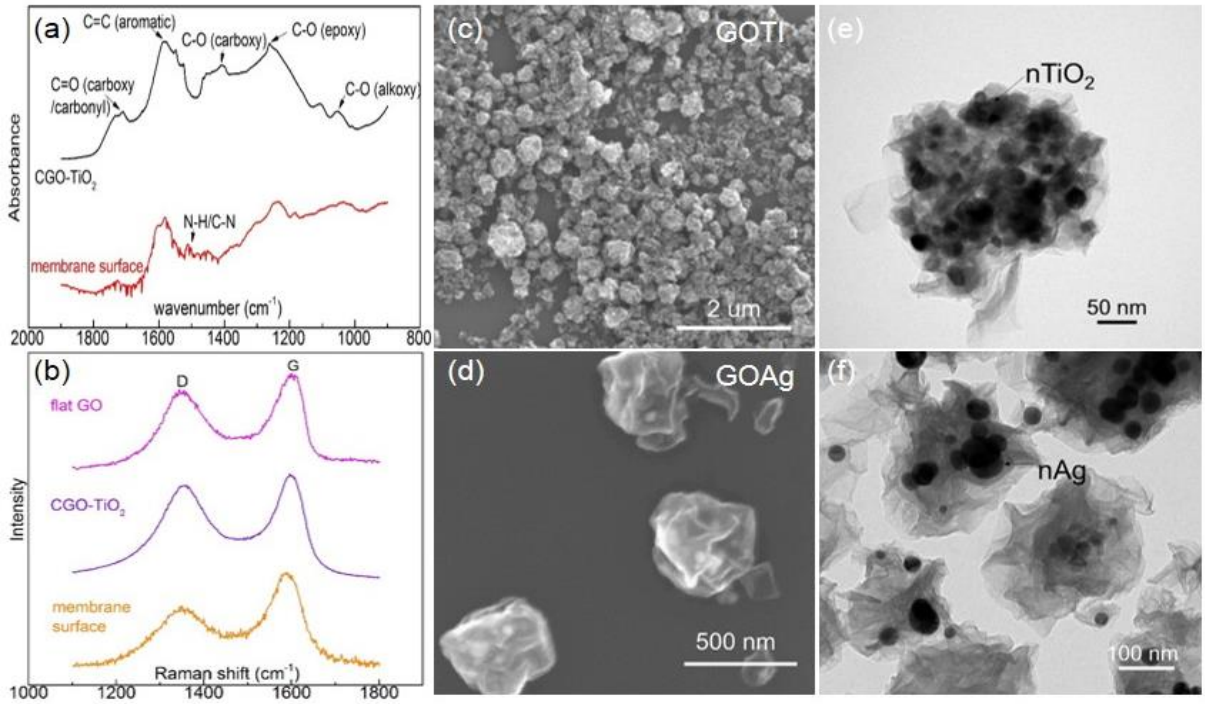

Figure 7.1 (a) FTIR spectra of GOTI and the membrane surface; (b) Raman spectra of flat GO, GOTI and membrane surface layer; (c) SEM image of GOTI; (d) SEM image of GOAg; (e) TEM image of GOTI; (f) TEM image of GOAg.

As key assembly components for described membrane assemblies, CGO nanocomposites were synthesized using a facile aerosol process (details in Supporting Information, Figure S7.1).[10, 11, 31] Fine water droplets of precursors containing GO and functional nanoparticles are carried by N_2 into a tube furnace, in which GO effectively crumples under the induced confinement force of rapid water evaporation, which subsequently encapsulates GO surface associated nanoparticles. Here, two specific CGO nanocomposites, namely GOAg (antimicrobial), GOTI (photo-reactive), were synthesized and characterized. As synthesized, CGO nanocomposites have relatively high

negative surface charges (GOTI: -51.5 ± 0.6 mV; GOAg: -42.5 ± 1.1 mV), indicating abundant hydrophilic oxygenated groups on the surface, which accounts for high monomeric aqueous stability. FTIR analysis (Figure 7.1(a)) indicates the presence of C-O (alkoxy), C-O (epoxy), C-O (carboxy), C=C (aromatic), and also C=O (carboxy/carbonyl) stretching.[30, 33] Raman analysis of the GOTI nanocomposites (Figure 7.1(b)) shows the two classic characteristic scattering bands for GO with a D band at ~1340 cm^{-1} and G band at ~1600 cm^{-1}.[37] The D band is associated with the distortion from the hexagonal lattice (such as sp^3 type defect); whereas the G band corresponds to pure sp^2 hybridized graphitic carbon.[38] Flat GO, used as the starting material and produced from the modified Hummers method[32] (via harsh oxidation of graphite), has significant oxygen-based functionality resulting in a D peak that is negligible for pure graphite/graphene.[37] To maintain hydrophilicity while achieving desired physical crumpling, a furnace temperature at 400 ℃ was intentionally selected based on previous reports.[10, 11] The ratio between intensities of D band and G band (I_D/I_G), was slightly increased from 0.86 (flat GO) to 0.91 (GOTI), indicating graphene regions (sp^2 sites) are partially restored within the so-called stage 2 defect regime (high defect density regime).[38] During thermal reduction of GO, physical defects are induced by loss of hydroxyl and epoxy groups, including vacancies created by loss of connected carbon atoms and even larger physical holes with dimensions ranging from sub-nm to a few nm.[39, 40] Further, evaporation-induced capillary force can also facilitate the formation of such vacancies\holes at the ridges (valleys) where stress is concentrated, thus providing additional (flow) channels. The abundance of oxygen-based functional groups coincides with the negative ζ-potential, and provides enhanced surface/pore hydrophilicity upon membrane assembly. Dynamic light scattering (DLS) size measurements show that average hydrodynamic sizes of GOTI and GOAg were 200 ± 1 nm, and 207 ± 1 nm respectively (Supporting Information Figure S7.3), which is

also confirmed by FESEM and TEM measurements. TEM and SEM graphs of GOTI and GOAg in Figure 7.1(c-f) show a clear core-shell nanostructure, with crumpled GO comprising the outer shell and TiO_2/Ag nanoparticles as part of the inner core. Such a core-shell structure enables not only reactivity by contained nanoparticles inside (and in few cases across the GO surface), but also maintains large contact surface area (ridges and valleys, creating intraparticle pores) along with high surface hydrophilicity – both of which are critical for fast water transport (flux) and high rejection performance regimes.

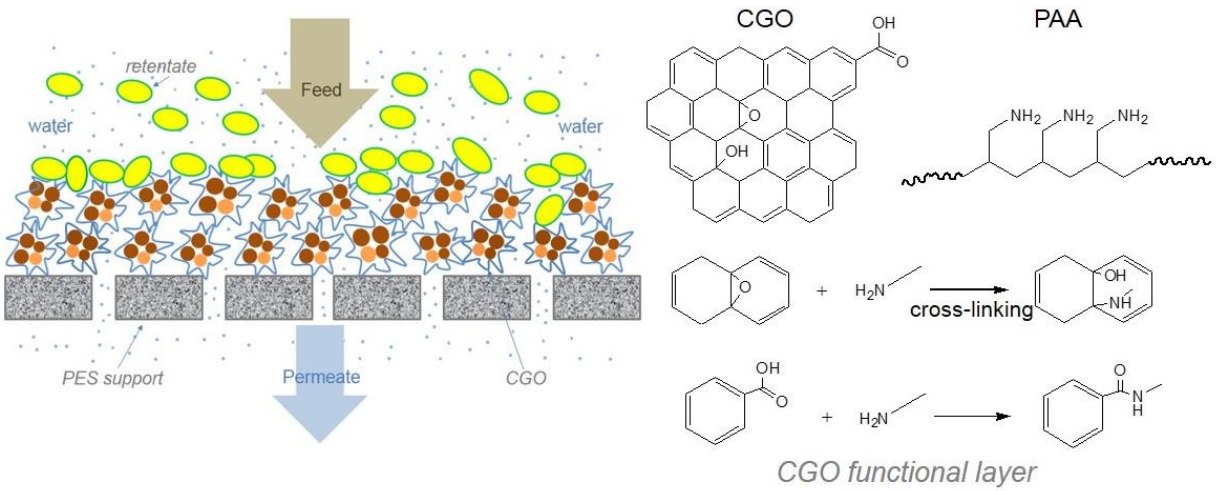

Figure 7.2 Schematic diagram of CGO membrane (left) and reaction (cross-linking) mechanism between CGO and PAA (right).

7.3.2 Membrane Synthesis and Characterization

Previously, multiwall and single wall carbon nanotubes have been directly deposited onto a membrane support via vacuum filtration for system enhancement and expansion of surface functionality. However, such structures lack stability, particularly under cross-flow conditions.[18, 41, 42] Here, stability issues were minimized, while tuning assembly pore sizes by using

polyallylamine (PAA) to chemically cross-link CGO nanocomposites. PAA has been reported previously to modify/stabilize and improve water treatment membranes.[43, 44] For example, together with polyacrylic acid, through the formation of polyelectrolyte multilayers (using a layer-by-layer approach), PAA functionalized polysulfone microfiltration membranes have been demonstrated and show considerably enhanced antifouling (bacterial anti-adhesive) properties when compared to unmodified surfaces.[44] Here, reactive amine groups on the long alkyl chain readily react with oxygen functional groups on the CGO surface, creating new C-N bonds, leading to broad chemical cross-linking, as shown by the scheme in Figure 7.2.[33] Upon assembly onto a commercial hydrophilic PES support membrane (Sterlitech, with heterogeneous pore size distribution, observed from 80 nm to 1 μm, as shown in the SEM image, Figure 7.3e), cross-linked CGO membrane showed considerably enhanced stability compared to unmodified deposits (*e.g.*, no monomeric detachment nor surface fissures observed after sonication).

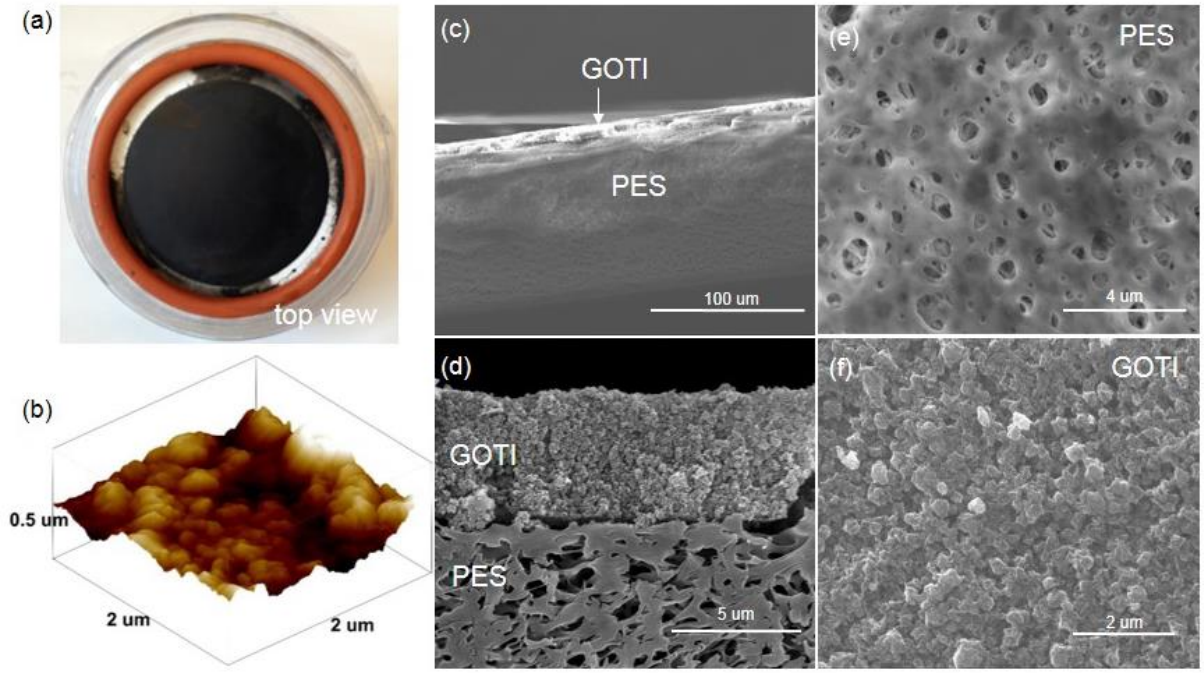

Figure 7.3 Characterization of GOTI membrane: (a) digital photo; (b) AFM 3D surface image; (c) SEM cross-sectional view (low magnification); (d) SEM cross-sectional view (high magnification); (e) SEM top view of blank PES support; (f) SEM top view of GOTI membrane surface.

A representative GOTI membrane with deposited mass of 6 mg (CGO) was characterized by FTIR, Raman spectroscopy, AFM, SEM, and water contact angle analysis (In addition, a 3 mg GOAg membrane was characterized, with no significant difference found as shown in Figure S7.4). In addition to previously identified oxygen functionality,[33] FTIR spectrum of the membrane surface shows new absorbance at ~1500 cm^{-1}, which corresponds to formation of C-N bonds, indicating successful cross-linking (Figure 7.1(a)), as a result of the reaction between epoxy/carboxyl and amine groups.[33, 45] C-N based cross-linking was also indirectly supported by decreasing of C-O (epoxy), C=O and C-O (carboxyl) stretching (relative) ratios (Figure 7.1(a)). Deposited, cross-linked CGO membrane assemblies appear black, typical of CGO nanocomposite, as shown in Figure 7.3(a). The membrane surface reveals peak-valley morphology, observed by

both AFM and SEM measurements (Figure 7.3(b) and (f)). The average surface roughness (R_a, deviation in height) and root mean square roughness (R_q, the standard deviation of surface heights) were determined to be 52.4 ± 5.8 nm and 66.2 ± 10.4 nm respectively through AFM analysis, which is smaller than previously reported flat GO-impregnated membranes.[34] In general, smoother surfaces have been shown to result in higher anti-fouling properties.[46] Figure 7.3(c), (d) and (f) shows the cross-sectional and top views of the membrane. A functional layer consisting of cross-linked GOTI nanocomposites was clearly observed on top of the PES support (Figure 7.3(c-f)). In this case, 6 mg deposited mass corresponds to 5.4 μm depth, which is a 5.1% increase (total) in thickness compared to the unmodified PES support (106 μm in thickness as measured by SEM). Quasi-spherical GOTI nanocomposites can be observed stacked tightly, with intrinsic pores formed between particles (Figure 7.3(f)). ImageJ analysis of surface SEM images (×80000 magnification) indicates that rough surface pore sizes are 22.1 ± 14.9 nm. Water contact angle measurements revealed very fast uptake and spread of droplet, indicative of a superhydrophilic surface.

7.3.3 CGO Membrane Performance

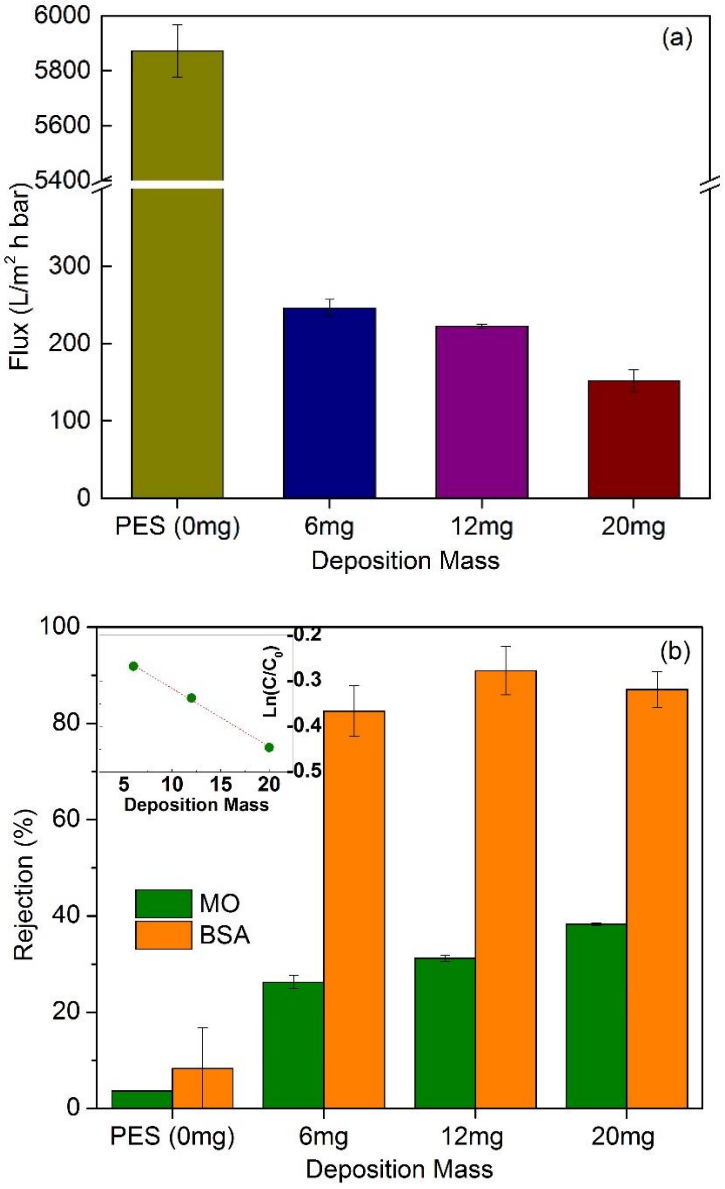

Figure 7.4 CGO membrane performance: (a) water flux with different deposited GOTI mass; (b) rejection of MO and BSA with different deposited GOTI mass (6-20 mg). The inset shows the negatively liner relationship of MO permeate concentration ($Ln(C/C_0)$) and deposited mass. The rejection tests are conducted with 7.5 mg/L MO and 10 mg/L BSA respectively.

Pure water flux measurements of CGO membranes with different deposited CGO masses (thickness) are shown in Figure 7.4(a). Background water flux through the PES support was measured to be 5872 ± 95 L/(m^2·h·bar). Upon the additional layer (atop the PES support) of cross-linked GOTI nanocomposites (6 mg, ~5.4 μm in thickness), water flux of 246 ± 11 L/(m^2·h·bar) was measured, indicating the decrease in effective pore size. Unlike coating with flat GO nanosheets, whereby water flux does not decrease monotonically as deposition mass increases,[30] flux for these assemblies decreases further to 152 ± 14 L/(m^2·h·bar) with a 20 mg GOTI assembly. Such an inverse relationship between permeability and layer depth (mass) is similar to trends observed in previous CNT filters studies,[18] and agrees with the classical Kozeny-Carman equation for flow through porous filters.[47] In addition, no statistical difference was found for GOTI and GOAg membranes on permeation performance. For example, the pure water flux was 453.5 ± 30.8 and 396.1 ± 58.4 L/(m^2·h·bar) for GOTI and GOAg membrane of 3 mg deposition respectively. Generally, water flux exceeded that of most commercial ultrafiltration membranes, which typically ranges from several L/(m^2·h·bar) (Molecular weight cut-off (MWCO): a few thousand Da) to ~150 L/(m^2·h·bar) (MWCO: 100,000 Da) (*e.g.*, GE Osmonics, TriSep, the flux was calculated using parameters provided by manufacturers). We hypothesize that such high flux can be attributed not only to the CGO hydrophilicity but also to the porous nature of CGO (intraparticle) structures themselves. Water molecules may transport through vertically tortuous nanochannels formed by pores between CGO nanocomposites in addition to through intrinsic physical defects (vacancies\holes) of CGO, which are formed during thermal reduction and crumpling as described above. Porosity analysis for this membrane using the Kozeny-Carman equation (using measured flux and pressure data and assuming a common tortuosity of 2.5 for ultrafiltration membranes) had a value of 0.21, and estimation based on material (*i.e.* volume) balance gave a value of 0.33

(Supporting Information). An 'open' CGO structure is also supported by the evolution of dissolved Ag^+ out of GOAg nanocomposites as discussed below.

The separation performance of the CGO membranes was evaluated by filtration of a model organic dye, methyl orange (MO, 327 Da) and a widely studied protein, bovine serum albumin (BSA, ~ 66.5 kDa). As seen in Figure 7.4(b), the PES support membrane rejects less than 10% of both MO and BSA. In contrast, a cross-linked, 6 mg GOTI assembly on the PES support enhanced rejection (retention) of MO and BSA to 26% and 83%, respectively. When the CGO deposition mass further increases, rejection of MO and BSA shows different trends, indicative of different filtration mechanisms (at 95% confidence interval, statistically different removal rates of MO are 26.4±1.5%, 31.2±0.8%, and 38.3±0.3% for 6, 12, and 20 mg depositions, respectively; for BSA, the rejection percentages are not statistically different for 6, 12, and 20 mg depositions at 82.6±5.9%, 91.0±5.7%, and 87.6±4.2%, respectively). As smaller molecules like MO have high diffusion velocities, significant deposition can occur on the CGO surface. As expected from depth filtration theory, the logarithm of the normalized permeate concentration ($Ln(C/C_0)$) is negatively proportional to the layer depth (mass), as shown in Figure 7.4(b) inset.[18, 48] However, this was not observed for BSA rejection. No increase of rejection efficiency is observed with thicker layers, thus revealing a size exclusion mechanism. Previous studies also report that surface/pore charge effects can play a significant role in the rejection mechanism(s) of GO membranes.[30] BSA has a point of zero charge at pH 5,[49] and was found to be negatively charged for these studies (measured by electrophoretic light scattering, pH: ~6.3). As CGO membrane is also negatively charged, it is possible that surface charge may play a role in these systems, which is being further investigated.

7.3.4 Antimicrobial Membrane Activity

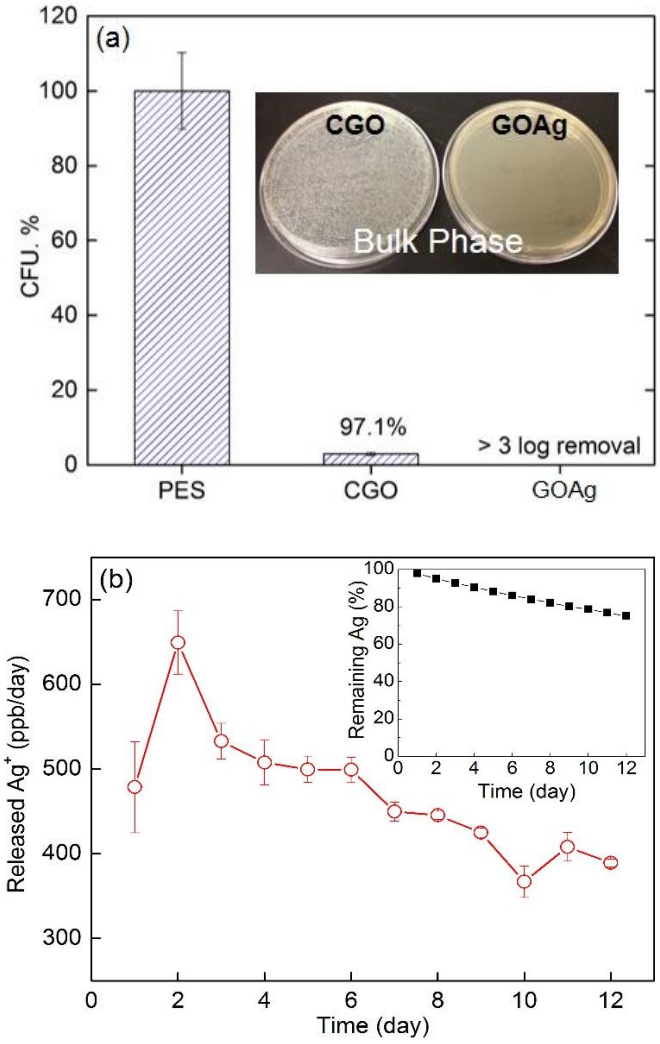

Figure 7.5 (a) Comparison of CFU after E. coli contacting with membrane surface (column) and in the bulk phase (inset picture). (b) Ag^+ released from GOAg membrane in batch mode. Deposited mass = 3 mg; pure water was changed every 24 h. (V_{water} = 25 mL). The inset shows the remaining percentage mass of Ag with time.

It has been reported that inactivation of bacteria by GO is due to induced cell membrane damage, as a result of physical disruption,[27] formation of reactive oxygen species,[28] and extraction of phospholipids from cell membrane.[29] In this work, antimicrobial properties of CGO membrane

assemblies were evaluated according to protocols previously reported.[19] *E. coli* dispersion (in 0.9% saline) was placed in contact with the active (deposited) side of the membrane, and after 2 h surface contact, the remaining viable *E. coli* population was compared to that contacted with blank PES. Compared to the control (PES support only) surface, it was found that only 3% of viable *E. coli* remains on pristine CGO assembly surface after 2 h of contact time (Figure 7.5(a)), which is a ca. 33% increase in effectiveness compared to previous studies on flat GO functionalization.[19] This observation may be due to a longer contact time compared to the previous study (2 h compared to 1 h).[26, 50] GOAg membrane assemblies exhibit even higher effective *E. coli* inactivation properties, with a > 3 log removal, again when compared to the PES support control. In addition, Figure 7.5(a) shows the direct comparison of *E. coli* CFU plated from aqueous bulk phase above CGO and GOAg membrane surface. Due to Ag^+ release and diffusion, complete *E. coli* inactivation is achieved, based on our detection limits, (Figure 7.5(a) inset right) in contrast to growth on the CGO membrane (Figure 7.5(a) inset left). This observation agrees with batch inhibition studies (Figure S7.5), which show that GOAg (as a suspended particle) can effectively inhibit *E. coli* growth at low concentrations (at or below 0.4 mg/L).

Enhanced microbial inactivation efficacy is attributed to the additional effects of Ag^+ release from encapsulated Ag NPs within GOAg assemblies. Figure 7.5(b) shows the release (rates) of Ag^+ into 25 mL water from 3 mg GOAg deposited membrane (18.9 wt. % silver). The accumulated Ag^+ concentration after 24 h immersion decreases gradually from 479 $\pm$ 54 ppb in day 1 to 389 $\pm$ 5 ppb in day 12. The measured day 1 release is smaller than that of day 2, due to initial adsorption of released Ag^+ onto CGO surface (strong electrostatic interaction between Ag^+ and negatively charged oxygen-based functional groups), similar to other cations (e.g., Cd^{2+} and Co^{2+}) sorption onto GO.[51] It is noteworthy that after 12 days, ca. 75% of the preloaded Ag (as nAg)

remained (undissolved) in the system (as shown in Figure 7.5(b) inset). Considering the very short residence time in the flow-through mode (t_{res} < 0.1 s), effective duration can be even longer. Eventually, the complete dissolution of Ag will lead to the diminishment of enhanced antimicrobial activity; to address this, an in situ regeneration strategy is being explored and will be the focus of future reports.

7.3.5 Photocatalytic Activity

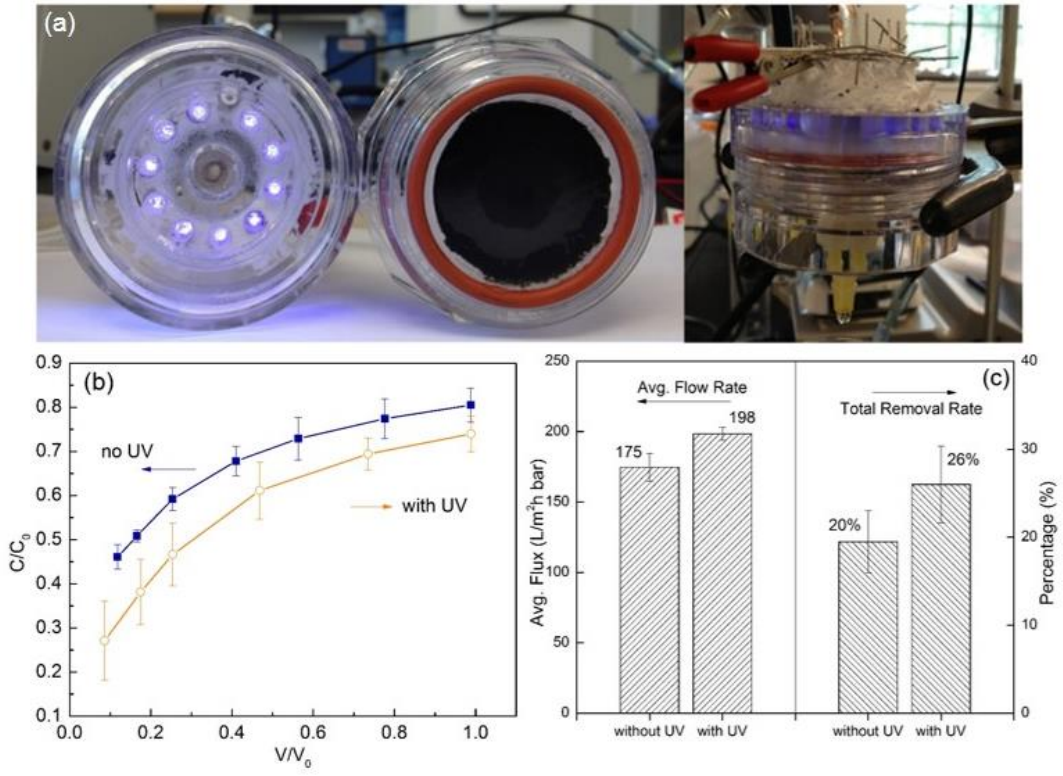

Figure 7.6 Simultaneous filtration and reaction of MO with GOTI membranes: (a) customized filter holder with 10 UV LED lights; (b) MO concentration (outflow tank concentration over inflow concentration C/C_0) changes with filtered solution volume (V/V_{total}, V_{total} = 180 mL) with/without UV light irradiation. (c) Comparison of average fluxes and total MO removal rates with/without UV light irradiation.

Compared to TiO_2 alone, monomeric GOTI nanocomposites were observed to have enhanced photocatalytic properties due to the production of both holes (h^+) and radicals (H_2O_2, O^{2-} ; OH ·), as reported in our recent work.[11] The photo-reactivity of GOTI as a membrane was evaluated here by degradation of MO in both batch and flow-through modes. For all systems evaluated, MO does not degrade under irradiated conditions alone (*i.e*. without GOTI). In a batch mode, the heterogeneous reaction of MO on the membrane surface resulted a reaction rate constant of 0.0061 min^{-1} (fitted as pseudo first-order reaction), which was on the same order magnitude for methylene blue degradation for a GO-TiO_2 membrane,[21] but lower than that of monomeric (suspended) GOTI nanocomposites as we previously described (0.0838 min^{-1}) (Figure S7.6).[11] Such difference can be attributed to available surface area and irradiation conditions (0.9 mW/cm^2 centered at 351 nm vs. 14.4 mW/cm^2 in the range between 250 and 387 nm for previous batch evaluations[11]), as irradiation light intensity, for similar systems, typically has a nonlinear power law relationship with reaction rates.[52] Building on batch observations, we evaluated the potential for GOTI as a photoreactive membrane assembly in flow-through mode. Taking advantage of high efficiency, long lifetime, and compact design, a customized, waterproof filter holder modified with 10 UV LED lights was built for flow-through evaluations (Figure 7.6(a)). Figure 7.6(b) shows the evolution of MO concentration in the outflow, as a function of filtration volume, under UV (light) / no UV (dark) scenarios. Under dark conditions, the outflow initially appears clear indicating sorption of MO onto/into CGO. As typical for depth filtration, the outflow concentration gradually increases in-line with CGO MO saturation. The evolution of MO concentration under UV irradiation shows a similar trend, however, at lower concentration levels, which can be attributed to simultaneous photo-degradation of MO. Further, under UV irradiation the observed flux rate increased, from 175 ± 10 (dark) to 198 ± 5 $L/(m^2 \cdot h \cdot bar)$. Effective removal due to photo-

degradation (the difference between two outflow concentrations under UV and dark conditions) decreased from >15% at the beginning to ~6% at the end of 180 mL solution (Figure 7.6 (b) and (c)), showing that intermediates produced may potentially 'foul' the membrane and hinder reactivity. It should be noted that this, to our knowledge, is the first demonstration of membrane photo-reactivity under fast flow (t_{res} = ~0.07- 0.08 s) using low-intensity, UV LED light irradiation. Future systems can be optimized/tailored via light irradiation conditions (e.g., wavelength, intensity), flow parameters, and reactor design to achieve target (reactive and separatory) performance regimes.

7.4 Environmental Applications

Taken together, this study clearly demonstrates potential applicability of CGO nanocomposites as a platform material for application in highly water permeable, selective and reactive (photo-reactive and antimicrobial) membrane assemblies. CGO based membrane assemblies have unique and inherent advantages over flat GO membranes, such as tailorable porosity and flow patterns within the assembly, in addition to simultaneous and tunable filtration and reactivity properties. The synthesis of functional CGO nanocomposites can be achieved via a relatively simple, fast, and continuous gas phase process, which utilizes GO, which can now be readily made available via oxidation and exfoliation from commercial graphite and commercially available functional nanomaterials, providing technical feasibility and for potential scale up. Further, broad functional possibilities (in addition to GOTI and GOAg composites) underpin a wide range of potential tailored CGO material applications for advanced water treatment technologies beyond what is demonstrated in this work.

Acknowledgements

This work is supported by the National Science Foundation's CAREER Award (CBET 1454656). The authors also thank McDonnell Academy Global Energy and Environment Partnership (MAGEEP), Washington University in St. Louis for funding support. Electron microscopy work was performed at the Nano Research Facility (NRF) at Washington University in St. Louis, a member of the National Nanotechnology Infrastructure Network (NNIN), supported by the National Science Foundation under Grant No. ECS-0335765.

References

1. Shannon, M. A.; Bohn, P. W.; Elimelech, M.; Georgiadis, J. G.; Marinas, B. J.; Mayes, A. M., Science and Technology for Water Purification in the Coming Decades. *Nature* 2008, *452*, (7185), 301-310.
2. Qu, X.; Brame, J.; Li, Q.; Alvarez, P. J. J., Nanotechnology for a Safe and Sustainable Water Supply: Enabling Integrated Water Treatment and Reuse. *Acc. Chem. Res.* 2012.
3. Zhao, G.; Jiang, L.; He, Y.; Li, J.; Dong, H.; Wang, X.; Hu, W., Sulfonated Graphene for Persistent Aromatic Pollutant Management. *Adv. Mater.* 2011, *23*, (34), 3959-3963.
4. Liu, M.; Chen, C.; Hu, J.; Wu, X.; Wang, X., Synthesis of Magnetite/Graphene Oxide Composite and Application for Cobalt(II) Removal. *J. Phys. Chem. C* 2011, *115*, (51), 25234-25240.
5. Nair, R. R.; Wu, H. A.; Jayaram, P. N.; Grigorieva, I. V.; Geim, A. K., Unimpeded Permeation of Water Through Helium-Leak-Tight Graphene-Based Membranes. *Science* 2012, *335*, (6067), 442-444.

6. Akhavan, O.; Ghaderi, E., Photocatalytic Reduction of Graphene Oxide Nanosheets on TiO_2 Thin Film for Photoinactivation of Bacteria in Solar Light Irradiation. *J. Phys. Chem. C* 2009, *113*, (47), 20214-20220.
7. Zhang, H.; Lv, X. J.; Li, Y. M.; Wang, Y.; Li, J. H., P25-Graphene Composite as a High Performance Photocatalyst. *ACS Nano* 2010, *4*, (1), 380-386.
8. Zhang, Y.; Tang, Z.-R.; Fu, X.; Xu, Y.-J., TiO_2−Graphene Nanocomposites for Gas-Phase Photocatalytic Degradation of Volatile Aromatic Pollutant: Is TiO_2−Graphene Truly Different from Other TiO_2−Carbon Composite Materials? *ACS Nano* 2010, *4*, (12), 7303-7314.
9. Agnoli, S.; Granozzi, G., Second Generation Graphene: Opportunities and Challenges for Surface Science. *Surf. Sci.* 2013, *609*, (0), 1-5.
10. Wang, W.-N.; Jiang, Y.; Biswas, P., Evaporation-Induced Crumpling of Graphene Oxide Nanosheets in Aerosolized Droplets: Confinement Force Relationship. *J. Phys. Chem. Lett.* 2012, *3*, (21), 3228-3233.
11. Jiang, Y.; Wang, W.-N.; Biswas, P.; Fortner, J. D., Facile Aerosol Synthesis and Characterization of Ternary Crumpled Graphene–TiO_2–Magnetite Nanocomposites for Advanced Water Treatment. *ACS Appl. Mater. Interfaces* 2014, *6*, (14), 11766-11774.
12. Cranford, S. W.; Buehler, M. J., Packing Efficiency and Accessible Surface Area of Crumpled Graphene. *Phys. Rev. B* 2011, *84*, (20), 205451.
13. Luo, J.; Jang, H. D.; Sun, T.; Xiao, L.; He, Z.; Katsoulidis, A. P.; Kanatzidis, M. G.; Gibson, J. M.; Huang, J., Compression and Aggregation-Resistant Particles of Crumpled Soft Sheets. *ACS Nano* 2011, *5*, (11), 8943-8949.

14. Lewis, S. R.; Datta, S.; Gui, M.; Coker, E. L.; Huggins, F. E.; Daunert, S.; Bachas, L.; Bhattacharyya, D., Reactive Nanostructured Membranes for Water Purification. *Proc. Natl. Acad. Sci. U. S. A.* 2011, *108*, (21), 8577–8582.

15. Mauter, M. S.; Wang, Y.; Okemgbo, K. C.; Osuji, C. O.; Giannelis, E. P.; Elimelech, M., Antifouling Ultrafiltration Membranes via Post-Fabrication Grafting of Biocidal Nanomaterials. *ACS Appl. Mater. Interfaces* 2011, *3*, (8), 2861-2868.

16. Zodrow, K.; Brunet, L.; Mahendra, S.; Li, D.; Zhang, A.; Li, Q.; Alvarez, P. J., Polysulfone Ultrafiltration Membranes Impregnated with Silver Nanoparticles Show Improved Biofouling Resistance and Virus Removal. *Water Res.* 2009, *43*, (3), 715-723.

17. Yin, J.; Yang, Y.; Hu, Z.; Deng, B., Attachment of Silver Nanoparticles (AgNPs) onto Thin-Film Composite (TFC) Membranes Through Covalent Bonding to Reduce Membrane Biofouling. *J. Membr. Sci.* 2013, *441*, (0), 73-82.

18. Brady-Estévez, A. S.; Kang, S.; Elimelech, M., A Single-Walled-Carbon-Nanotube Filter for Removal of Viral and Bacterial Pathogens. *Small* 2008, *4*, (4), 481-484.

19. Perreault, F.; Tousley, M. E.; Elimelech, M., Thin-Film Composite Polyamide Membranes Functionalized with Biocidal Graphene Oxide Nanosheets. *Environ. Sci. Technol. Lett.* 2013, *1*, (1), 71-76.

20. Xu, J.; Dozier, A.; Bhattacharyya, D., Synthesis of Nanoscale Bimetallic Particles in Polyelectrolyte Membrane Matrix for Reductive Transformation of Halogenated Organic Compounds. *J. Nanopart. Res.* 2005, *7*, (4-5), 449-467.

21. Gao, Y.; Hu, M.; Mi, B., Membrane Surface Modification with TiO_2–Graphene Oxide for Enhanced Photocatalytic Performance. *J. Membr. Sci.* 2014, *455*, (0), 349-356.

22. Li, H.; Song, Z.; Zhang, X.; Huang, Y.; Li, S.; Mao, Y.; Ploehn, H. J.; Bao, Y.; Yu, M., Ultrathin, Molecular-Sieving Graphene Oxide Membranes for Selective Hydrogen Separation. *Science* 2013, *342*, (6154), 95-98.
23. Joshi, R. K.; Carbone, P.; Wang, F. C.; Kravets, V. G.; Su, Y.; Grigorieva, I. V.; Wu, H. A.; Geim, A. K.; Nair, R. R., Precise and Ultrafast Molecular Sieving Through Graphene Oxide Membranes. *Science* 2014, *343*, (6172), 752-754.
24. Celebi, K.; Buchheim, J.; Wyss, R. M.; Droudian, A.; Gasser, P.; Shorubalko, I.; Kye, J.-I.; Lee, C.; Park, H. G., Ultimate Permeation Across Atomically Thin Porous Graphene. *Science* 2014, *344*, (6181), 289-292.
25. Novoselov, K. S.; Falko, V. I.; Colombo, L.; Gellert, P. R.; Schwab, M. G.; Kim, K., A Roadmap for Graphene. *Nature* 2012, *490*, (7419), 192-200.
26. Santos, C. M.; Tria, M. C. R.; Vergara, R. A. M. V.; Ahmed, F.; Advincula, R. C.; Rodrigues, D. F., Antimicrobial Graphene Polymer (PVK-GO) Nanocomposite Films. *Chem. Commun.* 2011, *47*, (31), 8892-8894.
27. Akhavan, O.; Ghaderi, E., Toxicity of Graphene and Graphene Oxide Nanowalls Against Bacteria. *ACS Nano* 2010, *4*, (10), 5731-5736.
28. Liu, S.; Zeng, T. H.; Hofmann, M.; Burcombe, E.; Wei, J.; Jiang, R.; Kong, J.; Chen, Y., Antibacterial Activity of Graphite, Graphite Oxide, Graphene Oxide, and Reduced Graphene Oxide: Membrane and Oxidative Stress. *ACS Nano* 2011, *5*, (9), 6971-6980.
29. Tu, Y.; Lv, M.; Xiu, P.; Huynh, T.; Zhang, M.; Castelli, M.; Liu, Z.; Huang, Q.; Fan, C.; Fang, H.; Zhou, R., Destructive Extraction of Phospholipids from Escherichia Coli Membranes by Graphene Nanosheets. *Nat. Nanotechnol.* 2013, *8*, (8), 594-601.

30. Hu, M.; Mi, B., Enabling Graphene Oxide Nanosheets as Water Separation Membranes. *Environ. Sci. Technol.* 2013, *47*, (8), 3715-3723.
31. Wang, W.-N.; Jiang, Y.; Fortner, J. D.; Biswas, P., Nanostructured Graphene-Titanium Dioxide Composites Synthesized by a Single-Step Aerosol Process for Photoreduction of Carbon Dioxide. *Environ. Eng. Sci.* 2014, *31*, (7), 428-434.
32. Hummers, W. S.; Offeman, R. E., Preparation of Graphitic Oxide. *J. Am. Chem. Soc.* 1958, *80*, (6), 1339-1339.
33. Park, S.; Dikin, D. A.; Nguyen, S. T.; Ruoff, R. S., Graphene Oxide Sheets Chemically Cross-Linked by Polyallylamine. *J. Phys. Chem. C* 2009, *113*, (36), 15801-15804.
34. Zhang, J.; Xu, Z.; Mai, W.; Min, C.; Zhou, B.; Shan, M.; Li, Y.; Yang, C.; Wang, Z.; Qian, X., Improved Hydrophilicity, Permeability, Antifouling and Mechanical Performance of PVDF Composite Ultrafiltration Membranes Tailored by Oxidized Low-Dimensional Carbon Nanomaterials. *J. Mater. Chem. A* 2013, *1*, (9), 3101-3111.
35. Tiraferri, A.; Vecitis, C. D.; Elimelech, M., Covalent Binding of Single-Walled Carbon Nanotubes to Polyamide Membranes for Antimicrobial Surface Properties. *ACS Appl. Mater. Interfaces* 2011, *3*, (8), 2869-2877.
36. Fortner, J. D.; Lyon, D. Y.; Sayes, C. M.; Boyd, A. M.; Falkner, J. C.; Hotze, E. M.; Alemany, L. B.; Tao, Y. J.; Guo, W.; Ausman, K. D.; Colvin, V. L.; Hughes, J. B., C60 in Water: Nanocrystal Formation and Microbial Response. *Environ. Sci. Technol.* 2005, *39*, (11), 4307-4316.
37. Tuinstra, F.; Koenig, J. L., Raman Spectrum of Graphite. *J. Chem. Phys.*1970, *53*, (3), 1126-1130.

38. Cançado, L. G.; Jorio, A.; Ferreira, E. H. M.; Stavale, F.; Achete, C. A.; Capaz, R. B.; Moutinho, M. V. O.; Lombardo, A.; Kulmala, T. S.; Ferrari, A. C., Quantifying Defects in Graphene via Raman Spectroscopy at Different Excitation Energies. *Nano Lett.* 2011, *11*, (8), 3190-3196.

39. Bagri, A.; Mattevi, C.; Acik, M.; Chabal, Y. J.; Chhowalla, M.; Shenoy, V. B., Structural Evolution During the Reduction of Chemically Derived Graphene Oxide. *Nat. Chem.* 2010, *2*, (7), 581-587.

40. Gómez-Navarro, C.; Meyer, J. C.; Sundaram, R. S.; Chuvilin, A.; Kurasch, S.; Burghard, M.; Kern, K.; Kaiser, U., Atomic Structure of Reduced Graphene Oxide. *Nano Lett.* 2010, *10*, (4), 1144-1148.

41. Vecitis, C. D.; Gao, G.; Liu, H., Electrochemical Carbon Nanotube Filter for Adsorption, Desorption, and Oxidation of Aqueous Dyes and Anions. *J. Phys. Chem. C* 2011, *115*, (9), 3621-3629.

42. Ajmani, G. S.; Goodwin, D.; Marsh, K.; Fairbrother, D. H.; Schwab, K. J.; Jacangelo, J. G.; Huang, H., Modification of Low Pressure Membranes with Carbon Nanotube Layers for Fouling Control. *Water Res.* 2012, *46*, (17), 5645-5654.

43. Jin, W.; Toutianoush, A.; Tieke, B., Use of Polyelectrolyte Layer-by-Layer Assemblies as Nanofiltration and Reverse Osmosis Membranes. *Langmuir* 2003, *19*, (7), 2550-2553.

44. Tang, L.; Gu, W.; Yi, P.; Bitter, J. L.; Hong, J. Y.; Fairbrother, D. H.; Chen, K. L., Bacterial Anti-Adhesive Properties of Polysulfone Membranes Modified with Polyelectrolyte Multilayers. *J. Membr. Sci.* 2013, *446*, (0), 201-211.

45. Satti, A.; Perret, A.; McCarthy, J. E.; Gun'ko, Y. K., Covalent Crosslinking of Single-Walled Carbon Nanotubes with Poly(allylamine) to Produce Mechanically Robust Composites. *J. Mater. Chem.* 2010, *20*, (37), 7941-7943.

46. Vrijenhoek, E. M.; Hong, S.; Elimelech, M., Influence of Membrane Surface Properties on Initial Rate of Colloidal Fouling of Reverse Osmosis and Nanofiltration Membranes. *J. Membr. Sci.* 2001, *188*, (1), 115-128.

47. Mulder, M., *Basic Principles of Membrane Technology*. 2nd ed.; Kluwer Academic Publishers: Dordrecht, 1996.

48. Tufenkji, N.; Elimelech, M., Correlation Equation for Predicting Single-Collector Efficiency in Physicochemical Filtration in Saturated Porous Media. *Environ. Sci. Technol.* 2004, *38*, (2), 529-536.

49. Valiño, V.; San Román, M. F.; Ibañez, R.; Ortiz, I., Improved Separation of Bovine Serum Albumin and Lactoferrin Mixtures Using Charged Ultrafiltration Membranes. *Sep. Purif. Technol.* 2014, *125*, (0), 163-169.

50. Mejias Carpio, I. E.; Santos, C. M.; Wei, X.; Rodrigues, D. F., Toxicity of a Polymer-Graphene Oxide Composite Against Bacterial Planktonic Cells, Biofilms, and Mammalian Cells. *Nanoscale* 2012, *4*, (15), 4746-4756.

51. Zhao, G.; Li, J.; Ren, X.; Chen, C.; Wang, X., Few-Layered Graphene Oxide Nanosheets As Superior Sorbents for Heavy Metal Ion Pollution Management. *Environ. Sci. Technol.* 2011, *45*, (24), 10454-10462.

52. Wang, Z.; Liu, J.; Dai, Y.; Dong, W.; Zhang, S.; Chen, J., Dimethyl Sulfide Photocatalytic Degradation in a Light-Emitting-Diode Continuous Reactor: Kinetic and Mechanistic Study. *Ind. Eng. Chem. Res.* 2011, *50*, (13), 7977-7984.

Chapter 7 Supporting Information

S7.1. Experimental

CGO Nanocomposite Synthesis. Graphene oxide (GO) was synthesized using the modified Hummers method[1] and was reported in our previous work.[2] To synthesize GOTI nanocomposite, 26.2 uL TiO_2 dispersion (Evonik Degussa Aerodisp 740X) was added into 200 mL GO solution (~0.1 mg/mL) and sonicated mildly for 15 min before spray. Similarly, to obtain GOAg nanocomposite, 164 uL Ag NP dispersion (10 wt.% in ethylene glycol, < 100 nm, Sigma Aldrich) was added into 200 mL GO.

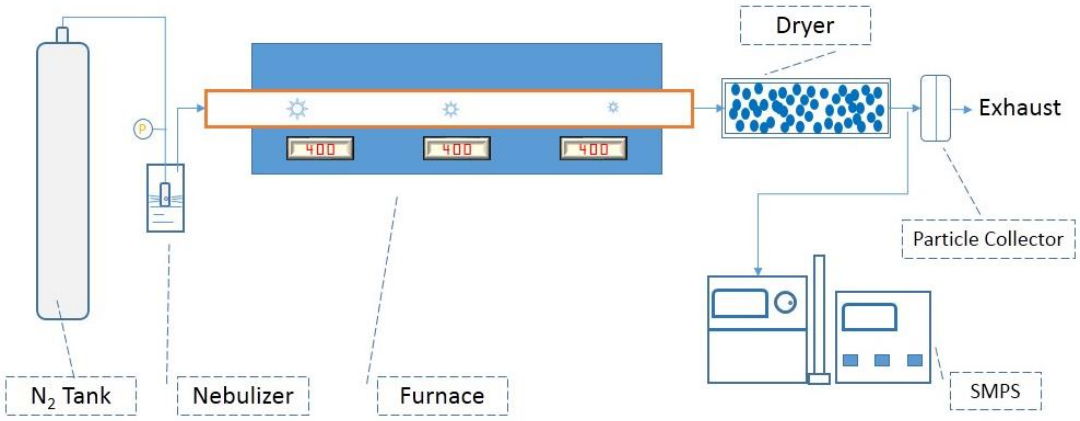

Figure S7.1. Scheme diagram of a FuAR

The aerosol synthesis process utilizes a furnace aerosol reactor (FuAR), which has been described before in our previous work (as shown in Figure S7.1).[2-4] Briefly, the precursor was initially atomized into micrometer-sized droplets by using a Collison nebulizer (BGI Incorporated). These water droplets containing GO and nanoparticles were subsequently delivered by N_2 into the tubular alumina reactor (1 m × 25 mm ID) maintained at 400 ℃, to enable the successful crumpling of GO, yet partially preserve the functional groups, such as carboxyl and

hydroxyl groups that are critical for nanocomposite stability in water due to electrostatic repulsion.[2] The flow rate was operated at 12.4 L/min (nebulizer pressure 14 psi (96.53 kPa)), resulting in ~1.6 s residence time. During the flight in the furnace, GO became crumpled under the evaporation-induced confinement force, and could effectively encapsulate nanoparticles dispersed in the precursor solution.[5] Finally, the nanocomposites were collected downstream of the reactor using a membrane filter (Millipore), weighed and dispersed into water to obtain 200 mg/L dispersion.

Photocatalytic Activity Evaluation

Flow-through mode. A customized filter holder modified with 10 UV LED lights (NSPU510CS, Nichia Corp., with peak wavelength 375 nm and operated at 3.6 V) was utilized. 180 mL 7.5 mg/L MO was filtered under 0.28 bar (4 psi) both with and without turning UV light on. The MO concentration in the outflow tank was monitored constantly by UV-vis spectroscopy (at peak 463 nm), and the total dispensing time was recorded.

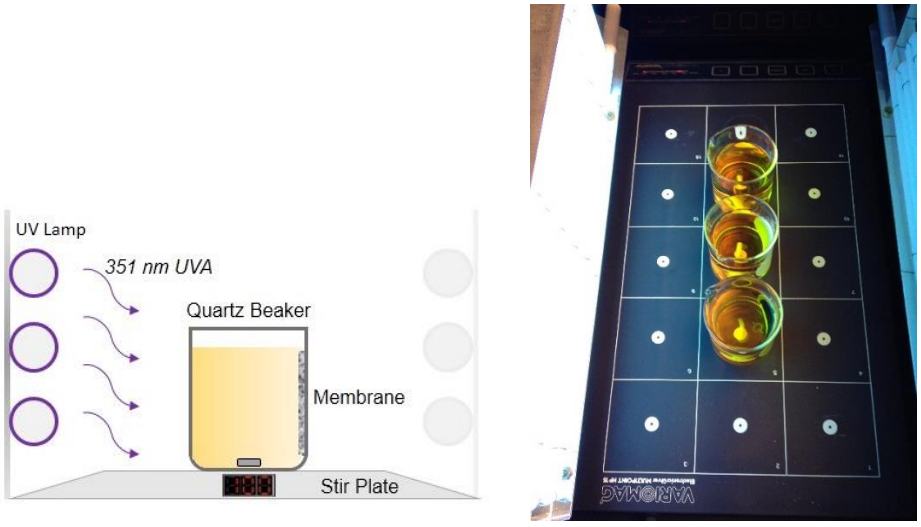

Figure S7.2. The photocatalytic degradation experimental setup-batch mode (Left: scheme; Right: photo)

Batch mode. A quartz beaker was used as the reactor and a customized UV reactor was applied to provide UV light irradiation, which is centered at 351 nm and with an intensity of 900 uw/cm^2 (Figure S7.2). 70 mL 7.5 mg/L MO was added into the beaker with GOTI membrane. In the first 30 min, the sets were kept in dark to achieve adsorption equilibrium. Then the UV was turned on. The solution was sampled at each 30 min and measured by UV-Vis. The MO concentration was determined by the absorbance at 463 nm. Blank PES membrane, and pure MO solution were irradiated at the same time as controls.

S7.2. Results and Discussion

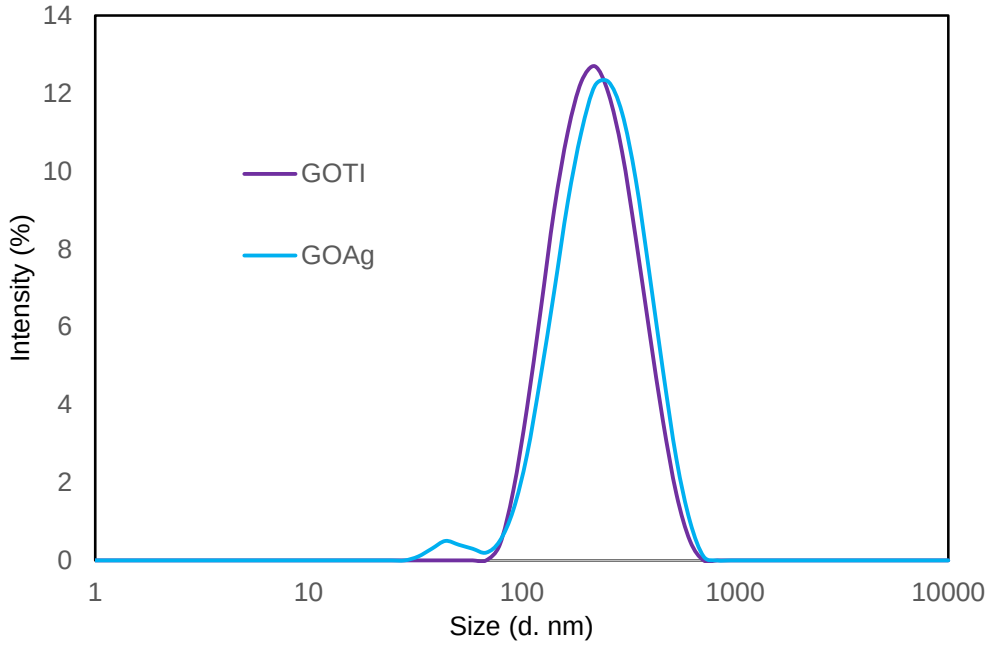

Figure S7.3. Hydrodynamic size distribution of GOTI and GOAg measured by DLS

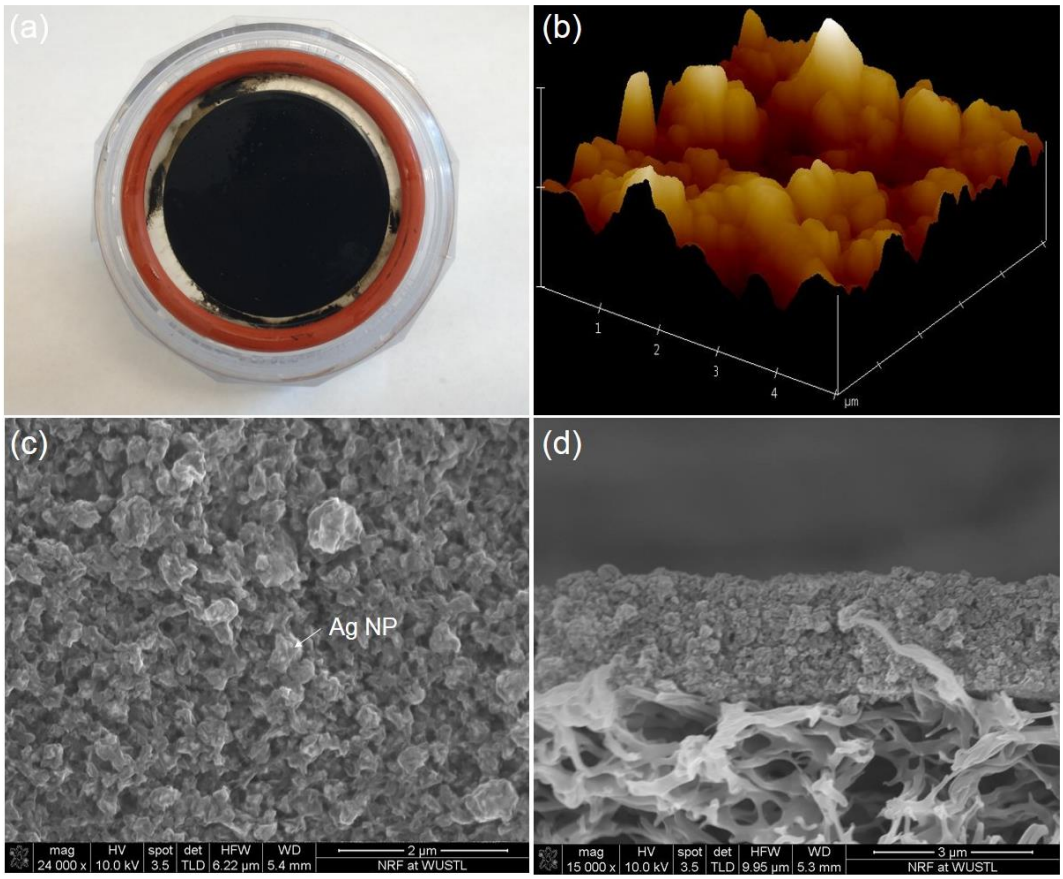

Figure S7.4. Characterization of GOAg membrane (with 3 mg GOAg deposition): (a) digital photo; (b) AFM 3D surface image (with mean roughness R_a = 75.3 ± 1.5 nm, R_q = 95.0 ± 0.4 nm); (c) SEM top view (with Ag NP visible and pointed out by the white arrow, due to its larger particle size compared to TiO_2 NPs); (d) SEM cross-sectional view, with 3 mg corresponding to a thickness of ~2.4 µm.

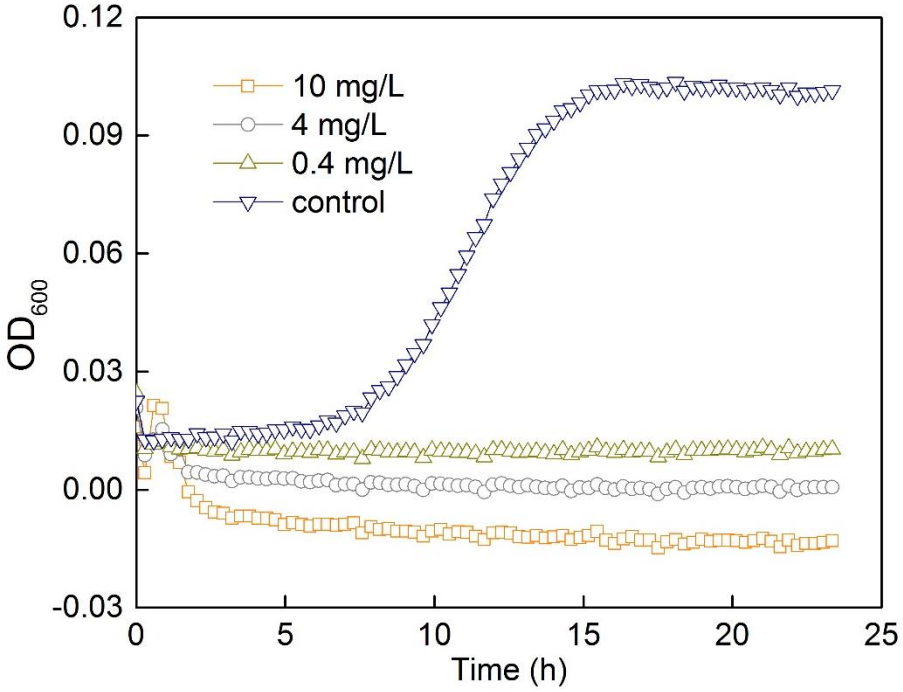

Figure S7.5. *E. coli* growth in minimal Davis media with the presence of GOAg (0-10 mg/L).

Photodegradation Batch Experimental Results. The batch experimental results clearly shows initial adsorption of Methyl Orange (MO) by GOTI membrane nearly approached 40% of the total MO in the solution (Figure S7.5). Then, with UV light irradiation, MO concentration with GOTI membrane presence began to decrease gradually. After 3 h UV reaction, about 35% still remains in the solution; while for other two cases (PES support/pure MO solution), the concentration did not decrease. In addition, light intensity has a significant impact on the photocatalytic degradation of MO. When light intensity decreased from 900 uW/cm^2 to 520 uW/cm^2, the pseudo first-order reaction rate constant also decreased from 0.0061 min^{-1} to 0.0036 min^{-1}.

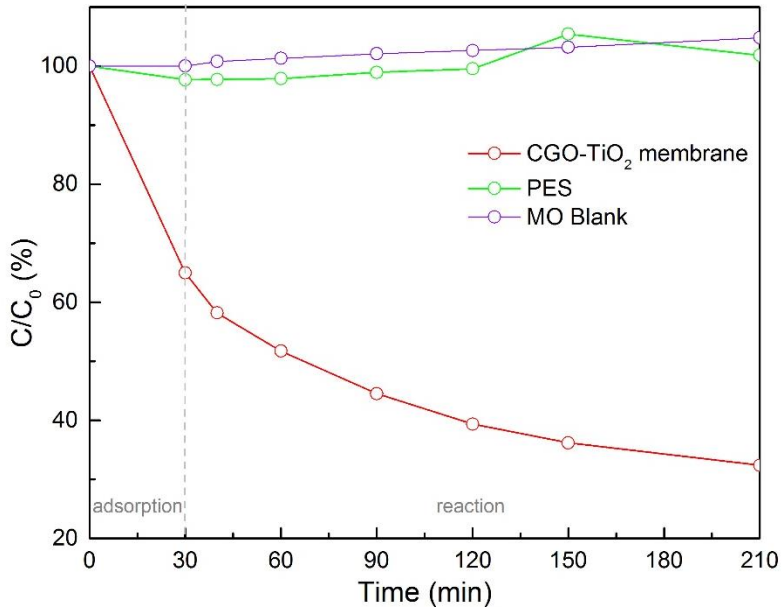

Figure S7.6. Photodegradation of MO using GOTI membrane in a batch mode

Flow through ultrafiltration membrane by Kozeny-Carman equation. The Kozeny-Carman equation describes the relation between pressure drop and flux of a fluid flowing through a porous filter,[6] which is given as:

$$\frac{\Delta P}{h} = J * \frac{72\mu\tau}{D_P^2}\frac{(1-\varepsilon)^2}{\varepsilon^3}$$

where ΔP is the pressure drop, h is the total height of the filter, J is the flux, μ is the viscosity of the fluid, ε is the porosity of the filter, τ is the tortuosity of the channels in the packed bed, and D_p is the diameter of the related spherical particle.

In this work, the parameters were determined as follows (Table S7.1):

Table S7.1. Membrane surface layer and filtration parameters

Parameter	Quantity	Unit
ΔP	10k	Pa
h	5.4	μm
viscosity	0.00089	Pa·s
D_p	200	nm
Flux	6.8×10^{-5}	m/s
Tortuosity	2.5	

The calculated porosity is 0.21 with selected tortuosity 2.5 (most common value for ultrafiltration membranes).

Estimation of porosity based on material balance. Assume GOTI nanocomposite contains x wt.% GO and y wt.% TiO_2, and each nanocomposite is compact closed core-shell nanostructure, then The density of the nanocomposite is

$$\rho_{CGO-nTiO2} = \frac{m_{CGO-TiO2}}{\frac{m_{GO}}{\rho_{GO}} + \frac{m_{TiO2}}{\rho_{TiO2}}} = \frac{1}{\frac{x}{\rho_{GO}} + \frac{y}{\rho_{TiO2}}}$$

Where density of GO and TiO_2 are 1.8 and 4.26 g/cm^3 respectively in this work.

Then a membrane with a deposited mass of m mg, has volume:

$$V_{CGO-TiO2} = \frac{m}{\rho_{CGO-TiO2}}$$

The membrane volume is:

$$V_{membrane} = S \times h$$

Where S is the deposited surface area (m^2), and h is the membrane thickness (m).

The membrane porosity is:

$$\varepsilon = 1 - \frac{V_{CGO-TiO2}}{V_{membrane}}$$

From the experiment, GOTI contains ca. 80% GO and 20% TiO_2 as identified by ICP-MS analysis. 6 mg surface layer corresponds to a thickness of 5.4 um. The deposited membrane surface area is 8.1×10^{-4} m^2. The porosity can be estimated to be ~0.33.

Supplementary References

1. Hummers, W. S.; Offeman, R. E., Preparation of Graphitic Oxide. *J. Am. Chem. Soc.* 1958, *80*, (6), 1339-1339.
2. Wang, W.-N.; Jiang, Y.; Biswas, P., Evaporation-Induced Crumpling of Graphene Oxide Nanosheets in Aerosolized Droplets: Confinement Force Relationship. *J. Phys. Chem. Lett.* 2012, *3*, (21), 3228-3233.

3. Jiang, Y.; Wang, W.-N.; Biswas, P.; Fortner, J. D., Facile Aerosol Synthesis and Characterization of Ternary Crumpled Graphene–TiO_2–Magnetite Nanocomposites for Advanced Water Treatment. *ACS Appl. Mater. Interfaces* 2014, *6*, (14), 11766-11774.
4. Wang, W.-N.; Jiang, Y.; Fortner, J. D.; Biswas, P., Nanostructured Graphene-Titanium Dioxide Composites Synthesized by a Single-Step Aerosol Process for Photoreduction of Carbon Dioxide. *Environ. Eng. Sci.*2014, *31*, (7), 428-434.
5. Chen, Y.; Guo, F.; Jachak, A.; Kim, S.-P.; Datta, D.; Liu, J.; Kulaots, I.; Vaslet, C.; Jang, H. D.; Huang, J.; Kane, A.; Shenoy, V. B.; Hurt, R. H., Aerosol Synthesis of Cargo-Filled Graphene Nanosacks. *Nano Lett.* 2012, *12*, (4), 1996-2002.
6. Bowen, W. R.; Jenner, F., Theoretical Descriptions of Membrane Filtration of Colloids and Fine Particles: An Assessment and Review. *Adv. Colloid Interface Sci.* 1995, *56*, (0), 141-200.

Chapter 8. In Situ Photocatalytic Synthesis of Ag Nanoparticles (nAg) by Crumpled Graphene Oxide Composite Membranes for Filtration and Disinfection Applications

Abstract

Graphene oxide (GO) materials have demonstrated considerable potential in next-generation water treatment membrane-based technologies, which include antimicrobial applications. GO antimicrobial properties can be further enhanced by preloading or chemically generating surface associated nanoscale silver particles (nAg). However, for these systems, enhanced antimicrobial functionality decreases over time as a function of Ag mass loss via dissolution (as Ag^{+}). In this work, we demonstrate facile photocatalytic in situ synthesis of nAg particles by crumpled GO-TiO_2 (GOTI) nanocomposites as an approach to (re)generate, and thus maintain enhanced antimicrobial activity over extended operation times. The described photocatalytic formation process is highly efficient and relatively fast, producing nAg particles over a size range of 40 to 120 nm and with active (111) planes. Additionally, we show in situ surface-based photocatalyzed synthesis of nAg particles at the surface of GOTI nanocomposite membrane assemblies, allowing for simultaneous filtration and disinfection. With ca. 3 log inactivation for both *Escherichia coli* and *Bacillus subtilis*, the described membrane assemblies with in situ formed nAg demonstrate enhanced antimicrobial activity compared to the GOTI membrane surface or the support membrane alone. Under typical conditions, the working/ operational time (Ag dissolution time) is calculated to be over two orders of magnitude higher than the loading (synthesis) time (e.g., 123 h vs. 0.5 h, respectively). Taken together, the results highlight the described material-based process as a potentially novel anti-fouling membrane technology.

8.1 Introduction

Membrane technologies are now widely employed for separation and reclamation processes for wastewater streams and for the desalination of sea and brackish waters, among other applications.[1, 2] As a size-selective sieve or a dense physical barrier technology, water treatment membranes allow for high separation efficacies, low chemical inputs, relatively low energy consumption and space requirements, and overall simplicity of operation.[3, 4] However, despite significant technological advancements, a number of challenges remain for membrane technologies, including chemical and biological fouling.[5]

Advances in nanoscale science and engineering now enable rational, molecular-scale material design. As an oxidized form of atomically thin graphene, graphene oxide (GO) can be superhydrophilic while maintaining extreme surface-area-to-volume ratios and broad functionalization possibilities. With structural (e.g., forming unique nanochannels and hydrophilicity[6]) and economic (scale-up) advantages,[7] GO holds considerable potential for use in water treatment membranes, including reverse osmosis,[8] nanofiltration,[9] and ultrafiltration.[10] To date, GO membranes have demonstrated enhanced water flux properties (ca. 4-10 times higher flux than that of commercial nanofiltration membranes[9]) and intrinsic antimicrobial properties via physical disruption,[11] production of reactive oxygen species,[12] and forced extraction of phospholipids from cell membranes.[13] We have demonstrated similar antimicrobial properties in our recent work with superhydrophilic, selective, and reactive crumpled graphene oxide (CGO) based membrane assemblies.[14] These membranes not only showed high water permeability, but also inactivation (> 99.9%) of *E. coli* when CGO composites were engineered to encapsulate Ag NPs, which allowed for Ag^+ release/dissolution.

As an antimicrobial, Ag NPs (also termed nAg) can function through multiple mechanisms, including direct (particle induced) cell membrane and/or DNA damage, and by Ag^+ ions.[15, 16] For such inactivation/disinfection applications, nAg mass dissolution is typically a limiting variable, as the complete dissolution of Ag leads to loss of activity.[14, 17, 18] Regeneration of antimicrobial properties can be achieved through in situ formation of Ag NPs on/in the membrane surface. To date, engineered reduction of Ag^+ to nAg has been focused on chemical reduction processes ($NaBH_4$ or oleylamine).[18, 19, 20, 21] Alternatively, photocatalyzed synthesis under UV[22] or ambient (sunlight) light irradiation,[23] offers an attractive, chemical free, synthesis route (i.e. no additional chemical reagents needed, other than Ag precursor). For all, (re)formation processes need to be rapid compared to dissolution rates for in situ (re)generation to be technically advantageous.

Previously, we have described an innovative, single step aerosol method to synthesize crumpled nanocomposites of CGO whereby a variety of functional materials can be incorporated, via encapsulation.[24] Further, we demonstrated these materials, as CGO-TiO_2 nanocomposite (GOTI) catalysts, exhibit enhanced photo-reductive properties by substantially increasing the occurrence and availability of electrons (through reducing hole-electron recombination).[25] Further, we have also shown that these composites can be readily assembled as superhydrophilic, selective, and photoreactive membranes.[14] In this work, we expand/advance the previous membrane technology, demonstrating rapid, photocatalyzed formation of Ag NPs on GOTI nanocomposites surfaces, via Ag^+ reduction, thus enabling CGO based membrane assemblies for concurrent filtration and disinfection. Photocatalyzed (re)formation of nAg on GOTI nanocomposites and assembled membranes is demonstrated under UV and simulated solar light (AM 1.5) irradiation conditions. Detailed characterization of resulting particle (nAg) morphology, size (evolution), and crystal structures is included. Membrane (surface-based) antimicrobial properties are

demonstrated for two model bacteria, *E. coli.* and *Bacillus subtilis* (*B. subtilis*). With ca. 3 log inactivation observed for both organisms, membranes with in situ produced nAg demonstrate enhanced antimicrobial activity compared with the GOTI and support membranes. Due to a short hydraulic residence time (< 0.1 s),[14] the leaching rate of Ag was much slower compared to the loading (formation) rate. Finally, a bench-scale system was successfully demonstrated (filter area of 8.1 cm^2), showing that with 0.5 h of Ag loading (i.e., photocatalyzed reduction of 15 mg/L $AgNO_3$ solution under 351 nm UV irradiation, 812 $\mu W/cm^2$) ca. 25 L of water can be filtered before Ag was completely leached from the system (or ~123 h of constant function time under operation pressure of 1 bar). Taken together, this study highlights the potential of GOTI composite based assemblies for photocatalytic, in situ NP (reduction based in this case) synthesis for novel anti-fouling water treatment membrane and disinfection technologies, among others.

8.2 Experimental

8.2.1 Formation of Ag NPs on GOTI

GOTI nanocomposites, with unique open core-shell structure (CGO encapsulating TiO_2 NPs), were synthesized, via an aerosol method, and characterized as reported in our previous work.[25, 26] As formed, nanocomposites were collected downstream of the reactor using a membrane filter (Millipore GTPP, 200 nm), weighed, and dispersed into water, resulting in a 200 mg/L suspension. The formation of Ag NPs by photocatalyzed reduction of Ag^+ on GOTI was firstly evaluated as batch reactions, under both UV and simulated solar light (AM 1.5) irradiation. Reactions under UV irradiation were conducted in a customized UV reactor (with variable light intensity (0-2 mW/cm^2) centered at 351 nm), while the solar light irradiation was performed by a solar light simulator (Oriel Newport 91160-1000, operated at 190 W with light intensity of 72 mW/cm^2 in the 250-950 nm range) (light spectra shown in Figure S8.1). 50 mL mixed solution of

GOTI (20 mg/L) and Ag^+ (10-30 mg/L $AgNO_3$, Sigma-Aldrich) were added into a quartz reactor and then stirred in dark for 1 h to achieve adsorption equilibrium before being placed under either UV or solar light irradiation. At each time interval (0, 5, 10, 20, 40 and 60 min), aliquots of 2 mL were sampled and further filtered using a syringe filter (Millipore PES, 0.22 um pore size), and the filtrate was then diluted properly with 2% HNO_3 for inductively coupled plasma mass spectrometry (ICP-MS, Agilent 7500cc) measurements to determine the Ag^+ concentration in the solution. Each experiment was conducted in triplicate.

Composite morphology and size of pristine GOTI and formed Ag NPs were examined by field emission scanning electron microscopy (FESEM, NOVA NanoSEM 230), transmission electron microscopy (TEM, Tecnai TM Spirit), and high-resolution TEM (HR-TEM, JEOL 2100) with Gatan Imaging Filter (GIF).

8.2.2 GOTI Membrane Synthesis and Characterization

Synthesis of GOTI membranes were accomplished via vacuum filtration which evenly deposited GOTI nanocomposites onto a poly(ethersulfone) support (PES, Sterlitech, with heterogeneous pore size distribution from 80 nm to 1 μm), as detailed previously.[14] In brief, 15 mL of 0.2 mg/mL GOTI dispersion (mass = 3 mg) was mixed with 75 μL polyallylamine solution (PAA, Sigma-Aldrich, Mw ~ 12000, 20 wt. % in H_2O, ρ =1.02 g/mL) and the mixture was then sonicated for 2 h in a bath sonicator (Branson 2510). During the sonication, amine groups on the long alkyl chain of PAA readily react with oxygen functional groups on the CGO surface, creating new C-N bonds and leading to broad chemical cross-linking.[27] The mixture was eventually vacuum filtered onto the PES support membrane (pre-soaked in 1% PAA solution for 2 h) at a low flow rate (~0.3 mL/min), resulting superhydrophilic, selective, and photoreactive top layer (~0.8-0.9 μm thick/mg deposition) with a mass density of 3.7 g/m^2.[14]

Membrane characterization was performed by FESEM and atomic force microscopy (AFM) (membrane morphology and surface roughness), water contacting angle (surface hydrophilicity), Fourier transform infrared spectroscopy (FTIR) and Raman scattering (functionality and C-C bonding), as detailed in our previous work.[14]

8.2.3 In situ Ag NPs Formation on Membrane Surface

Similar to batch experiment, as-synthesized GOTI membrane (3 mg deposition) was initially placed in 70 mL 15 mg/L $AgNO_3$ (Sigma-Aldrich) solution to achieve adsorption equilibrium for 1 h. After that, the membrane coupon was taken out of the solution and placed in the quartz beaker with another 70 mL 15 mg/L $AgNO_3$ solution. The 30 min reaction was conducted in the customized UV reactor (351 nm centered with measured intensity of 812 $\mu W/cm^2$) in which the membrane coupon was placed, with the active (deposited) side towards the UV light direction (SI, Figure S8.2). The concentrations of Ag^+ before and after adsorption and reaction were measured using ICP-MS according to the same procedure described above.

Membrane water permeability with and without Ag formation was evaluated under a direct flow and constant pressure dead-end filtration mode, while measuring the permeated water flux. The constant pressure (1 bar) was provided by a compressed N_2 gas tank (Airgas NI 300), and the feed water was pumped from a pressurized 'storage' tank (Millipore Amicon 8200) to a 47 mm filter holder (Pall Life Science). Permeated solution was measured over time (thus flux) by an integrated electronic balance and the data was automatically logged at 60 s interval. Filtration properties of GOTI and GOTI-Ag membranes were evaluated by filtering two model contaminants of different molecular weights, methyl orange (MO, 7.5 mg/L, Mw= 327.3 Da, Sigma-Aldrich) and bovine serum albumin (BSA, 10 mg/L, Mw = ~66.5 kDa, Sigma-Aldrich) as done in our

previous work.[14] The concentrations of MO and BSA were analyzed using a UV−vis spectrophotometer (Varian Bio 50) at wavelengths of 463 and 220 nm, respectively.

Meanwhile, the Ag^+ releasing in the flow-through mode was monitored by measuring the Ag^+ concentration in the outflow. 50 mL Milli-Q water was passed through the holder and the Ag^+ concentration in the solution was measured by ICP-MS, and meanwhile the flow rate was monitored. The experiments were repeated for 5 times (with 3 reacted membranes) when Ag^+ concentration in the outflow was found to have gradually reached a steady state.

8.2.4 Antimicrobial Property Evaluation

The membrane antimicrobial activity against *E. coli* (Gram-negative, ATCC 11775) and *B. subtilis* (Gram-positive, ATCC 6633),[28, 29] was tested for both unmodified and modified membranes. Overnight bacterial culture (0.5 %) was inoculated into fresh LB medium and then cultured under 37 ^oC to reach exponential growth phase. The bacterial suspension was then centrifuged and washed with 0.9% saline solution twice before being dispersed again into 0.9% saline solution with a final concentration of 10^7 CFU/mL. Antimicrobial properties were evaluated by the inactivation of cells on the membrane surfaces as described in protocols reported by Elimelech's group.[17, 19, 30] Briefly, 400 μL of suspension was placed in contact with the active side of the membrane (4.3 cm^2) coupon for 2 h (the side with deposited GOTI and formed Ag NPs). After 2 h, the upper bulk suspension was removed and the membrane coupon was rinsed by sufficient 0.9% saline solution to remove the unattached cells on the surface. Next, the rinsed membrane coupon was sonicated mildly in 5 mL 0.9% saline solution for 7 min. 100 μL of the suspension was withdrawn, serially diluted, and spread over LB plates. The plates were then incubated at 37 ^oC for overnight in dark before counting the bacterial colonies (CFUs). All antibacterial tests were conducted at least in triplicate.

8.3 Results and Discussion

8.3.1 Formation Kinetics of Ag NPs on GOTI

GO, with ultrahigh theoretical specific surface area (2675 m^2/g),[31] contains electron rich, oxygen-functionalities while retaining aromatic basal plane regions.[32] Such structure provides highly favorable enthalpic interactions for both positively charged ions and aromatic/hydrophobic molecules. Reported GO sorption capacities for metal ions are among the highest material values reported, including Cd^{2+} (106.3 mg/g) and Co^{2+} (68.2 mg/g).[33] In this work, significant adsorption of Ag^+ (363.1 mg Ag^+/g GOTI) was observed after 1 h adsorption in dark (Eqn. 1), which is comparable to values reported for other carbon materials, including carbon nanospheres (152 mg/g)[34] and highly oxidized carbon fibers (400 mg/g).[35]

$$GOTI + (Ag^+)_n \rightarrow GOTI\text{-}(Ag^+)_n \quad (1)$$

Under standard conditions, direct reduction of Ag^+ to Ag^0 is not thermodynamically favorable due to potential of the reaction (E^0 = -1.8 V vs. NHE); however, the reaction becomes thermodynamically possible if Ag^+ exist on/at stable silver clusters (Ag^0) (reduction potential E^0 = 0.799 V vs. NHE).[36,37] The initial existence of silver clusters was indicated by the UV-vis absorption peak at ~325 nm (Figure S8.3).[36] Additionally, TiO_2, as a semiconductor, produces electron-hole pairs under UV irradiation with energies greater than its band gap (3.2 eV) (Eqn.2).[38] The presence of graphene decreases the recombination rate of holes and electrons, and as a result, the occurrence and availability of electrons can be significantly increased, leading to enhanced reduction reactions.[25] The photo-induced (available) electrons have relatively strong redox potentials (E^0 = -0.7 V vs. SCE),[39] which can reduce Ag ions to form Ag^0 (Eqn. 3). The predominant appearance of Ag NPs on GOTI supports heterogeneous photodeposition as the major

mechanism, via which photo-induced electrons reduced silver cations that were adsorbed on the surface of GO/TiO_2 (Eq. 1-3).[22]

$TiO_2 + h\nu \rightarrow TiO_2 + h^+ + e^-$ (2)

GOTI-$(Ag^+)_n + Ag^0_\infty$ (cluster) + $e^- \rightarrow$ GOTI-$(Ag^+)_{n-1} + Ag^0_\infty$ (particle) $E^0 = 0.799$ V vs. NHE (3)

This reaction takes place rapidly under UVA irradiation (351 nm centered with intensity of 1230 $\mu W/cm^2$, Figure 8.1a). Ag^+ concentration in the solution continued to decrease over the entire reaction period, with ca. 25% of the original concentration remaining in the solution after 60 min reaction (C_0 = 30 mg/L $AgNO_3$, $C_{60\ min}/C_0 = 0.24 \pm 0.08$). The total amount of reduced Ag was calculated to be 854 mg/g GOTI. However, for reactions under simulated solar light irradiation, Ag^+ concentration decreased slightly to C/C_0 = ~0.9 in the first 5 min and then was constant in the following reaction time, indicating slower reaction kinetics, suggesting that formed Ag NPs were mainly from pre-adsorbed Ag^+ (Figure 8.1a). The difference between AM 1.5 and UV reaction kinetics indicates that, for this reaction, GOTI is primarily UV (as UVA) active.

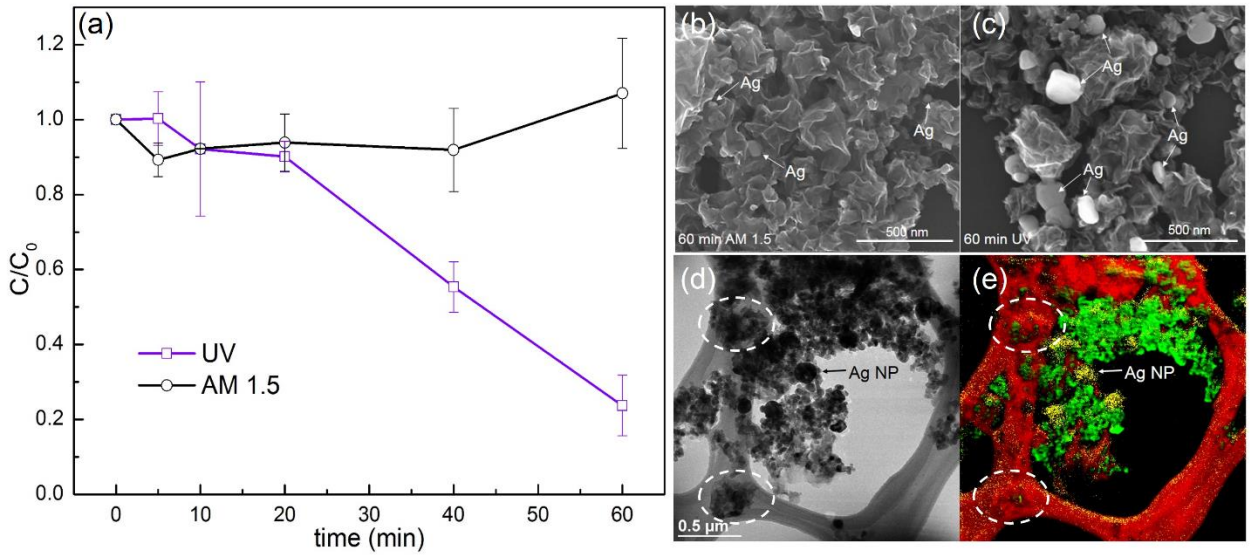

Figure 8.1 (a) Evolution of Ag^+ concentration (C/C_0) in the solution with the presence of 20 mg/L GOTI under UV and solar light irradiation; (b) and (c) SEM images of GOTI and formed Ag NPs after 60 min solar and UV light irradiation, respectively; (d) and (e) TEM and reconstructed TEM-GIF images of GOTI and formed Ag NP under UV irradiation (yellow: Ag; red: carbon; green: Ti). C_0 = 30 mg/L $AgNO_3$.

SEM micrographs also reveal a difference between the as formed nAg for the two irradiation conditions evaluated (Figure 8.1b and c). Under simulated solar light, fewer Ag NPs can be observed after 60 min reaction (Figure 8.1b) and with small sizes (usually < 100 nm) (indicated by white arrow in the figure). Under UVA irradiation, an increased number of Ag NPs were formed with generally larger sizes ranging from tens of nm to a few hundred nm. The formation of Ag NPs was further examined and confirmed by TEM based EELS (Figure 8.1d and e). In Figure 8.1e, GOTI nanocomposites correspond to the red bulks 'bumped' from the (TEM) grid plane (circled in white), with CGO as the shell (carbon in red color) and TiO_2 as the core (which is encapsulated). As we reported previously,[25] encapsulation limits can be maximized if TiO_2 concentration in the precursor is high, leading to aggregation of TiO_2 nanoparticles on the outer surface of CGO. This was also observed here by the appearance of (separated) TiO_2

nanoparticles/agglomerates (Titanium in green, Figure 8.1e) on the composite surface. Ag NPs were observed (silver in yellow, Figure 8.1) among GOTI and TiO_2 structures, with sizes in between TiO_2 (~ 20 nm) and GOTI (200-400 nm).

8.3.2 Size, Morphology and Structure of Ag NPs

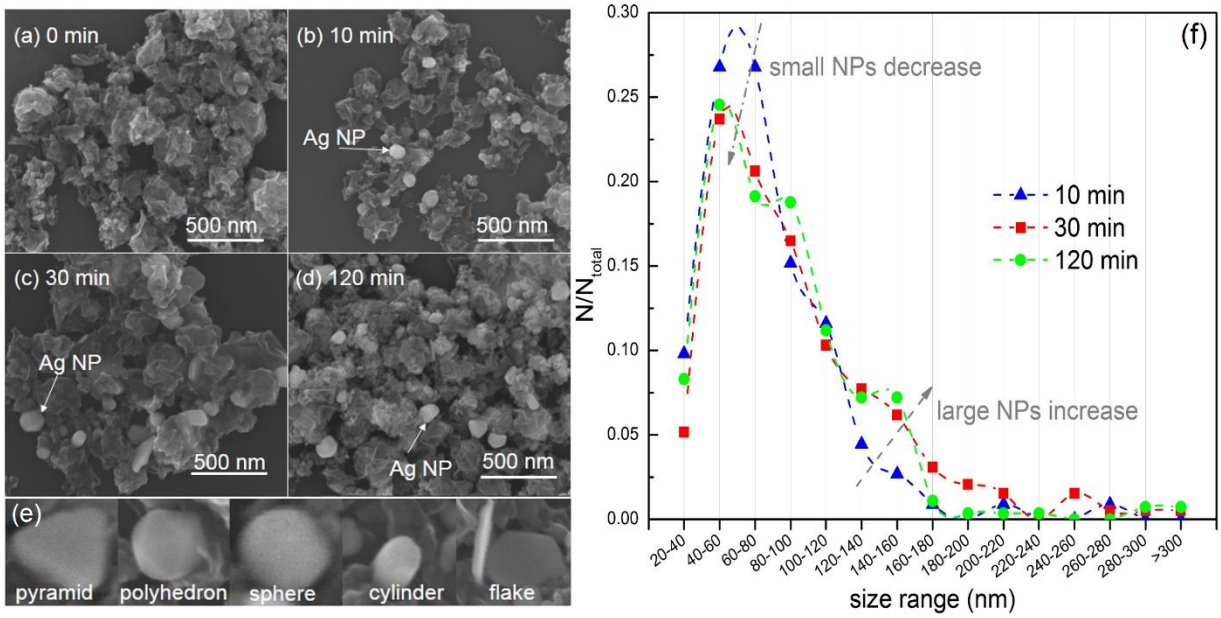

Figure 8.2 Size and morphology evolution of Ag NPs by photocatalytic reduction of Ag^+ on GOTI nanocomposites after 10, 30 and 120 min reaction. (a-d) show the SEM images of pristine GOTI (a) and as-synthesized Ag NPs at 10 min (b), 30 min (c), and 120 min (d). (e) Ag NPs formed with different morphologies. (f) size distribution of Ag NPs at different reaction time. Dash lines are guided lines for the eye only. C_0 = 10 mg/L.

Size and morphology of evolved Ag NPs as a function of irradiation time is shown in Figure 8.2. Initially, only GOTI nanocomposites can be observed (Figure 8.2a), with the typical crumpled 'paper-ball-like' morphology described above.[25] Upon 10 min of UV irradiation, large amounts of Ag NPs were observed, most of which are in polyhedron shapes (white dots indicated by the white arrows in the Figure 8.2b-d). Ag NPs were further observed to have grown into larger sizes after

30 min reaction (Figure 8.2c), and more shapes were found, which include pyramid, sphere, cylinder and flake (Figure 8.2e).

Particle size was reported as the longest structural dimension imaged (by SEM, Figure 8.2a-d), and for each size distribution, > 150 Ag NPs were randomly sampled (total counts: 583). Size distribution analysis shows that most NPs are between 40 and 120 nm regardless of the reaction time (the peak range in Figure 8.2f). According to the Mie theory, a strong, sharp extinction peak located at 380-420 nm (due to surface plasmon resonance effect) exists for silver particles < ca. 40 nm in diameter.[37] The UV-vis spectra of these nanoparticles showed no such peaks (Figure S8.3), agreeing with the observed size distribution (mostly between 40 and 120 nm). While Ag NPs were rapidly formed in the first 10 min of the reaction, from 10 min to 30 min, the fraction of small NPs decreased (mostly 20-80 nm) and the number of large particles increased (as ca. 140-220 nm) (Figure 8.2f). Further, the size distribution did not change significantly after 30 min (to 120 min). For example, at 10 min, particles with sizes between 40-80 nm account for 54% of the total; while at 30 min and 120 min, that has decreased to 45% and 44% respectively, due to the production of larger particles (in the size range between 120-160 nm increased from 7% at 10 min to 14% at 30/120 min). Additional TEM examination also supported the observation that formed Ag NPs were mainly between 40 and 120 nm (Figure S8.4).

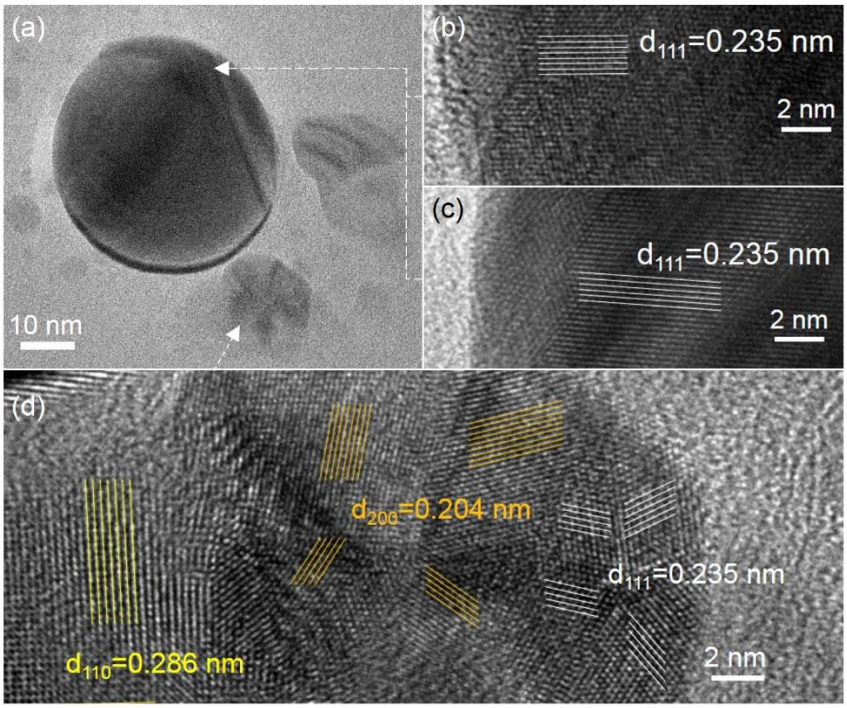

Figure 8.3 HRTEM characterization of representative formed Ag NPs on GOTI. (b), (c) and (d) are enlarged parts of the particles in (a) (as pointed out by white arrows).

High-resolution (HR) TEM was employed to identify the crystal structure of formed Ag NPs (Figure 8.3). Ag NPs consist of three planes, including (111) plane (d = 0.235 nm), (110) plane (d = 0.286 nm), and (200) plane (d = 0.204 nm), consistent with the face centered cubic (fcc) crystal structure of Ag with a lattice length a = 0.409 nm.[22] For larger particles, (111) planes were identified, consistent with previous reports (Figure 8.3b and c).[22] Multiple crystal structures were identified in one particle, indicating growth of large particles possibly by diffusion coalesce (Figure 8.3d), as observed by others.[40] It has been demonstrated that the reactivity of Ag NPs is relatively enhanced for high-atom-density planes such as (111) plane, with particle geometries containing more reactive (111) planes to be relatively more biologically active than other shapes.[41]

8.3.3 Surface Formation of Ag NP on GOTI Membranes

The fabrication, characterization, and performance evaluation of CGO based membranes have been previously detailed in our recent work.[14] As assembled, membrane surfaces reveal peak-valley morphology (Figure 8.4c), and maintain surface enhanced hydrophilicity (via oxygen functionality), as identified by FTIR, Raman Spectroscopy and water contact angle measurements. Here 3 mg of GOTI composites were deposited onto a PES support, resulting in a water flux of 454 ± 31 L/(m^2 ħ ƀar), which decreased from > 5800 L/(m^2 ħ ƀar) for the PES support only (Figure 8.4a). This is in line with water flux results obtained previously, and agrees with classic Kozeny-Carman description for porous filters (i.e. water flux decreases monotonically as deposition mass increases).[5]

For 3 mg GOTI membranes, adsorbed Ag^+ mass was measured to be 53.5 ± 8.0 μg (18 mg Ag^+/g GOTI), which is one order of magnitude lower than that of suspended, monodisperse GOTI nanocomposites (363.1 mg Ag^+/g GOTI). This decrement is likely due to loss/blocking of adsorption sites and accessibility due to packing and cross-linking of CGOs. Photocatalytic reduction experiment showed an average of 160.4 ± 44.7 μg in additional mass of Ag (as Ag(0) NPs) onto/into the membrane within 30 min (53 mg Ag^+/g GOTI), which is almost 3 times that of adsorption alone. Impregnated membranes were then examined by SEM, as shown in Figure 8.3d-f. After 30 min UV irradiation, Ag NPs were observed periodically over the entire membrane surface (Figure 8.3d). Further, unlike Ag NPs formed on monodisperse GOTI during batch reactions, which have multiple shapes (Figure 8.2e), in situ, surface formed Ag NPs are primarily flake shaped (Figure 8.2d inset). Ag NPs were only observed at a depth of a few hundred nm below the upper assembly surface, likely corresponding to the dimension of one CGO nanocomposite

(Figure 8.2e and f), thus indicating that photocatalytic reduction is typically localized to the topmost composite layer (or a few hundred nm).

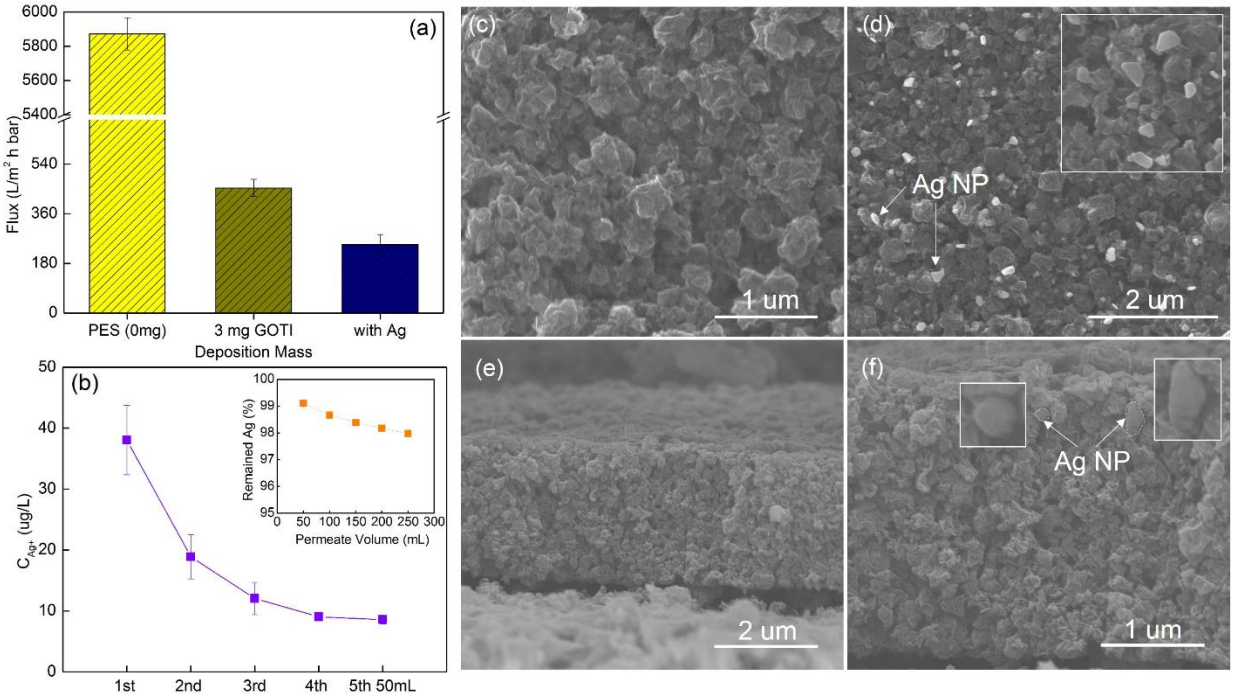

Figure 8.4 (a) pure water flux of the PES support, GOTI modified membrane, and membrane with Ag NPs; (b) Ag^+ concentration in the permeate (pure water), and remained Ag as a (mass) percentage of total loaded Ag with permeate volume (in the inset); (c) SEM image of unmodified CGO membrane surface; (d) SEM image of the membranes with formed Ag NPs (top view), with enlarged image in the inset; (e) and (f) cross-sectional view of the membrane surface with two magnifications (d: ×20000; e: ×40000), in Figure f. inset graphs are the enlarged Ag NPs indicated by the white arrows.

Upon Ag NP formation, additional decrement of pure water flux is observed (249 ± 35 L/(m^2 h bar)), due to pore blocking (Figure 8.4a). This phenomenon is expected based on our previous work,[14] whereby similar assembled membranes have effective pores which are relatively small compared to the sizes of formed Ag NPs. The membranes were also evaluated by filtering

aqueous solutions of two different sized molecules, using methyl orange (MO, M_w = 327 Da) and bovine serum albumin (BSA, M_w = 66.5 kDa). Rejection of MO and BSA were 24 ± 9% and 64 ± 12% for GOTI membranes, which increased to 47 ± 26% and 77 ± 7% for GOTI membranes with Ag NPs (formed under 351 nm centered UV irradiation (812 $\mu W/cm^2$) for 30 min). These results are consistent with the estimation of surface pore sizes through analyzing SEM imaging (10-30 nm range).[14]

Ag leaching was monitored by measuring Ag^+ concentration in the collected permeate. For the first 50 mL of permeate (Milli-Q water as feed water), Ag^+ (bulk) concentration was 38.1 ± 5.7 μg/L, which then decreased to 18.9 ± 3.7, 12.1 ± 2.7, 9.0 ± 0.1, and 8.6 ± 0.7 μg/L for the following four flushes of 50 mL Milli-Q water (Figure 8.3b). This concentration level is at the same order of magnitude observed by others for Ag dissolution from Ag NPs on membranes (a few ppb),[18, 42, 43] and is far below the US EPA standard of 100 ppb.[18] Higher concentration of Ag^+ in the initial stage of the permeation was likely from remaining (associated/sorbed) Ag^+, as the penetration depth of light likely limits the photoreductive process regime. Ag^+ permeate concentration eventually stabilized (~ 9 μg /L).

Due to short residence time through the membrane (< 0.1 s),[14] the leaching of Ag was relatively slow. As shown in the inset graph in Figure 8.4b, 98% of Ag remained in/on the membrane after permeation of 0.25 L water. Based on material balance and rate of observed dissolution, such a bench-top system (47 mm filter holder, Pall Life Science), with a filter area of 8.1 cm^2, could filter up to 24.9 L of water before Ag was depleted from the system (or ~123 h of constant function time under operation pressure of 1 bar).

8.3.4 Enhanced Surface Inactivation of Bacteria

Previous studies have shown that flat GO functionalized membranes can significantly reduce the surface attachment and viability of *E. coli*.[30] Additionally, our previous study demonstrated CGO-Ag composite membranes with > 3 log inactivation of *E. coli*.[14] In that case, Ag NPs were encapsulated within the crumpled GO structure with enhancement in antimicrobial activity attributed primarily to dissolution of Ag^{+}.[14]

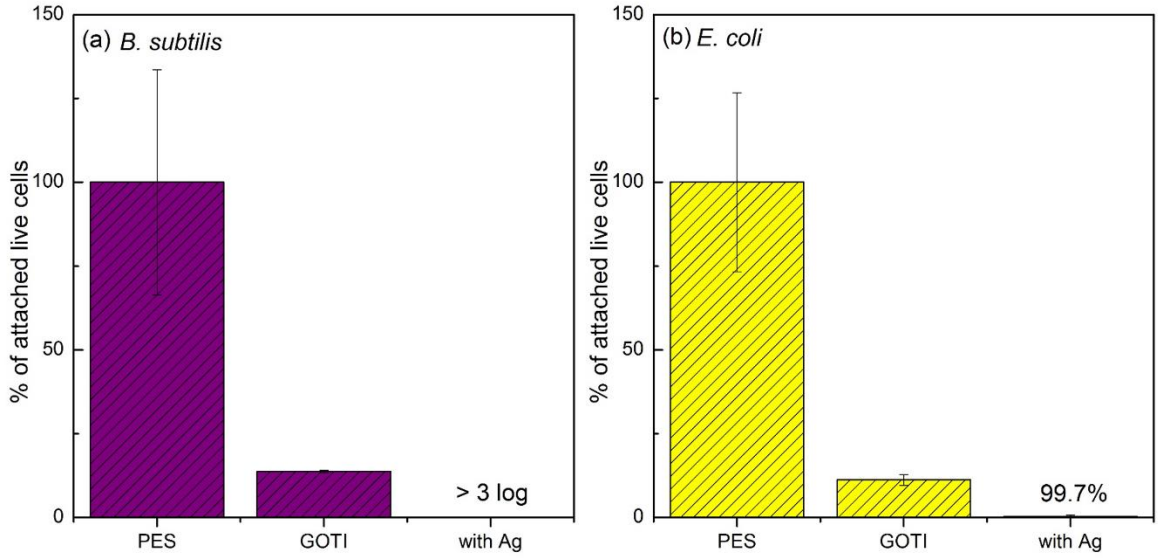

Figure 8.5 Comparison of surface attached live cells after contacting with membrane surfaces (a) *B. subtilis*; (b) *E. coli*. The attached live cells on PES surface were taken as control (100%).

Unlike encapsulated Ag NPs, in situ formed Ag NPs were localized onto/at the GOTI outer shell, thus the membrane surface itself. Here, we examined surface inactivation of *E. coli* and *B. subtilis* on PES, GOTI-PES, and GOTI-Ag-PES membranes. Bacteria dispersion (in 0.9% saline) was placed in contact with the active (deposited and reacted) side of the membrane, and after 2 h surface contact, the remaining viable bacteria population was compared to that contacted with blank PES. Compared to PES only membrane (PES membrane as 100%), GOTI-PES membrane

retains approximately 13.7% and 11.2% of living *B. subtilis* and *E. coli.* cells respectively, which agrees with our previous result on CGO membrane.[14] Inactivation of bacteria by graphene/GO has been reported to be due to cell membrane damage, including physical disruption,[11] formation of reactive oxygen species,[12] and extraction of phospholipids from cell membranes.[13] Again, with Ag formation, the GOTI-Ag-PES membranes reached ca. 3 log removal of both bacteria (Figure 8.5). Small Ag NPs (< 10 nm) have been observed to effectively penetrate into/through cell membranes, leading to significant increase in cell membrane permeability and DNA damage;[15] Ag^+ ions, can interact directly with thiol groups in proteins, resulting in denaturation, and even inhibiting DNA replication.[16, 44] As shown in the previous section, most of as-formed Ag NPs have sizes > 10 nm, thus it is unlikely that the large Ag NPs penetrate into the cells directly. It is thus hypothesized that the enhancement in activity is mainly due to dissolution of Ag^+ and subsequent cellular interactions. However, the effect of direct contact of (such large) Ag NPs with bacteria on the antimicrobial activity remains unclear. Further, the activity crystal facets, as discussed above, affect inactivation of the bacteria is worthy future investigations.

8.4 Environmental Applications

Recent GO membrane-based separation applications have demonstrated material advantages over other engineered carbon nanomaterials, such as carbon nanotubes. These advantages include economic synthesis routes (i.e., simple oxidation and exfoliation of graphite),[7] broad(er) chemical functionalization routes, and the possibility of large arrays of highly tailored, composite materials/assemblies.[45] In addition to physical separations, such membranes can be efficiently (re)generated with regard to antimicrobial properties, without additional reagents besides Ag^+. For future applications, GOTI nanocomposites may also be surface-tethered (similar to what has been demonstrated in this work) onto the outside tube walls of hollow fiber

membranes, or incorporated into the top polymeric layer during the membrane fabrication (phase-inversion) process. Currently, we envision our modified membranes operating like unmodified membranes, with the addition/synthesis of Ag NPs occurring during the regular membrane cleaning processes/cycle. In other words, the modified membranes do not need to be operated under continuous UV irradiation, but instead can be irradiated intermittently. Ideally, the reloading time can be optimized to meet the cleaning cycle (i.e., ca. 1-3 months for most UF membranes in practical applications). As GOTI photocatalyst reactivity is further extended into the visible light regimes, which have been recently demonstrated, facile synthesis/regeneration of Ag NPs, among other reduced nanoparticles, will be possible via simple sunlight irradiation. Building on this, crumpled graphene oxide composite-based water treatment membranes, with enhanced antimicrobial properties through photocatalytic in situ (re)formation of Ag NPs, have potential in regenerative, point-of-use water treatment and reuse systems.

Acknowledgements

This work is supported by the National Science Foundation's CAREER Award (CBET 1454656). The authors also thank McDonnell Academy Global Energy and Environment Partnership (MAGEEP), Washington University in St. Louis for partial funding support. Electron microscopy work was performed at the Nano Research Facility (NRF) at Washington University in St. Louis, a member of the National Nanotechnology Infrastructure Network (NNIN), supported by the National Science Foundation under Grant No. ECS-0335765.

References

1. Shannon, M. A.; Bohn, P. W.; Elimelech, M.; Georgiadis, J. G.; Marinas, B. J.; Mayes, A. M., Science and Technology for Water Purification in the Coming Decades. *Nature* 2008, *452* (7185), 301-310.
2. Elimelech, M.; Phillip, W. A., The Future of Seawater Desalination: Energy, Technology, and the Environment. *Science* 2011, *333* (6043), 712-717.
3. Lewis, S. R.; Datta, S.; Gui, M.; Coker, E. L.; Huggins, F. E.; Daunert, S.; Bachas, L.; Bhattacharyya, D., Reactive Nanostructured Membranes for Water Purification. *Proc. Natl. Acad. Sci. U. S. A.* 2011, *108* (21), 8577–8582.
4. Celik, E.; Park, H.; Choi, H.; Choi, H., Carbon nanotube blended polyethersulfone membranes for fouling control in water treatment. *Water Res.* 2011, *45* (1), 274-282.
5. Mulder, M., *Basic Principles of Membrane Technology*. 2nd ed.; Kluwer Academic Publishers: Dordrecht, 1996.
6. Nair, R. R.; Wu, H. A.; Jayaram, P. N.; Grigorieva, I. V.; Geim, A. K., Unimpeded Permeation of Water Through Helium-Leak-Tight Graphene-Based Membranes. *Science* 2012, *335* (6067), 442-444.
7. Arvidsson, R.; Kushnir, D.; Sandén, B. A.; Molander, S., Prospective Life Cycle Assessment of Graphene Production by Ultrasonication and Chemical Reduction. *Environ. Sci. Technol.* 2014, *48* (8), 4529-4536.
8. Cohen-Tanugi, D.; Grossman, J. C., Nanoporous graphene as a reverse osmosis membrane: Recent insights from theory and simulation. *Desalination* 2015, *366*, 59-70.
9. Hu, M.; Mi, B., Enabling Graphene Oxide Nanosheets as Water Separation Membranes. *Environ. Sci. Technol.* 2013, *47* (8), 3715-3723.

10. Zhang, J.; Xu, Z.; Mai, W.; Min, C.; Zhou, B.; Shan, M.; Li, Y.; Yang, C.; Wang, Z.; Qian, X., Improved Hydrophilicity, Permeability, Antifouling and Mechanical Performance of PVDF Composite Ultrafiltration Membranes Tailored by Oxidized Low-Dimensional Carbon Nanomaterials. *J. Mater. Chem. A* 2013, *1* (9), 3101-3111.
11. Akhavan, O.; Ghaderi, E., Toxicity of Graphene and Graphene Oxide Nanowalls Against Bacteria. *ACS Nano* 2010, *4* (10), 5731-5736.
12. Liu, S.; Zeng, T. H.; Hofmann, M.; Burcombe, E.; Wei, J.; Jiang, R.; Kong, J.; Chen, Y., Antibacterial Activity of Graphite, Graphite Oxide, Graphene Oxide, and Reduced Graphene Oxide: Membrane and Oxidative Stress. *ACS Nano* 2011, *5* (9), 6971-6980.
13. Tu, Y.; Lv, M.; Xiu, P.; Huynh, T.; Zhang, M.; Castelli, M.; Liu, Z.; Huang, Q.; Fan, C.; Fang, H.; Zhou, R., Destructive extraction of phospholipids from Escherichia coli membranes by graphene nanosheets. *Nat. Nanotechnol.* 2013, *8* (8), 594-601.
14. Jiang, Y.; Wang, W.-N.; Liu, D.; Nie, Y.; Li, W.; Wu, J.; Zhang, F.; Biswas, P.; Fortner, J. D., Engineered Crumpled Graphene Oxide Nanocomposite Membrane Assemblies for Advanced Water Treatment Processes. *Environ. Sci. Technol.* 2015, *49* (11), 6846-6854.
15. Morones, J. R.; Elechiguerra, J. L.; Camacho, A.; Holt, K.; Kouri, J. B.; Ram ́ırez, J. T.; Yacaman, M. J., The bactericidal effect of silver nanoparticles. *Nanotechnology* 2005, *16* (10), 2346.
16. Zodrow, K.; Brunet, L.; Mahendra, S.; Li, D.; Zhang, A.; Li, Q.; Alvarez, P. J., Polysulfone ultrafiltration membranes impregnated with silver nanoparticles show improved biofouling resistance and virus removal. *Water Res.* 2009, *43* (3), 715-723.

17. Mauter, M. S.; Wang, Y.; Okemgbo, K. C.; Osuji, C. O.; Giannelis, E. P.; Elimelech, M., Antifouling Ultrafiltration Membranes via Post-Fabrication Grafting of Biocidal Nanomaterials. *ACS Appl. Mater. Interfaces* 2011, *3* (8), 2861-2868.
18. Tang, L.; Livi, K. J. T.; Chen, K. L., Polysulfone Membranes Modified with Bioinspired Polydopamine and Silver Nanoparticles Formed in Situ To Mitigate Biofouling. *Environ. Sci. Technol. Lett.* 2015, *2* (3), 59-65.
19. Ben-Sasson, M.; Lu, X.; Bar-Zeev, E.; Zodrow, K. R.; Nejati, S.; Qi, G.; Giannelis, E. P.; Elimelech, M., In situ formation of silver nanoparticles on thin-film composite reverse osmosis membranes for biofouling mitigation. *Water Res.* 2014, *62* (0), 260-270.
20. Wu, J.; Yu, C.; Li, Q., Regenerable antimicrobial activity in polyamide thin film nanocomposite membranes. *J. Membr. Sci.* 2015, *476* (0), 119-127.
21. Shen, C.; Hui, C.; Yang, T.; Xiao, C.; Tian, J.; Bao, L.; Chen, S.; Ding, H.; Gao, H., Monodisperse Noble-Metal Nanoparticles and Their Surface Enhanced Raman Scattering Properties. *Chem. Mater.* 2008, *20* (22), 6939-6944.
22. Taing, J.; Cheng, M. H.; Hemminger, J. C., Photodeposition of Ag or Pt onto TiO_2 Nanoparticles Decorated on Step Edges of HOPG. *ACS Nano* 2011, *5* (8), 6325-6333.
23. Zhang, L.; Yu, J. C.; Yip, H. Y.; Li, Q.; Kwong, K. W.; Xu, A.-W.; Wong, P. K., Ambient Light Reduction Strategy to Synthesize Silver Nanoparticles and Silver-Coated TiO_2 with Enhanced Photocatalytic and Bactericidal Activities. *Langmuir* 2003, *19* (24), 10372-10380.
24. Wang, W.-N.; Jiang, Y.; Biswas, P., Evaporation-Induced Crumpling of Graphene Oxide Nanosheets in Aerosolized Droplets: Confinement Force Relationship. *J. Phys. Chem. Lett.* 2012, *3* (21), 3228-3233.

25. Jiang, Y.; Wang, W.-N.; Biswas, P.; Fortner, J. D., Facile Aerosol Synthesis and Characterization of Ternary Crumpled Graphene–TiO_2–Magnetite Nanocomposites for Advanced Water Treatment. *ACS Appl. Mater. Interfaces* 2014, *6* (14), 11766-11774.
26. Wang, W.-N.; Jiang, Y.; Fortner, J. D.; Biswas, P., Nanostructured Graphene-Titanium Dioxide Composites Synthesized by a Single-Step Aerosol Process for Photoreduction of Carbon Dioxide. *Environ. Eng. Sci.* 2014, *31* (7), 428-434.
27. Park, S.; Dikin, D. A.; Nguyen, S. T.; Ruoff, R. S., Graphene Oxide Sheets Chemically Cross-Linked by Polyallylamine. *J. Phys. Chem. C* 2009, *113* (36), 15801-15804.
28. Zhang, H.; Chen, G., Potent Antibacterial Activities of Ag/TiO_2 Nanocomposite Powders Synthesized by a One-Pot Sol−Gel Method. *Environ. Sci. Technol.* 2009, *43* (8), 2905-2910.
29. Yoon, K. Y.; Byeon, J. H.; Park, C. W.; Hwang, J., Antimicrobial Effect of Silver Particles on Bacterial Contamination of Activated Carbon Fibers. *Environ. Sci. Technol.* 2008, *42* (4), 1251-1255.
30. Perreault, F.; Tousley, M. E.; Elimelech, M., Thin-Film Composite Polyamide Membranes Functionalized with Biocidal Graphene Oxide Nanosheets. *Environ. Sci. Technol. Lett.* 2013, *1* (1), 71-76.
31. Cranford, S. W.; Buehler, M. J., Packing Efficiency and Accessible Surface Area of Crumpled Graphene. *Phys. Rev. B* 2011, *84* (20), 205451.
32. Bagri, A.; Mattevi, C.; Acik, M.; Chabal, Y. J.; Chhowalla, M.; Shenoy, V. B., Structural evolution during the reduction of chemically derived graphene oxide. *Nat. Chem.* 2010, *2* (7), 581-587.

33. Zhao, G.; Li, J.; Ren, X.; Chen, C.; Wang, X., Few-Layered Graphene Oxide Nanosheets As Superior Sorbents for Heavy Metal Ion Pollution Management. *Environ. Sci. Technol.* 2011, *45* (24), 10454-10462.

34. Song, X.; Gunawan, P.; Jiang, R.; Leong, S. S. J.; Wang, K.; Xu, R., Surface activated carbon nanospheres for fast adsorption of silver ions from aqueous solutions. *J. Hazard. Mater.* 2011, *194* (0), 162-168.

35. Yue, Z. R.; Jiang, W.; Wang, L.; Toghiani, H.; Gardner, S. D.; Pittman Jr, C. U., Adsorption of precious metal ions onto electrochemically oxidized carbon fibers. *Carbon* 1999, *37* (10), 1607-1618.

36. Henglein, A., Non-metallic silver clusters in aqueous solution: stabilization and chemical reactions. *Chem. Phys. Lett.* 1989, *154* (5), 473-476.

37. Gentry, S. T.; Fredericks, S. J.; Krchnavek, R., Controlled Particle Growth of Silver Sols through the Use of Hydroquinone as a Selective Reducing Agent. *Langmuir* 2009, *25* (5), 2613-2621.

38. Williams, G.; Seger, B.; Kamat, P. V., TiO_2-Graphene Nanocomposites. UV-Assisted Photocatalytic Reduction of Graphene Oxide. *ACS Nano* 2008, *2* (7), 1487-1491.

39. Li, W.; Li, D.; Xian, J.; Chen, W.; Hu, Y.; Shao, Y.; Fu, X., Specific Analyses of the Active Species on $Zn_{0.28}Cd_{0.72}S$ and TiO_2 Photocatalysts in the Degradation of Methyl Orange. *J. Phys. Chem. C* 2010, *114* (49), 21482-21492.

40. Jak, M. J. J.; Konstapel, C.; van Kreuningen, A.; Verhoeven, J.; Frenken, J. W. M., Scanning tunnelling microscopy study of the growth of small palladium particles on TiO_2(110). *Surf. Sci.* 2000, *457* (3), 295-310.

41. Pal, S.; Tak, Y. K.; Song, J. M., Does the antibacterial activity of silver nanoparticles depend on the shape of the nanoparticle? A study of the gram-negative bacterium Escherichia coli. *Appl. Environ. Microbiol.* 2007, *73* (6), 1712-1720.
42. Diagne, F.; Malaisamy, R.; Boddie, V.; Holbrook, R. D.; Eribo, B.; Jones, K. L., Polyelectrolyte and Silver Nanoparticle Modification of Microfiltration Membranes To Mitigate Organic and Bacterial Fouling. *Environ. Sci. Technol.* 2012, *46* (7), 4025-4033.
43. Yin, J.; Yang, Y.; Hu, Z.; Deng, B., Attachment of silver nanoparticles (AgNPs) onto thin-film composite (TFC) membranes through covalent bonding to reduce membrane biofouling. *J. Membr. Sci.* 2013, *441* (0), 73-82.
44. Sondi, I.; Salopek-Sondi, B., Silver nanoparticles as antimicrobial agent: a case study on E. coli as a model for Gram-negative bacteria. *J. Colloid Interface Sci.* 2004, *275* (1), 177-182.
45. Geim, A. K.; Novoselov, K. S., The Rise of Graphene. *Nat. Mater.* 2007, *6* (3), 183-191.

Chapter 8 Supporting Information

The light spectra of the customized UV reactor and simulated solar light, scheme of formation of Ag NPs on membrane surface, evolution of UV-vis absorption spectra of the GOTI-Ag composites with time under UV, and additional TEM and SEM images of GOTI and formed Ag NPs are included.

Figure S8.1. Light spectra of the customized UV reactor and simulated solar light (AM 1.5).

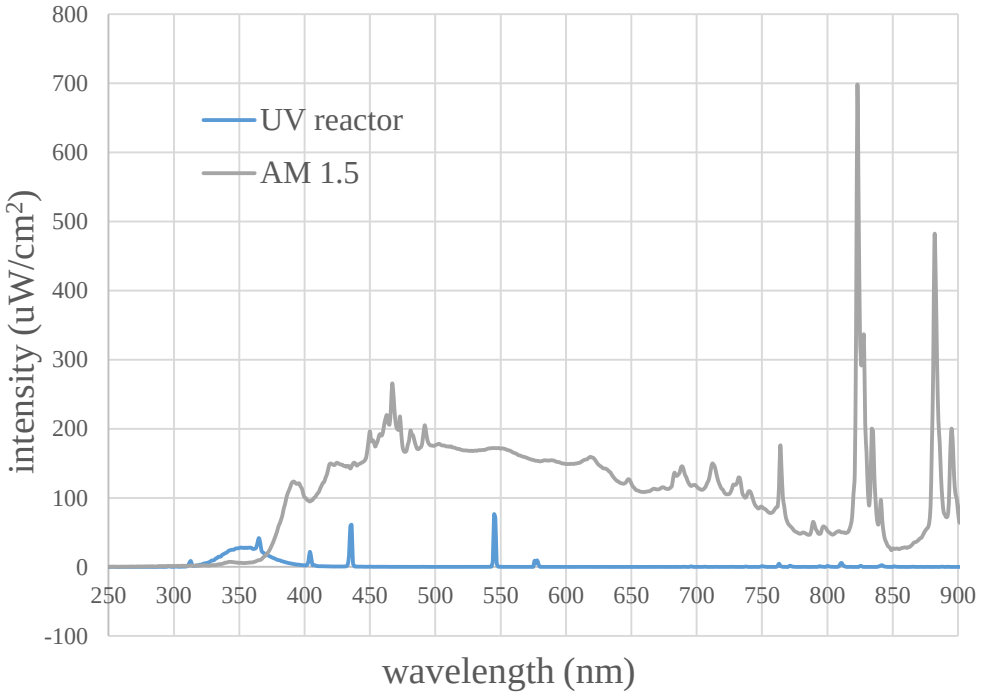

Figure S8.2. Scheme of Ag NPs formation on membrane surface (batch mode). The reaction was conducted in the customized UV reactor (351 nm centered with measured intensity of 1230 $\mu W/cm^2$) in which the membrane coupon was placed, with the active (deposited) side towards the UV light direction.

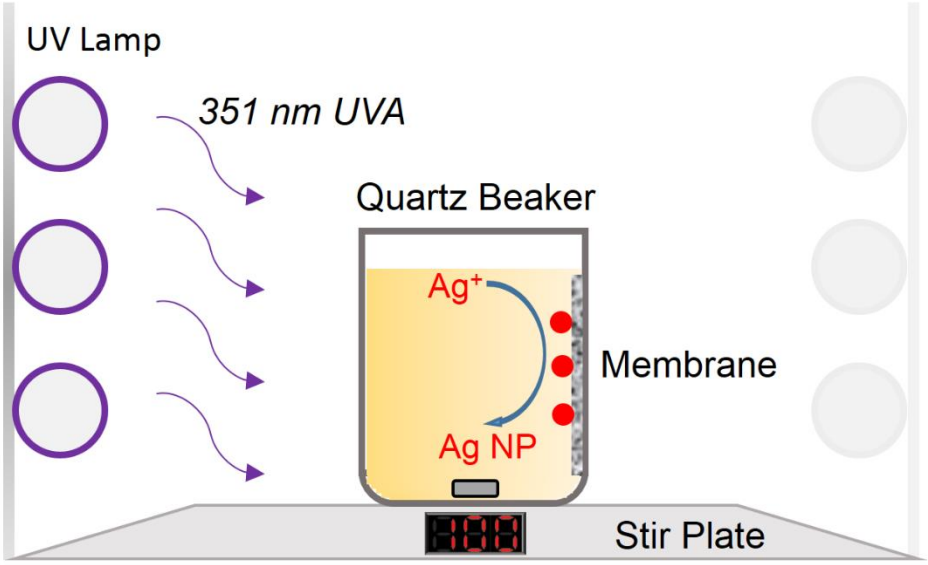

Figure S8.3. Evolution of UV-vis absorption spectra of the GOTI (and formed Ag NPs) with time under UV irradiation.

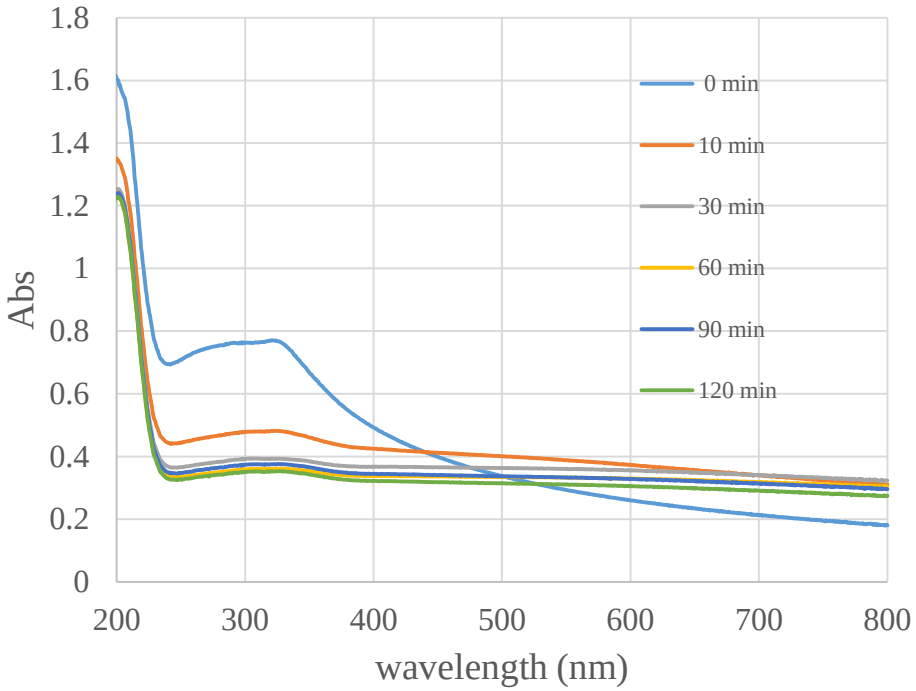

Figure S8.4. TEM images of GOTI and formed Ag NPs. Quasi-spherical, core-shell (also termed sack-cargo) nanostructures were observed for all GOTIs as shown in the image. The sizes of GOTI nanocomposites are approximately between 200-400 nm. HR-TEM analysis reveals that TiO_2 nanoparticles have an orientation of anatase (101) plane.

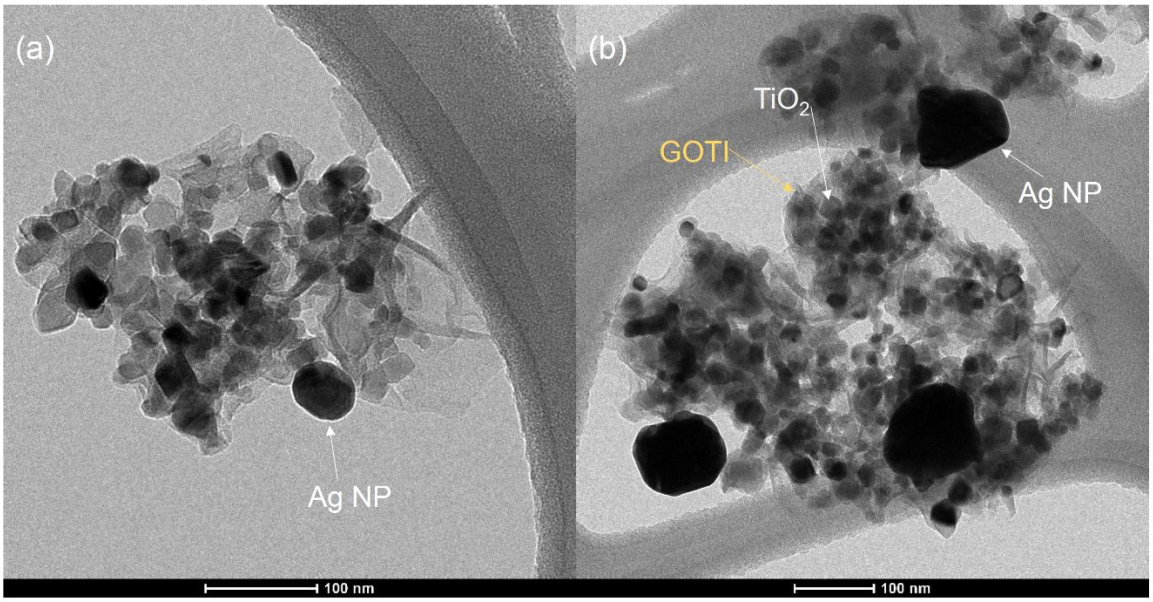

Figure S8.5. SEM images of GOTI and formed Ag NPs after 60 min solar (a) and UV (b) light irradiation.

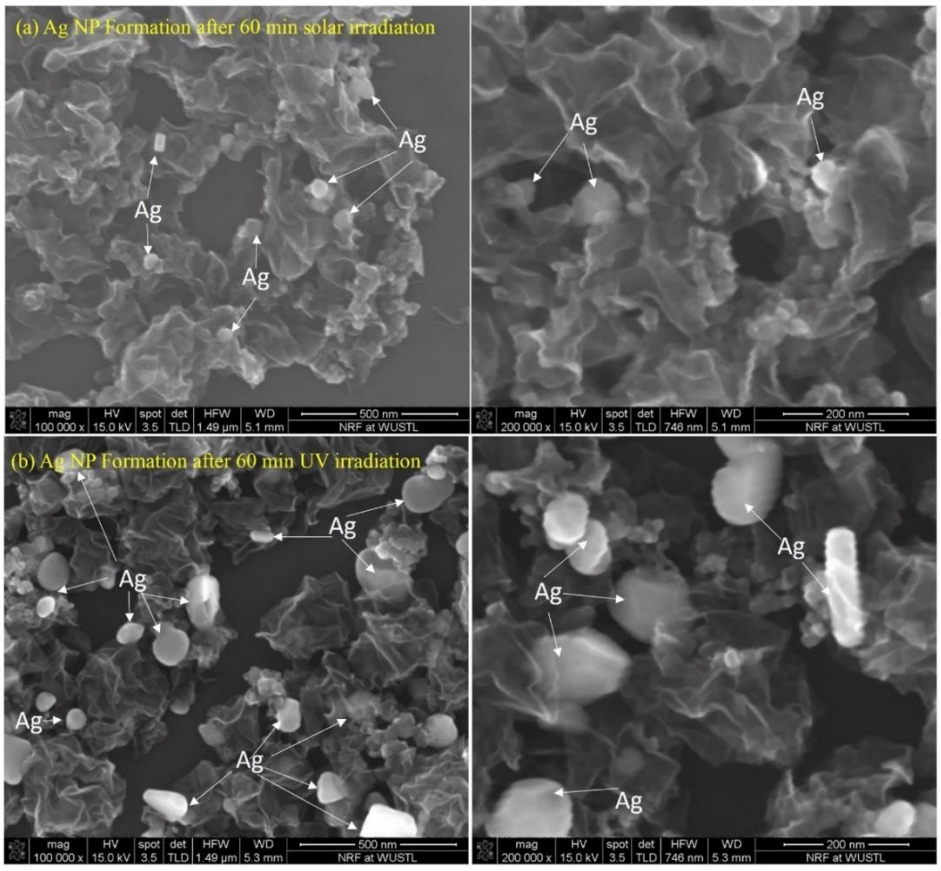

Chapter 9. Conclusions and Future Directions

9.1 Conclusions

This dissertation has described a novel engineering approach to produce aggregation-resistant crumpled graphene oxide (CGO)-based platform nanomaterials, and demonstrated their unique applications in a suite of advanced water treatment technologies, including photocatalysts and water treatment membranes. Conclusions drawn from this work are likely to have a lasting impact on the fields of aerosol processing of materials, environmental nanotechnology, environmental catalysis, water treatment membranes, and others.

The major conclusions from the dissertation are as follows:

I. A systematic description of the transformations of GO nanosheets during aerosol processing and their subsequent impact on material colloidal behaviors was provided.

1) With respect to physical crumpling, a temperature-dependent morphological evolution of CGO materials was observed. A semi-empirical equation for crumpling of self-avoiding sheets at the macroscale successfully describes the nanoscale phenomenon of GO crumpling. Further, both calculation and experimental results revealed that the evaporation rate plays an important role in controlling the crumpling process.

2) With regard to chemical transformation, a temperature-dependent removal of surface functionality was observed. The characterization results revealed that the thermal reduction started with the removal of basal plane functional groups (e.g., epoxy) and then proceeded to the removal of more (chemically) stable carbonyl and carboxyl functionalities at the material edge.

3) Material properties, including morphological and surface chemical properties (ζ-potentials, C/O ratios, carboxyl, and C-C fractions), were for the first time, quantitatively correlated to fundamental material behaviors in water. The CCC values were found to increase by 23-80%

when GO is crumpled as CGO. ζ-potentials were observed to be strongly correlated with CCC values (R^2 = 0.94-0.99), which is (mathematically) consistent with classic DLVO theory. Further, for all cases, edge-based carboxyl functional groups are highly correlated to observed CCC values (R^2 = 0.89-0.95). Observations support the deprotonation of carboxyl groups with low acid dissociation constants (pKa) as the main contributors to ζ-potentials and thus to material aqueous stability.

4) NOM is found to have considerably increased the critical coagulation concentrations (CCC) of all GO evaluated, the stability enhancement for CGO is at least one order of magnitude higher than flat GO, regardless of surface chemistry. This augmented stability is primarily due to enhanced steric repulsion via adsorbed NOM, although electrostatic repulsion also plays a role in the case of highly reduced GO (e.g., CGO-800). Further, based on adsorption results, higher adsorption density and extended configurations of NOM on crumpled surfaces may be the reason for much higher CCC of CGOs. NOM with higher (net) aromaticity was correlated with increased (relative) stability enhancements, suggesting π-π interactions likely play a key role in the interaction mechanisms, which is similar to previous reports describing carbon nanotube – NOM interactions.

II. A library of CGO-based nanomaterials with desired properties and functionalities was developed, based on synthesis process optimization/engineering from Part I knowledge.

5) The aerosol process was modified to incorporate nanoparticles. Binary and ternary nanostructures, including CGO-TiO_2, CGO-Ag, CGO-magnetite, and CGO-TiO_2-magnetite, were successfully synthesized with desired sizes and surface chemistries (water stability). This synthesis protocol can be further employed universally to synthesize CGO-based functional composite materials.

6) The as-synthesized CGO-TiO_2-magnetite (GOTIM) ternary core-shell nanostructures were shown to possess superior aqueous-based photocatalytic properties (over a 20-fold enhancement in some cases) compared to TiO_2 alone. Total GOTIM photocatalytic reactivity was confirmed to also include efficient photo-reduction reaction pathways, in addition to the expected oxidation routes typical of TiO_2 based photocatalysts, significantly expanding CGO-TiO_2 based-photocatalysts' application potential compared to TiO_2 alone. Further, with the addition of hole scavengers such as EDTA, and/or lowering the O_2 concentration, further enhancement of photocatalyzed reduction reactions was demonstrated, suggesting the potential for directed, controlled reduction applications. In addition to robust aqueous stability, low-field magnetic susceptibility is also demonstrated, allowing for low-energy in situ material separations, which are critical for material recycling and reuse.

7) Rapid photo-reduction of Ag^+ into nano-Ag particles by GOTI nanocomposites was demonstrated under both UV and solar light irradiations, and GOTI was found to be primarily UV (as UVA) active. Size distribution analysis shows that most NPs are between 40 and 120 nm, regardless of the reaction time. High-resolution (HR) TEM was employed to identify the crystal structure of formed Ag NPs. As-synthesized Ag NPs consist of three planes, including the (111) plane (d = 0.235 nm), (110) plane (d = 0.286 nm), and (200) plane (d = 0.204 nm).

III. Two schemes for CGO applications in water treatment membranes, as advanced, reactive water treatment membrane assemblies and nanoscale membrane fillers, were developed and demonstrated.

8) Nanoscale, monomeric CGO nanoparticles (GOTI and GOAg, as a quasi core-shell structure) were assembled into composite membranes. These membranes not only allow high water flux via vertically tortuous nanochannels, achieving a water flux of 246 $\pm$11 L/(m^2·h·bar)

with the deposition density of 7.4 g/m^2, outperforming comparable commercial ultrafiltration membranes. They also demonstrate excellent separation efficiencies for model organic and biological foulants. Further, multifunctionality is demonstrated through the in situ photocatalytic degradation of methyl orange (MO), as a model organic, under fast flow conditions (t_{res} < 0.1 s). Superior antimicrobial properties, evaluated with GOAg, were observed for both biofilm (contact) and suspended growth scenarios (> 3 log effective removal, *Escherichia coli*).

9) In situ surface-based photocatalyzed synthesis of nAg particles at the surface of GOTI nanocomposite membrane assemblies was demonstrated, allowing for simultaneous filtration and disinfection. With ca. 3 log inactivation for both *Escherichia coli* and *Bacillus subtilis,* the described membrane assemblies (with in situ formed nAg) demonstrate enhanced antimicrobial activity compared to the GOTI membrane surface or the support membrane alone. Under typical conditions, the working/operational time (Ag dissolution time) is calculated to be over two orders of magnitude higher than the loading (synthesis) time (e.g., 123 h vs. 0.5 h, respectively). These results highlight the described material-based process as a potentially novel anti-fouling membrane technology.

10) CGO and GO particles were incorporated into the polysulfone ultrafiltration membrane matrix during the phase inversion process. The membranes incorporated with GO/CGO showed much enhanced water permeability and similar rejection efficiencies for BSA.

9.2 Future Directions

9.2.1. Material Synthesis and Behaviors

1) A universally applicable theoretical framework needs to be developed to describe the nanoscale crumpling of 2D materials into 3D structures. While in this work initial efforts have

been made by employing existing knowledge at the macroscale, the verification of the scaling law between the confinement force and material properties will require subtle nanoscale measurements, which may be daunting. To reach such a goal, experiments can be combined with computational approaches, such as molecular dynamic simulations.

2) For industrial-scale production of CGO materials, the FuAR process needs to be further optimized, in particular with regard to diffusion loss. Particle deposition onto the reactor tube wall needs to be alleviated to increase the overall throughput. Furthermore, the as-synthesized particles are somewhat polydispersed, so other aerosol generation methods may be preferred, such as electrospray. Moreover, ambient temperature crumpling of GO sheets has been demonstrated in some previous reports, however, synthesis of functional composite materials through encapsulation under these conditions has yet to be demonstrated. This synthesis will be of great interest to applications requiring preservation of the GO surface chemistry, and will dramatically reduce overall energy consumption.

3) There are many opportunities for surface chemical functionalization of GO. Of particular interest will be the development of a one-step process which simultaneously completes the chemical functionalization during the aerosol process. Functionalization can bring about tailored approaches for specific adsorption of a particular ion or compound.

4) There lacks a systematical understanding of the interaction mechanisms between natural organic matters and GO materials. The configuration of humic substances on GO surface impacts the steric repulsion, and thus aqueous stability significantly, which needs to be further resolved, preferably quantitatively. Such findings will also have broader implications for GO fate and transport in more complex real aquatic environments.

9.2.2. Photocatalyst Development

5) This work has shown that the photocatalytic activity, including both oxidative and reductive pathways, is dependent on the material composition(s) and structures. This finding should lead to new strategies to design and synthesize shape-dependent photocatalyst which could enhance the reduction pathways by containing oxidation reactions within the shell structure. This type of photocatalysts would have potential applications in reductive removal of a range of aqueous oxyanion pollutants, among others.

6) Photocatalysts responsive to visible light/ sun light will also be of great interest. Doping of graphene will be a feasible avenue to achieve this goal.

9.2.3. Water Treatment Membranes

7) There still lacks a fundamental description of 'structure-property-performance' relationships of GO-enabled membranes. This requires more convenient approaches to control GO size, shape, and surface chemistry, and characterization of resulting properties, such as hydrophilicity and antifouling property.

8) For practical applications of the reactive membranes developed here, other polymeric cross-linker and cross-linking reaction schemes have to be studied to considerably enhance the stability of CGO particles on top of the support. The cross-linker, additionally, has to meet the requirement of being UV-resistant for photoreactive membranes. The CGO layer needs to be better characterized in terms of intrinsic structure, and also the water transport mechanism (e.g., pathway) needs to be elucidated. Further, the application regime of these membranes should be defined for membranes to be optimized accordingly.

9) The application of CGO nanomaterials in other membrane types has yet to be demonstrated. Such potential applications include thin film nanocomposite (TFN) membranes that

incorporate CGO nanomaterials in the polyamide layer, and also the surface functionalization of commercial UF/NF/RO membranes.

10) There is a demand for novel fabrication processes for nano- or advanced material-enabled membranes. These processes need to be scalable. Current approach of adding nanoparticles as nanofillers does not allow control of the distribution of nanoparticles, for example, into the selective layer. Additionally, surface functionalization has not been demonstrated in a continuous fashion, which also limits potential industrial applicability.

9.2.4. Life-cycle Assessment

11) The chemical stability of GO under various conditions (e.g., UV and oxidant exposure) should be evaluated for longer time regimes. These knowledge will be essential to a full understanding of the environmental benefits and drawbacks of graphene-based treatment technologies.

Appendix I. Fabrication of Polysulfone UF Membranes Incorporated with Graphene Oxides

A preliminary study on fabrication of polysulfone (Psf) UF membranes incorporated with GO and CGO nanoparticles is presented in this section. Psf membranes with different GO and CGO loadings (0, 0.25, 0.5, and 1% weight percentage with respect to polymer) were synthesized by a phase inversion method. Preliminary results include membrane characterization, permeability and rejection performance evaluation.

A1. Introduction

Membrane technologies have recently experienced significant nano-enabled technological advancements while growing as key process components towards integrated water treatment and reuse.[1] Among a number of membrane processes, low-pressure ultrafiltration (UF) has been used extensively for many separation and filtration purposes, including water and wastewater treatment, oil-water separation, and chemicals separation, among others. The majority of UF membranes are fabricated from inert polymeric materials such as polysulfone (Psf), polyethersulfone (PES), and polyvinylidene difluoride (PVDF), in which nanoparticles can be easily incorporated by blending into the solvents during the phase inversion process. Nanoparticles as matrix fillers have been shown to usually bring about improvements in hydrophilicity and anti-fouling properties, and up to date, such incorporation has been demonstrated with nanomaterials including TiO_2, SiO_2, Ag, and carbon nanomaterials.[2, 3]

Interests in carbon nanomaterials for separation applications may have rooted in the unique phenomenon of ultrafast transport of water molecules in the confined carbon tubular nanopores. Water permeation through carbon nanotubes (CNT) was demonstrated 3-5 orders of magnitude

faster than upper limits predicated by the Hagen-Poiseuille equation due to violation of no-slip boundary conditions.[4] However, major breakthroughs have not been achieved in the past decade in the development of an economic scale-up fabrication process of such CNT membranes. In the past few years, research interests in graphene oxide (GO), the oxidized derivatives of a lately discovered two-dimensional carbon allotrope-graphene, emerged rapidly as evidenced by increasing numbers of publications and patents each year. Graphene oxide can have some unique material advantages compared to CNTs. For example, its manufacturing consumes considerably less energy (500-1000 MJ/Kg by solvent exfoliation of graphite oxide, compared to 100,000 MJ/Kg of CNTs).[5] In addition, it has more tailorability with regard to size, surface chemistry, and morphology.

In a similar manner, small amounts of GO (usually 0.1-2 wt.% with respect to polymer) were incorporated into conventional polymer UF membranes structures, including Psf,[6, 7] PES,[8] and PVDF.[9] GO is hypothesized to migrate to the top membrane surface during the phase inversion, making it more hydrophilic, which is supported by the observation of an average decrease of ca. 20 ° in water contacting angle measurements. In addition to increase in surface hydrophilicity, overall porosity also increased, and as a result, 2-20 fold enhancements in water fluxes have been observed (due to GO additions).[7, 8] Rejection improvement can vary from a few percent[8] to almost 3 times,[9] depending on the polymers, GO percentage, and test foulants. Generally, optimal GO percentage balances water permeability and rejection rates, which conforms to the classical trade-off between permeability and selectivity associated with nano- to ultrafiltration membranes.

Although these GO-enabled UF membranes have demonstrated great potentials, fundamental questions remain, such as the relationships of GO properties (size, surface chemistry, etc.) with fabrication processes and the eventual performance. GO materials typically vary in

nature due to the random functionalization of each layer and variations in physical structures.[10, 11] The degree of oxidation can differ significantly from a few to dozens of percent in terms of atomic ratio.[11] Further, 2D GO can be physically modified, resulting in 3D structures, such as crumpled paper ball-like spheres[12, 13] and corrugated (wrinkled) surfaces.[14] These variations were shown to have great impacts on its aggregation states in solvents and subsequently interaction with aquatic constituents such as natural organic matters in our earlier work.[15]

These physical and chemical variations of GO materials could also have relevant implications for membrane performances when acting as nanoscale fillers. However, such relationships, according to the authors' knowledge, has yet to be revealed. In this work, GO and crumpled GO (CGO) were synthesized, and incorporated into Psf UF membranes at different material loadings (0, 0.25, 0.5, and 1% weight percentage with respect to polymer) during the phase inversion process. The membranes were characterized and evaluated with regard to permeability and rejectivity. Preliminary results show that increased hydrophilicity is likely one major reason for enhanced water permeability after nanoparticle incorporation.

A2. Experimental

A2.1 Synthesis of Flat and Crumpled Graphene Oxide

GO was synthesized by oxidation and subsequent exfoliation of graphite, namely the modified Hummer's method,[16] as described in detail in our previous work.[13] The obtained flat GO nanosheets were used as the starting material to synthesize CGO particles by a furnace aerosol reactor (FuAR) method.[13, 15] In this aerosol-assisted process, flat GO sheets are crumpled in a water droplet under the capillary compression induced by rapid water evaporation. The CGO

nanoparticles were finally collected using a membrane filter (Nylon, 200 nm, Whatman) at the end stream of the reactor, weighed and dispersed in solvents.

Detailed material characterization methods were described in our earlier work.[15] The morphology and size of the GO and CGO samples were examined by transmission electron microscopy (TEM, TecnaiTM Spirit, FEI Co.), field emission scanning electron microscopy (FESEM, NOVA NanoSEM 230, FEI Co.), and atomic force microscopy (AFM, Veeco Nanoman). For GO SEM imaging, samples were sputter-coated with gold for 90 s (Headway PWM32-PS-CB15PL). ζ-potential and hydrodynamic diameter (D_h) (in 40 mg/L aqueous solution) were measured with a ZetaSizer Nano ZS instrument (Malvern Instruments, Worcestershire). Surface chemistry information was obtained with fourier transform infrared spectrometer (FTIR, Nicolette Nexus 470) and X-ray photoelectron spectroscopy (XPS, PHI 5000 VersaProbe II equipped with monochromatic Al Kα (1486.6 eV) X-ray source).

A2.2 Membrane Casting and Characterization

Psf membranes were fabricated by a phase inversion method.[6] A casting solution was prepared by mixing 8.1 g of 1-Methyl-2pyrrolidinone (NMP, Sigma-Aldrich), 0.1 g of polyvinylpyrrolidone (PVP, Mw 10,000, Sigma-Aldrich), and 1.8 g of Psf (beads, average Mn ~22,000, Sigma-Aldrich) while adding a desired amount of GO/CGO (wt. 0-1.0%). The mixture was stirred for 24 h on a heating plate at 60 ℃ to obtain a homogeneous dispersion. After 24 h, the casting solution was cooled to room temperature and remove bubbles. The membrane casting was performed using a casting knife (EQ-Se-KTQ-150D, MTI Corp.), on a clean glass plate with a denominated thickness of 200 μm. Immediately after casting, the thin film was immersed into a water bath to initiate the phase inversion. The membrane sheet was then obtained and stored in water before being used for test and characterization.

Table A1. Compositions of Psf membrane casting solutions

Membrane type	Components of the casting Solution			
	PSf (g)	NMP (g)	PVP (g)	GO/CGO (g)
Psf only	1.8	8.1	0.1	-
0.25% NPs	1.8	8.1	0.1	0.0045
0.5% NPs	1.8	8.1	0.1	0.009
1% NPs	1.8	8.1	0.1	0.018

A2.3 Membrane Characterization

Membrane surface and cross-sectional images were obtained using field emission scanning electron microscopy (FESEM, NOVA NanoSEM 230, FEI Co.). The membrane cross-sections were exposed by fracturing the coupons in liquid nitrogen. For SEM imaging, all samples were sputtered with gold for 90 s (Headway PWM32-PS-CB15PL). Membrane surface morphology and roughness was also investigated using an atomic force microscopy (AFM Veeco NanoMan) in a tapping mode (spring constant of 40 N/ m, resonance frequency of 325 kHz, tip radius of 8 nm). Further, membrane surface hydrophilicity was studied by measuring water contact angle using a sessile drop method (Pheonix-300). At least ten measurements were conducted for each membrane and the average value was obtained and reported.

A2.4 Membrane Permeability and Selectivity

To investigate the performance of the as-synthesized membranes, permeability and rejection tests were performed according to established procedures.[17] Pure water permeability were evaluated under a direct flow and constant pressure dead-end filtration mode, while the permeated water flux was directly measured. Solutions (water or bovine serum albumin, Mw ~66 kDa Sigma-Aldrich) in the storage tank (Millipore Amicon 8200) were pressurized by nitrogen gas at a certain

pressure (i.e., 1 bar) and connected to the filter holder (47 mm, Pall Life Science) in which the synthesized membrane was placed. The permeated solution was measured over time using an integrated electronic balance (Mettler Toledo ML1502E) and data was logged automatically at 60 s intervals. With this interval, the average water flux was calculated.

For the rejection test, the membranes were challenged by 1 g/L BSA solution. The concentration of BSA was measured using a UV-vis spectrophotometer (Varian Bio 50) at an absorption peak of 278 nm. The solute rejection percentage was calculated using the following equation:

$$\text{rejection } (\%) = \left(1 - \frac{C_p}{C_f}\right) \times 100$$

Where C_p and C_f are the concentrations of BSA in the permeate and feed solutions, respectively.

A3. Results and Discussion

A3.1 Characterization of As-synthesized Graphene Oxides

The size, morphology, and surface chemistry of GO and CGO-400 were characterized in detail using TEM and XPS (Figure A1).[15] The TEM examination of GO sheets show a rough size distribution from a few hundred nanometers to over 1 μm, which is also confirmed by earlier AFM measurements (Figure A1a). CGO-400, synthesized via the aerosol route using flat GO as the starting material, have a distinctive crumpled morphology (Figure A1b). CGO has a quasi-spherical morphology with relatively smooth surfaces and sharp ridges.

GO is known as one-atom-thick highly oxidized graphene sheet, with oxygen-containing functional groups which include basal hydroxyl and epoxy, and edge-associated carbonyl and carboxyl groups.[18] Under furnace temperatures of 400 ℃, those oxygen functional groups are expected to be partially removed. The evolution of surface functional groups was analyzed from

XPS spectra. The high-resolution carbon 1 S peak from XPS spectra was deconvoluted into five chemical states, which represent most commonly accounted surface functional components, including the C-C (284.8 eV), C-OH (286.2 eV, 1-1.5 eV shift to higher binding energy (BE)), C-O-C (287.1 eV, higher BE compared to C-OH group), C=O (287.7 eV, 2.5-3 eV shift to higher BE) and COOH (288.8 eV, 4-4.5 eV shift to higher BE) functionalities.[19, 20] As shown in Figure A1c, being highly oxidized, GO is with abundant oxygen functional groups, including C-OH (~13% of area ratio), C-O-C (~ 35%), C=O (~6%), and COOH (~5%). With thermal reduction at 400 ℃, the oxygenated functionality decreased, accompanied by the restoration of C-C aromatic regions. For example, the C-C area ratios increased gradually from ~41 ±4 % of GO to ~61 ±2 % of CGO-400, and the C-O (C-OH and C-O-C) area ratios decreased from around 48.2% to 30.1% (Figure A1 c and d).

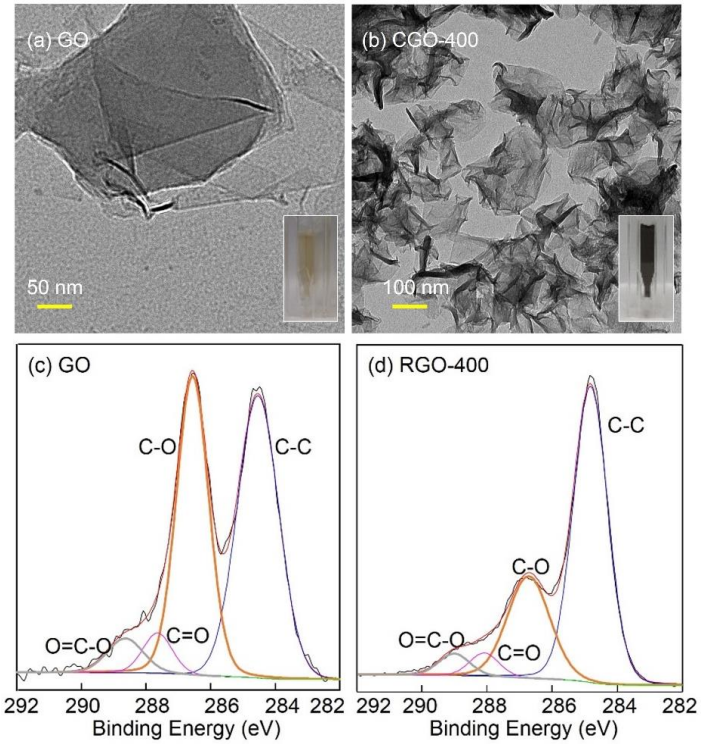

Figure A1. TEM images and XPS spectra of GO and CGO-400.

A3.2 Characterization of As-synthesized Membranes

The membranes with varied materials and loadings can be distinguished by their colors (Figure A2). The original Psf membrane has a white color, with the shiny side of the dense layer shown in Figure A2. With addition of GO/CGO, the color becomes darker. With 1% of CGO loading, the membrane turns black (Figure A2). This change suggests the successful incorporation of CGO in the membrane matrix, which is also reflected in the SEM images. SEM images of the original Psf show a smooth surface, and more GO/CGO particles emerged to the membrane surface with higher material loadings (Figure A3). The cross-sectional view of the membranes exhibit a finger-like morphology, which is typical for Psf UF membranes made by the phase inversion method (Figure A4).

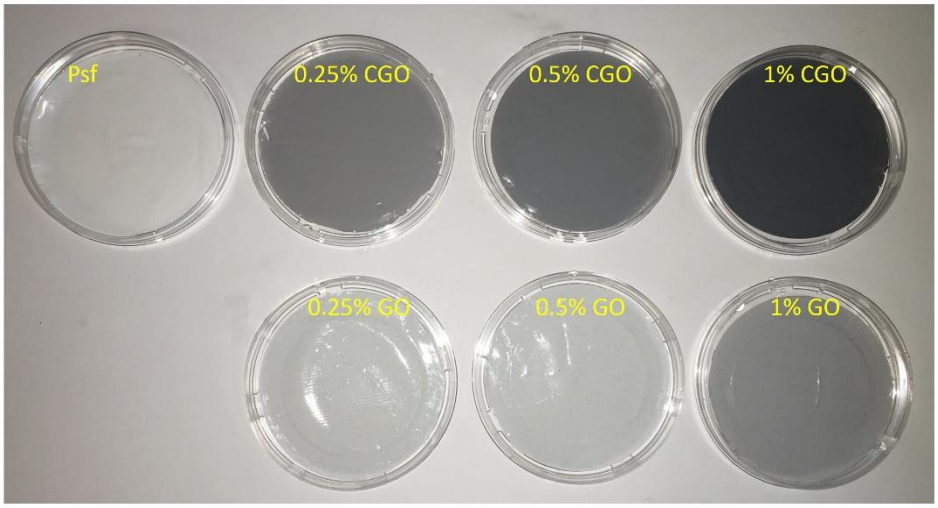

Figure A2. Digital photos of pristine Psf and GO, CGO-Psf membranes with varied material loadings.

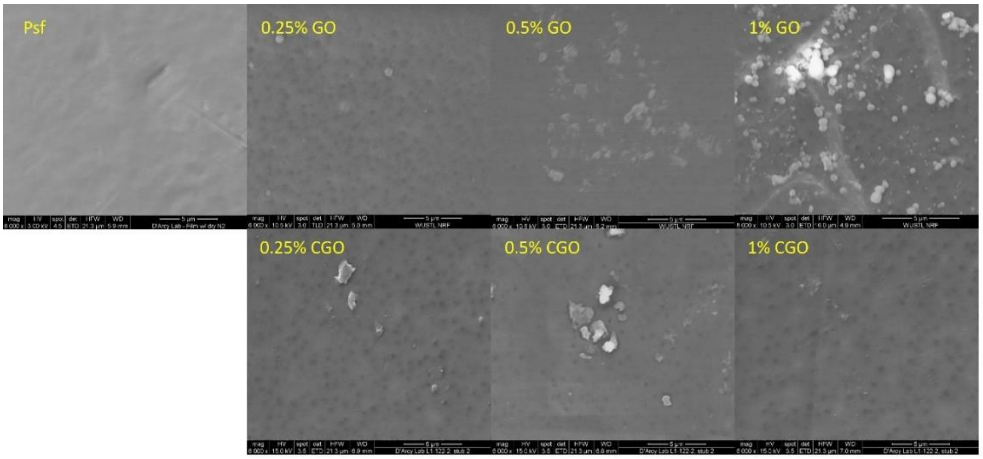

Figure A3. SEM images (top view) of pristine Psf and GO, CGO-Psf membranes with varied material loadings.

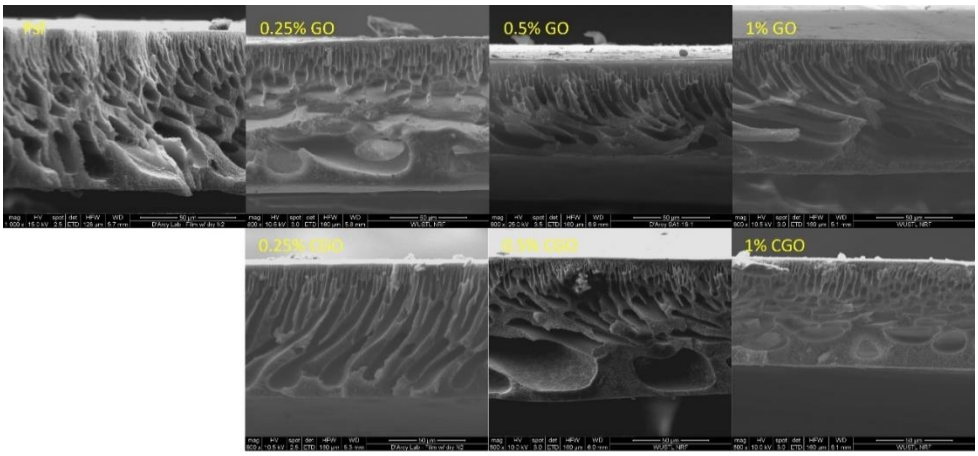

Figure A4. SEM images (cross-sectional view) of pristine Psf and GO, CGO-Psf membranes with varied material loadings.

A3.3 Membrane Permeability and Rejection

Figure A5 shows pure water permeability of pristine, GO-, and CGO-Psf membranes with different material loadings. Pure water permeability through the original Psf membrane was measured to be 14.4$\pm$ 4.1 L/(m^2 h) (LMH). When 0.25% of CGO was introduced into the casting solution, the permeability increased to 21.7 $\pm$ 11.0 LMH (Figure A5). This result was consistent with previous studies showing a similar increasing trend [6 7] and likely resulted from an increase in

the hydrophilicity and porosity of the membrane due to addition of CGO. However, the permeability of pure water decreased as the CGO loading further increased to 0.5% (6.4 ± 3.7 L/(m^2 ħ)) and 1% (9.9 ± 5.2 L/(m^2 ħ)) (Figure A5). This decrease appears to deviate from the trend of GO-Psf membranes, which needs to be understood in the future work.

The separation test of the CGO membranes was evaluated by filtration of BSA solution (Figure A6). A decrease in the permeability of BSA solution was observed for all membranes due to the fouling of BSA. With regard to rejection performances, the incorporation of GO or CGO particles did not decrease the rejection rates of BSA in this preliminary study. The rejection percentages of BSA were not significantly different for different material loadings, ranging from 92% to 98% (Figure A6).

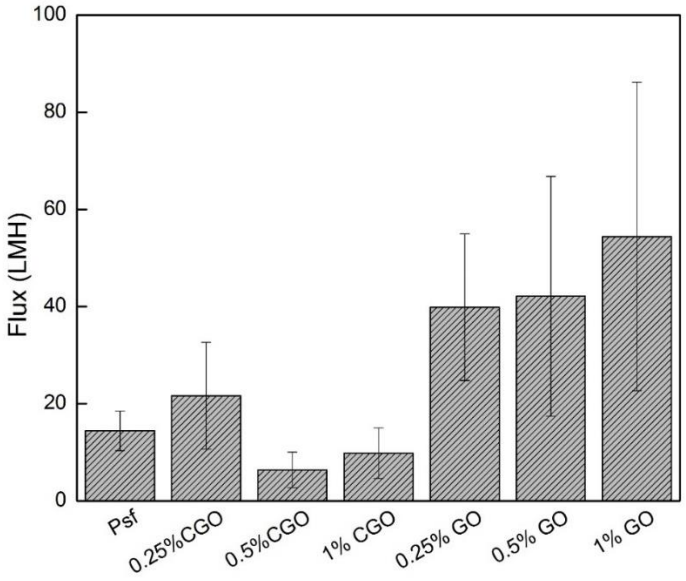

Figure A5. Pure water permeability of the pristine Psf and GO/CGO-Psf membranes.

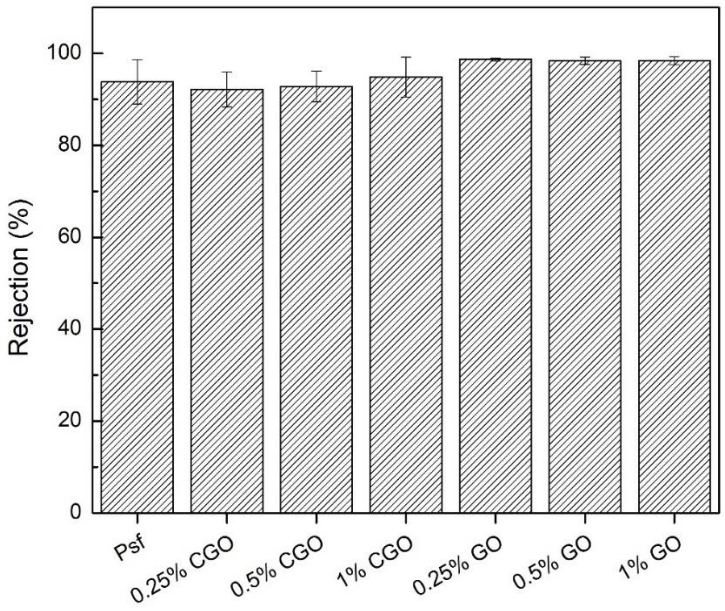

Figure A6. Rejection of BSA of the pristine Psf and GO, CGO-Psf membranes.

A4. Conclusions

Our preliminary study demonstrates the successful incorporation of GO and CGO particles into polysulfone membrane structures via modifying the casting solutions in the phase inversion process. The membranes could have higher water flux and maintain or even increase the rejection efficiencies. Future work is needed to fundamentally elucidate the underlying mechanisms for the augmented performances through studying more material variations and correlating the material properties with the membrane performances.

References

1. Shannon, M. A.; Bohn, P. W.; Elimelech, M.; Georgiadis, J. G.; Marinas, B. J.; Mayes, A. M., Science and Technology for Water Purification in the Coming Decades. *Nature* **2008,** *452* (7185), 301-310.

2. Yin, J.; Deng, B., Polymer-matrix nanocomposite membranes for water treatment. *J. Membr. Sci.* **2015,** *479* (0), 256-275.
3. Lee, A.; Elam, J. W.; Darling, S. B., Membrane materials for water purification: design, development, and application. *Environmental Science: Water Research & Technology* **2016,** *2* (1), 17-42.
4. Holt, J. K.; Park, H. G.; Wang, Y.; Stadermann, M.; Artyukhin, A. B.; Grigoropoulos, C. P.; Noy, A.; Bakajin, O., Fast Mass Transport Through Sub-2-Nanometer Carbon Nanotubes. *Science* **2006,** *312* (5776), 1034-1037.
5. Arvidsson, R.; Kushnir, D.; Sandén, B. A.; Molander, S., Prospective Life Cycle Assessment of Graphene Production by Ultrasonication and Chemical Reduction. *Environ. Sci. Technol.* **2014,** *48* (8), 4529-4536.
6. Ganesh, B. M.; Isloor, A. M.; Ismail, A. F., Enhanced hydrophilicity and salt rejection study of graphene oxide-polysulfone mixed matrix membrane. *Desalination* **2013,** *313* (0), 199-207.
7. Crock, C. A.; Rogensues, A. R.; Shan, W.; Tarabara, V. V., Polymer nanocomposites with graphene-based hierarchical fillers as materials for multifunctional water treatment membranes. *Water Res.* **2013,** *47* (12), 3984-3996.
8. Zinadini, S.; Zinatizadeh, A. A.; Rahimi, M.; Vatanpour, V.; Zangeneh, H., Preparation of a novel antifouling mixed matrix PES membrane by embedding graphene oxide nanoplates. *J. Membr. Sci.* **2014,** *453* (0), 292-301.
9. Zhang, J.; Xu, Z.; Mai, W.; Min, C.; Zhou, B.; Shan, M.; Li, Y.; Yang, C.; Wang, Z.; Qian, X., Improved Hydrophilicity, Permeability, Antifouling and Mechanical Performance of PVDF Composite Ultrafiltration Membranes Tailored by Oxidized Low-Dimensional Carbon Nanomaterials. *J. Mater. Chem. A* **2013,** *1* (9), 3101-3111.

10. Cai, W.; Piner, R. D.; Stadermann, F. J.; Park, S.; Shaibat, M. A.; Ishii, Y.; Yang, D.; Velamakanni, A.; An, S. J.; Stoller, M.; An, J.; Chen, D.; Ruoff, R. S., Synthesis and Solid-State NMR Structural Characterization of 13C-Labeled Graphite Oxide. *Science* **2008,** *321* (5897), 1815-1817.

11. Bagri, A.; Mattevi, C.; Acik, M.; Chabal, Y. J.; Chhowalla, M.; Shenoy, V. B., Structural evolution during the reduction of chemically derived graphene oxide. *Nat. Chem.* **2010,** *2* (7), 581-587.

12. Luo, J.; Jang, H. D.; Sun, T.; Xiao, L.; He, Z.; Katsoulidis, A. P.; Kanatzidis, M. G.; Gibson, J. M.; Huang, J., Compression and Aggregation-Resistant Particles of Crumpled Soft Sheets. *ACS Nano* **2011,** *5* (11), 8943-8949.

13. Wang, W.-N.; Jiang, Y.; Biswas, P., Evaporation-Induced Crumpling of Graphene Oxide Nanosheets in Aerosolized Droplets: Confinement Force Relationship. *J. Phys. Chem. Lett.* **2012,** *3* (21), 3228-3233.

14. Wang, M. C.; Chun, S.; Han, R. S.; Ashraf, A.; Kang, P.; Nam, S., Heterogeneous, Three-Dimensional Texturing of Graphene. *Nano Lett.* **2015,** *15* (3), 1829–1835.

15. Jiang, Y.; Raliya, R.; Fortner, J. D.; Biswas, P., Graphene Oxides in Water: Correlating Morphology and Surface Chemistry with Aggregation Behavior. *Environ. Sci. Technol.* **2016,** *50* (13), 6964–6973.

16. Hummers, W. S.; Offeman, R. E., Preparation of Graphitic Oxide. *J. Am. Chem. Soc.* **1958,** *80* (6), 1339-1339.

17. Jiang, Y.; Wang, W.-N.; Liu, D.; Nie, Y.; Li, W.; Wu, J.; Zhang, F.; Biswas, P.; Fortner, J. D., Engineered Crumpled Graphene Oxide Nanocomposite Membrane Assemblies for Advanced Water Treatment Processes. *Environ. Sci. Technol.* **2015,** *49* (11), 6846-6854.

18. Mkhoyan, K. A.; Contryman, A. W.; Silcox, J.; Stewart, D. A.; Eda, G.; Mattevi, C.; Miller, S.; Chhowalla, M., Atomic and Electronic Structure of Graphene-Oxide. *Nano Lett.* **2009,** *9* (3), 1058-1063.

19. Ganguly, A.; Sharma, S.; Papakonstantinou, P.; Hamilton, J., Probing the Thermal Deoxygenation of Graphene Oxide Using High-Resolution In Situ X-ray-Based Spectroscopies. *J. Phys. Chem. C* **2011,** *115* (34), 17009-17019.

20. Yumitori, S., Correlation of C1s chemical state intensities with the O1s intensity in the XPS analysis of anodically oxidized glass-like carbon samples. *J. Mater. Sci.* **2000,** *35* (1), 139-146.

Curriculum Vitae

Yi Jiang

EDUCATION

Washington University in St. Louis, MO, USA 2011- 2016
Ph.D., Energy, Environmental and Chemical Engineering

Peking University, Beijing, China 2007-2010
M.S., Environmental Sciences

Huazhong University of Science & Technology, Wuhan, China 2003-2007
B.E., Environmental Engineering

HONORS AND AWARDS

- Environmental Chemistry Graduate Student Award, American Chemical Society, 2016
- Doctoral Student Research Award, Washington University in St. Louis, 2015
- Travel Grant, Gordon Research Conference on Environmental Nanotechnology, 2015
- Charles & Marlene Buescher Graduate Fellowship Honoring Dr. D.W. Ryckman, 2011
- Dow Chemical Sustainability Innovation Student Challenge Encouragement Award, 2009
- Graduate Academic Excellence Scholarship, Peking University, 2007-2010
- Selected Participant, Inspire Antarctica Expedition, 2009
- Highest Graduation Honor (top 3%), Huazhong University of Science & Technology, 2007
- Undergraduate Academic Excellence Scholarship, Huazhong University of Science & Technology, (2003-2007)

PUBLICATIONS

Peer-Reviewed Publications

1. **Jiang, Y.**; Raliya, R.; Fortner, J. D.; Biswas, P., Graphene oxides in water: correlating morphology and surface chemistry with aggregation behavior. *Environ. Sci. Technol.* **2016**, 50 (13), 6964–6973.
2. **Jiang, Y**.; Liu, D.; Cho, M.; Lee, S.; Zhang, F.; Biswas, P.; Fortner, J. D., In situ photocatalytic synthesis of Ag nanoparticles (nAg) by crumpled graphene oxide composite membranes for filtration and disinfection applications. *Environ. Sci. Technol.* **2016,** *50* (5), 2514-2521.
3. Hu, Y.; Wang, Y.; Jiang, H.; Li, Y.; Cohen, T.; **Jiang, Y.**; Wang, B.; Zhang, L.; Biswas, P.; Li, C., Engieering the outermost layers of TiO_2 nanoparticles using in situ Mg doping in a flame aerosol reactor. *AIChE J*. DOI: 10.1002/aic.15451.

4. Nie, Y.; Wang, W.-N.; **Jiang, Y.;** Fortner, J. D.; Biswas, P., Aminated reduced graphene oxide-titanium dioxide nanocomposites for simultaneous carbon dioxide adsorption and photoreduction. *Catal. Sci. Technol.* **2016**, 6 (16), 6187-6196. (**Back Cover Article**)
5. **Jiang, Y**.; Wang, W.-N.; Liu, D.; Nie, Y.; Li, W.; Wu, J.; Zhang, F.; Biswas, P.; Fortner, J. D., Engineered crumpled graphene oxide nanocomposite membrane assemblies for advanced water treatment processes. *Environ. Sci. Technol.* **2015,** *49* (11), 6846-6854.
6. **Jiang, Y.**; Wang, W.-N.; Biswas, P.; Fortner, J. D., Facile aerosol synthesis and characterization of ternary crumpled graphene–TiO_2–magnetite nanocomposites for advanced water treatment. *ACS Appl. Mater. Interfaces* **2014,** *6* (14), 11766-11774.
7. Wang, W.-N.; **Jiang, Y**.; Fortner, J. D.; Biswas, P., Nanostructured graphene-titanium dioxide composites synthesized by a single-step aerosol process for photoreduction of carbon dioxide. *Environ. Eng. Sci.* **2014,** *31* (7), 428-434.
8. Wang, W.-N.; **Jiang, Y**.; Biswas, P., Evaporation-induced crumpling of graphene oxide nanosheets in aerosolized droplets: confinement force relationship. *J. Phys. Chem. Lett.* **2012,** *3* (21), 3228-3233.
9. Xing, X.; Zhu, X.; Li, H.; **Jiang, Y**.; Ni, J., Electrochemical oxidation of nitrogen-heterocyclic compounds at boron-doped diamond electrode. *Chemosphere* **2011**, 86(4), 368-375.
10. Zhu, X.; Ni, J.; Xing, X.; Li, H.; **Jiang, Y.**, Synergies between electrochemical oxidation and activated carbon adsorption in three-dimensional boron-doped diamond anode system. *Electrochim. Acta* **2011,** *56* (3), 1270-1274.
11. **Jiang, Y.**; Zhu, X.; Li, H.; Ni, J., Effect of nitro substituent on electrochemical oxidation of phenols at boron-doped diamond anodes. *Chemosphere* **2010,** *78* (9), 1093-1099.
12. Li, H.; Zhu, X.; **Jiang, Y.**; Ni, J., Comparative electrochemical degradation of phthalic acid esters using boron-doped diamond and Pt anodes. *Chemosphere* **2010,** *80* (8), 845-851.
13. Zhu, X.; Ni, J.; Wei, J.; Xing, X.; Li, H.; **Jiang, Y.**, Scale-up of BDD anode system for electrochemical oxidation of phenol simulated wastewater in continuous mode. *J. Hazard. Mater.* **2010,** *184* (1-3), 493-498.
14. Zhu, X.; Ni, J.; Li, H.; **Jiang, Y.**; Xing, X.; Borthwick, A. G., Effects of ultrasound on electrochemical oxidation mechanisms of *p*-substituted phenols at BDD and PbO_2 anodes. *Electrochim. Acta* **2010,** *55* (20), 5569-5575.
15. Yuan, S.; Xi, Z.; **Jiang, Y.**; Wan, J.; Wu, C.; Zheng, Z.; Lu, X., Desorption of copper and cadmium from soils enhanced by organic acids. *Chemosphere* **2007,** *68* (7), 1289-1297.

Manuscripts in Review/Preparation

1. **Jiang, Y**.; Raliya, R.; Fortner, J. D.; Biswas, P., Graphene oxide aqueous aggregation: interplay between material and natural organic matter propterties. To be submitted to *Environ. Sci. Technol.*

2. **Jiang, Y.,** Biswas, P.; Fortner, J. D., A review of recent developments in graphene-enabled water treatment membranes. submitted to *Environ. Sci.: Water Res. Technol.*
3. **Jiang, Y.**; Biswas, P.; Fortner, J. D., Graphene oxide functionalized polysulfone ultrafiltration membranes: effects of material properties. In preparation for *J. Membr. Sci.*
4. Liao, P.; Li, W.; Wang, D.; **Jiang, Y**.; Fortner, J.D.; Yuan, S., Effect of reduced humic acid on the transport of ferrihydrite nanoparticles under anoxic conditions. Submitted to *Water Res.*
5. Hu, Y.; Xu, N.; Wang, Y.; Nie, Y.; **Jiang, Y**.; Biswas, P.; Li, C., Anatase porous TiO_2 microspheres: aerosol spray pyrolysis synthesis and tailored photocatalytic activity. To be submitted to *Che. Eng. J.*
6. Lu, L.; Hu, Y.; Jiang, H.; Wang, Y.; **Jiang, Y**.; Niu, X.; Biswas, P.; Li, C., Ultra-high lithium storage by synergistic effect of doping of mesoporous structure for multi-shell $LiMn_2O_4$ cathode. To be submitted to *Small*.
7. Soundappan, T.; **Jiang, Y.**; Raliya, R.; Biswas, P., Aerosol-based crumpled graphene oxide film modified electrodes for electrochemical biosensing applications. In preparation for *Bioelectrochemistry*.
8. Liao, P.; Li, W.; **Jiang, Y**.; Wu, J.; Yuan, S.; Fortner, J.D.; Giammar, D.E., Formation, aggregation and deposition of NOM-iron colloids formed at anoxic-oxic interfaces. In preparation for *Environ. Sci. Technol*.
9. Liao, P.; Pan, C.; Ding, W.; Wu, J.; Li, W.; **Jiang, Y.**; Yuan S.; Fortner, J.D.; Giammar, D.E., Chromium redox cyclying, complexation, and transport by NOM-Fe colloids formed at anoxic-oxic interfaces. In preparation for *Environ. Sci. Technol.*

Book Chapters:

1. Contributing author. Transformation: case studies of global innovation cities, 2011, Tsinghua University Press: Beijing, China. (In Chinese)
2. Contributing author. From Strategy to Action: An overview of sustainable development in the European Union, 2008, Social Sciences Academic Press: Beijing, China. (In Chinese)

SELECTED PRESENTATIONS (*Presenter with **)**

1. **Jiang, Y**.*, Crumpled graphene oxide: aerosol synthesis and environmental applications. China University of Geosciences, Wuhan, China, June 17, 2016.
2. **Jiang, Y.**, Biswas, P., Fortner, J. D.*, Engineered crumpled graphene oxide nanocomposite membrane assemblies for advanced water treatment processes. The 251st ACS National Meeting, San Diego, CA, March 13-17, 2016.
3. Li, W.*, Liao, P., **Jiang, Y.**, Yuan S., Giammar, D., Fortner, J. D., Adsorption of natural organic matter (NOM) onto environmental surfaces. The 251st ACS National Meeting, San Diego, CA, March 13-17, 2016.

4. **Jiang, Y.***, Crumpled graphene oxide: aerosol synthesis and environmental applications. Department of Energy, Environmental and Chemical Engineering, Washington University in St. Louis, St. Louis, MO, March 4, 2016.
5. Li, W.*, Lee S., Wu, J., **Jiang, Y.**, Kim, C., Hinton, C., Fortner, J. D., Engineering superparamagnetic iron oxide nanocrystals for environmental applications. The 250th ACS National Meeting, Boston, MA, August 16-20, 2015. (Poster)
6. **Jiang, Y.***, Raliya, R., Fortner, J. D., Biswas, P., Aqueous stability of reduced graphene oxide: effects of surface chemistry, morphology, and humic acids. Gordon Research Conference on Environmental Nanotechnology, Mount Snow Resort, VT, June 20-26, 2015. (Poster)
7. **Jiang, Y.***, Biswas, P., Fortner, J. D., Engineered crumpled graphene oxide nanocomposite membrane assemblies for advanced water treatment processes. Gordon Research Conference on Environmental Nanotechnology, Mount Snow Resort, VT, June 20-26, 2015. (Poster)
8. **Jiang, Y.***, Raliya, R., Fortner, J. D., Biswas, P., Aqueous stability of reduced graphene oxide: effects of surface chemistry, morphology, and humic acids. AEESP Research and Education Conference, New Haven, CT, June 13-16, 2015. (Poster)
9. Li, W.*, Hinton, C., Lee S., Wu, J., **Jiang, Y.**, Fortner, J. D., Surface engineering magnetic nanoparticles for aqueous applications: design and characterization of tailored organic bilayers. The 249th ACS National Meeting, Denver, CO, March 22-26, 2015.
10. **Jiang, Y.***, Wang, W. N., Liu, D., Nie, Y., Li, W., Wu, J., Zhang, F., Biswas, P., Fortner, J. D., Engineered crumpled graphene oxide nanocomposite membrane assemblies for advanced water treatment processes. Mid-America Environmental Engineering Conference, Missouri University of Science and Technology, Rolla, MO, November 15th, 2014.
11. Nie, Y.*, Wang, W. N., **Jiang, Y.**, Fortner J. D., Biswas, P., Aminated reduced graphene oxide-titanium dioxide nanocomposites (AGOTi) for carbon dioxide capture and photoreduction, The 33rd AAAR Annual Conference, Orlando, FL, October 21-24, 2014.
12. **Jiang, Y.***, Wang, W. N., Nie, Y., An, S., Biswas, P., Fortner, J. D., Engineered crumpled graphene nanocomposites for photocatalytic environmental reduction applications. The 248th ACS National Meeting, San Francisco, CA, August 10-14, 2014.
13. **Jiang, Y.***, Liu, D., Wang, W. N., Nie, Y., Li, W., Wu, J., Zhang, F., Biswas, P., Fortner, J. D., Crumpled graphene oxide nanocomposites for multifunctional water treatment membrane structures. The 248th ACS National Meeting, San Francisco, CA, August 10-14, 2014.
14. Wang, W. N., **Jiang, Y.**, Fortner J. D., Biswas, P.*, Development of crumpled graphene-TiO_2 nanocomposites for CO_2 photoconversion into hydrocarbon fuels, Conference on Aerosol Technology, Karlsruhe, Germany, June 16-18, 2014.

15. **Jiang, Y.***, Wang, W. N., Biswas, P., Fortner, J. D., High performance crumpled graphene-TiO_2 photocatalysts for water treatment technologies. The 247th ACS National Meeting, Dallas, TX. March 16-20, 2014.
16. Wu, J.*, Li, W., Petrie, L., **Jiang, Y.**, Fortner, J. D., Reduction of hydroxylated C60 (fullerenol) by Zn (0) in water: reaction kinetics and product characterization. Mid-American Environmental Engineering Conference, Washington University in St. Louis, St. Louis, MO, September 21, 2013.
17. Wang, W. N.*, **Jiang, Y.**, Fortner J. D., Biswas, P., Development of crumpled graphene-based nanocomposites via aerosol route for environmental applications, The 32nd AAAR Annual Conference, Portland, OR, September 30-October 4, 2013.
18. **Jiang, Y.**, Wang, W. N., Biswas, P., Fortner, J. D.*, Engineered crumpled graphene oxide-based nanocomposites as platform materials for advanced water treatment technologies. Gordon Research Conference on Environmental Nanotechnology, Stoweflake Resort and Conference Center Stowe, VT, June 2-7, 2013. (Poster)
19. Fortner, J. D.*, Wu, J., Li, W., Alemany, L., Petrie, L., Welker, C. G., **Jiang, Y.**, Reduction of hydroxylated fullerene (fullerenol) by Zn(0) in water: reaction kinetics and product characterization. Gordon Research Conference on Environmental Science -Water, Holderness, NH, June 24-29, 2012. (Poster)

PATENTS

Fortner, J. D., Biswas, P.; **Jiang, Y.**; Wang, W.-N., Composite Nanostructures Having a Crumpled Graphene Oxide Shell. International Patent Application PCT/US2015/021084

JOURNAL REVIEW ACTIVITY

Chemosphere, Desalination and Water Treatment, Energy & Fuels, Environmental Science & Technology, Industrial & Engineering Chemistry Research, Journal of Hazardous Materials, Materials Science in Semiconductor Processing, Nanomaterials and Nanotechnology, New Journal of Chemistry, RSC Advances, Water, Air, & Soil Pollution.